UNIVERSIDADE TÉCNICA DE LISBOA

INSTITUTO SUPERIOR TÉCNICO

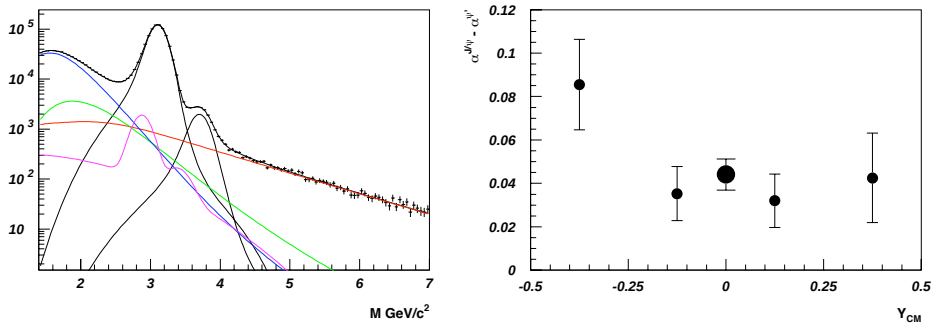

J/ψ and ψ' production in 450 GeV pA interactions and its dependence on the rapidity and X_F

Ruben Shahoyan

(Licenciado)

Dissertação para obtenção do Grau de Doutor em Física

Orientador:	Doutor Peter Arnold August Sonderegger
Co-Orientador:	Doutor João Carlos Carvalho de Sá Seixas
Júri:	
Presidente:	Reitor da Universidade Técnica de Lisboa
Vogais:	Doutor Helmut Satz
	Doutora Maria da Conceição Abreu e Silva
	Doutor Jorge Venceslau Comprido Dias de Deus
	Doutor Peter Arnold August Sonderegger
	Doutora Maria Paula Frazão Bordalo e Sá
	Doutor João Carlos Carvalho de Sá Seixas

Abril 2001

UNIVERSIDADE TÉCNICA DE LISBOA

INSTITUTO SUPERIOR TÉCNICO

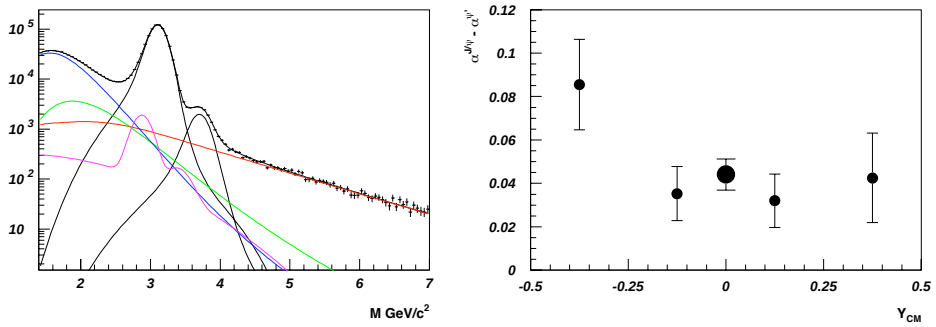

J/ψ and ψ' production in 450 GeV pA interactions and its dependence on the rapidity and X_F

Ruben Shahoyan

(Licenciado)

Dissertação para obtenção do Grau de Doutor em Física

Orientador:	Doutor Peter Arnold August Sonderegger
Co-Orientador:	Doutor João Carlos Carvalho de Sá Seixas
Júri:	
Presidente:	Reitor da Universidade Técnica de Lisboa
Vogais:	Doutor Helmut Satz
	Doutora Maria da Conceição Abreu e Silva
	Doutor Jorge Venceslau Comprido Dias de Deus
	Doutor Peter Arnold August Sonderegger
	Doutora Maria Paula Frazão Bordalo e Sá
	Doutor João Carlos Carvalho de Sá Seixas

Abril 2001

Abstract

This report presents the results of the study of the J/ψ and ψ' production in pA interactions at 450 GeV beam energy and its dependence on the rapidity and X_F variables.

The suppression of the charmonia in the nucleus-nucleus collisions is considered to be the most reliable signature of the Quark-Gluon Plasma formation but it should be distinguished from their suppression due to the hadronic interactions. For this reason it is important to understand the details of the production of J/ψ and ψ' in pA interactions and the difference in the suppression of these two states.

Two different sets of pA interactions data collected by the NA50 dimuon experiment at the CERN SPS between 1996 and 2000, on Be, Al, Cu, Ag and W targets were analyzed. The work with one of these sets, obtained at very high beam intensity and thus having very large statistics, required modifications in the standard NA50 reconstruction package.

While measuring the pA cross section of J/ψ production in the dimuon channel is a relatively easy task, due to the cleanness of the signal, the precise measurement of the ψ' meson is more problematic due to the low $\mu\mu$ branching ratio and in the case of the NA50 experiment due to the difficulty in accounting for the presence of the J/ψ tail, caused by the insufficient mass resolution.

The high statistics data allowed to compute the cross sections of the J/ψ and ψ' mesons in narrow kinematical bins and, more important, to measure the difference of the dependence of these cross sections on the mass number of the target. The accuracy of the measurement is good enough to conclude that the ψ' suffers more suppression than the J/ψ, which is consistent with a similar observation made at 800 GeV beam energy by the E866/NuSea collaboration.

Key words

Proton-nucleus interactions; Dimuon production; Drell-Yan and charmonia cross sections; Quark-Gluon-Plasma; Charmonia suppression; Track reconstruction.

Resumo

Este trabalho apresenta o resultado do estudo da produção dos estados charmonia J/ψ e ψ' em colisões pA a 450 GeV e da sua dependência em função da rapidez e da variavel x_F.

A supressão destes estados charmonia em colisões núcleo-núcleo é considerada como a assinatura mais fiável da formação do plasma de quarks e gluões. Há no entanto que distingui-la da sua supressão devido às interacções hadrónicas. Por esta razão é importante a compreensão detalhada da produção das ressonâncias J/ψ e ψ' em colisões pA e da diferença entre a supressão dos dois estados.

Neste trabalho foram analisados dois conjuntos diferentes de dados obtidos pela experiência NA50 no CERN SPS entre 1996 e 2000 com alvos de Be, Al, Cu, Ag e W. O tratamento de um destes conjuntos, obtido com intensidades de feixe muito elevadas, e tendo portanto muita estatística, necessitou de modificações no programa de reconstrução de NA50.

A medida da secção eficaz de produção do J/ψ no canal dimuão é relativamente fácil graças à clareza do sinal. No entanto a medida da produção do mesão ψ' é mais problemática devido à sua baixa taxa de decaímento no canal dimuão e também à insuficiente resolução em massa da experiência NA50, o que dificulta o ajuste desta ressonância na presenca da cauda do J/ψ.

Os dados de alta estatística permitem o cálculo das secções eficazes dos mesões J/ψ e ψ' em janelas cinemáticas pequenas e a medida da diferença da dependência destas secções eficazes com o número de massa do alvo. A precisão desta medida é suficiente para concluir que o ψ' é mais suprimido que o J/ψ, confirmando observações similares realizadas com feixe de protões de 800 GeV pela colaboração E866/NuSea.

Palavras chave

Interacções protão-núcleo; Produção de dimuões; Secções eficazes de Drell-Yan e charmonia; Plasma de quarks e gluões; Supressão de estados charmonia; Reconstrução de traços;

Acknowledgements

I would like to thank all people who somehow helped me to do this work.

First of all I am expressing my gratitude to my supervisors João Seixas and Peter Sonderegger for their long time support.

I am grateful to many of my colleagues from NA50 experiment, particularly Paula Bordalo, João Cruz, Hrant Gulkanyan, Louis Kluberg, Carlos Lourenço and Siocha Ramos for very informative discussions and comments.

I express my deep gratitude to the whole collective of LIP (Laboratório de Instrumentação e Física Experimental de Partículas) where the most of the work was done for their hospitality and attention and particularly its NA50 group for the financial support. I also want to acknowledge the help of its computer experts Jorge Gomes and João Martins.

The work was supported by the Fundação para Ciência e a Tecnologia under the contract RPAXIS XXI/BD/16116/98.

Contents

Abstract **i**

Resumo **iii**

Acknowledgements **v**

Introduction **1**

1 Physics Overview **3**
1.1 Quark Gluon Plasma . . . 3
1.2 QGP Signatures . . . 4
1.2.1 Thermodynamic Variables . . . 4
1.2.2 Strangeness Enhancement . . . 5
1.2.3 Chiral Symmetry Restoration Signatures . . . 5
1.2.4 Thermal Photons and Dileptons . . . 6
1.2.5 Charmonia Suppression . . . 6
1.3 Processes Contributing to the Dimuon Spectrum . . . 7
1.3.1 Drell-Yan Process . . . 7
1.3.2 Open Charm . . . 9
1.3.3 Charmonia . . . 12
1.4 Drell-Yan and Charmonia production in *pA* and *AB* collisions . . . 17

2 Experiment Description **23**
2.1 General description . . . 23
2.2 Beam and its Monitoring . . . 24
2.2.1 Argon Counters . . . 24
2.2.2 Beam Hodoscope . . . 24
2.3 Target System . . . 24
2.4 Muon Spectrometer . . . 25
2.4.1 Hadron Absorber . . . 25
2.4.2 Magnet . . . 26
2.4.3 Proportional Chambers . . . 27
2.4.4 Trigger System . . . 28
2.5 Centrality Measurement . . . 29
2.5.1 Electromagnetic Calorimeter . . . 29
2.5.2 Zero-Degree Calorimeter . . . 29
2.5.3 Multiplicity Detector . . . 30
2.6 Kinematics Resolution . . . 30

3 Data Reconstruction and Selection **33**
3.1 Data Taking . . . 33
3.2 Data Reconstruction . . . 33
3.2.1 Standard Reconstruction Procedure . . . 33

3.2.2 Modified Reconstruction Algorithm . . . 35
3.2.3 Reconstruction Efficiency Estimation . . . 35
3.3 Data Selection . . . 41
3.3.1 Run Selection . . . 41
3.3.2 Event Selection Cuts . . . 42

4 Analysis Procedure **45**
4.1 Non-Signal Contributions . . . 45
4.1.1 Estimation of the Combinatorial Background . . . 45
4.1.2 Target-Out Contribution . . . 47
4.2 Functional Forms for Different Signals . . . 49
4.2.1 Drell-Yan and Open Charm spectra . . . 49
4.2.2 J/ψ and ψ' spectra . . . 50
4.3 The Fitting Procedure . . . 53
4.4 Acceptances Calculation . . . 55
4.5 Absolute Cross Section Calculation . . . 57
4.5.1 Counting the Number of Incident Protons . . . 57
4.5.2 Systematic Errors of the Absolute Normalization . . . 59
4.5.3 Summary of the Different Data Sets . . . 62

5 Results **63**
5.1 General features of the fitted data . . . 63
5.2 Results for the absolute cross sections . . . 65
5.2.1 J/ψ cross section . . . 65
5.2.2 ψ' cross section . . . 71
5.2.3 Drell-Yan cross section . . . 76
5.3 Results for the cross sections ratios . . . 79
5.3.1 ψ' to J/ψ ratio . . . 79
5.3.2 J/ψ to Drell-Yan ratio . . . 84
5.4 Comparison with Previous Results . . . 85

6 Conclusions and Outlook **87**
6.1 Summary of the results . . . 87
6.2 Future: NA60 Experiment . . . 88

References **91**

7 Appendix **95**
7.1 Acceptance values for different processes . . . 95
7.2 The Fitted Data Samples . . . 95

List of Tables

1.1 The comparison of the different suppression parametrizations for *Be*, *Al*,*Cu*,*Ag* and *W* targets. The second column shows calculated $< \rho\ L >$ according to Eq.1.34 and the third one is the L variable obtained with $\rho_0 = 0.138 fm^{-3}$ (average nuclear density). The columns 3,4 and 5 show the predictions of the full Glauber model with absorption cross section $\sigma_{abs} = 5\ (10)\ mb$, the suppression factors obtained by the $\exp\{-\sigma_{abs} < \rho L >\}$ parametrization and the results of the fit of the Glauber model points by the A^{α} parametrization, respectively. The last two columns show the relative deviations (in %) of the $< \rho L >$ parametrization and of the A^{α} fit from the Glauber model predictions. 21

2.1 Parameters of the targets for the *pA* data used in this work. 25

4.1 Summary of the analyzed data sets. The data sets for which there was no **Trigger Efficiency Run** taken are marked by '*'. The measured value of the closest in time data set is assumed for these cases. 62

5.1 J/ψ cross section per nucleon in *nb* (not corrected for the $\mu\mu$ branching ratio) for the integrated data and in the four Y_{CM} bins. 65

5.2 J/ψ cross section per nucleon in *nb* (not corrected for the $\mu\mu$ branching ratio) for the integrated data and in the four X_F bins. 66

5.3 J/ψ suppression parameters fitted in Y_{CM} (top part) and X_F (bottom part) bins. For each data set the values are: α parameter of the $\sigma_A = \sigma_0 A^{\alpha}$ parametrization, absorption cross section (in *mb*) for the $\sigma_A = \sigma_0 e^{-<\rho\ L>\sigma_{abs}}$ parametrization (marked as "σ_{abs} [ρL]") and the absorption (marked as "σ_{abs} [Glb.]") and the *pN* production (in *nb*) (marked as "σ_0 [Glb.]") cross sections from the complete Glauber model fit. 70

5.4 ψ' cross section per nucleon in *nb* (not corrected for the $\mu\mu$ branching ratio) for the integrated data and in the four Y_{CM} bins. 71

5.5 ψ' cross section per nucleon in *nb* (not corrected for the $\mu\mu$ branching ratio) for the integrated data and in the four X_F bins. 72

5.6 ψ' suppression parameters for various parametrizations fitted in Y_{CM} (top part) and X_F (bottom part) bins. For each data set the values are: α parameter of the $\sigma_A = \sigma_0 A^{\alpha}$ parametrization, absorption cross section (in *mb*) for the $\sigma_A = \sigma_0 e^{-<\rho\ L>\sigma_{abs}}$ parametrization (marked as "σ_{abs} [ρL]") and the absorption (marked as "σ_{abs} [Glb.]") and the *pN* production (in *nb*) (marked as "σ_0 [Glb.]") cross sections from the complete Glauber model fit. 74

5.7 Cross sections per nucleon (isospin corrected) for Drell-Yan in the $2.9 < M < 4.5\ GeV/c^2$ range as a function of the rapidity in the center of mass. 77

5.8 Cross sections per nucleon (isospin corrected) for Drell-Yan in the $2.9 < M < 4.5\ GeV/c^2$ range as a function of the X_F. 77

5.9 Ratios of the ψ' and J/ψ cross sections (not corrected for the $\mu\mu$ branching ratios) for the integrated data and in the four Y_{CM} bins. 80

5.10 Ratio of the ψ' and J/ψ cross sections (not corrected for the $\mu\mu$ branching ratio) for the integrated data and in the four X_F bins. 81

5.11 Parameters of the suppression of ψ' with respect to the J/ψ fitted in Y_{CM} (Top) and X_F (Bottom) bins: For each data set the values are: $\Delta\alpha$ and R_0 (marked as "R_0 [A^{α}]") of the $R_0 A^{\Delta\alpha}$ parametrization; absorption cross section (in *mb*) and R_0 (marked as "R_0 [ρL]") for the $R_0 e^{-<\rho L>\Delta\sigma_{abs}}$ parametrization. 83
5.12 J/ψ cross section per nucleon in *nb* (not corrected for the $\mu\mu$ branching ratio) measured by NA38 (pC, Al, Cu and W targets) [83] and NA51 (pp and pD) [82] experiments at 450 GeV. The first column shows the original values from the references, while the second one shows the rescaled cross sections. 85
7.1 The acceptances (in %) for the J/ψ, ψ' and Drell-Yan dimuons in the $2.9 < M < 4.5\ GeV/c^2$ range in different rapidity bins. 95
7.2 The acceptances (in %) for the J/ψ, ψ' and Drell-Yan dimuons in $2.9 < M < 4.5\ GeV/c^2$ range in different X_F bins. 95

List of Figures

1.1 Phase diagram of the strongly interacting matter as a function of the **baryon density** and the temperature T. 3
1.2 Energy density and pressure divided by T^4 for the first order Hadron Gas - QGP phase transition in the 2-flavour Lattice-QCD model. The dashed lines show the Stefan-Boltzmann ideal gas density for the two states. 5
1.3 The measured NA50 dimuon spectrum for masses above the light vector mesons. The fitted contributions from J/ψ, ψ', Drell-Yan and $D\overline{D}$ are shown. 7
1.4 The leading order diagram responsible for the Drell-Yan dileptons. 7
1.5 The K-factor for Drell-Yan production measured at beam energies $160-450\ GeV/A$ in pA and $nucleus-nucleus$ interactions. The MRSA N^o43 parton distribution functions are used for the calculated cross section. 8
1.6 Measured nuclear dependence α parameter as a function of X_F for Drell-Yan production at 800 GeV (W and D targets) by E772 [27] (a) and computed one (for the same targets) at 120 GeV (b). The theoretical curves account for different models of the nuclear shadowing effect (from [26]). 9
1.7 Ratios of the measured Drell-Yan cross section per nucleon versus P_T. Solid circles are for the ratios of Fe/Be and W/Be measured by E866/NuSea collaboration [33] and the open circles are for the ratios of Fe/C and W/C are from E772 measurements [27]. The solid curves are shadowing predictions for the E866/NuSea data from leading-order calculations using EKS98 [28] code with MRST [29] parton distribution functions. Figure is taken from [33]. 10
1.8 Cross section per nucleon for forward ($X_F > 0$) $D^0, \overline{D}^0$ (left) and D^+, D^- (right) production in proton and pion induced reactions, as a function of the center of mass energy. The data were taken from NA16 [39], NA27 [40], E743 [41], E653 [42], E789 [43], E769 [44], NA32 [45], WA92 [46], and E706 [47]. The solid lines represent the pp PYTHIA calculations (with $m_c = 1.35\ GeV/c^2$) with K-factor = 3.5 for neutral and 7.0 for charged D-mesons applied. The compilation is taken from [36]. 11
1.9 Evolution with N_{part} of the factor by which the expected charm yield must be scaled in order to describe the yield of intermediate mass dimuons collected by NA38 and NA50 [21]. 12
1.10 The J/ψ production diagrams in Colour Singlet (Left) and Colour Octet (Right) Models. 13
1.11 The phenomenological parametrization (Eq.1.17, [53]) for the J/ψ production energy dependence. The compilation is from [63] 14
1.12 Measured J/ψ yield divided by the normal nuclear absorption, as a function of the energy density reached in pA, SU and $PbPb$ collisions [71]. 15
1.13 (Left) $\psi'/J/\psi$ ratio as a function of the product of the atomic masses of the colliding nuclei, averaged over all collision centralities; (Right) $\psi'/Drell-Yan$ ratio [65] as a function of the variable L (Eq.1.18). No correction for the $\mu\mu$ branching ratio is applied. 16
1.14 α parameters of the J/ψ and ψ' suppression as a function of X_F obtained from comparison of pBe, pFe and pW cross sections [72]. 16

1.15 The definitions of the geometrical parameters of a $nucleus - nucleus$ collision with impact parameter b. 17

1.16 The suppression factors $S(A) = \frac{\sigma_{pA}^{J/\psi}}{\sigma_{NNA}}$ in pA collisions for two values of J/ψ absorption cross section σ_{abs}: 5. mb (circles) and 10. mb (triangles) according to **a)** (filled symbols) Glauber model predictions (Eq. 1.31), **b)** $\exp\{-\sigma_{abs} < \rho L >\}$ parametrization with $< \rho L >$ calculated by Eq.1.34, **c)** A^{α} parametrization for different values of α (dashed lines).
The solid lines show the result of the fit of the Glauber model predictions for five nuclei: Be,Al,Cu,Ag and W by the form $S(A) = s_0 A^{\alpha}/A$ (the 2% error bars are added just to distinguish the fitted nuclei). The numerical values of $\{s_0, \alpha\}$ obtained from the fits are $\{1.107, 0.922\}$ and $\{1.184, 0.860\}$ for $\sigma_{abs} = 5$ and 10 mb respectively. 20

2.1 General layout of the NA50 experiment. 23

2.2 Hadron Absorber used for NA50 pA runs 25

2.3 Frontal (left) and lateral (right) view of the toroidal magnet. 26

2.4 The three planes of the MWPC. 27

2.5 R_1 - R_4 trigger hodoscopes. 28

2.6 $V_i = R_1^i \times R_2^i$ trigger condition on each muon. 29

2.7 Kinematics resolution of NA50 experiment: dimuon mass (for Drell-Yan), rapidity, transverse momentum and X_F (for J/ψ) resolutions as a function of these variables. 31

3.1 Definitions used in the description of the Track Reconstruction procedure. The solid lines show the MWPC wires fired by a muon. 34

3.2 The tracks with a wrong ('ghost') hit attached are often rejected. The solid line showa the MWPC wires fired by the muon. 35

3.3 Ratio of the number of reconstructed dimuons with $2.7 < M < 3.5 \ \ GeV/c^2$ to the value of $Argo1$ counter (accounting for the dead time of the detector) as a function of the beam intensity of the run. The hollow points show the result of the reconstruction by the standard program, while the filled ones are from the upgraded algorithm. 36

3.4 Occupancies per plane (left) and detection efficiencies (right) for MWPC1 and MWPC5 - first chambers of Forward and Backward Telescopes respectively, as a function of the beam intensity. 37

3.5 Result of the reconstruction of the MC J/ψ and Drell-Yan dimuons superimposed on real high intensity run MWPC and hodoscopes data by the standard and upgraded programs. 39

3.6 Ratio between the number of reconstructed and generated events, by the standard program (top) and by the upgraded one (bottom). The numbers on the top are the estimates of the dimuon reconstruction efficiency in two mass bins: $2.7 - 3.5$ and $4.1 - 6.5 \ \ GeV/c^2$, the bottom numbers show the ratio of the number of reconstructed and generated events in these mass bins. 39

3.7 Ratio of the number of reconstructed dimuons with $2.7 < M < 3.5 \ \ GeV/c^2$ corrected by $\varepsilon_{\mu\mu}$, to the value of $Argo1$ counter (accounting for the dead time of the detector) as a function of the beam intensity of the run. The hollow points show the result of the reconstruction by the standard program, while the filled ones are from the upgraded algorithm. 40

3.8 Evolution of the dimuon reconstruction efficiency with the beam intensity obtained with the standard (hollow points) and upgraded (filled points) algorithms. The points deviating from the main sequence are due to hardware problems in the MWPCs. 40
3.9 (Left) Cut on the J/ψ pole position. The runs with the pole deviating by more than 15 MeV/c^2 from the average value are rejected; (Right) Mass resolution for each run at the J/ψ mass. (For $pAl97$ data). 41
3.10 Run selection according to the fraction of the muons triggered in each sextant. The hollow points show the ratio of the μ's triggered in a given sextant to the total amount of muons. The black points show the number of standard deviations of this fraction from its average value (excluding the anomalous points). The runs with more than 3 standard deviations (outside the hatched region) are rejected. (For $pW98$ data) 42
3.11 (Left) χ^2 -estimated probability distributions for the muon to come from the target for the sample of dimuons of mass $2.7 < M < 3.5$ GeV/c^2 in the normal data taking runs (marked as **Tgt.In**) and in the runs without target (**Tgt.Out**). (Right) The corresponding $\mu^+\mu^-$ mass spectra without any PDTARG cut (solid lines) and after the 1% probability cut (error bars). The data are from the pW96 runs. 43
4.1 $\mu^+\mu^+$ and $\mu^-\mu^-$ spectra and their parametrizations for the $pW96$ data with $\oplus$ magnet current polarity. The fitted parameters shown correspond to the $++$ sample fit. 47
4.2 Opposite-sign **Target Out** run spectrum of the $pW96$ data set. The fitted $''signal''$ and $OS =''signal'' + ''CombinatorialBackground''$ functional forms are shown by solid lines. 48
4.3 Shapes of the simulated (generated and reconstructed) Drell-Yan (Left) and Open-Charm (Right) contributions to the pW dimuon spectrum. 50
4.4 Shape of the mass-dependent 'dispersion' extracted according to Eq.4.7 from the Monte-Carlo generated J/ψ mass distribution. 51
4.5 Shapes of the simulated (generated and reconstructed) J/ψ (Left) and ψ' (Right) spectra fitted by the forms $4.6 - 4.9$ 52
4.6 (Left) Results of the $\sigma_{J/\psi}(M)$ fit with three different values of the $M_{high}^{merge} = 3.4, 3.45$ and 3.5 GeV/c^2: the dotted curve corresponds to the results of the Monte-Carlo fit ($\sigma_{J/\psi}^{MC}(M)$), the dot-dashed is for $\sigma_{J/\psi}^{inside}(M)$ adjusted to data inside the region $2.7 - M_{high}^{merge}$ and the solid and dashed curves are the final $\sigma_{J/\psi}^{data}(M)$; (Right) results of the J/ψ and ψ' fits with the two extreme values of M_{high}^{merge}: solid curves are for 3.4 and dashed ones are for 3.5 GeV/c^2. 54
4.7 Acceptance (in percent) for the Drell-Yan process, as a function of the dimuon mass. 55
4.8 Acceptances (in percent) of the J/ψ originated in 450 GeV pA collisions as a function of the dimuon a) rapidity in the laboratory frame, b) transverse momentum, c) Feinman X, d) $\cos\theta$. 56
4.9 Run by run ratios of the three argon counters: from top to bottom : Argo1/Argo2, Argo1/Argo3 and Argo3/Argo2. The left plot shows their dependence on run number (time) while the Right one suggests that the deviations from the average values are caused by their slightly different dependences on the beam intensity. 58

4.10 Ratios of the three argon counters, averaged over the selected runs of each data set in a chronological order of the data taking period. 58
4.11 Ratio of the number of reconstructed dimuons with $2.7 < M < 3.5$ to the value of $Argo1$ counter (accounting for the dead time of the detector) corrected for dimuon trigger and reconstruction efficiencies as a function of the run number (Left) and the beam intensity of the run. The ratio of the RMS to the average value is taken as a systematic error on the product of the reconstruction and trigger efficiencies 61
5.1 (Left) The correlation between the binings in Y_{CM} and X_F used in this analysis for the dimuons with $2.7 < M < 3.5\ GeV/c^2$; (Right) The acceptances (in %) for the J/ψ in the chosen Y_{CM} and X_F bins and outside of them. 63
5.2 Data sample with the "worst" χ/NDF obtained (Top) and bin by bin square of the difference between the measured and the fitted values (Bottom). 64
5.3 J/ψ cross section per nucleon in nb (not corrected for the $\mu\mu$ branching ratio) as a function of the rapidity in the center of mass for (Left) High and (Right) Low Intensity data. 65
5.4 J/ψ cross section per nucleon in nb (not corrected for the $\mu\mu$ branching ratio) as a function of X_F for (Left) High and (Right) Low Intensity data. 66
5.5 Ratio of the J/ψ cross sections (in the $-0.5 < Y < 0.5$ range) from the High and Low intensity data fitted by a constant line ($R = 0.957 \pm 0.025$). 67
5.6 J/ψ cross sections per nucleon (for the High (HI) and Low (LI) intensity data sets) in the $-0.5 < Y_{CM} < 0.5$ (Top) and $-0.1 < X_F < 0.1$ (Bottom) ranges fitted by the: (Left) parametrization $\sigma_A = \sigma_0 A^{\alpha}$ (the results are shown on the first line of the legend) and the complete Glauber model (second line); (Right) parametrization $\sigma_A = \sigma_0 e^{-<\rho L>\sigma_{abs}}$. The values for the σ_0 and σ_{abs} are in nb and mb respectively. 68
5.7 J/ψ suppression parameters for various parametrizations fitted in Y_{CM} (Left) and X_F (Right) bins: α parameter (Top); absorption cross section (mb) from the (Middle) complete Glauber model and (Bottom) $\sigma_A = \sigma_0 e^{-<\rho\ L>\sigma_{abs}}$ parametrization. 69
5.8 ψ' cross section per nucleon in nb (not corrected for the $\mu\mu$ branching ratio) as a function of the rapidity in the center of mass for (Left) High and (Right) Low Intensity data. 71
5.9 ψ' cross section per nucleon in nb (not corrected for the $\mu\mu$ branching ratio) as a function of X_F for (Left) High and (Right) Low Intensity data. 72
5.10 Ratio of the ψ' cross sections (in the $-0.5 < Y < 0.5$ range) from the High to the ones of the Low intensity data fitted by a constant line ($R = 0.946 \pm 0.0285$.) 73
5.11 ψ' cross sections per nucleon (for the High (HI) and Low (LI) intensity data sets) in the $-0.5 < Y_{CM} < 0.5$ (Top) and $-0.1 < X_F < 0.1$ (Bottom) ranges fitted by the: (Left) parametrization $\sigma_A = \sigma_0 A^{\alpha}$ (the results are shown on the first line of the legend) and complete Glauber model (second line); (Right) parametrization $\sigma_A = \sigma_0 e^{-<\rho L>\sigma_{abs}}$. The values for σ_0 and σ_{abs} are in nb and mb respectively. . 73
5.12 ψ' suppression parameters for various parametrizations fitted in Y_{CM} (Left) and X_F (Right) bins: α parameter (Top); absorption cross section (mb) from the (Middle) complete Glauber model and (Bottom) $\sigma_A = \sigma_0 e^{-<\rho\ L>\sigma_{abs}}$ parametrization. 75

5.13 Cross sections per nucleon (isospin corrected) for the Drell-Yan in the $2.9 < M < 4.5\ GeV/c^2$ range as a function of the rapidity in the center of mass for High (Left) and Low (Right) intensity data. 76

5.14 Cross sections per nucleon (isospin corrected) for Drell-Yan in the $2.9 < M < 4.5\ GeV/c^2$ range as a function of the X_F for High (Left) and Low (Right) intensity data. 77

5.15 Ratio of the Drell-Yan cross sections (in the $-0.5 < Y < 0.5$ range) from the High and Low intensity data fitted by a constant line. 78

5.16 Ratios of the ψ' and J/ψ cross sections (not corrected for the $\mu\mu$ branching ratios) as a function of the rapidity in the center of mass for (Left) High and (Right) Low Intensity data. 79

5.17 Ratios of the ψ' and J/ψ cross sections (not corrected for the $\mu\mu$ branching ratios) as a function of the X_F bin for (Left) High and (Right) Low Intensity data. 80

5.18 Ratios of the values of ψ' / J/ψ cross sections (in the $-0.5 < Y < 0.5$ range) from the High and Low intensity data fitted by a constant line ($R = 0.987 \pm 0.015$). 81

5.19 Ratio of the ψ' and J/ψ cross sections (for the High (HI) and Low (LI) intensity data sets) in the $-0.5 < Y_{CM} < 0.5$ (Top) and $-0.1 < X_F < 0.1$ (Bottom) ranges fitted by the: (Left) parametrization $R_0 A^{\Delta\alpha}$; (Right) parametrization $R_0 e^{-<\rho L>\Delta\sigma_{abs}}$. The values for the $\Delta\sigma_{abs}$ are in mb. 82

5.20 Parameters of the suppression of the ψ' with respect to the J/ψ for various parametrizations fitted in Y_{CM} bins: (Left) $R_0 A^{\Delta\alpha}$ parametrization , (Right) $R_0 e^{-<\rho L>\Delta\sigma_{abs}}$ parametrization. 82

5.21 Ratios of J/ψ cross sections to the isospin corrected cross sections of Drell-Yan in the $2.9 < M < 4.5\ GeV/c^2$ range (for the High (HI) and Low (LI) intensity data sets) in the $-0.5 < Y_{CM} < 0.5$ (Top) and $-0.1 < X_F < 0.1$ (Bottom) ranges fitted by the: (Left) parametrization RA^{α}(the results are shown on the first line of the legend) and the complete Glauber model (second line); (Right) parametrization $Re^{-<\rho L>\sigma_{abs}}$. The values for the σ_{abs} are in mb. 84

5.22 Fit of the dependence of the J/ψ cross section per nucleon on the target mass number with (Left) A^{α} parametrization; (Center) complete Glauber model calculation; (Right) $e^{-<\rho L>\sigma_{abs}}$ parametrization. Each plot compares three different combinations of data sets: NA51 measurements of pp and pd cross sections with NA38 results for pC, pAl and pW (solid line), NA51 with High (dashed) and Low (dotted) intensity data. 85

5.23 Drell-Yan cross sections per nucleon (in nb) obtained by the NA51 experiment compared with the results of the present study. 86

6.1 (Left) α parameters for the J/ψ and ψ' as a function of the Y_{CM} obtained from the absolute cross sections fit; (Right) Their difference obtained from the fit of the ψ' to J/ψ cross sections ratios. 87

6.2 (Left) Absorption cross sections (mb) from $\sigma_A = \sigma_0 e^{-<\rho L>\sigma_{abs}}$ parametrization for the J/ψ and ψ' as a function of the Y_{CM} obtained from the absolute cross sections fit; (Right) Their difference obtained from the fit of the ψ' to J/ψ cross sections ratios. 88

6.3 Layout of the NA60 experiment. 90

7.1 Fit for all data sets in the $-0.5 < Y_{CM} < 0.5$ range. For each histogram the total numbers of the fitted opposite sign events, obtained χ^2/NDF of the fit, number of the J/ψ dimuons, ratio of the ψ' to the J/ψ and of the J/ψ to the Drell-Yan events in the $2.9 < M < 4.5\ GeV/c^2$ range (shown by the dotted lines) is printed (not corrected for the acceptance). The errors shown in the parenthesis are for the corresponding last digits. 97
7.2 Fit for all data sets in the $-0.5 < Y_{CM} < -0.25$ range. 98
7.3 Fits for all data sets in the $-0.25 < Y_{CM} < 0.0$ range. 99
7.4 Fits for all data sets in the $0.0 < Y_{CM} < 0.25$ range. 100
7.5 Fits for all data sets in the $0.0 < Y_{CM} < 0.5$ range. 101
7.6 Fits for all data sets in the $-0.1 < X_F < 0.1$ range. 102
7.7 Fits for all data sets in the $-0.1 < X_F < -0.05$ range. 103
7.8 Fits for all data sets in the $-0.05 < X_F < 0.0$ range. 104
7.9 Fits for all data sets in the $0.0 < X_F < 0.05$ range. 105
7.10 Fits for all data sets in the $0.05 < X_F < 0.1$ range. 106
7.11 The J/ψ cross sections per nucleon (for the High (HI) and Low (LI) intensity data sets) in four Y_{CM} bins fitted by the: (Left) parametrization $\sigma_A = \sigma_0 A^\alpha$ (the results are shown on the first line of the legend) and the complete Glauber model (second line); (Right) parametrization $\sigma_A = \sigma_0 e^{-<\rho L>\sigma_{abs}}$. The values for the σ_0 and σ_{abs} are in *nb* and *mb* respectively. 107
7.12 The J/ψ cross sections per nucleon (for the High (HI) and Low (LI) intensity data sets) in four X_F bins fitted by the: (Left) parametrization $\sigma_A = \sigma_0 A^\alpha$ (the results are shown on the first line of the legend) and the complete Glauber model (second line); (Right) parametrization $\sigma_A = \sigma_0 e^{-<\rho L>\sigma_{abs}}$. The values for the σ_0 and σ_{abs} are in *nb* and *mb* respectively. 108
7.13 The ψ' cross sections per nucleon (for the High (HI) and Low (LI) intensity data sets) in four Y_{CM} bins fitted by the: (Left) parametrization $\sigma_A = \sigma_0 A^\alpha$ (the results are shown on the first line of the legend) and complete Glauber model (second line); (Right) parametrization $\sigma_A = \sigma_0 e^{-<\rho L>\sigma_{abs}}$. The values for the σ_0 and σ_{abs} are in *nb* and *mb* respectively. 109
7.14 The ψ' cross sections per nucleon (for the High (HI) and Low (LI) intensity data sets) in four X_F bins fitted by the: (Left) parametrization $\sigma_A = \sigma_0 A^\alpha$ (the results are shown on the first line of the legend) and complete Glauber model (second line); (Right) parametrization $\sigma_A = \sigma_0 e^{-<\rho L>\sigma_{abs}}$. The values for the σ_0 and σ_{abs} are in *nb* and *mb* respectively. 110
7.15 The ratio of the ψ' to J/ψ cross sections per nucleon (for the High (HI) and Low (LI) intensity data sets) in four Y_{CM} bins fitted by the: (Left) parametrization $R_0 A^{\Delta\alpha}$; (Right) parametrization $R_0 e^{-<\rho L>\Delta\sigma_{abs}}$. The values for the $\Delta\sigma_{abs}$ are in *mb*. 111
7.16 The ratio of the ψ' to J/ψ cross sections per nucleon (for the High (HI) and Low (LI) intensity data sets) in four X_F bins fitted by the: (Left) parametrization $R_0 A^{\Delta\alpha}$; (Right) parametrization $R_0 e^{-<\rho L>\Delta\sigma_{abs}}$. The values for the $\Delta\sigma_{abs}$ are in *mb*. 112

Introduction

The long time search of the Quark Gluon Plasma (QGP) at the CERN SPS recently yielded results which hint the production of such state of the matter in the collisions of ultra-relativistic heavy ions. One of the most reliable signatures of the QGP formation is considered to be the suppression of the J/ψ and ψ' charmonia states due to the colour screening in the deconfined matter, which was predicted already in 1986 by Matsui and Satz. Already in 1987 the NA38 experiment (predecessor of NA50) reported an observation of such effect in nucleus-nucleus collisions, but later it was realized that the charmonia should be suppressed already in the normal nuclear matter due to their interactions with the hadrons.

The interest in the study of charmonia production got a new boost after the observation by the NA50 experiment that the J/ψ cross section in the PbPb 158 GeV/cA collisions is suppressed more than what one could expect from the models of pure hadronic suppression, an effect called "anomalous suppression". Special attention is given to the pattern of this suppression, having one step at relatively peripheral interactions and another one at very small impact parameters of the collision. Since it is known that part of the measured J/ψ's come from the decays of the ψ' and χ_c states which are more vulnerable due to the smaller binding energy, the present interpretation of this observation assumes that the first step corresponds to the QGP suppression of these heavy charmonia states while the second one is due to the suppression of the directly produced J/ψ.

At the same time there is clear lack of precise data about the behaviour of the ψ' even in proton-nucleus collisions. The reason for this is the weakness of the signal from ψ' in the dimuon channel and the difficulty of its measurement due to the insufficient mass resolution in the case of the NA50 experiment, where there is a considerable contribution from the J/ψ tail under the ψ' peak. For a long time the precision of the available data did not allow to see any difference in the level of suppression of the J/ψ and ψ' in proton-nucleus collisions although it was observed long time ago by the NA38 experiment that in the SU interactions the ψ' is more suppressed than the J/ψ. The lack of any observed difference in pA interactions and the unexpectedly high absorption cross section lead to the hypothesis that what is suppressed in such a small system due to the hadronic absorption is not the final resonance but an intermediate coloured preresonance state. The additional suppression of the ψ' in the nucleus-nucleus collision is assumed to be due to the interactions of this charmonia state formed outside of the nucleus with the multiple secondaries produced in the collision - so called "comovers".

The situation became less clear once the E866/NuSea collaboration [72] observed in pA 800 GeV interactions a difference in the suppression of J/ψ and ψ' over a broad range of X_F. The motivation of this work was to look for such an effect in the vast data on proton-nucleus interactions at 450 GeV beam energy collected by the NA50 experiment between 1996 and 2000. The special interest was to look if there is any systematic dependence of the suppression level on the rapidity or X_F of the meson, since the mentioned preresonance suppression model predicts that the slow (in the target system) charmonia should suffer less suppression since the corresponding coloured $c\bar{c}$ pairs convert earlier to the final state, which has a smaller absorption cross section.

One should note that a large amount of these data was obtained at very high beam intensities and for a long time was not analyzed since it was noticed that the standard NA50 reconstruction package produced results inconsistent with the low intensity data. For this reason the work with

these high statistics data required considerable changes in the reconstruction software.

The work is organized in the following way. The Chapter 1 presents a short review of QGP and dimuon physics. The description of the NA50 apparatus is given in the Chapter 2 and it is followed by the Chapter 3 presenting the methods of data reconstruction and selection with emphasis on the mentioned modifications done in the standard software. Chapter 4 describes the methods used for the analysis of the dimuon spectrum and cross sections calculation and errors estimation. The final results are presented in the Chapter 5.

1 Physics Overview

1.1 Quark Gluon Plasma

The fundamental property of the QCD - theory of strong interactions is the increase of the strong coupling α_s with the distance between the interacting particles. This feature, caused by the non-abelian nature of the underlying $SU(3)$ symmetry group is believed to be the reason for the **confinement**: binding of the coloured quarks and gluons into the colour-singlet hadrons only and impossibility to separate them on distances larger than that of the typical hadronic size ($\sim 1fm$).

Inversely, as the quarks and gluons approach closer, the interaction coupling drops down: property called **asymptotic freedom**. This property has inspired the phenomenological **MIT bag** hadron model [1], where the partons inside the hadron are considered noninteracting and kept together in the bag by the negative vacuum pressure.

One could consider the possibility that when the hadrons are squeezed to high enough densities and start to overlap they lose their identity and form one single bag. The transition to such state, called **Quark Gluon Plasma, (QGP)**, is expected to occur at densities ≥ 5 times the one of the nuclear matter ($\sim 0.17fm^{-3}$). Alternatively, the transition point may be reached by heating the nuclear matter to high enough temperatures. Application of Lattice-QCD techniques [2] predicts such transition at $T \sim 150 - 200MeV$[1]. The exact value of the transition temperature and the order of the phase transition is still under investigation due to the strong dependence on the lattice model details (number of quark flavours, their masses, etc.). Another prediction of

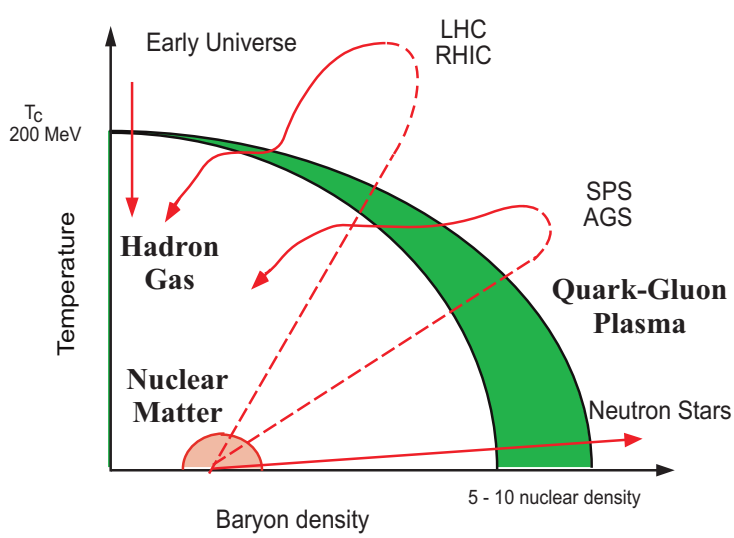

Figure 1.1: Phase diagram of the strongly interacting matter as a function of the **baryon density** and the temperature T.

[1]This temperature is very close to the limiting temperature of Hagedorn [3,4] for the existence of the hadronic matter, although in his theory it was a consequence of the assumed exponential hadronic mass spectrum.

Lattice-QCD is that in parallel with the QCD phase transition the spontaneously broken **chiral symmetry** restores [5].

It is believed that the QGP existed in nature only in the first $10\mu s$ of the existence of the Universe which subsequently hardonized. But ultra-relativistic Heavy Ion Collisions (HIC) offer the possibility to create this state in the laboratory conditions. Fig. 1.1 shows the phase diagram of the strongly interacting matter as a function of the baryonic chemical potential and of the temperature. The domains covered by present and future accelerators are marked. There is strong evidence that the QGP transition was observed already in HIC at the SPS [6].

1.2 QGP Signatures

Despite a quite clear understanding of the nature of the QGP and lack of any doubt in its existence, its observation cannot be a straightforward task due to its rapid hadronization. Thus one should find indirect **signatures**: observables which are affected by the QGP state. This section presents a short review of the most popular ones.

1.2.1 Thermodynamic Variables

This kind of signatures are based on the detection of change of such global variables as the energy density ε, pressure P or entropy density s of the interacting matter as a function of the temperature T and baryon density μ_B.

In a very simplified form, the non-interacting massless hadron gas has essentially three degrees of freedom while even the two-flavour QGP (with massless u and d quarks) has 16 gluonic and 12 quark degrees of freedom. Thus, the energy density in case of QGP formation, according to the Stefan-Boltzmann law, should jump from

$$\varepsilon_{HG} = 3\ \varepsilon_\pi = 3\frac{\pi^2}{30}T^4 \tag{1.1}$$

to

$$\varepsilon_{QGP} = 16\ \varepsilon_g + 12\ (\varepsilon_q + \varepsilon_{\bar{q}}) = 16\frac{\pi^2}{30}T^4 + 12\frac{7}{4}\frac{\pi^2}{30}T^4 = 37\frac{\pi^2}{30}T^4 \tag{1.2}$$

Fig. 1.2 shows the energy density and the pressure obtained from Lattice-QCD calculations [2] with the two quark flavours included.

There are more or less commonly accepted recipes for the extraction of these variables from the directly measurable observables [7, 8]: T is usually fitted from the inverse m_T slope of the produced particles (after accounting for the possible hydrodynamical transverse flows), s is identified with the hadrons rapidity density dN/dy and the simplest way to estimate the energy density reached in the central region of the collision (far enough from the target and projectile fragmentation parts) is the Bjorken relation [9], connecting it with the transverse energy E_T produced per unit of rapidity:

$$\varepsilon = \frac{\frac{dE_T}{dy}\big|_{y=0}}{A_T \cdot \tau} \quad [GeV/fm^3] \tag{1.3}$$

where A_T is the transverse area of the collision and τ is the characteristic thermalization time ($\sim 1fm$).

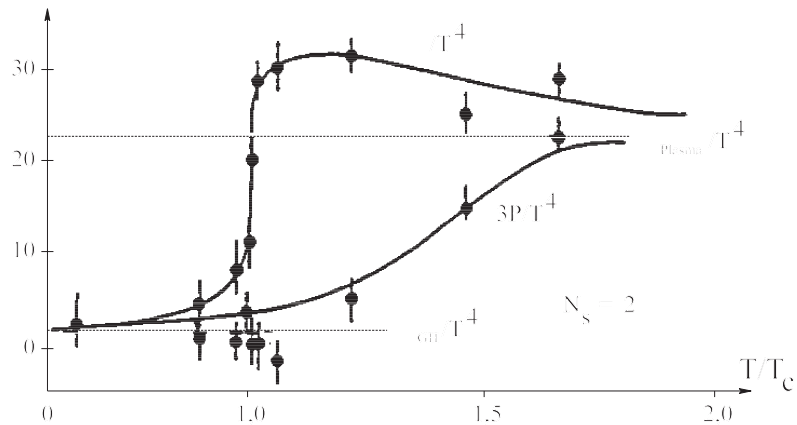

Figure 1.2: Energy density and pressure divided by T^4 for the first order Hadron Gas - QGP phase transition in the 2-flavour Lattice-QCD model. The dashed lines show the Stefan-Boltzmann ideal gas density for the two states.

1.2.2 Strangeness Enhancement

In the hadronic phase the production of the hadrons including strange quarks is suppressed relative to the yield of those containing only up and down quarks due to the higher mass of the s quark. In case of QGP formation the threshold for the production of $s\bar{s}$ production is just $\sim 2m_s$ (with m_s being the current mass of the strange quark, i.e. close to the thermal energy of the partons) and the content of the strange quarks should rapidly saturate to its thermal equilibrium value mainly via gluons interactions [10]. Thus one could expect an enhanced yield of hadrons with strange quarks in case of QGP formation, although the exact enhancement factor should by affected by the hadronization and final state interaction processes.

1.2.3 Chiral Symmetry Restoration Signatures

The spontaneously broken chiral symmetry of the QCD vacuum at low temperatures and baryon densities should be restored near the QGP transition point. This is characterized by the vanishing of the $< q\bar{q} >$ condensate and should affect the spectral properties of the mesons [11, 12]. Perhaps the most useful signal of this kind is the modification of the ρ-meson pole which could be detected via its in-medium $\rho \rightarrow l\bar{l}$ decay. This signature called a closer attention after finding by the NA45/Ceres experiment [13] of a strong excess in the dielectron production rate in the mass range $0.3 < M < 0.7\ GeV/c^2$ in the $S-Au$ and $Pb-Au$ collisions when compared with the signal expected from the pA rescaled data. A Range of the phenomenological models which give satisfactory agreement with thses data were created [14–17]. However, there is, so far, no common agreement about the quantitative description of the in-medium modifications of the spectral properties: while it seems to be accepted that the width of the ρ-meson should increase, depending on the approach to the problem the decrease or even increase of its mass is predicted.

Another possible effect of the chiral symmetry restoration is the formation of domains of Disoriented Chiral Condensates [18]: local misalignments of the chiral order parameter $< q\bar{q} >$, manifesting itself at the hadronization stage by non-statistical fluctuations of the ratio N_{π^o}/N_π from its normal value, $1/3$.

1.2.4 Thermal Photons and Dileptons

Both the hot hadronic gas and the QGP should emit the thermal radiation (real as well as virtual photons, the latter being detected via the $\gamma_* \rightarrow l\bar{l}$ decay). The advantage of this kind of signals is that since they are not affected by the final state interactions they can convey the signals directly from the QGP phase.

For the direct thermal photons the dominant source in the hadron gas phase is the $\pi\rho \rightarrow \gamma\rho$ process while in the case of the QGP it is $gq \rightarrow \gamma q$ [19]. Although at the temperatures close to T_c the yields and the spectral shape of the direct photons from both phases are nearly equal, the radiation from the initially very hot plasma could be visible at high transverse momenta ($2-5\ GeV/c$). Unfortunately, at presently achievable energies the signal from the direct photons is hidden under the background from the hadronic decays and for the moment only upper limits for their production are defined.

The thermal dileptons, created in $q\overline{q}$ (in the QGP) or $\pi^+\pi^-$ (in the hadron gas phase) annihilation, were the primary aim of the NA38 experiment, predecessor of NA50. Their detection, even at high masses, is complicated due to the background from the hadronic resonances decay and from the Drell-Yan process. Nevertheless, this signal could be responsible for the excess in the dimuon spectrum [20] at masses $1.5 < M < 2.5\ GeV/c$ observed by the NA38/50 experiments in S-U and Pb-Pb collisions [21].

1.2.5 Charmonia Suppression

The suppression of the charmonia production cross section [22] is probably the most reliable signature of QGP formation. At high densities, Debye screening in the QGP reduces the range of the attractive force between the c and $\overline{c}$ quarks and above some critical density it prevents the formation of the bound states. The states with low binding energy: ψ' and χ_c are expected to be suppressed just above T_c while for the smaller J/ψ the suppression should start at temperatures $\sim 1.3T_c$.

The study of J/ψ and ψ' production was the main goal of the NA50 experiment, and this topic will be reviewed in more detail in the Section 1.3.

1.3 Processes Contributing to the Dimuon Spectrum

This section gives a short review of the processes contributing to the dimuon spectrum in the mass region $1.4 < M_{\mu\mu} < 7\ GeV/c^2$, relevant for present analysis (Fig. 1.3): Drell-Yan, Open Charm ($D\overline{D}$) and charmonia J/ψ and ψ' production. The production of the ρ, ω and ϕ vector mesons, important for the lower masses, is not considered here.

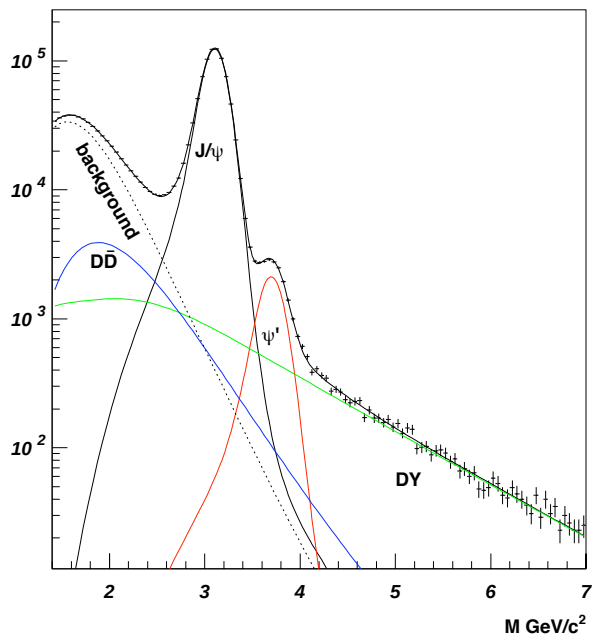

Figure 1.3: The measured NA50 dimuon spectrum for masses above the light vector mesons. The fitted contributions from J/ψ, ψ', Drell-Yan and $D\overline{D}$ are shown.

1.3.1 Drell-Yan Process

The Drell-Yan dileptons originate in the annihilation of a $q\bar{q}$ pair into a virtual photon. At Leading Order the (purely electromagnetic) diagram for this process (Fig.1.4) predicts the cross section

$$\frac{d\widehat{\sigma}}{dM} = \frac{8\pi\alpha^2}{9M} e_q^2 \delta(x_1 x_2 s - M^2) \tag{1.4}$$

where M is the virtual photon (dilepton) invariant mass and x_1 and x_2 are the projectile and

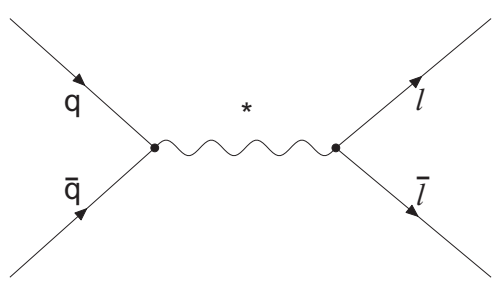

Figure 1.4: The leading order diagram responsible for the Drell-Yan dileptons.

target nucleons momentum fractions carried by the partons with charge e_q in the collision with center of mass system energy $\sqrt{s}$.

In order to obtain the cross section in pA collisions as a function of pair mass, M, and x_F, one must fold the partonic cross section with the quark and antiquark densities (evaluated at scale M).

$$\frac{d\sigma^{DY}}{dx_F dM} = \frac{8\pi\alpha^2}{9M}\int_0^1 dx_1 dx_2 \delta(x_1 x_2 s - M^2)\delta(x_F - x_1 + x_2) \times \sum_q e_q^2 \left[f_q^p(x_1,M^2) f_{\bar{q}}^A(x_2,M^2) + f_{\bar{q}}^p(x_1,M^2) f_q^A(x_2,M^2) \right] \tag{1.5}$$

After integrating the delta functions, the leading order cross section accounting for the isospin of the target nucleus, is

$$\frac{d\sigma^{DY}}{dx_F dM} = \frac{8\pi\alpha^2}{9M}\frac{1}{\sqrt{x_F^2 s^2 + 4M^2 s}}\sum_q e_q^2 [f_q^p(x_1,M^2)(z_A f_{\bar{q}}^p(x_2,M^2) + n_A f_{\bar{q}}^n(x_2,M^2)) + f_{\bar{q}}^p(x_1,M^2)(z_A f_q^p(x_2,M^2) + n_A f_q^n(x_2,M^2))] \tag{1.6}$$

with $z_A = Z/A$ and $n_A = N/A$ the fractions of protons and neutrons respectively in the target nucleus. This Leading Order cross section is responsible only for some fraction of the

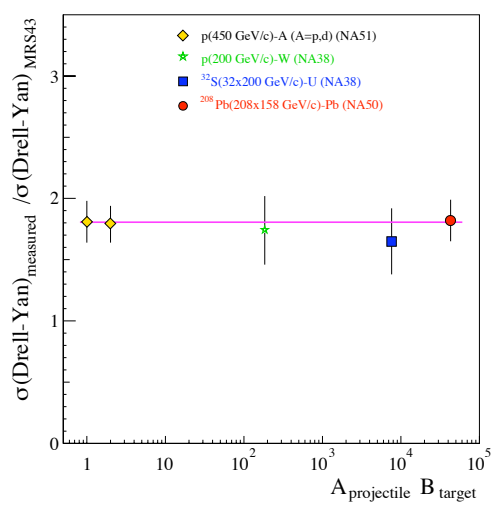

Figure 1.5: The K-factor for Drell-Yan production measured at beam energies $160-450$ GeV/A in pA and $nucleus-nucleus$ interactions. The MRSA $N^o 43$ parton distribution functions are used for the calculated cross section.

experimentally measured Drell-Yan cross section. Depending on the collision energy and the parton distribution functions used for the convolutions in Eq.1.5, one should introduce a factor $\sim 1.7-2.5$ (so called K-factor) in order to account for the higher order diagrams. The values measured by NA38/NA51/NA50 at beam energies $160-450$ GeV/A for different targets in pA and $nucleus-nucleus$ collisions are all consistent with $K \sim 1.8$ (with LO calculations using MRSA [23] $N^o 43$ parton distribution functions from the **PDFLIB** package [24] , Fig.1.5). The Next-to-Leading-Order diagrams increase the theoretical cross section $\sim 1.4-2$ times, still slightly missing the experimentally measured one [25].

Being originated in a hard process and avoiding final state interactions, the Drell-Yan dileptons from pA collisions should have in first approximation a cross section linearly increasing[2] with the target mass number A, i.e. the nuclear dependence parameter α (Section 1.4) is ~ 1. In principle, the parton distribution functions used in Eq.1.6 should account for the nuclear shadowing and parton energy loss effects. Fig.1.6 (from [26]) shows the measured [27] α parameter as a function of X_F and its theoretical predictions, accounting for the different nuclear shadowing parametrizations. One can see that at small X_F's the effect of such corrections is very small, and in the X_F range relevant for NA50 ($|X_F| < 0.15$) one can use the Drell-Yan process as a reference for the detection of the deviations of the α parameters of other processes (e.g J/ψ, ψ') from unity. As for the P_T behaviour of the Drell-Yan process, the Leading Order diagram

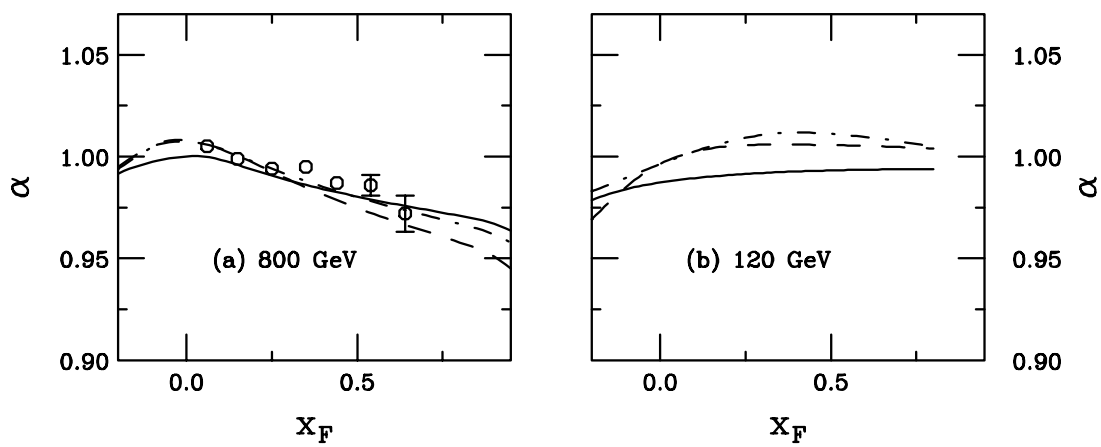

Figure 1.6: Measured nuclear dependence α parameter as a function of X_F for Drell-Yan production at 800 *GeV* (W and D targets) by E772 [27] (a) and computed one (for the same targets) at 120 *GeV* (b). The theoretical curves account for different models of the nuclear shadowing effect (from [26]).

(assigning to the virtual photon the total P_T of the annihilating quarks) predicts much softer P_T distribution than the measured one. Inclusion of diagrams with virtual corrections improves the description. In order to improve the P_T description of the data in the LO calculations one can increase "by hand" the transverse momentum of the partons inside the nucleon (the 'primordial' k_T).

In the pA and $nucleus - nucleus$ collisions the partons initial-state scattering (Cronin effect, [30, 31]) and their energy loss make the P_T spectrum harder, thus introducing a slight P_T and A dependence in the α parameter of the Drell-Yan cross section [27, 32, 33]. At small P_T's it becomes slightly smaller than 1, while at large P_T's it exceeds unity (Fig 1.7). Nevertheless, since this effect does not change the total cross section integrated over the full P_T range, it does not spoil the validity of the Drell-Yan as a reference for the measurement of the α parameter of other processes.

1.3.2 Open Charm

Being a hard process, according to the QCD factorization theorem [34] the hadroproduction of the $c\bar{c}$ pair in LO may be computed in the same way as for the Drell-Yan process, with an additional contribution (apart from the $q\bar{q}$ annihilation) from gluon fusion. For the general case

[2] After accounting for the isospin composition of different nuclei.

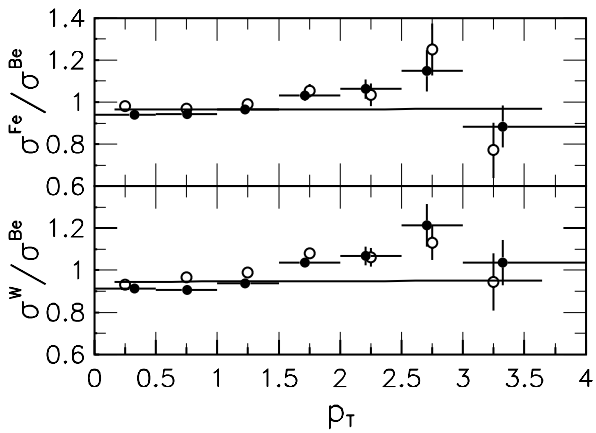

Figure 1.7: Ratios of the measured Drell-Yan cross section per nucleon versus P_T. Solid circles are for the ratios of Fe/Be and W/Be measured by E866/NuSea collaboration [33] and the open circles are for the ratios of Fe/C and W/C are from E772 measurements [27]. The solid curves are shadowing predictions for the E866/NuSea data from leading-order calculations using EKS98 [28] code with MRST [29] parton distribution functions. Figure is taken from [33].

of *nucleus* − *nucleus* (AB) collisions the cross section for the production of the free $c\bar{c}$ pair with invariant mass m and x_F longitudinal momentum fraction of the center-of-mass *nucleon* − *nucleon* collision energy $\sqrt{s}$ is [35]:

$$\begin{aligned} \frac{d\sigma^{c\bar{c}}}{dx_F dm^2} &= \int_0^1 dx_1 dx_2\, \delta(x_1 x_2 s - m^2)\, \delta(x_F - x_1 + x_2) H_{AB}(x_1, x_2; m^2) \\ &= \frac{H_{AB}(x_{01}, x_{02}; m^2)}{\sqrt{x_F^2 s^2 + 4m^2 s}}\,, \end{aligned} \tag{1.7}$$

where x_1 and x_2 are the fractions of the hadron momentum carried by the projectile and target partons respectively and $x_{01,02} = \frac{1}{2}(\pm x_F + \sqrt{x_F^2 + 4m^2/s})$.

$H_{AB}(x_{01}, x_{02}; m^2)$ is the convolution of the partonic cross sections and the parton densities:

$$H_{AB}(x_1, x_2; m^2) = f_g^A(x_1, m^2) f_g^B(x_2, m^2) \sigma_{gg}(m^2) \tag{1.8}$$

$$+ \sum_{q=u,d,s} [f_q^A(x_1, m^2) f_{\bar{q}}^B(x_2, m^2) + f_{\bar{q}}^A(x_1, m^2) f_q^B(x_2, m^2)] \sigma_{q\bar{q}}(m^2) \tag{1.9}$$

where the parton densities $f_i(x, m^2)$ are evaluated at momentum fraction x and scale $m^2 = x_1 x_2 s$ and m is the invariant mass of the $c\bar{c}$ pair. The LO partonic cross sections accounting for (light flavours) $q\bar{q}$ annihilation and gluon fusion are [35]:

$$\sigma_{gg}(m^2) = \frac{\pi\alpha_s^2(m^2)}{3m^2} \left\{ \left(1 + \frac{4m_c^2}{m^2} + \frac{m_c^4}{m^4}\right) \ln\left(\frac{1+\lambda}{1-\lambda}\right) - \frac{1}{4}\left(7 + \frac{31 m_c^2}{m^2}\right)\lambda \right\}, \tag{1.10}$$

$$\sigma_{q\bar{q}}(m^2) = \frac{8\pi\alpha_s^2(m^2)}{27m^2} \left(1 + \frac{2m_c^2}{m^2}\right)\lambda\,, \tag{1.11}$$

with $\lambda = \sqrt{1 - 4m_c^2/m^2}$.

Since the dominant contribution ($\simeq 80\%$) to the $c\bar{c}$ cross section at $X_F < 0.5$ comes from the gluon-gluon fusion, the charm production is pA collisions is virtually insensitive to the isospin composition of the target nucleus. Although most ($\sim 90\%$) of the produced $c\bar{c}$ pairs hadronize to

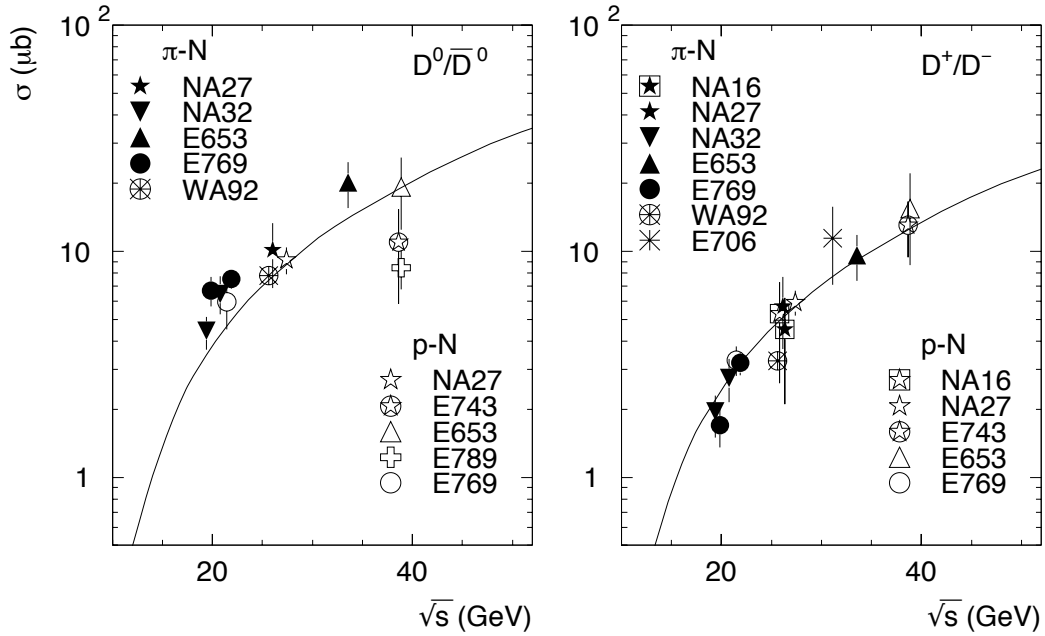

Figure 1.8: Cross section per nucleon for forward ($X_F > 0$) $D^0, \overline{D}^0$ (left) and D^+, D^- (right) production in proton and pion induced reactions, as a function of the center of mass energy. The data were taken from NA16 [39], NA27 [40], E743 [41], E653 [42], E789 [43], E769 [44], NA32 [45], WA92 [46], and E706 [47]. The solid lines represent the pp PYTHIA calculations (with $m_c = 1.35\ GeV/c^2$) with K-factor = 3.5 for neutral and 7.0 for charged D-mesons applied. The compilation is taken from [36].

Open Charm ($D\overline{D}$ mesons or Λ_c baryon) [37], the theoretical description of the production of the specific states and their kinematics is more complicated due to the nonperturbative character of the hadronization. The uncertainties in the fragmentation schemes, precise mass of the c-quark mass and higher order effects [38] lead not only to much higher values of the K-factor (~ 5) needed to match the LO calculation with measured data than for the Drell-Yan case, but force to apply different K-factors to different Open Charm species. Fig. 1.8 shows the compilation (from [36]) of neutral $D^0, \bar{D}^0$ (left) and charged D^+, D^- (right) production cross sections per nucleon for various π and proton induced reactions on different nuclear targets. The solid lines are the PYTHIA predictions (with c-quark mass assumed to be 1.35 GeV/c^2). While they describe reasonably well the shape of the energy dependence, in order to match the data one should scale up the calculated cross section by factor 3.5 for neutral and 7.0 for charged mesons (surely, these factors depend on the such a details of the calcultion as a c-quark mass, Q^2 scale, etc.).

As for the case of the Drell-Yan production the value of α in the parametrization $\sigma_{pA} = \sigma_{pN} A^{\alpha}$ is expected to be unity (Eq 1.26 in Section 1.4), which is consistent with existing pA measurements. The E789 experiment has measured $\alpha = 1.02 \pm 0.03 \pm 0.02$ for $0.0 < X_F < 0.08$ at beam energy 800 GeV comparing Be and Au targets [43]. The indirect measurements of $D\overline{D}$ cross section by NA38/NA50 in pA collisions for various nuclear targets in the beam energy range $200 - 450\ GeV$ are also fully consistent with $\sigma_{pA} \sim A$ scaling. The situation in

nucleus – *nucleus* collisions is less clear: the excess of dimuon production (with respect to the *pN* cross section rescaled by *AB*) in the mass range between the ϕ and J/ψ peaks, measured by NA38/NA50 in *SU* (200 GeV/A) and *PbPb* (158 GeV/A) has a kinematical distribution closely resembling the one of the expected $D\bar{D}$ originated dimuons. If they are the reason of the observed excess, the $D\bar{D}$ production cross section per nucleon in central *PbPb* collisions should be rescaled by factor ~ 3 with respect to σ_{pN} [21]. Fig.1.9 shows the dependence of the enhancement of the Open Charm cross section on the number of nucleons participating in the collision, required to explain the observed excess.

The proposed explanation [48] that the excess is caused by final-state rescattering of the $D\overline{D}$ mesons seems to be ruled out by [49]. An alternative hypothesis that the source of the excess are the long-sought thermal dimuons [20] seems also to be compatible with the data [50]. The final answer requires the direct measurement of the $D\overline{D}$ production, which is one of the main goals of the NA60 experiment (the successor of NA50).

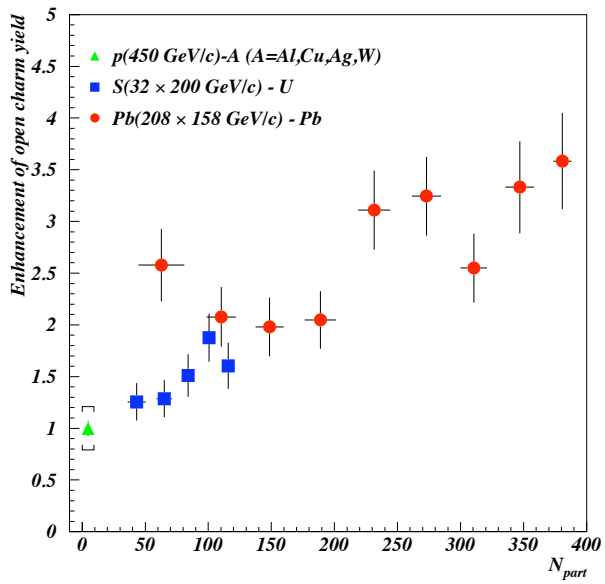

Figure 1.9: Evolution with N_{part} of the factor by which the expected charm yield must be scaled in order to describe the yield of intermediate mass dimuons collected by NA38 and NA50 [21].

1.3.3 Charmonia

The production of charmonia states (mainly J/ψ and ψ') in *pA* and *nucleus* – *nucleus* interactions, being recognized as one of the most promising QGP signatures, became the matter of intensive research, both theoretical and experimental. On the theoretical side, for a long time the accepted model of the charmonia production was the Colour Singlet Model (CSM) [51–53] assuming that each state is produced directly from the $c\bar{c}$ pair possessing its quantum numbers and neutralizing its colour by hard gluon emission on the perturbative scale (left plot of Fig. 1.10). After the Tevatron data have shown [54] that the CSM seriously underestimates the J/ψ and ψ' cross section, especially in the high P_T domain, the preference was given to the Colour Octet Model (COM) [55], assuming that first the colour octet preresonant $c\bar{c}g$ pair is formed, not necessarilly with the quantum numbers of the considered charmonium state, which

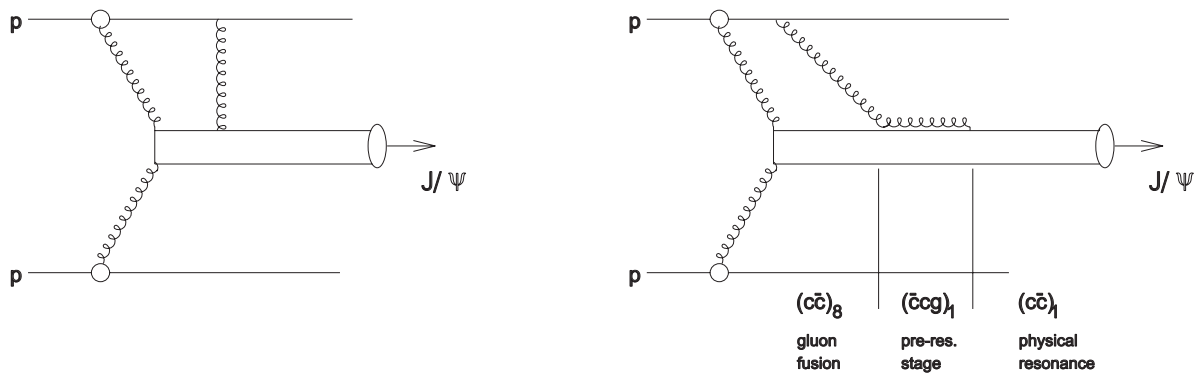

Figure 1.10: The J/ψ production diagrams in Colour Singlet (Left) and Colour Octet (Right) Models.

propagating through the nuclear matter is converted to one of the final singlet states by soft (non-perturbative) gluon emission (right plot of Fig. 1.10).

Before reviewing the status of the experimental data on charmonium production it is worth to speak about its predicted behaviour in case of QGP formation: J/ψ suppression [22].

The $c\bar{c}$ pair can be considered as a two-body system, where one of the quarks is connected with its counterpart, separated by the distance r, by a confining linear potential:

$$V_{lin}(r) = kr \tag{1.12}$$

with k being the string tension coefficient. Apart from that it sees its Coulomb-type colour potential (gluon exchange):

$$V_0(r) = \frac{q}{4\pi r} \tag{1.13}$$

As the temperature of the system increases, the string tension drops down, vanishing at the QGP transition point [56, 57]. The remaining Coulomb potential is also modified in the bath of deconfined quarks and gluons due to the Debye screening of the colour charge, becoming the short-range Yukawa-type potential (for the case of the massless q and $\bar{q}$ gas):

$$V(r) = \frac{q}{4\pi r}\frac{e^{-r/\lambda_D}}{r} \tag{1.14}$$

where λ_D is the Debye screening length. Within the one-loop pQCD calculations [58]

$$\lambda_D = 1/\sqrt{\left(\frac{N_c}{3} + \frac{N_f}{6}\right) g^2 T} \tag{1.15}$$

while the lattice calculations predict a factor ~ 2 shorter screening length than the lowest order pQCD [59]. Due to this inverse proportionality of the λ_D on the QGP temperature at some $T > T_c$ the screening length becomes so small that the attractive potential between the c and $\bar{c}$ becomes ineffective and the charmonium state dissociates, producing Open Charm after the subsequent hadronization.

Since different charmonium states have different radii [60], the more excited ones, χ_c ($r \sim 0.70 fm$) and ψ' ($r \sim 0.88 fm$), are expected to melt down at much lower temperatures (close

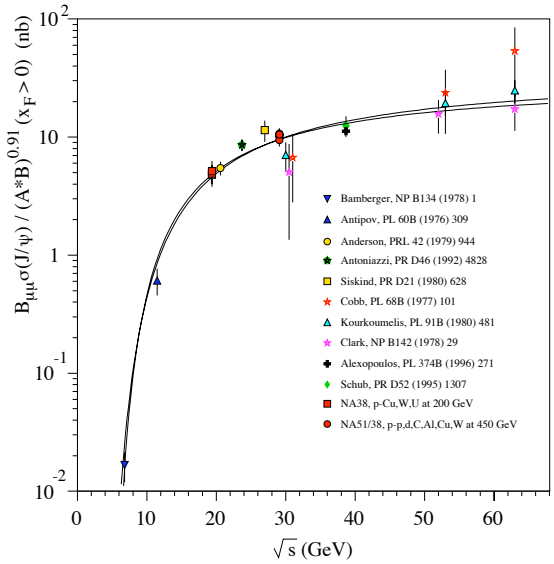

Figure 1.11: The phenomenological parametrization (Eq.1.17, [53]) for the J/ψ production energy dependence. The compilation is from [63]

to the QGP transition T_c) than the J/ψ ($r \sim 0.45 fm$). Taking into account that the decays of the χ_c contribute $\sim 30\%$ (and $\psi' \sim 12\%$) to the measured J/ψ 'normal' hadroproduction cross section, this should lead to a two-step-like pattern of the 'anomalous' J/ψ suppression due to the QGP dissociation, the first drop corresponding to melting of the χ_c and ψ' and the second one, at higher temperatures (or energy densities) to the suppression of the 'prompt' J/ψ's.

After the NA38 experiment reported the observation that the J/ψ production cross section per nucleon is suppressed for heavier targets in pA and in $nucleus - nucleus$ collisions ([61,66]), it was realized that the J/ψ should be suppressed even in the normal confined hadronic matter due to the final state interactions

$$J/\psi + h \rightarrow D + \bar{D} + X \tag{1.16}$$

A large amount of data was accumulated about J/ψ production and suppression in different pA and AB collisions, which allowed to deduce the scaling law (with some reservations, see 1.4) for the suppression $\sigma_{AB}^{J/\psi} = \sigma_0(AB)^{\alpha}$ with σ_{pN} being the $proton - nucleon$ J/ψ production cross section and α being in the range $0.9 - 0.95$ depending on the collision energy and kinematical domain [66].

The energy dependence of the proton-nucleon J/ψ production cross section is well described (see Fig.1.11) by the phenomenological parametrization [53],

$$\sigma_0(s) = \sigma_0 \left(1 - \frac{M_{J/\psi}}{\sqrt{s}}\right)^n \tag{1.17}$$

with $\sigma_0 \sim 0.64 \mu b$ (f.ph.sp.) and $n = 12$.

A better parametrization (see Section 1.4) is

$$\sigma_{AB}^{J/\psi} = \sigma_0 AB e^{-\rho_0 L \sigma_{abs}} \tag{1.18}$$

where $\rho_0 \sim 0.138$ $nucleon/fm^3$ is the density of the normal nuclear matter, L is the average distance travelled by the J/ψ (or preresonant state) in the colliding nuclei and σ_{abs} is the effective

cross section of the process 1.16. This expression describes better the nuclear absorption of the J/ψ suppression [64, 67–69]. The value of σ_{abs} obtained for the NA50 kinematical domain is $6.3 \pm 1.0mb$. All existing pA and SU data are well described by this nuclear absorption model.

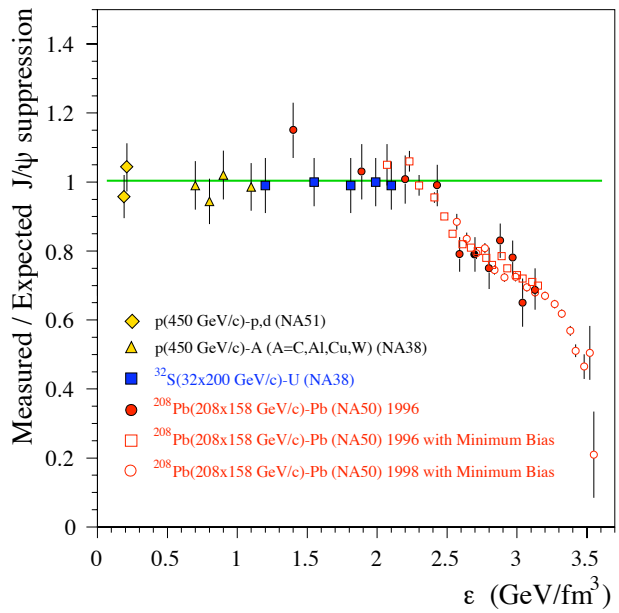

Figure 1.12: Measured J/ψ yield divided by the normal nuclear absorption, as a function of the energy density reached in pA, SU and $PbPb$ collisions [71].

The 1995 $PbPb$ data, however, show a much stronger suppression (factor 0.77) than predicted by this model [70]. None of the presently existing models involving only hadronic absorption is able to describe consistently the whole set of data with these $PbPb$ points included, even after taking into account the possible interactions of the J/ψ with the 'comovers' secondary hadrons having enough energy in the J/ψ h center-of-mass frame to break the J/ψ into Open Charm [64].

The more refined data taking conditions and analysis of the 1996 and 1998 data showed an even more intriguing pattern of the J/ψ suppression, closely resembling the expected double-step suppression curve, Fig.1.12.

As for the ψ', untill recently all available pA data showed the same level of suppression as of the J/ψ. In $nucleus - nucleus$ interactions ψ' is more suppressed, the effect becoming more prominent with increasing the centrality of the collision or the mass numbers of the colliding nuclei. The left plot of Fig.1.13 shows the $\psi'/J/\psi$ ratio as a function of AB (no correction for the $\mu\mu$ branching ratio is applied; the data on nuclear collisions is integrated over all centralities) while the plot on the right presents the $\psi'/Drell - Yan$ ratio as a function of the variable L (Eq.1.18) for the different collision centralities.

The lack of any noticeable difference between the ψ' and J/ψ suppressions in pA interactions is consistent with the Colour Octet Model of charmonium production, indicating that the object propagating and being suppressed in the nucleus is not one of the two final mesons but a common predecessor $c\bar{c}g$ colour state. The additional suppression of the ψ' in the $nucleus - nucleus$ collisions was assigned to its final-state interactions with the comovers [64]: they do not strongly influence the ψ' in pA collisions, where their density in negligible but should be accounted in AB interactions.

The situation became less clear once the E866/NuSea collaboration [72] observed in pA

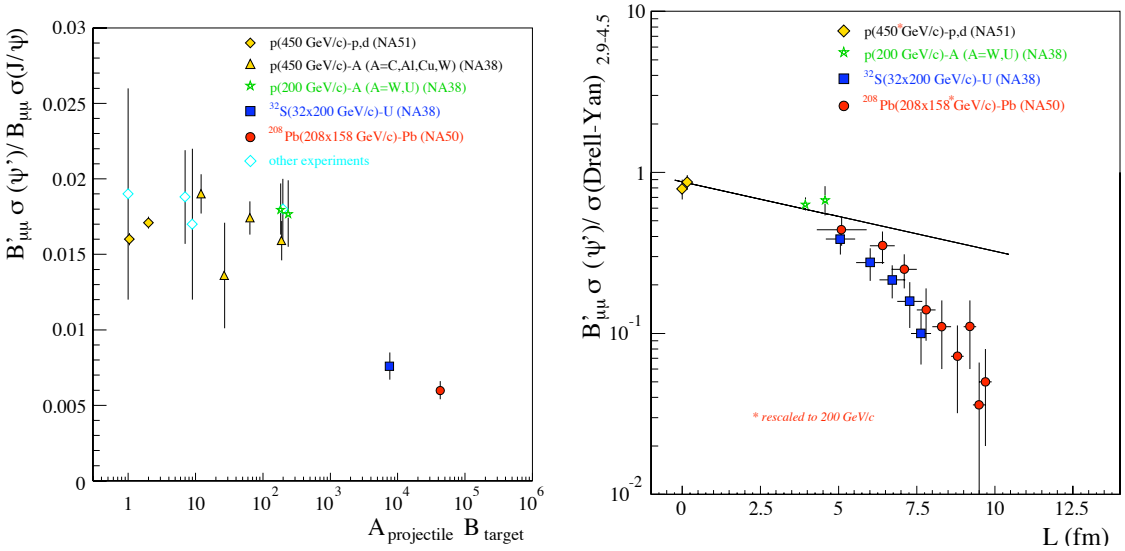

Figure 1.13: (Left) $\psi'/J/\psi$ ratio as a function of the product of the atomic masses of the colliding nuclei, averaged over all collision centralities; (Right) $\psi'/Drell-Yan$ ratio [65] as a function of the variable L (Eq.1.18). No correction for the $\mu\mu$ branching ratio is applied.

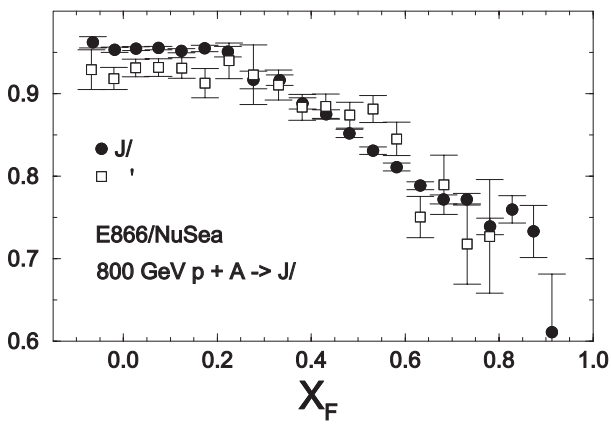

Figure 1.14: α parameters of the J/ψ and ψ' suppression as a function of X_F obtained from comparison of pBe, pFe and pW cross sections [72].

800 GeV interactions a difference in the suppression of J/ψ and ψ' over the broad range of X_F. Fig.1.14 shows the absorption parameters α for the two charmonium states obtained from the comparison of pBe, pFe and pW data. In a short time various models where proposed which give satisfactory agreement with these data by introducing a different formation times and $charmonium-nucleon$ interaction cross sections for J/ψ and ψ' states [73–75]. However, none of these models seems to try to asses the whole set of the charmonium data in the ligh of the E866/NuSea findings.

1.4 Drell-Yan and Charmonia production in pA and AB collisions

This section gives a short review of the different parametrizations used to describe the suppression of the charmonia states due to hadronic interactions in pA and AB collisions.

Within the Glauber model [76] the nucleus-nucleus (AB) interaction [3] is considered as a set of the independent interactions of the nucleons of the target and projectile. It is assumed that the properties of the nucleons do not change after experiencing the first collision. In particular, they can interact further with other nucleons with the same cross section. Thus, the possible effect of creation of excited baryonic states is neglected.

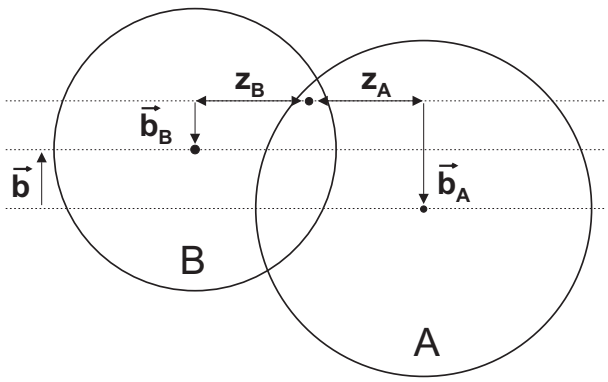

Figure 1.15: The definitions of the geometrical parameters of a $nucleus-nucleus$ collision with impact parameter b.

Consider two nuclei A (target) and B (projectile) colliding with impact parameter b (see Fig.1.15). Knowing their nuclear density profiles $\rho_{A(B)}(\vec{b},z)$ (the nuclei here are assumed to be spherically symmetric, so the transverse position of the point inside the nucleus relative to its axis parallel to the beam, $\vec{b}$, can be substituted by the distance), one can write down the probability of occurrence of $nucleon-nucleon$ collisions as

$$T_{AB}(\vec{b})\sigma_{NN} = \int d\vec{s} \int dz_A\, \rho_A(\vec{s},z_A) \int dz_B\, \rho_B(\vec{b}-\vec{s},z_B)\sigma_{NN} \tag{1.19}$$

where $T_{AB}(\vec{b})$ is the **collision nuclear thickness** function and σ_{NN} is the $nucleon-nucleon$ inelastic collision cross section. Defining the **nuclear thickness** function

$$T(\vec{b}) = \int_{-\infty}^{\infty} dz\, \rho(b,z) \tag{1.20}$$

normalized in such a way that

$$\int d\vec{b}\, T_A(\vec{b}) = 1 \;, \qquad \int d\vec{b}\, T_B(\vec{b}) = 1 \tag{1.21}$$

one can rewrite Eq.1.19 as

$$T_{AB}(\vec{b})\sigma_{NN} = \int d\vec{s}\, T_A(\vec{s})\; T_B(\vec{b}-\vec{s})\sigma_{NN} \tag{1.22}$$

[3] The case of the pA interactions is obtained by setting the mass of one of the nuclei to 1.

Since the probability for the occurrence of exactly n inelastic collisions follows the binomial distribution

$$P(n,\vec{b}) = C_{AB}^{n}\left(T_{AB}(\vec{b})\sigma_{NN}\right)^{n}\left(1-T_{AB}(\vec{b})\sigma_{NN}\right)^{AB-n} \tag{1.23}$$

the total probability for an inelastic event in a collision with impact parameter $\vec{b}$ is:

$$\frac{d\sigma_{AB}^{in}}{d\vec{b}} = \sum_{n=1}^{AB} C_{AB}^{n}\, P(n,\vec{b}) = 1-\left(1-T_{AB}(\vec{b})\sigma_{NN}\right)^{AB} \tag{1.24}$$

Consider now a hard process in a AB collision, like Drell-Yan or $c\bar{c}$ pair creation. Since any binary interaction has equal chances to produce such a process, its cross section should be described by Eq.1.24 with σ_{NN} substituted by the σ_{NN}^{hard} - the hard process cross section in a $nucleon-nucleon$ collision. Due to the very small values of the hard processes cross sections, the AB cross section will be dominated by the first term $(n=1)$ of the sum in Eq.1.24:

$$\frac{d\sigma_{AB}^{hard}}{d\vec{b}} = AB\, T_{AB}(\vec{b})\sigma_{NN}^{hard} \tag{1.25}$$

and taking into account that $T_{AB}(\vec{b})$ is normalized to unity, one obtains

$$\sigma_{AB}^{hard} = AB\int d\vec{b}\; T_{AB}(\vec{b})\sigma_{NN}^{hard} = AB\sigma_{NN}^{hard} \tag{1.26}$$

Consider now the case when the particle after having been produced via a hard process in the AB collision may interact (and lose its identity) with the surrounding nuclear matter with cross section σ_{abs}. Then the (survival) probability that the particle after its production at the point $\left\{z_A,\vec{b_A}\right\}$ ($\left\{z_B,\vec{b_B}\right\}$) will avoid such an interaction in the target (projectile) nucleus $A(B)$ is

$$P_{surv,A} = \left[1-T_{A>}(\vec{b_A},z_A)\sigma_{abs}\right]^{A-1} \quad , \quad P_{surv,B} = \left[1-T_{B<}(\vec{b_B},z_B)\sigma_{abs}\right]^{B-1} \tag{1.27}$$

where the -1 in the exponential indices is to exclude the nucleons which produce this particle and the thickness functions $T_{A>}(\vec{b_A},z_A)$ and $T_{B<}(\vec{b_B},z_B)$ are the transverse densities of the matter seen by the particle on its way out from the nuclei:

$$T_{A>}(\vec{b_A},z_A) = \int_{z_A}^{\infty} dz'\; \rho(b_A,z') \quad , \quad T_{B<}(\vec{b_B},z_B) = \int_{-\infty}^{z_B} dz'\; \rho(b_B,z') \tag{1.28}$$

The final production cross section for this case is obtained in the same way as for the Drell-Yan, with the only difference that the T_{AB} (Eq.1.19,1.22) should be convoluted with the survival probabilities:

$$\begin{aligned}\sigma_{AB}^{J/\psi} &= AB\sigma_{NN}^{J/\psi}\int d\vec{b}\int d\vec{s}\int dz_A\; \rho_A(\vec{s},z_A)[1-T_{A>}(\vec{s},z_A)\sigma_{abs}]^{A-1} \\ &\times\int dz_B\; \rho_B(\vec{b}-\vec{s},z_B)\left[1-T_{B<}(\vec{b}-\vec{s},z_B)\sigma_{abs}\right]^{B-1}\end{aligned} \tag{1.29}$$

Taking into account that

$$\rho_A(\vec{s},z_A)[1-T_{A>}(\vec{s},z_A)\sigma_{abs}]^{A-1}\sigma_{abs}\mathrm{d}z_A = \frac{1}{A}\mathrm{d}\left([1-T_{A>}(\vec{s},z_A)\sigma_{abs}]^A\right) \tag{1.30}$$

(and the same relation for the nucleus B), one can rewrite Eq.1.30 as

$$\sigma_{AB}^{J/\psi} = \frac{\sigma_{NN}^{J/\psi}}{\sigma_{abs}^2}\int \mathrm{d}\vec{b}\int \mathrm{d}\vec{s}\,[1-T_A(\vec{s})\sigma_{abs}]^A\left[1-T_B(\vec{b}-\vec{s})\sigma_{abs}\right]^B \tag{1.31}$$

Expanding the expressions in the [] and keeping the terms up to σ_{abs}^2 one obtains an expression resembling the usual absorption formulae:

$$\sigma_{AB}^{J/\psi} = \sigma_{NN}\,AB\,(1-\sigma_{abs}<\rho L>) \simeq \sigma_{NN}\,AB\,e^{-\sigma_{abs}<\rho L>} \tag{1.32}$$

where $<\rho L>$ is the average amount of matter seen by the particle before it leaves the colliding nuclei:

$$<\rho L> = \frac{1}{2}\int \mathrm{d}\vec{b}\int \mathrm{d}\vec{s}\,T_A(\vec{s})\,T_B(\vec{b}-\vec{s})\left[(A-1)T_A(\vec{s})+(B-1)T_B(\vec{b}-\vec{s})\right] \tag{1.33}$$

Usually, the more easily interpretable but somewhat misleading $\rho_0 L$ expression is used in Eq.1.32 instead of $<\rho L>$, where ρ_0 is the "average" nuclear density and L is the average path traversed by the particle inside the nuclei. One should bear in mind that L is defined not only by the mass numbers of the colliding nuclei, but also depends on their specific density profiles, $L = <\rho L>/\rho_0$.

For the case of pA interactions, $B=1$, one obtains instead of Eqs.1.32,1.33:

$$\sigma_{pA}^{J/\psi} = \simeq \sigma_{NN}\,A\,e^{-\sigma_{abs}<\rho L>}\quad,\quad <\rho L> = \frac{(A-1)}{2}\int \mathrm{d}\vec{b}\,\left[T_A(\vec{b})\right]^2 \tag{1.34}$$

One can connect these parametrizations with the widely used experimental one of the form $(AB)^\alpha$ (or A^α for pA case): expanding it in powers of $(1-\alpha)$ and keeping the linear term only (for $\alpha\sim 1$), one obtains for the suppression factor

$$\frac{\sigma_{AB}^{J/\psi}}{\sigma_{NN}AB} \simeq (AB)^{-(1-\alpha)} \simeq e^{-(1-\alpha)\ln AB} \tag{1.35}$$

and the comparison of the exponents of the Eq.1.35 and Eq.1.32 leads to

$$\alpha = 1-\sigma_{abs}\frac{<\rho L>}{\ln AB} \tag{1.36}$$

It is obvious that one should not expect to describe with a single value of the α parameter the suppression on different nuclei and that the discrepancy with the L parametrization (moreover with the original Glauber model predictions) will increase with the rise of the absorption cross section.

It is instructive to compare the quantitative discrepancies between the different parametrizations for the typical J/ψ absorption magnitude. As a parametrization of the nuclear density profiles the Fermi oscillator model for the nuclei with $A<17$ and Woods-Saxon distribution

otherwise were used. The parameters were taken from [77] (for some nuclei, missing in this paper, the parametrizations from the *FRITIOF* 7.02 Monte-Carlo code [78] were used)

Fig.1.16 shows the suppression factors $S(A) = \sigma_{pA}^{J/\psi}/(\sigma_{NN}A)$ in pA collisions for two values of the absorption cross section σ_{abs}: 5 *mb* (circles) and 10 *mb* (triangles) according to **a)** (filled symbols) Glauber model predictions (Eq. 1.31), **b)** $\exp\{-\sigma_{abs} < \rho L >\}$ parametrization with $< \rho L >$ calculated by Eq.1.34, **c)** A^{α} parametrization for different values of α (dashed lines).

The calculated points of the Glauber model for five nuclei: *Be*,*Al*,*Cu*,*Ag* and *W* (the 2% error bars are added just to distinguish them) were fitted by the suppression function $S(A) = s_0 A^{\alpha}/A$ as it is usually done with the experimental data. The results of the fit are shown by the solid lines. The numerical values of $\{s_0, \alpha\}$ obtained from the fits are $\{1.10, 0.92\}$ and $\{1.17, 0.86\}$ for $\sigma_{abs} = 5$ and 10 *mb* respectively.

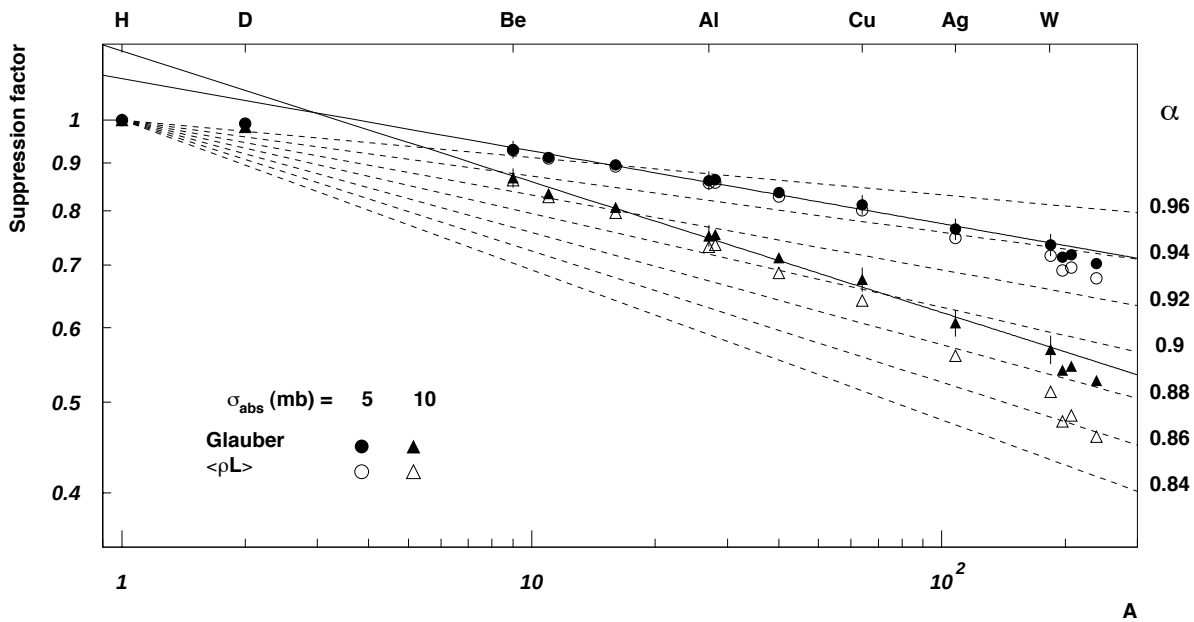

Figure 1.16: The suppression factors $S(A) = \frac{\sigma_{pA}^{J/\psi}}{\sigma_{NN}A}$ in pA collisions for two values of J/ψ absorption cross section σ_{abs}: 5. *mb* (circles) and 10. *mb* (triangles) according to **a)** (filled symbols) Glauber model predictions (Eq. 1.31), **b)** $\exp\{-\sigma_{abs} < \rho L >\}$ parametrization with $< \rho L >$ calculated by Eq.1.34, **c)** A^{α} parametrization for different values of α (dashed lines).
The solid lines show the result of the fit of the Glauber model predictions for five nuclei: *Be*,*Al*,*Cu*,*Ag* and *W* by the form $S(A) = s_0 A^{\alpha}/A$ (the 2% error bars are added just to distinguish the fitted nuclei). The numerical values of $\{s_0, \alpha\}$ obtained from the fits are $\{1.107, 0.922\}$ and $\{1.184, 0.860\}$ for $\sigma_{abs} = 5$ and 10 *mb* respectively.

The Table 1.1 shows in more detail the predictions of the different parametrizations and their relative deviation from the Glauber model for the absorption cross sections $\sigma_{abs} = 5$ and 10 *mb*. One should note that although in this example the deviations of the A^{α} fit from the Glauber model points are smaller than for the $\exp\{-\sigma_{abs} < \rho L >\}$ parametrization, its usage for the extrapolation of the suppression factor to the nuclei outside the fitted range may be more dangerous, in particular it "predicts" an "enhancement factor" 1.107 (1.184) for $\sigma_{abs} = 5(10)$ *mb* for the proton point.

A	$<\rho\, L>$ (N/fm^2)	L (fm)	Suppression Factor			Dev. from Glauber,%	
			Glauber	$e^{-\sigma_{abs}\rho L}$	Fit A^{α}	$e^{-\sigma_{abs}\rho L}$	Fit A^{α}
Be	0.161	1.16	0.924(0.857)	0.923(0.852)	0.927(0.859)	0.2(0.6)	-0.3(-0.3)
Al	0.335	2.43	0.852(0.737)	0.846(0.715)	0.851(0.736)	0.8(3.0)	0.2(0.1)
Cu	0.474	3.44	0.801(0.659)	0.789(0.622)	0.795(0.653)	1.5(5.5)	0.7(0.9)
Ag	0.579	4.20	0.764(0.607)	0.749(0.560)	0.763(0.606)	2.1(7.7)	0.1(0.1)
W	0.697	5.05	0.727(0.557)	0.706(0.478)	0.732(0.563)	2.9(10.6)	-0.8(1.0)

Table 1.1: The comparison of the different suppression parametrizations for *Be*, *Al*,*Cu*,*Ag* and *W* targets. The second column shows calculated $<\rho\ L>$ according to Eq.1.34 and the third one is the L variable obtained with $\rho_0 = 0.138 fm^{-3}$ (average nuclear density). The columns 3,4 and 5 show the predictions of the full Glauber model with absorption cross section $\sigma_{abs} = 5\ (10)\ mb$, the suppression factors obtained by the $\exp\{-\sigma_{abs} < \rho L >\}$ parametrization and the results of the fit of the Glauber model points by the A^{α} parametrization, respectively. The last two columns show the relative deviations (in %) of the $<\rho L>$ parametrization and of the A^{α} fit from the Glauber model predictions.

2 Experiment Description

The NA50 experiment at the CERN SPS, built for the study of dimuon production in Pb-Pb collisions, is the continuation of NA38, which in turn inherited its main components from the NA10 experiment. Apart from Pb-Pb runs it has collected a vast amount of pA data, which are the object of the study presented in this work.

The distinctive feature of this experiment is the highly selective dimuon trigger, which allows to work with very high interaction rates ($\sim 0.5 \times 10^9$ p-A interactions/sec) and thus to study processes with very low cross section.

This chapter gives a description of the experimental apparatus, mentioning the differences between the setups optimized for p-A and Pb-Pb runs.

2.1 General description

Fig.2.1 presents the schematic layout of the experiment.

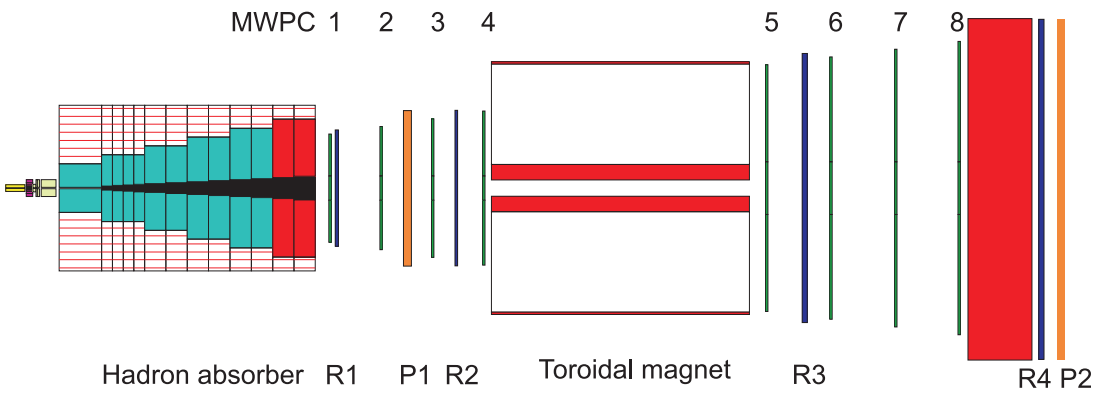

Figure 2.1: General layout of the NA50 experiment.

The heart of the experiment is the Muon Spectrometer (inherited from NA10) [79]. It consists of eight MWPCs (PC1-PC8), grouped in two pairs of four chambers each and separated by a toroidal magnet. The trigger is provided by four scintillator hodoscopes (R_1-R_4), two of them (R_1 and R_2) located upstream of the magnet. The most downstream hodoscope (R_4) is shielded from the rest of the system by a 120 cm thick Iron wall, which ensures that only muons trigger the DAQ. In order to stop the flux of particles from the target, the chambers and hodoscopes are separated from the target region by a hadron absorber.

Depending on the type of beam, either a single target (for p-A runs) or a segmented active target (for Pb-Pb runs) is used. The beam itself is monitored by special detectors: in the case of the proton beam these are three argon-filled ionization chambers, while the ion beam is controlled by a Cerenkov counter made of quartz blades. In the case of the Pb-Pb runs, Electromagnetic and Zero Degree Calorimeters are used to measure the centrality of the collision. The first one measures the energy of the neutral particles emitted in the central rapidities range, while the second one is meant to detect the spectator nucleons of the projectile nucleus measuring the hadronic energy in the very forward cone. The Multiplicity Detector, placed just after the target system, measures the charged particle multiplicity.

Below follows the detailed description of each detector and its design strategy and features.

2.2 Beam and its Monitoring

The NA50 experiment, located in the ECN3 hall on the North Area of the SPS, uses the primary high intensity proton (450 GeV/c) or ion (400 GeV/c per charge, equivalent to 158 GeV/c per nucleon for Pb-Pb) beams. The intensities used are typically $\sim 5 \times 10^7$ Pb ions per 4.0 sec burst for Pb-Pb runs or up to $\sim 3 \times 10^9$ protons per 2.1 sec for proton runs. The limiting factors for the beam intensity are:

- **for Pb-Pb runs:** the pile-up rate (more than one ion arriving during the relevant detectors readout gates), which is typically kept at the level of $\sim 10\%$.
- **for p-A runs:** the MWPC's detection efficiencies (and hence the muon reconstruction efficiencies), which degrade with increasing occupancy. In fact, the vast p-A statistics obtained with $1-3 \times 10^9$ p/burst during the 1996-1998 runs was not used for a long time due to the problems with the reconstruction efficiency at such intensities and untill the September 2000 run, the usual beam intensity was $2-6 \times 10^8$ p/burst. This problem is described in more details in the Section 4.5.1.

The detectors used for the beam control are:

2.2.1 Argon Counters

These are the multi-foil ionization chambers (filled by Argon) and used to count the incident proton flux by integrating the total ionization current. Three such counters are located a few meters upstream of the target. Their calibration is done with the aid of two scintillator counters (operated in the coincidence mode) at relatively low intensities (up to $\sim 5 \times 10^6$ p/burst). Unfortunately, the last time they were calibrated was in 1996 and there is evidence that since that time their detection efficiencies have changed by a few percent, which must be accounted for in the systematic errors of the absolute cross section results (more details in Section 4.5.1).

2.2.2 Beam Hodoscope

This is a Cerenkov counter, made of 16 quartz blades, located 22 m upstream of the target system. Each blade is equipped with its own photomultiplier and their dimensions are adapted to count approximately the same fraction of the beam. This detector is reliable up to intensities $\sim 10^8$ ions/burst. The special scintillator counters placed outside of the beam just after the BH allow to tag the ions interacting in the latter.

2.3 Target System

All the p-A data were taken with a single target. For each target used the density was measured with a precision of $\sim 0.2\%$. The table 2.1 collects the parameters of the targets used in the present analysis.

In the Pb-Pb runs the situation is more complicated, due to the non-negligible probability that the fragments from a primary Pb-Pb collision may interact afterwards in the target and

Target	Lenght (mm)	Interaction prob.(%)
Be	130	27.4
Al	120	26.3
Cu	75	39.2
Ag	75	39.0
W	45	37.2

Table 2.1: Parameters of the targets for the *pA* data used in this work.

produce the triggered dimuon (so called **reinteractions**). Since the experiment is interested in dimuons created only in Pb-Pb collisions, such events should be tagged and rejected. For these reason the so called **active target system** was built. It consists of 7 Pb subtargets, each 1*mm* thick (2.5% interaction probability) and 2.5 *mm* in diameter (except the most upstream one, with diameter 5 *mm*). The distance between the subtargets is 25*mm* and each of them is followed by two quartz blades. These Cerenkov detectors are used for the identification of the target where the interaction took place and, more important, for the tagging of the reinteractions. The efficiency of the interacting subtarget identification algorithm strongly depends on the multiplicity (i.e. centrality) of the collision, being $\sim 85\%$ in average for the collisions with transverse energy greater than 5 *GeV*.

2.4 Muon Spectrometer

2.4.1 Hadron Absorber

It consists of three parts (Fig. 2.2):

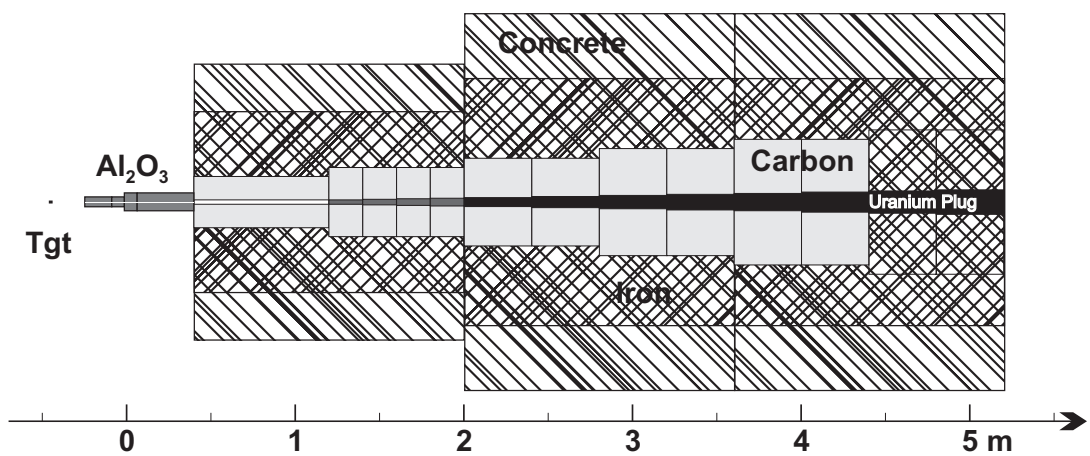

Figure 2.2: Hadron Absorber used for NA50 pA runs

- the central part is the tungsten-uranium conical core (outside of the spectrometer acceptance) that stops the protons or ions which did not interact in the target. In order to minimize the amount of triggers on dimuons originating from interactions in this beam dump, it starts ~ 235 *cm* downstream of the center of the target system (in the original NA10 configuration this distance was 120 *cm*, but NA50 substituted the first 65*cm* by the ZDC and shifted the target center upstream by 45 *cm*)

- the muon filter, covering the spectrometer acceptance (from 35 to 140 *mrad*). It starts at ~ 25 *cm* downstream of the center of the target by the 60*cm* long preabsorber, made from low A materials (Al_2O_3 for pA and BeO for Pb-Pb runs) in order to minimize the muon's multiple scattering close to the interaction vertex. The preabsorber is continued by 400 *cm* of carbon followed by 80 *cm* of iron. In total this amounts to $\sim 18\lambda_I$, which is enough to stop the hadronic showers, but the price paid for that are $\sim 70X_o$ travelled by the muons before they enter in the proportional chambers. As it was mentioned, an additional muon filter (a 120 *cm* thick iron wall) is placed between the last MWPC and the last trigger hodoscope (R_4), not influencing the tracking since all the measurements are done before.

- the last part of the absorber are the iron and concrete shielding blocks, surrounding the muon filter.

2.4.2 Magnet

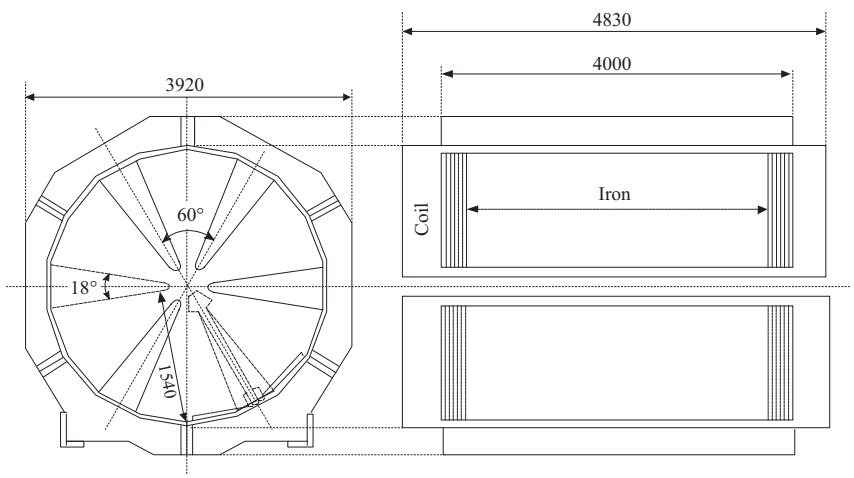

Figure 2.3: Frontal (left) and lateral (right) view of the toroidal magnet.

The NA50 muon spectrometer uses a air-core 480 *cm* long toroidal magnet, centered at 11.3 *m* downstream of the target. With a total radius of 205 *cm* the active area goes from $R_{in} = 29.5$ *cm* to $R_{out} = 154$ *cm*, which essentially defines the angular acceptance of the experiment. Six radial coils split the azimuthal acceptance into sextants (Fig. 2.3). In order to keep the mass resolution on acceptable level, muons passing through the coils or iron poles are rejected. For this reason 18° out of 60° in each sextant are excluded from the acceptance. The designed field dependence

$$B(\Phi, R) = B_o/R \tag{2.1}$$

is essentially azimuthal, with homogeneity on the level of 0.1% up to a radius of 95 *cm*. A pulsed current of 7 *kA* (instead of 10 *kA* in NA10), synchronized with the SPS cycle, provides $B_o = 0.38\ Tm$.

The advantage of such a field is that a particle emitted from a point on the magnet axis is deflected only in the plane crossing this axis and the change in polar angle, to a good approximation, is inversely proportional to the particle's P_T: the deflection angle, $\delta\theta$, over the

infinitesimal element of path, δs, is given by

$$\delta\theta = \frac{\delta s}{\rho(s)} = \frac{q \cdot B(r)}{p}\,\delta s \tag{2.2}$$

where ρ is the radius of curvature of the (helicoidal) path followed by a particle of charge q in the magnetic field B. For energetic particles the deflection is small and the integration path, s, can be replaced by $r\,/\,\sin(\theta)$, leading to

$$\Delta\theta = \int \frac{q \cdot B(r)}{p}\frac{\mathrm{d}r}{\sin(\theta)} = \frac{q \cdot B_0}{p \cdot \sin(\theta)}\int \frac{\mathrm{d}r}{r} = \frac{q \cdot B_0}{p_{\mathrm{T}}}\,\ln(z_2/z_1) \tag{2.3}$$

z_1 and z_2 being the effective entrance and exit planes of the magnetic field, relative to the target position.

This property allows to apply a fast on-line cut on the single muon P_T at the trigger level using only the information from the hodoscopes (more details in the Section 2.4.4).

2.4.3 Proportional Chambers

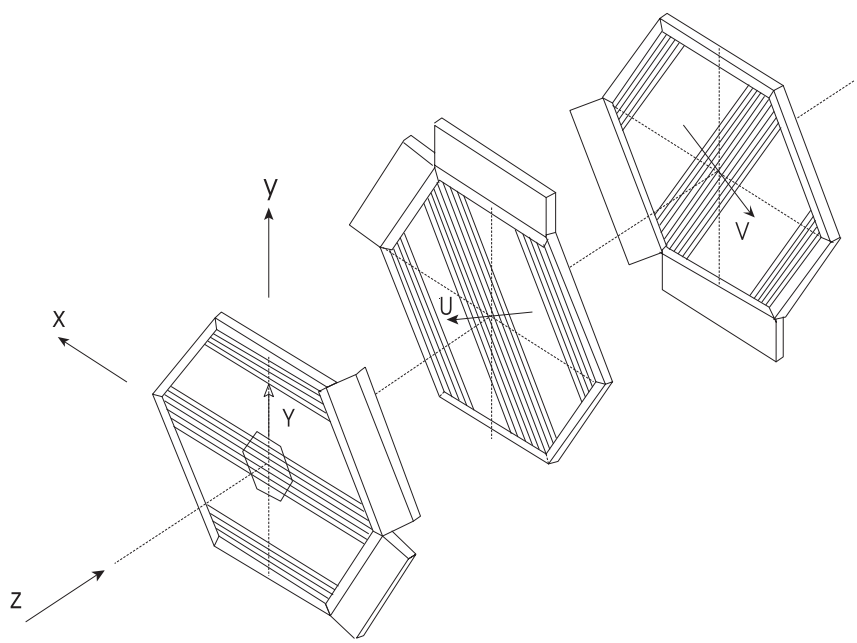

Figure 2.4: The three planes of the MWPC.

The eight MWPCs form two groups of four: the large chambers (1229 wires per plane) downstream of the magnet and the small ones (749 wires per plane) upstream (but only the wires which are in the acceptance window are equipped with preamplifiers). Each chamber consists of three independent planes with two graphited Mylar cathodes and one anode wire plane. Each plane of a chamber is rotated by 60° with respect to the other two (Y,U,V coordinates, Fig. 2.4). The spacing between the gold-plated 20 μm diameter tungsten wires is 0.3 cm and the gap between the wire plane and the cathode is 0.6 cm.

The gas mixture used contains 80% of argon 19.8% of isobutane and 0.2% of freon. The nominal operating voltage is 2800 V but is lowered to 2400 V between the bursts.

2.4.4 Trigger System

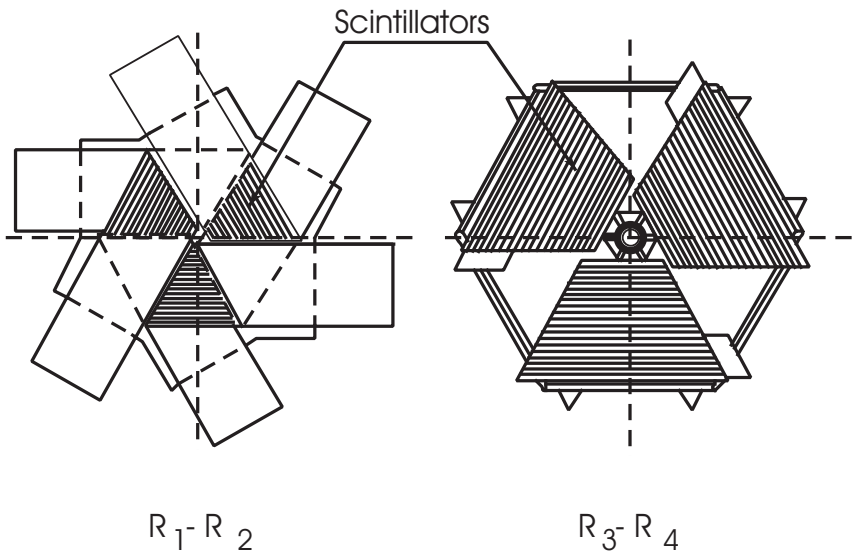

Figure 2.5: R_1 - R_4 trigger hodoscopes.

The dimuon trigger is realized with the aid of four hodoscopes, two upstream of the magnet (R_1 and R_2) and two downstream of it (R_3 and R_4). The design of the R hodoscopes is adapted to the sixfold symmetry of the magnet. They also split into six sextants, each sextant being covered by scintillator slabs perpendicular to its median (Fig. 2.5). The hodoscopes R_1 and R_2 have 30, R_3 - 23 and R_4 - 32 slabs per sextant. Since each scintillator slab is read only at one of its ends, the time taken by the (scintillating) light to reach the PM depends on the point where the muon hit the slab, originating time fluctuations in the trigger (jitter). To prevent such a systematic bias the R_2 hodoscope was inverted (already in the NA38 period) in relation to its position in the NA10 configuration, so that the slabs in R_2 are read from the end opposite to the one used in the reading of the corresponding R_1 slabs. Both signals are then sent into a 'mean timer' making the final signal quite insensitive to the specific muon trajectories.

The R_1 and R_2 hodoscopes have homothetic geometry so that a particle originated in the target hits the slabs with the same number. The width of their slabs follows a geometrical progression, so that each corresponding n-th pair views approximately the same polar angle. The pair of R_1 and R_2 slabs indices gives a rough estimate of the production polar angle of the muon.

The single muon trigger condition on R_1 and R_2 requires the existence of the coincidence $V_i = R_1^i \times R_2^i$ in a given sextant, Fig.2.6. In fact, to account for the finite length of the target system and the multiple scattering in the absorber, the $V_i = R_1^i \times R_2^{i-1}$ coincidence is also allowed. The dimuon trigger requires at least two such coincidences in different sextants.

The R_3 and R_4 hodoscopes have slabs of fixed width (5.5 cm). The coincidence $V_i \times R_4^j$ can be used for a rough estimate of the particle deflection angle in the magnet and thus of its P_T (thanks to the mentioned property of the toroidal magnetic field). The information of the R_3 hodoscope adds redundancy to the trigger and allows to reduce the number of random coincidences between independent tracks. After finding the V coincidence in the first stage of the trigger, a special hardwired processor checks for the allowed $V \times R_3 \times R_4$ values and even assigns the P_T bin to the triggered muon (A,B,C and D limited by 4, 2,1.4 and 0.6 GeV/c

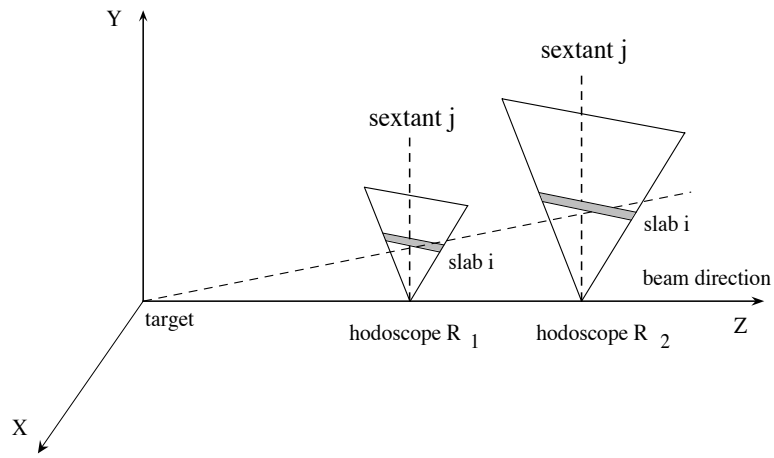

Figure 2.6: $V_i = R_1^i \times R_2^i$ trigger condition on each muon.

respectively). Howerever, there was no cut applied on P_T at the trigger level for the data used in this work.

Two additional trigger hodoscopes, P_1 (located upstream of the magnet) and P_2 (behind the iron wall) are only used for the trigger efficiency calculation, during special runs.

2.5 Centrality Measurement

Although the detectors for the collision centrality measurements are used only during the Pb-Pb runs, for completeness the following section briefly describes them.

2.5.1 Electromagnetic Calorimeter

It is used to measure the neutral transverse energy, produced in the pseudorapidity range $1.1 < \eta < 2.3$. **EM** is made of polystyrene scintillating fibers, parallel to the beam direction, embedded in a lead-bismuth alloy (with volume ratio 1/2). The calorimeter follows the hexagonal symmetry of the muon spectrometer and is subdivided in three rings, each covering $\Delta\eta = 0.34$ units in pseudorapidity. Having only 14 *cm* in length (15.5 X_o), it is positioned 32 *cm* downstream of the target (in fact, it is physically present only during the Pb-Pb runs). The energy resolution is $\sim 5\%$ at $E_T = 200\ GeV$.

2.5.2 Zero-Degree Calorimeter

Made of 900 quartz fibres (365 μm diameter) embedded in a tantalum converter (volumic ratio 1/17) and read-out by five PMs, it measures the Cerenkov light produced by the projectile spectator nucleons showering in the converter. Being very compact (65 *cm* in length and $5 \times 5\ cm^2$ in cross section) it is positioned 165 *cm* downstream of the target system center, right on the path on the beam. In order to minimize the contribution from the secondaries produced in a very forward cone, its angular acceptance is narrowed by a 60 *cm* long copper collimator

with a conical hole slightly larger than the beam divergence. Its resolution at full Pb ion energy 33 TeV is $\sim 5\%$.

Apart from being a very valuable tool for the determination of the collision centrality (thanks to the simple correlation between the number of spectator nucleons and the impact parameter) the **ZDC** is also very useful for the identification of pile-up events.

2.5.3 Multiplicity Detector

Being used only for the Pb-Pb runs, this detector is located between the last subtarget and the *BeO* preabsorber. It consists of two identical disks, each containing ~ 7000 silicon microstrips arranged in arcs and measuring the charged particles in the pseudo-rapidity range $1.5 < \eta < 3.9$.

2.6 Kinematics Resolution

The kinematics resolution of the NA50 experiment is determined by three factors:

- the multiple scattering of the muons in the target and hadron absorber ($\sim 70X_0$);
- their energy loss;
- the proper error of the measurement in the MWPC.

the last one being negligible compared with the first two.

Neglecting the mass of the muon, the invariant mass of the dimuon can be represented as

$$M^2 = 2P_{\mu 1}P_{\mu 1}(1 - \cos\theta_{\mu\mu}) \tag{2.4}$$

where $P_{\mu i}$ is the total mamomentum of each muon and $\theta_{\mu\mu}$ is the opening angle between them.

Since the average single muon momentum strongly increases with mass (being ~ 10 and ~ 25 GeV/c for ω and J/ψ dimuons respectively), the multiple scattering (contributing to the angular error) is more important at low masses while in opposite to this, the energy loss has a stronger contribution as the dimuon mass increases. The experiment was optimized in such a way that these two sources have approximately equal contributions to the dimuon mass measurement error at the J/ψ mass.

Fig.2.7 shows the typical resolution of the dimuon mass (for Drell-Yan), rapidity, transverse momentum and X_F (for J/ψ) measurements plotted as a function of these variables.

Unfortunately, as it will be discussed later, the NA50 simulation package does not reproduce fully adequately the detector response and the real experimental resolution is around $\sim 10\%$ larger than the one predicted from the Monte-Carlo. An additional specific error is caused by the ($\lesssim 1\%$) uncertainty in the magnetic field value which may lead from run to run to a "change of the scale" of the reconstructed kinematic parameters (see Section 3.3.1).

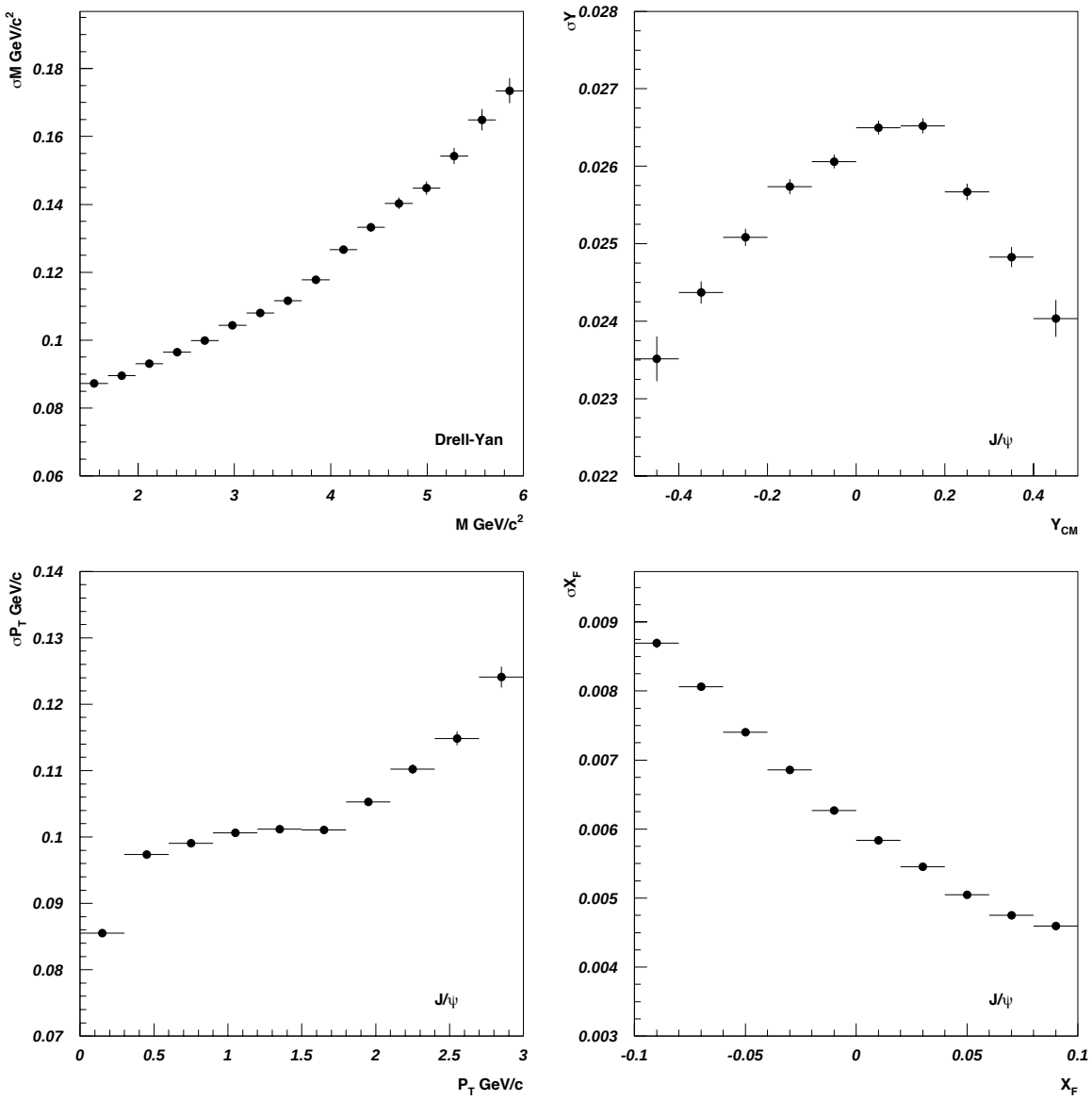

Figure 2.7: Kinematics resolution of NA50 experiment: dimuon mass (for Drell-Yan), rapidity, transverse momentum and X_F (for J/ψ) resolutions as a function of these variables.

3 Data Reconstruction and Selection

This chapter describes the general scheme of the p-A data collection and its preparation for the physics analysis. Since in the course of the present work it appeared that the standard dimuon reconstruction program has certain drawbacks, the emphasis is made on the principal modifications done in the reconstruction and its efficiency calculation algorithms.

3.1 Data Taking

The data collected by NA50 is organized in **runs** each containing from few hundreds up to few thousands bursts (depending on the beam intensity and the trigger rate). The data corresponding to each burst has its own header, containing the various scalers for the luminosity calculations and the quality control. NA50 usually takes three types of data during the p-A runs:

- **Normal** data-taking for the physics analysis with all relevant components of the detector working;
- Although normally after the appropriate cuts the contamination of the data by dimuosns originated outside from the target (in the beam dump, beam counters etc.) is $\lesssim 1\%$, this contribution and its mass distribution may be very important for certain types of analysis. For this reason, special **Target Out** runs are taken with the total number of incoming protons comparable to the one of the normal runs. The only difference of these runs from the normal ones is the absence of the target.
- **Trigger Efficiency** runs are taken (usually one or two per data-taking period) in order to estimate the efficiency of the $R_1 - R_4$ hodoscopes based trigger system. These are usually low-intensity runs where the trigger is provided by coincidences in the special P_1 and P_2 hodoscopes. The efficiency of the normal trigger is defined as the fraction of the P_1P_2 triggered events where all the required conditions in $R_1 - R_4$ are satisfied (the usual trigger efficiency is on the level of $\sim 90\%$).

Since for the background estimation the like sign dimuon triggers are also collected, in order to avoid any bias due to the specific sign of the magnet current, its polarity is periodically changed.

3.2 Data Reconstruction

3.2.1 Standard Reconstruction Procedure

The reconstruction of dimuon data, done by the standard NA50 software (DIMUREC), consists of the following main steps (Fig. 3.1 shows the definitions used):

- Building the **Projected Tracks (PrT)** in the Backward telescope: set of the active **Y**,**U** or **V** projection wires in each MWPC laying approximately in the same plane. The hits in at least three MWPCs out of four possible are requested. The wires which entered in **PrT** are marked and not used for subsequent searchs.

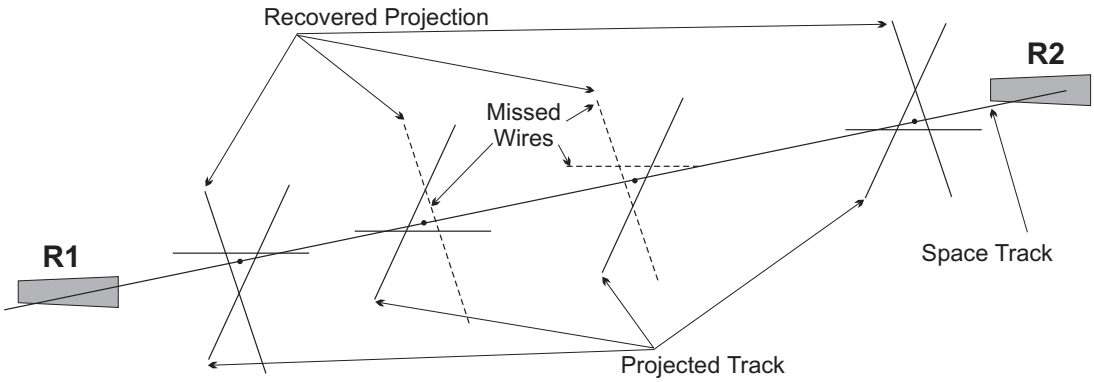

Figure 3.1: Definitions used in the description of the Track Reconstruction procedure. The solid lines show the MWPC wires fired by a muon.

- Binding the **PrT** into the **Space Tracks (SpT)** : for each pair of **YU**, **YV** or **UV PrT** their intersection line is computed and then the complementary **V**,**U** or **Y PrT** sought, with the condition that the distance between its plane and the intersection line does not exceed predefined tolerances. Then each such triplet is fitted by a straight line. Finally, some checks are applied: the tracks which after extrapolation to the magnet are hitting its iron parts are rejected. Tracks which do not hit any active slab of the **R3**,**R4** hodoscopes are also discarded.

- Recovering of the tracks with missed hits: essentially the same procedure as in the previous step, but now, instead of the Projected Tracks, the separate wires not involved yet to any of them, are checked for being close to the intersection of the pair of **PrT**. At least two points (out of four possible) are required to complete the missing **Y**,**U** or **V** projection.

- Since the occupancy in the Forward telescope is usually much higher than in the Backward one, in order to reduce the reconstruction time the tracks from the Backward telescope are extrapolated to the bending plane of the magnet and then this extrapolation point is connected with the center of the target. After taking into account the finite length of the target and the possibility of the deflection of the muon in the absorber due to multiple scattering, a region in each MWPC of the Forward telescope is defined where the tracks are sought.

- The same procedures of Projected Tracks reconstruction, binding them to Space Tracks and the checks for hitting the Iron in the magnet or missing the active slabs of the **R1** or **R2** hodoscopes are repeated for the Forward telescope, but this time looking only in the mentioned regions.

- The tracks in the Forward and Backward telescopes are associated one to another. This is done by finding the point of the closest approach for each pair of Forward/Backward telescopes tracks in the same sextant and by applying cuts on the closeness of this point to the bending plane of the magnet and on the relative distance between the tracks at the Z-coordinate of this point.

- Some reconstruction level cuts are applied, the most essential of them being the **V/R3/R4** verification: for each **V** value (i.e **R1/R2** coincidence, which is a rough measure of the track's polar angle in the Forward telescope) there is a set of allowed **R3/R4** active slabs

traversed by the track. Since the **R3/R4** combination measures the polar angle of the track in the Backward telescope, the **V/R3/R4** cut selects the muons pointing to the target region and deflected in the toroidal magnet within some restricted angle. This allows to cut soft muons (mainly from combinatorial background) and random coincidences of different track fragments.

This procedure works without problems when the beam intensity is not too high: at 1×10^8 protons per 2.4 sec. burst nearly 100% of the signal dimuons satisfying the trigger conditions are reconstructed. The problems arise when the beam intensity increases.

3.2.2 Modified Reconstruction Algorithm

First of all, as the occupancy in the most illuminated Forward telescope increases, many spurious tracks appear. Most often, they consist of a few hits belonging to real muons with a 'ghost' hit (from a track passing nearby) attached (Fig.3.2). Since the standard algorithm marks any hit entered in a Projected Track as a used one and forbids its usage for further reconstruction, the hits belonging to a muon track will be lost if such a spurious **PrT** is rejected at the Space Track binding stage. Additionally, even if the **PrT** entered into some Space Track, due to the wrong hit it may miss the active slabs of the trigger hodoscopes or do not pass the Forward-Backward association.

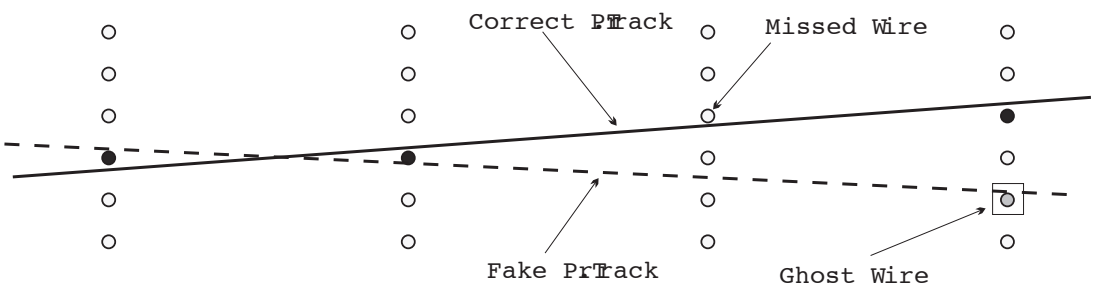

Figure 3.2: The tracks with a wrong ('ghost') hit attached are often rejected. The solid line showa the MWPC wires fired by the muon.

The obvious solution of this problem is to check all possible combinations of wires which may produce a Projected Track, without suppressing any of them and if after the Space Track binding stage some hits appear to belong to more than one track, to chose the one which gives the best χ^2 for binding and Forward-Backward association. The corresponding subroutines have been rewritten and the Fig.3.3 presents the result of the $pW96$ (mainly) high intensity data reconstructed both with the standard (hollow points) and the upgraded algorithms. It shows the ratio of the number of reconstructed dimuons with $2.7 < M < 3.5 \;\; GeV/c^2$ to the value of the Argo1 counter (accounting for the dead time of the detector) as a function of the beam intensity of the run.

3.2.3 Reconstruction Efficiency Estimation

The second problem appearing at high intensity is the estimation of the reconstruction efficiency, which is directly related to the chamber detection efficiency. The latter is defined for each MWPC plane as the fraction of events when the reconstructed Projected Track did not

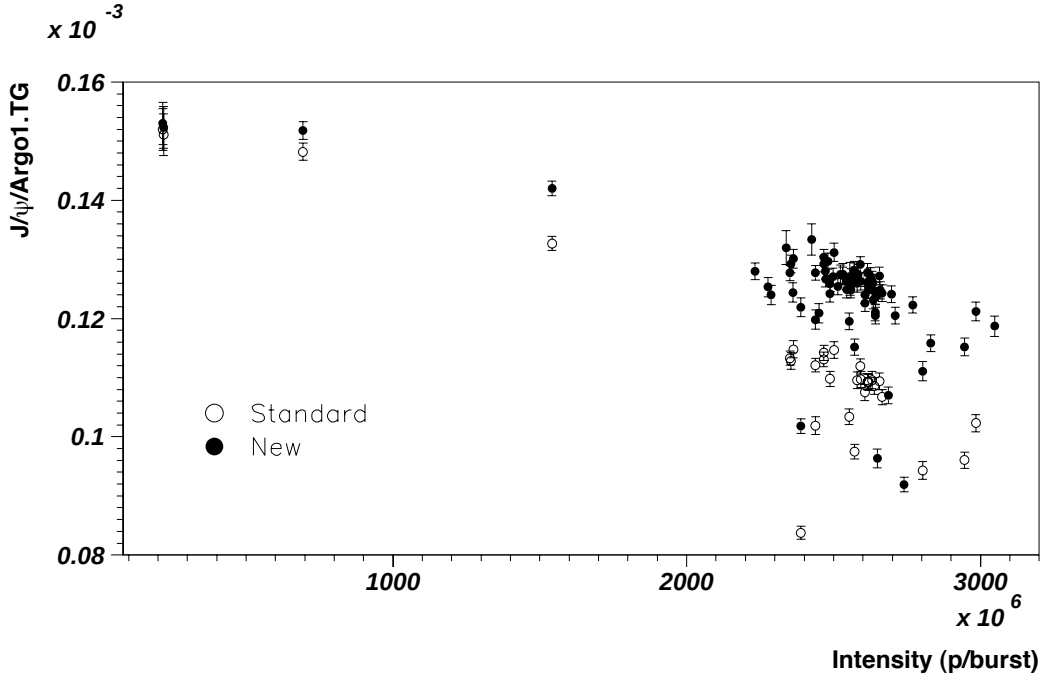

Figure 3.3: Ratio of the number of reconstructed dimuons with $2.7 < M < 3.5\ \ GeV/c^2$ to the value of $Argo1$ counter (accounting for the dead time of the detector) as a function of the beam intensity of the run. The hollow points show the result of the reconstruction by the standard program, while the filled ones are from the upgraded algorithm.

leave a hit in this plane to the total amount of tracks. Obviously, only the **PrT** which passed all the reconstruction cuts are used for such calculations.

After having defined detection efficiencies ε_i for each MWPC plane, one can estimate different combinatorial probabilities:
to have a **PrT** with 4 hits:

$$\varepsilon_{P4} = \prod_{i=1}^{4} \varepsilon_i \tag{3.1}$$

to have only 3 hits in a **PrT**:

$$\varepsilon_{P3} = \sum_{i=1}^{4} (1-\varepsilon_i) \prod_{j\neq i;1}^{4} \varepsilon_j \tag{3.2}$$

to have only 2 hits (recovered **PrT**):

$$\varepsilon_{P2} = \sum_{i=1}^{4} (1-\varepsilon_i) \prod_{k\neq i;1}^{4} \varepsilon_k \prod_{j\neq i,k;1}^{4} \varepsilon_j \tag{3.3}$$

to have a **PrT** with at least 3 hits:

$$\varepsilon_P = \varepsilon_{P4} + \varepsilon_{P3} \tag{3.4}$$

to have a Space Track with at least 3 normal **PrT**:

$$\varepsilon_{S0} = \prod_{P=Y,U,V} \varepsilon_P \tag{3.5}$$

to have a Space Track with 2 normal and 1 recovered **PrT**:

$$\varepsilon_{S1} = \sum_{P2=Y,U,V} \varepsilon_{P2} \prod_{P\neq P2}^{P=Y,U,V} \varepsilon_P \tag{3.6}$$

to have a **PrT** satisfying the validity criterion of not more than one recovered **PrT**:

$$\varepsilon_S = \varepsilon_{S0} + \varepsilon_{S1} \tag{3.7}$$

to reconstruct the single muon both in Forward and Backward Telescopes:

$$\varepsilon_\mu = \varepsilon_S^{FWD} \times \varepsilon_S^{BWD} \tag{3.8}$$

to reconstruct the dimuon:

$$\varepsilon_{\mu\mu} = \varepsilon_\mu \times \varepsilon_\mu \tag{3.9}$$

Again, this method works well until the occupancies in the chambers are low enough and the detection efficiencies are high. As the occupancies in the chambers increase, the detection efficiency drops down. As it is shown on Fig. 3.4, at a beam intensity of 3×10^9 protons/burst the detection efficiency of the most illuminated first MWPC drops to 80% from virtually 100% at 1×10^8 protons/burst.

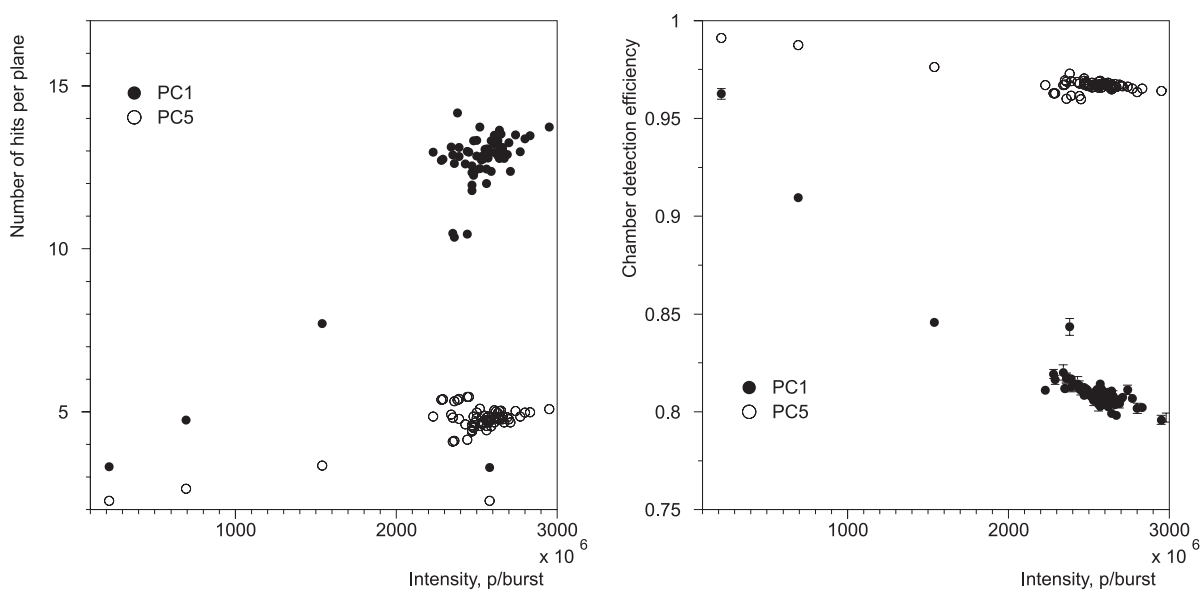

Figure 3.4: Occupancies per plane (left) and detection efficiencies (right) for MWPC1 and MWPC5 - first chambers of Forward and Backward Telescopes respectively, as a function of the beam intensity.

As a result, due to the higher occupancy and to the increased probability that the correct hit is missing, a wrong ('ghost') hit is often attached to the track instead of the missing hit, leading to the overestimation of the chamber detection efficiencies. Assuming that the real chamber

efficiency is ε_{real} and that due to the high occupancy in the chambers there is a probability ν that a 'ghost' hit, not belonging to the real muon track is attached to it instead of the missed hit, the probability to count a given plane as efficient is

$$\varepsilon = \varepsilon_{real} + (1 - \varepsilon_{real}) \times \nu \tag{3.10}$$

To cope with this problem I applied a kind of "mixed events technique": for each chamber the information about the hits found in the track is accounted in the usual way like in the standard efficiency ε_i computation, but the track is stored into a buffer. Then, analysing another (random) event, it is checked for each chamber if it has a hit which being attached to the stored track does not prevent it from passing all the selection cuts. The probability ν_i is defined as the fraction of such checks which give the matching 'ghost' hit. Then the real efficiency is estimated as

$$\varepsilon_{real} = (\varepsilon_i - \nu_i)/(1 - \varepsilon_i) \tag{3.11}$$

Surely, this is not an ideal solution, since sometimes the 'ghost' hit may help to reconstruct the track which otherwise would be lost (e.g. if the track had only one 'real' hit in some of the projections) or in opposite, to prevent the reconstructible track from being reconstructed (e.g. if it deflects the track so much that it misses the active slabs of the hodoscopes). The ideal way to solve the problem of efficiency estimation would be to apply the full 'mixed events technique' on the track reconstruction level: to add the hits of the track, reconstructed in one event to chamber information of another one, to try to reconstruct it again and assign the weights according to the results. Unfortunately, within the framework of the existing program this task is too complicated.

Nevertheless, the check shows that even the described partial solution of this problem greatly improves the situation. To verify the validity of the method Monte-Carlo data for J/ψ was generated and the obtained hits were added on top of the real high intensity run chamber information. The inefficiency for the J/ψ hits was introduced "by hand" (on the level of the experimental values). The following insert shows the output of the upgraded reconstruction program for the chamber efficiencies averaged over the Y,U and V planes, and the final dimuon reconstruction efficiency estimate (both accounting for and neglecting the 'ghost' hits). `AVE, GHOST, and FINAL` stay for ε_i, ν_i and ε_{real}, respectively.

```
FWD TEL      CH 1          CH 2          CH 3          CH 4
AVE       83.06+-0.12   84.52+-0.12   82.83+-0.12   86.60+-0.11
GHOST     12.44+-0.09    9.65+-0.08    7.91+-0.08    9.23+-0.08
FINAL     80.65+-0.14   82.87+-0.13   81.36+-0.14   85.24+-0.13
injected MC
efficiency     80.0          83.0          81.0          85.0
BWD TEL      CH 1          CH 2          CH 3          CH 4
AVE       96.17+-0.05   96.11+-0.05   96.02+-0.05   94.96+-0.06
GHOST      2.57+-0.04    2.17+-0.04    1.99+-0.04    2.21+-0.04
FINAL     96.07+-0.05   96.02+-0.05   95.94+-0.06   94.85+-0.06
injected MC
efficiency     96.0          96.0          96.0          96.0
DIMUON RECONSTRUCTION EFFICIENCY
NOT ACCOUNTING FOR GHOST HITS    :86.11+-0.39
ACCOUNTING FOR GHOST HITS        :81.53+-0.26
```

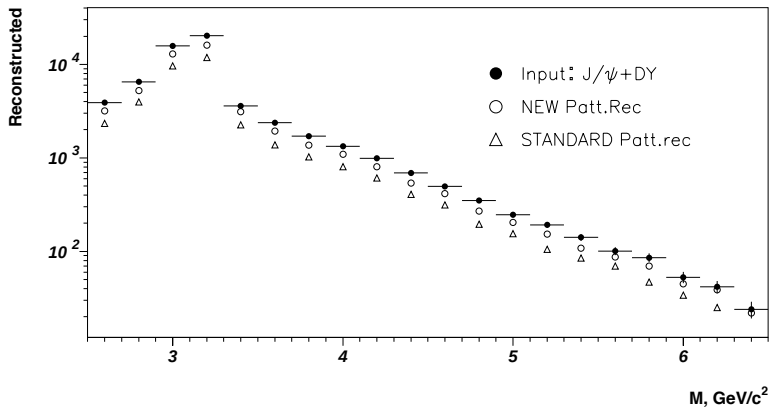

Figure 3.5: Result of the reconstruction of the MC J/ψ and Drell-Yan dimuons superimposed on real high intensity run MWPC and hodoscopes data by the standard and upgraded programs.

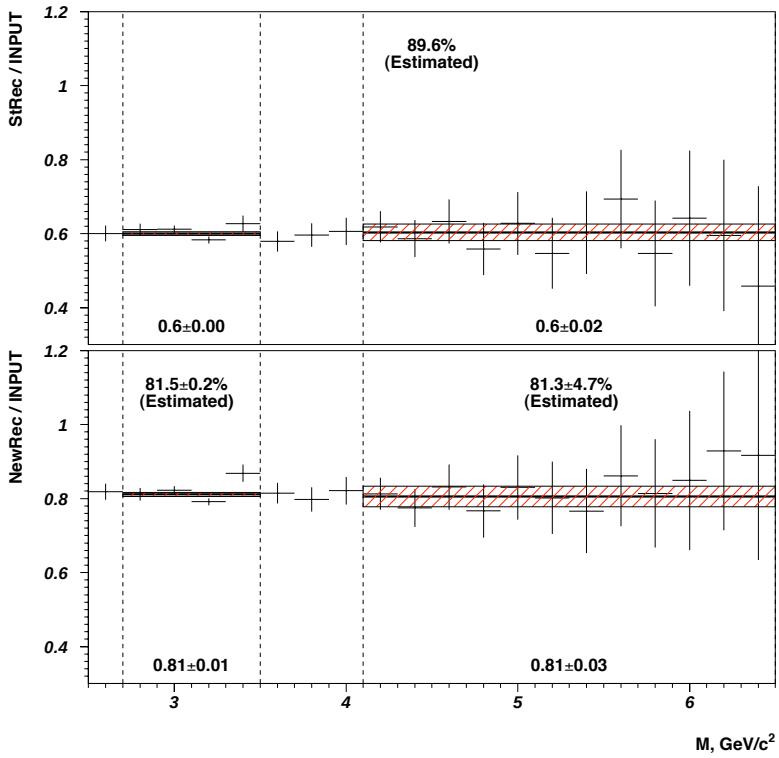

Figure 3.6: Ratio between the number of reconstructed and generated events, by the standard program (top) and by the upgraded one (bottom). The numbers on the top are the estimates of the dimuon reconstruction efficiency in two mass bins: $2.7-3.5$ and $4.1-6.5$ GeV/c^2, the bottom numbers show the ratio of the number of reconstructed and generated events in these mass bins.

The real dimuon reconstruction efficiency (as the ratio of the numbers of reconstructed and generated Monte-Carlo J/ψ) was $82.3 \pm 0.7\%$.

In order to verify that the estimated reconstruction efficiency does not depend on the dimuon mass, the following test was done: 30000 J/ψ and 30000 Drell-Yan dimuons were generated and their hits were superimposed on real high intensity (3×10^9 protons/burst) MWPC and hodoscopes data. Again, realistic inefficiencies where added "by hand". Then the reconstruction and efficiency estimation was done both by the standard and upgraded programs. Fig.3.5 shows the generated and reconstructed mass spectra.

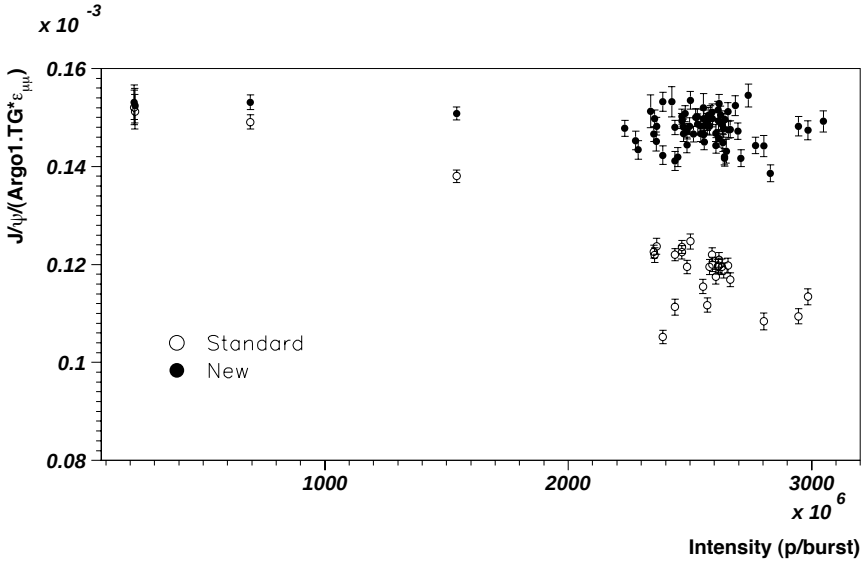

Figure 3.7: Ratio of the number of reconstructed dimuons with $2.7 < M < 3.5\ \ GeV/c^2$ corrected by $\varepsilon_{\mu\mu}$, to the value of $Argo1$ counter (accounting for the dead time of the detector) as a function of the beam intensity of the run. The hollow points show the result of the reconstruction by the standard program, while the filled ones are from the upgraded algorithm.

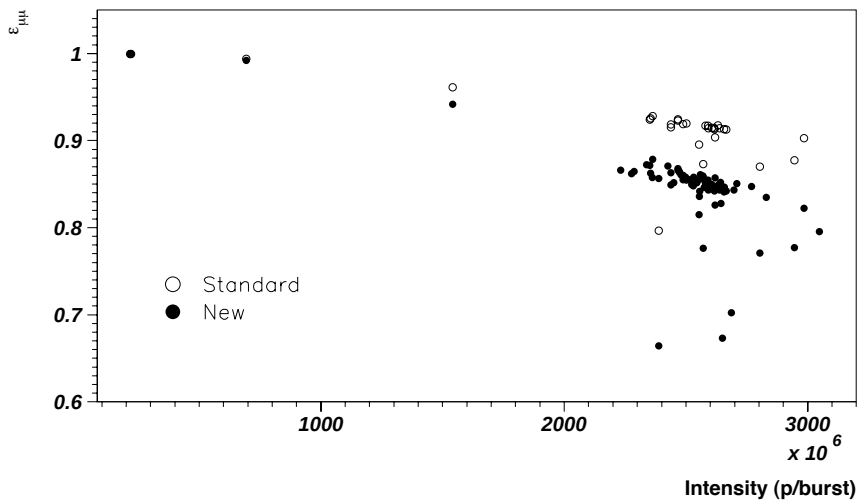

Figure 3.8: Evolution of the dimuon reconstruction efficiency with the beam intensity obtained with the standard (hollow points) and upgraded (filled points) algorithms. The points deviating from the main sequence are due to hardware problems in the MWPCs.

The top plot of the Fig.3.6 shows the ratio of the reconstructed and generated events, when the standard program was used while the bottom one is for the upgraded algorithm. The numbers on the top are the estimates of the dimuon reconstruction efficiency in two mass bins: $2.7-3.5$ and $4.1-6.5\ \ GeV/c^2$, the bottom numbers show the ratio of the total reconstructed and generated number of events in these mass bins. One can see that both algorithms do not show any dependence of the reconstruction efficiency on the dimuon mass.

Finally, Fig.3.7 shows for $pW96$ data (same as on the Fig.3.3) run by run the number of dimuons in the mass range $2.7-3.5\ \ GeV/c^2$, corrected for the reconstruction efficiency and

normalized on the values of the *Argo*1 counter, as a function of the beam intensity. One can see that the ratio corresponding to the reconstruction by the upgraded program has no systematic dependence on the beam intensity.

Fig.3.8 shows the dependence of the reconstruction efficiency (evaluated both by the standard and upgraded algorithms) as a function of the beam intensity. The points which are out of the main sequence are due to some hardware problems in the chambers.

3.3 Data Selection

After the reconstruction of the data ($\sim 30-50\%$ of the collected triggers survive the selection cuts) one should reject a certain amount of bad runs (or bursts) in order to ensure the correct normalization for the cross sections calculation, besides doing some cleaning on the event by event level to minimize the contamination by the dimuons originated outside of the target.

3.3.1 Run Selection

In the present analysis the following cuts were applied on the run level:

- the current in the toroidal magnet is kept on the nominal (7000A) level with the precision of $\lesssim 1\%$ which leads to similar error in the reconstructed mass. For this reason the runs with anomalously shifted ($> 15 MeV$) J/ψ pole position were eliminated. Fig. 3.9 shows this cut for the *pAl*97 data (left) and the J/ψ mass resolution (from a Gaussian fit in the proximity of the pole) for each run (right);

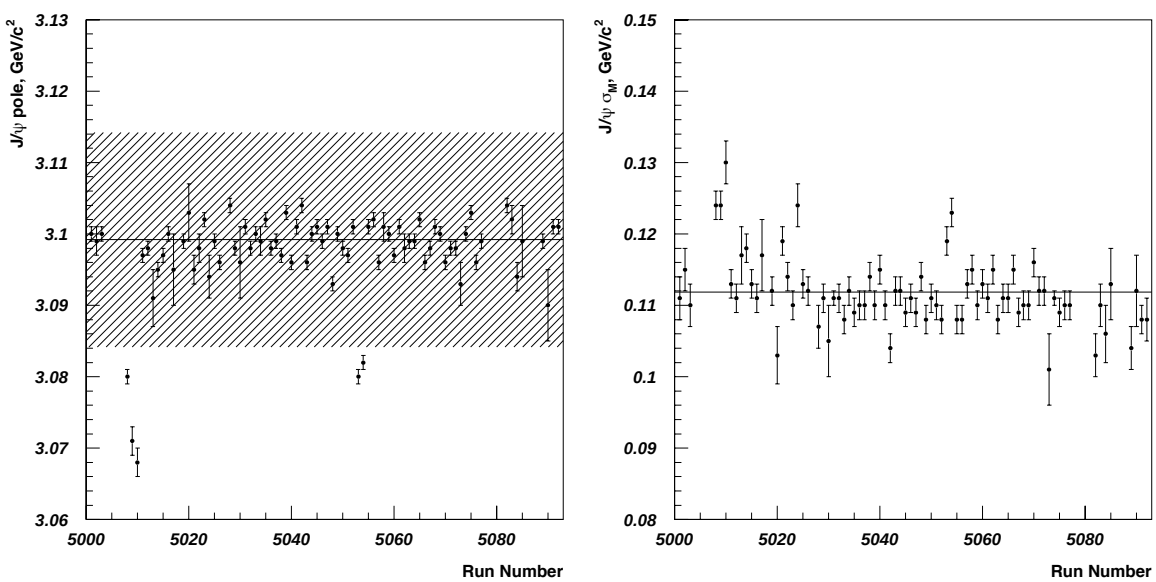

Figure 3.9: (Left) Cut on the J/ψ pole position. The runs with the pole deviating by more than 15 MeV/c^2 from the average value are rejected; (Right) Mass resolution for each run at the J/ψ mass. (For *pAl*97 data).

- from time to time, due to a malfunction in the electronics or in the power supplies of the trigger hodoscopes, the trigger efficiency of some sextant may decrease. For this reason I

reject the runs where the fraction of muons triggered in some sextant differs by more than 3 standard deviations from the corresponding value averaged over the whole data taking period (Fig. 3.10).

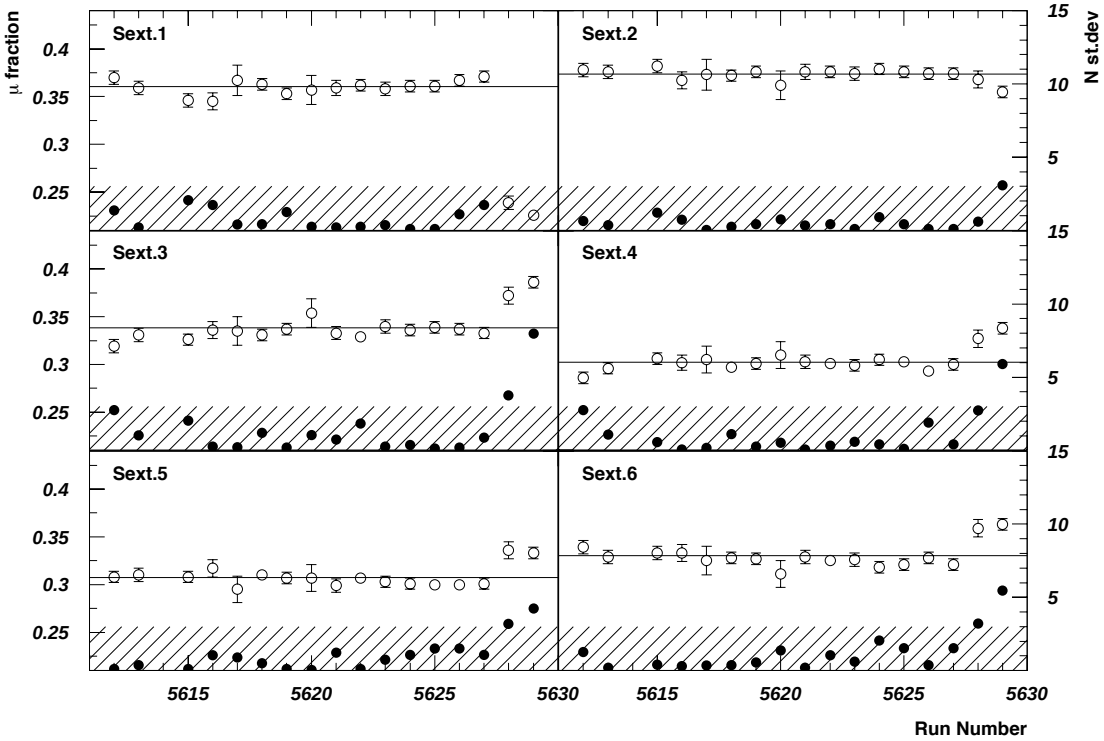

Figure 3.10: Run selection according to the fraction of the muons triggered in each sextant. The hollow points show the ratio of the μ's triggered in a given sextant to the total amount of muons. The black points show the number of standard deviations of this fraction from its average value (excluding the anomalous points). The runs with more than 3 standard deviations (outside the hatched region) are rejected. (For $pW98$ data)

- the runs with anomalous values of the ratios of the different argon counters were rejected.

3.3.2 Event Selection Cuts

First, the **Fiducial** cuts are applied, which ensure that each reconstructed muon

- does not pass through the insensitive regions of any MWPC;
- passes through active scintillator slabs both in the R_1 and in the R_2 trigger hodoscopes;
- has a $V(R_1,R_2)R_3R_4$ combination compatible with being produced in the target.

The most important event by event cut applied to the data, intended to minimize the number of dimuons produced outside of the target and to eliminate some fraction of the combinatorial background, is the **PDTARG** cut. It rejects all events where at least for one muon the product of its impact parameter at the target center and its momentum is higher than some predefined value.

First, for the sample of $\mu^+\mu^-$ dimuons from the J/ψ mass region ($2.7 < M < 3.5\ GeV/c^2$), which have the minimal contamination of off-target events, the Gaussian widths of the $P \times dX$ and $P \times dY$ distributions for 16 bins in momentum from 5 to 85 GeV/c were extracted and parametrized as a function of the momentum. Then, for each muon the χ^2 probability of coming from the target was estimated according to

$$\chi^2 = \left(\frac{PdX}{\sigma_{PdX}(P)}\right)^2 + \left(\frac{PdY}{\sigma_{PdY}(P)}\right)^2 \tag{3.12}$$

The left plot of Fig. 3.11 shows the corresponding probability distributions for the muons from two samples: opposite sign dimuons from the mass region $2.7 < M < 3.5\ GeV/c^2$ from the normal data taking runs with the target in its place (marked as **Tgt.In**) and from the pairs of runs without the target (marked as **Tgt.Out**). In order to avoid the bias induced by the specific acceptance of each sign of muons, such distributions are prepared separately for the convergent and divergent trajectories.

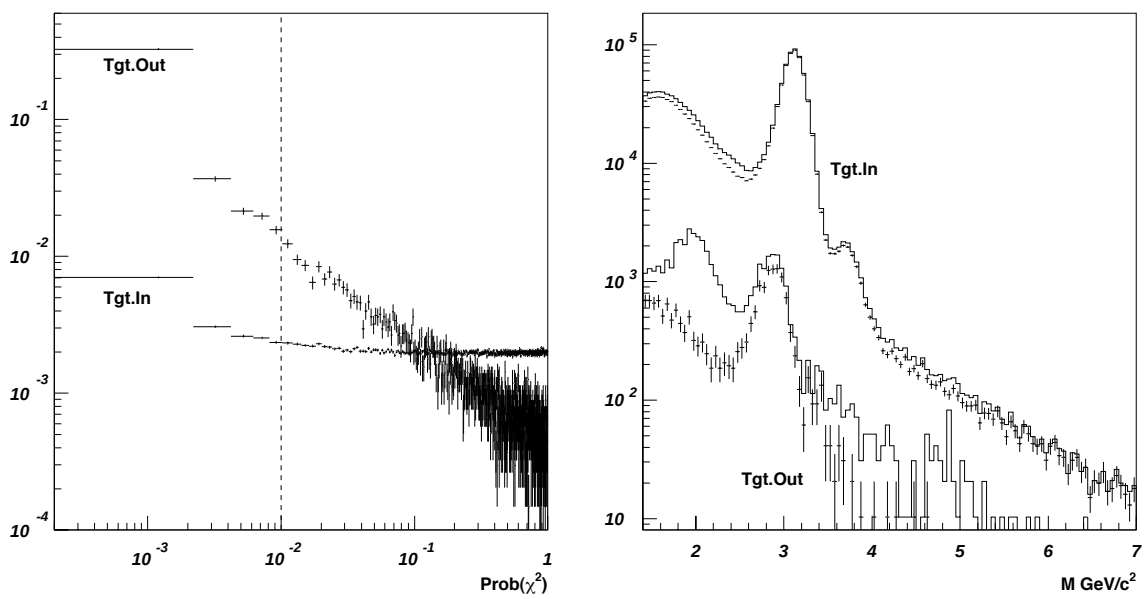

Figure 3.11: (Left) χ^2 -estimated probability distributions for the muon to come from the target for the sample of dimuons of mass $2.7 < M < 3.5\ GeV/c^2$ in the normal data taking runs (marked as **Tgt.In**) and in the runs without target (**Tgt.Out**). (Right) The corresponding $\mu^+\mu^-$ mass spectra without any PDTARG cut (solid lines) and after the 1% probability cut (error bars). The data are from the pW96 runs.

The right plot of Fig. 3.11 shows the **Tgt.In** and **Tgt.Out** mass spectra before (solid lines) and after the application of the 1%-probability cut to pW96 data. In the data to be analyzed the pairs with at least one muon having probability less than 1% are rejected, which means a loss of 1.99% of 'good' pairs [1] originating on the target (since the probability distribution of the muons from such pairs is flat). At the same time this 1%-probability cut eliminates $\sim 60\%$ of the dimuons collected in the runs without target.

[1] In fact, the muons originated on the target but having the low probabilities (high values of χ^2) are mainly the ones which suffered the strongest multiple scattering in the absorber, thus the 'good' pairs rejected by this cut have a deteriorated mass resolution.

As it will be explained later, the background subtraction procedure used in NA50 is valid only if the muons of both signs have the same acceptance. This is ensured by a special (**Image**) cut, rejecting any reconstructed muon which after inversion of its sign fails to satisfy the reconstruction and selection criteria.

4 Analysis Procedure

This chapter describes the procedures used for data analysis: estimation of the combinatorial background and of the contribution of dimuons originated in interactions outside of the target, disentangling of the different physics signals from the dimuon spectrum, calculation of the acceptances for each of them and luminosity calculation for extracting the absolute cross sections.

4.1 Non-Signal Contributions

These are the processes whose contribution should be estimated and subtracted from the dimuon spectrum in order to extract the useful physics signals we are interested in.

4.1.1 Estimation of the Combinatorial Background

Despite the presence of the hadron absorber, even in the pA collisions one of the strongest contributions to the dimuon spectrum is the background from the uncorrelated meson decays (mainly $\pi \to \mu + \nu$ and $K \to \mu + X$). Thanks to its combinatorial nature[1] the shape (and the magnitude to lesser extent) of this contribution to the opposite sign dimuon spectrum may be estimated from the (also measured) like sign dimuons spectra, where there are no other processes but CB.

Indeed, let $P(N^+)$ ($P(N^-)$) be the effective probability to produce N^+ positively (N^- negatively) charged mesons in a pA collision (or during the detector readout time, if the interaction rate is so high that during this time few collisions happen), and p_d the probability for a single meson to decay to $\mu + X$. Assuming that the probabilities for the pair of the muons to be accepted and pass all selection cuts are A^{++}, A^{--} and A^{+-} for respective sign combinations, the number of combinatorial dimuons detected in N_o events will be:

$$N^{++} = N_o A^{++} \int P(N^+) \frac{N^+ {p_d}^2 (N^+ - 1)}{2} \mathrm{d}N^+ = \frac{N_o}{2} A^{++} {p_d}^2 (< N^{+2} > - < N^+ >)$$

$$N^{--} = N_o A^{--} \int P(N^-) \frac{N^- {p_d}^2 (N^- - 1)}{2} \mathrm{d}N^- = \frac{N_o}{2} A^{--} {p_d}^2 (< N^{-2} > - < N^- >)$$

$$N^{+-} = N_o A^{+-} \int P(N^+) P(N^-) N^+ N^- {p_d}^2 \mathrm{d}N^+ \mathrm{d}N^- = N_o A^{+-} {p_d}^2 < N^+ >< N^- >$$

Assuming that the multiplicity distributions follow the Poisson law and using its property $< N >^2 =< N^2 > - < N >$ one gets:

[1] Apart from the pairs of the muons from these sources (and heavier mesons decaying to single $\mu + X$), surely, the combination of one muon from π, K decay and another one from, for example, $J/\psi \to \mu^+ \mu^-$, is also possible. The arguments below only use the lack of the correlations between the production of the two muons, thus remain valid even for the latter case.

$$N^{+-} = 2\sqrt{N^{++}N^{--}} \times \frac{A^{+-}}{A^{++}A^{--}} \tag{4.1}$$

Thus, if the acceptance of the pair does not depend on the sign combination, one can use the simple estimate

$$N^{+-} = 2\sqrt{N^{++}N^{--}} \tag{4.2}$$

As it was mentioned in the Section 3.3.2, the independence of the acceptance from the charge is reached by the special **Image** cut.

In reality the phase space and charge conservation constraints lead to deviations of the multiplicity distributions from the Poisson law and to charge correlations (for instance, in the single p-nucleon collision it is easier to produce $\pi^+\pi^-$ than $\pi^-\pi^-$). In order to cope with such physical correlations, one introduces an empirical R-factor in front of the $\sqrt{}$. It can be estimated from Monte-Carlo simulations or assumed to be a free parameter of a fit. Since the correlations are absent if the parent mesons of the triggered muons were originated in different p-nucleon collisions, the R-factor drops down as the target mass number increases and behaves as $\sim 1/N_{coll}$ where N_{coll} is the average number of interactions during the detector readout gate. This leads to an inverse dependence of the R-factor on the beam intensity[2].

Since the Eq.4.2 should be applied to each kinematical bin of the data to be fitted, there is a risk of underestimating the $+-$ background if some like-sign bin happens to be empty. In order to avoid such situation, instead of using the measured bin by bin numbers, one can use the parametrizations of the like sign CB spectra. In the present analysis the mass distributions of the $++$ and $--$ spectra for each kinematical region studied (rapidity, X_F) were fitted by the empirical function

$$\frac{\mathrm{d}N^{++(--)}}{\mathrm{d}M} = a_0 \times \left\{ \exp\frac{-(M-M_1)^2}{2\sigma_1^2(M)} + a_1 \exp\frac{-(M-M_2)^2}{2{\sigma_2}^2} \right\} \tag{4.3}$$

$$\sigma_1(M) = \begin{cases} \sigma_1 & \text{if} \quad M \le \hat{M}_1 \\ \sigma_1\left(1 + b_1(M - \hat{M}_1)\right) & \text{if} \quad M > \hat{M}_1 \end{cases}$$

where a_0, a_1, b_1, M_1, $\hat{M}_1$, M_2, σ_1 and σ_2 are the free parameters of the fit. In order to avoid any bias due to the specific sign of the magnetic field, the parametrizations of $++$ and $--$ spectra were done separately for the data taken with the two signs. Fig.4.1 shows the example of the $++$ and $--$ dimuon spectra (from the $pW96$ data set) and their parametrizations.

Finally, the opposite sign CB contribution is estimated as:

$$\frac{\mathrm{d}N_{Bg}^{+-}}{\mathrm{d}M} = 2R \times \left\{ \sqrt{\left.\frac{\mathrm{d}N}{\mathrm{d}M}\right|_{\oplus}^{++} \cdot \left.\frac{\mathrm{d}N}{\mathrm{d}M}\right|_{\oplus}^{--}} + \sqrt{\left.\frac{\mathrm{d}N}{\mathrm{d}M}\right|_{\ominus}^{++} \cdot \left.\frac{\mathrm{d}N}{\mathrm{d}M}\right|_{\ominus}^{--}} \right\} \tag{4.4}$$

[2]Monte-Carlo simulations show that in case of low interaction rate (no pile-up) the R-factor for the pW collison system is ~ 1.24, see [80].

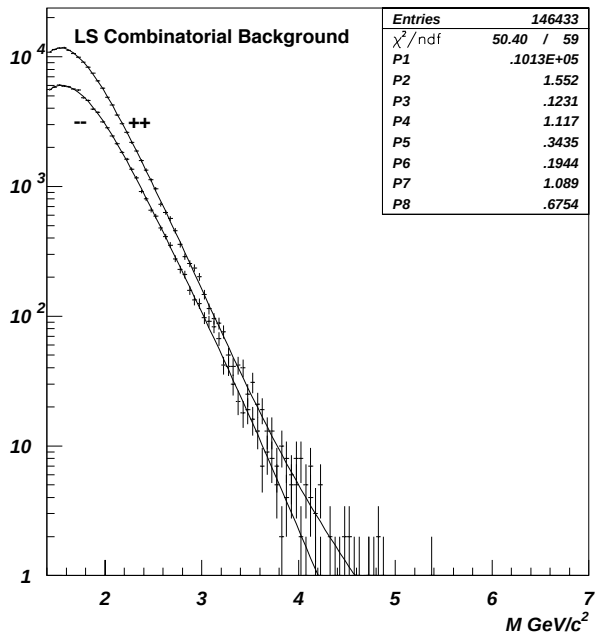

Figure 4.1: $\mu^+\mu^+$ and $\mu^-\mu^-$ spectra and their parametrizations for the $pW96$ data with $\oplus$ magnet current polarity. The fitted parameters shown correspond to the $++$ sample fit.

4.1.2 Target-Out Contribution

As one can see on Fig.3.11 even after the application of the **PDTARG** cut the contribution of the dimuons from the interactions outside of the target remains non-negligible. Being a few percents under the J/ψ and ψ' peaks, it can easily affect their ratio by a similar factor because its shape resembles the contribution of these resonances. The application of a more severe **PDTARG** cut seems to be inappropriate, since in any case the target-out contribution is never eliminated entirely, especially from the region in the proximity of the target (beginning of the preabsorber). Thus this contribution should be estimated from the special **Target Out** runs data and fixed in the **Normal** data fits.

One should note that the target out spectrum has the same composition as the usual spectrum of the **Normal** data, i.e. it has the contribution of the combinatorial background, J/ψ, continuum, etc., the only difference being that since the interactions occur far from the target but the reconstruction algorithm assumes that the interaction vertex is located at the nominal target center, the reconstructed mass suffers a shift towards the higher masses if the interaction took place upstream of the target (i.e. the assumed vertex position artificially opens the angle between the muons) and **vice versa**. Since the combinatorial background contribution to the opposite sign target-out spectrum is accounted for automatically during the above described background estimation procedure, as the 'signal' target-out contribution one should use not the measured and rescaled spectrum of the **Target Out** runs, but rather what is left from it after the subtraction of its own the combinatorial background, estimated from the like sign dimuon spectra of these runs. Because the total flux of protons for the **Target-Out** runs is lower than the one of the **Normal** data (the usual ratio is arount 1 to 10), the simple subtraction of the rescaled 'signal' target-out spectrum will lead to under/over-estimation of this contribution in certain bins. Instead, in the present analysis the following procedure is used:

- For the *TargetOut* runs of the given data set, the like-sign spectra for each kinematical

region studied are parametrized by the functional forms 4.3;

- The opposite-sign *TargetOut* spectrum is fitted as the sum of the combinatorial background computed as usually according to Eq.4.4 (with the R-factor set to be equal to 1) and the functional form representing the proper 'signal' contribution:

$$\frac{\mathrm{d}N_{TGO}}{\mathrm{d}M} = a_0 \times \left\{ \exp\frac{-(M-M_1)^2}{2{\sigma_1}^2} + a_1 \times \exp\frac{-(M-M_2)^2}{2{\sigma_2}^2} + a_2 \times \exp\frac{-(M-M_3)^2}{2{\sigma_3}^2} \right\} \tag{4.5}$$

with a_0, a_1, a_2, M_1, M_2, M_3, σ_1, σ_2 and σ_3 being the free parameters of the fit. The first two gaussians represent the two separate J/ψ peaks from the interactions upstream[3] and downstream of the target, while the third gaussian describes the 'continuum' contribution. Fig.4.2 demonstrates the opposite-sign **Target Out** run spectrum of the $pW96$ data set and the results of the fitting procedure.

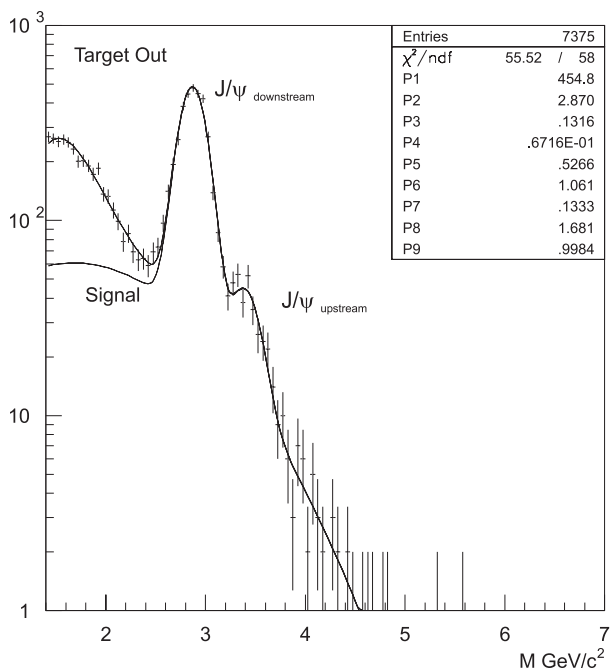

Figure 4.2: Opposite-sign **Target Out** run spectrum of the $pW96$ data set. The fitted $''signal''$ and $OS = ''signal'' + ''CombinatorialBackground''$ functional forms are shown by solid lines.

- In order to fix the target-out 'signal' contribution in the **Normal** run spectrum the overall normalization coefficient a_0 is rescaled by the factor

$$C = \frac{(Argo3 \times \varepsilon_{rec})_{Tg.In}}{(Argo3 \times \varepsilon_{rec})_{Tg.Out}}$$

where $Argo3_{Tg.In}$ ($Argo3_{Tg.Out}$) is the value of the Argon3 (most stable) counter cumulated over all **Normal** (**Target Out**) runs and the ε_{rec} is the corresponding estimated dimuon reconstruction efficiency.

[3]Note, that the J/ψ's produced upstream (downstream) of the target are reconstructed with a higher (lower) mass, because the reconstruction algorithm always assumes that the vertex is in the target center, thus artifically opening (closing) the angle between the two muons

- In order to account for the large statistical uncertainties of the target-out contribution, the errors of the **Normal** data histograms are quadratically added with the errors (square root of the bin content) of this rescaled 'signal' contribution

Unfortunatelly, not all data sets have the corresponding **Target Out** runs taken. Especially this concerns the low intensity runs (see. the Table 4.1 in the end of this Chapter), where, even if such data were collected, its statistics is not enough to do the fit described above. For this reason the following was done: for the high intensity **pCu97** data the **Target Out** runs of its preceding **pAg97** data set were used; for all the low intensity runs the **Target Out** data averaged over the all high intensity data sets (except the **pBe98** which shows some anomalies) were used.

4.2 Functional Forms for Different Signals

In order to decompose (fit) the measured mass spectra in a superposition of the known physical processes, for each of them the mass spectral distribution was obtained by feeding the Monte-Carlo generated events into the detector simulation/reconstruction program. The obtained histograms (for each studied kinematical region) were fitted by a empirically selected functional forms. Ideally, the dimuon spectra should be then fitted as superposition of these functional forms, with only the amplitudes of each form allowed as free parameters. Unfortunately, the practice shows that the simulation package is not fully adequate to the real detector response, thus certain parameters describing the shapes of the different signal processes also have to be adjusted with data. This is particularly important when the data has such high statistics as the samples studied in this work. This section describes the shape functions used for each signal contribution and the way they are corrected in order to reproduce the data.

4.2.1 Drell-Yan and Open Charm spectra

As a generator for both the Drell-Yan and Open Charm contributions the PYTHIA package [81] was used with the MRSA N^o43 [23] parton density distributions (which properly reproduce the $\bar{u}$ and $\bar{d}$ quarks isospin asymmetry) and the mass of the c-quark was set to 1.5 GeV/c^2. For Drell-Yan both pp and pn contributions were generated separately in order to account for the isospin asymmetry. Since at small X_F-s, relevant for the NA50 experiment, $c\bar{c}$ production occurs almost exclusively via gluon fusion, only pp collisions were generated for the Open Charm sample.

The parametrization of the histograms obtained after the reconstruction of the generated Monte-Carlo data was done in the following way:

- For the Drell-Yan contribution in the pA dimuon spectrum, the pp and pn histograms (normalized to a single $p-nucleon$ collision) were added with the weights N_p and N_n, respectively, and obtained histogram was fitted by

$$\frac{\mathrm{d}N_{DY}}{\mathrm{d}M} = a_0 \times \left\{ \exp\frac{-(M-M_1)^2}{2\sigma_1{}^2} + a_1 \exp(-c_1 M) + a_2 \exp(-c_2 M) \right\}$$

with a_0, M_1, σ_1, c_1 and c_2 as free parameters.

- the Open Charm contribution histogram was fitted by

$$\frac{\mathrm{d}N_{D\overline{D}}}{\mathrm{d}M} = a_0 \times \exp\frac{-(M-M_1)^2}{2\sigma_1(M)^2}$$

$$\sigma_1(M) = \begin{cases} \sigma_1 & \text{if} \quad M \leq \hat{M}_1 \\ \sigma_1\left(1+b_1(M-\hat{M}_1)\right) & \text{if} \quad M > \hat{M}_1 \end{cases}$$

with a_0, b_1, M_1, $\hat{M}_1$ and σ_1 as a free parameters.

Fig.4.3 shows the Monte-Carlo histograms and the fitted shapes for the Drell-Yan (Left) and Open Charm (Right) contributions to the pW dimuon spectrum.

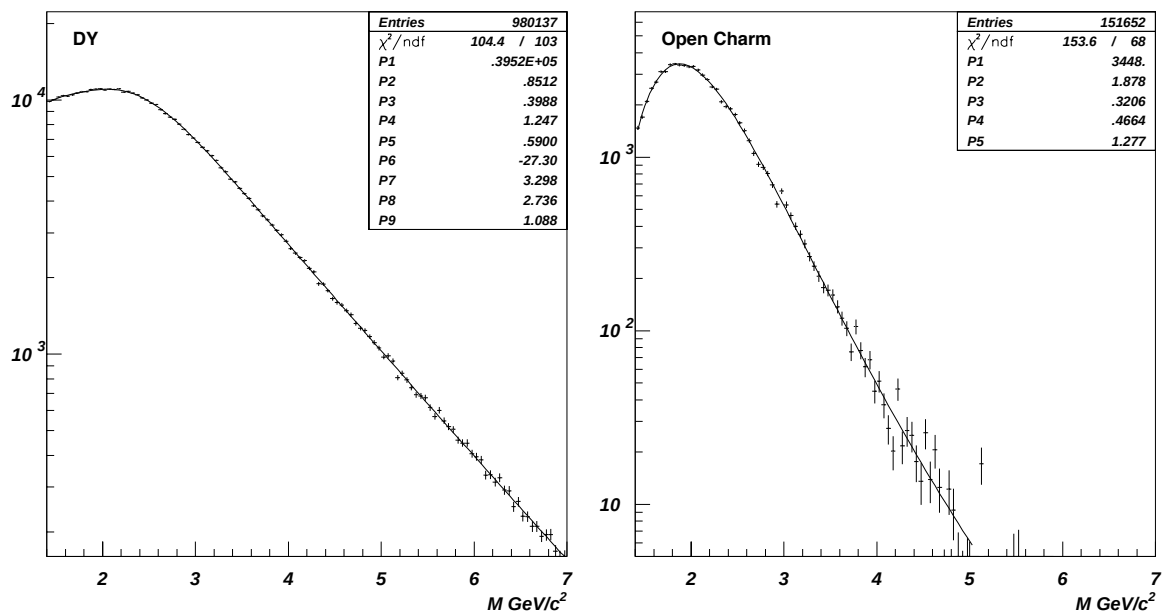

Figure 4.3: Shapes of the simulated (generated and reconstructed) Drell-Yan (Left) and Open-Charm (Right) contributions to the pW dimuon spectrum.

During the fit to the real data, the shapes of both Drell-Yan and Open Charm contributions obtained from the Monte-Carlo were kept unchanged, only their normalizations (a_0^{DY} and $a_0^{D\bar{D}}$ or their ratio) being free parameters of the fit.

4.2.2 J/ψ and ψ' spectra

Since the study of the J/ψ and ψ' resonances is the main objective of this work, the details of their fitting procedure deserve a more thorough description.

The generation of the Monte-Carlo data was done using a Gaussian distribution in rapidity and a thermal one in P_T. The parameters of the distributions were tuned to reproduce the observed spectra: $\sigma_y = 0.75$ and $T = 295MeV$.

The very high statistics (hence, very small error bars) to be fitted and especially the interplay between the high-mass tail of the J/ψ and the ψ' do not allow to use for their fit simple

gaussians. Instead, the Monte-Carlo generated peaks are fitted with a 'gaussian' with a mass dependent variance:

$$\frac{\mathrm{d}N_{J/\psi(\psi')}}{\mathrm{d}M} = a_0 \times \exp\frac{-(M-M_1)^2}{2\sigma(M)^2} \tag{4.6}$$

Fig. 4.4 shows the 'dispersion' of the Monte-Carlo generated J/ψ shape for three different targets, extracted as

$$\sigma(M) = \sqrt{-\frac{(M-M_{pole})^2}{2\ln\frac{\mathrm{d}N}{\mathrm{d}M}}} \tag{4.7}$$

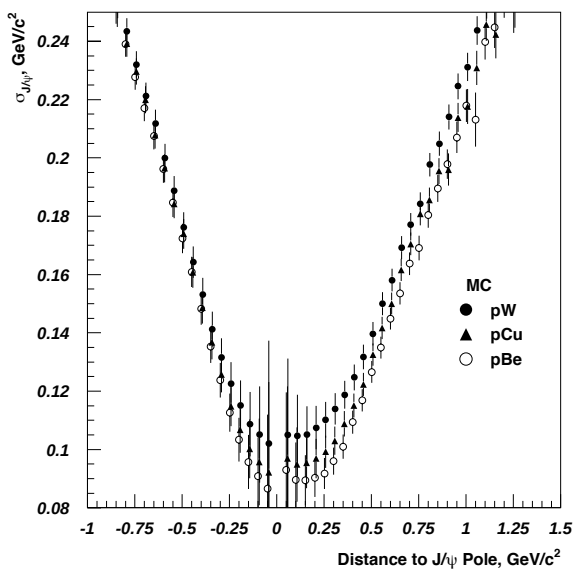

Figure 4.4: Shape of the mass-dependent 'dispersion' extracted according to Eq.4.7 from the Monte-Carlo generated J/ψ mass distribution.

The apparent asymmetry even in the proximity of the pole is caused by different processes: while the multiple scattering of the muons in the hadron absorber contributes both above and below the pole, the error in the compensation of the muon's energy loss in the absorber contributes mainly to the low-mass tail of the J/ψ reconstructed spectrum, since the energy of the muons whose stragling corresponds to the Landau tail of the energy loss spectrum remains undercompensated.

The shape of the J/ψ dispersion is well described by the functional form:

$$\sigma_{J/\psi}(M) = \begin{cases} \sigma_1 + b_1(c_1M_0 - M)^{d_1 - g_1\sqrt{c_1M_0 - M}} & \text{if} \quad M \le c_1M_0 \\ \sigma_1 & \text{if} \quad c_1M_0 < M \le M_0 \\ \sigma_2 & \text{if} \quad M_0 \le M < c_2M_0 \\ \sigma_2 + b_2(c_2M_0 - M)^{d_2 - g_2\sqrt{c_2M_0 - M}} & \text{if} \quad M \ge c_2M_0 \end{cases} \tag{4.8}$$

where the parameters c_1 and c_2 are fixed to be 0.97 and 1.05 respectively and the rest (M_0,σ_1,σ_2, b_1, b_2, d_1, d_2, g_1 and g_2) are the free parameters of the fit.

The case of the ψ' is similar to the J/ψ, with the only difference that due to the lower statistics and the much smaller region of the measured mass spectrum where it is the dominant contribution, I use the same 'constant term' for the description of the dispersion:

$$\sigma_{\psi'}(M) = \begin{cases} \sigma_0 + b_1(c_1M_0 - M)^{d_1 - g_1\sqrt{c_1M_0 - M}} & \text{if} \quad M \leq c_1M_0 \\ \sigma_0 & \text{if} \quad c_1M_0 < M < c_2M_0 \\ \sigma_0 + b_2(c_2M_0 - M)^{d_2 - g_2\sqrt{c_2M_0 - M}} & \text{if} \quad M \geq c_2M_0 \end{cases} \tag{4.9}$$

Fig.4.5 shows the Monte-Carlo mass distributions for J/ψ (left) and ψ' (right) fitted by the described functions.

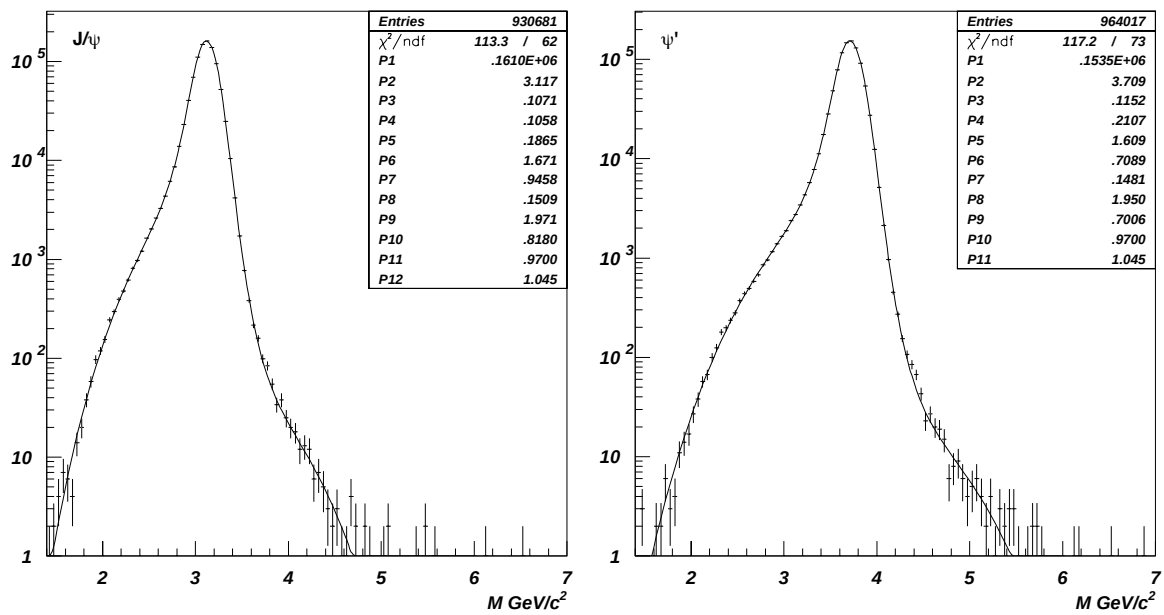

Figure 4.5: Shapes of the simulated (generated and reconstructed) J/ψ (Left) and ψ' (Right) spectra fitted by the forms 4.6 − 4.9

Unfortunately, as was mentioned above, the NA50 simulation package is not adequate enough to the real detector response, so one cannot use the fitted Monte-Carlo shapes as they are, adjusting only the normalization coefficients. In particular, the parameters determining the mass-dependent variation of the pseudo-Gaussian used for the resonances fit need to be readjusted with the data. This is especially important for the J/ψ, since a small error in the continuation of its high-mass tail under the ψ' peak[4] may lead to a few percent error in the estimation of the ψ' contribution. For this reason the following multistep procedure was used in the present analysis.

As it will be described in the 4.3 section, first the normalizations of the different components of the dimuon spectrum are roughly fixed, in order to estimate the relatively precise nonresonant contributions under the J/ψ and ψ' peaks (mainly from $Drell-Yan$ and $D\overline{D}$). Since the J/ψ peak contributes $\sim 95\%$ to the signal in the mass range $2.7 < M < 3.5\ GeV/c^2$, the only free parameters of the fit at this stage, apart from the normalization coefficients, are the J/ψ pole

[4]Which by itself cannot change the estimated J/ψ cross section, since only $\sim 0.3\%$ of the J/ψ's are reconstructed with a mass greater than 3.5 GeV/c^2.

position ($M_0^{J/\psi}$), left/right dispersions in the proximity of the pole ($\sigma_1^{J/\psi}$ and $\sigma_2^{J/\psi}$) and the mass difference between the J/ψ and ψ' poles.

After approximately fixing the $Drell-Yan$ and $D\overline{D}$ amplitudes, the precise fit of the J/ψ and ψ' shapes and amplitudes is done according to the following receipt in the mass range $2.7 < M < 4.1\ GeV/c^2$. The J/ψ is fitted according to Eqs. 4.6, 4.8 with all the parameters (except $c_{1,2}$) free in order to reproduce the dimuon mass spectrum in the mass window $M_{low}^{merge} < M < M_{high}^{merge}$ (M_{low}^{merge} is fixed to be 2.7 GeV/c^2 and $M_{high}^{merge} \sim 3.4-3.5\ GeV/c^2$)[5]. This gives the $\sigma_{J/\psi}^{inside}(M)$. Outside of this mass region the value of $\sigma_{J/\psi}(M)$ is obtained by merging the results of this fit with the ones obtained from Monte-Carlo according to:

$$\sigma_{J/\psi}^{outside}(M) = \sigma_{J/\psi}^{MC}(M) + \left\{\sigma_{J/\psi}^{inside}(M_{merge}) - \sigma_{J/\psi}^{MC}(M_{merge})\right\} \tag{4.10}$$

In what concerns the fit of the ψ' contribution, its amplitude and pole position are free parameters, while $\sigma_{\psi'}^{data}(M)$ is obtained from its Monte-Carlo fitted value $\sigma_{\psi'}^{MC}(M)$ (Eq.4.9) after its rescaling by a factor reflecting the widening of the J/ψ shape going from the MC to the data:

$$\sigma_{\psi'}^{data}(M) = \sigma_{\psi'}^{MC}(M) \times \frac{\int \exp\frac{-(M-M_1^{J/\psi})^2}{2\sigma_{J/\psi}^{data}(M)^2}\mathrm{d}M}{\int \exp\frac{-(M-M_1^{J/\psi})^2}{2\sigma_{J/\psi}^{MC}(M)^2}\mathrm{d}M} \tag{4.11}$$

The left plot of Fig. 4.6 shows the results of $\sigma_{J/\psi}(M)$ fit with three different values of the M_{high}^{merge}. The dotted curve corresponds to the results of the Monte-Carlo fit ($\sigma_{J/\psi}^{MC}(M)$), the dot-dashed is for the $\sigma_{J/\psi}^{inside}(M)$ (the tails outside the region $M_{low}^{merge} - M_{high}^{merge}$ are not used), while the solid and dashed curves are the final $\sigma_{J/\psi}^{data}(M)$. One can see that there is a significant difference between the $\sigma_{J/\psi}^{data}(M)$ corresponding to different merging points. The right plot of Fig. 4.6 shows the results of the J/ψ and ψ' fits with the two extreme values of M_{high}^{merge}: solid curves for 3.4 and dashed ones for 3.5 GeV/c^2. Both merging points give a χ^2/NDF of the fit close to 1, but the resulting $\psi'/J/\psi$ ratio is quite different. In order to avoid a systematical bias due to the uncertainty in the behaviour of the J/ψ tail under the ψ' peak, the results for the ψ' are obtained with $M_{high}^{merge} = 3.45\ GeV/c^2$, while the maximum difference between the results with $M_{high}^{merge} = 3.4$ and 3.5 GeV/c^2 will be treated as a systematic error of the fit[6].

4.3 The Fitting Procedure

This section summarizes how the experimental data are fitted using the different contributions described above.

First the data integrated over the entire NA50 acceptance window is fitted in following steps:

- For each data set the **Target Out** contribution is estimated and fixed, as described in the Section 4.1.2.

[5] In this mass window the J/ψ is the dominant contribution (at least 50%).

[6] The values 3.4 and 3.5 GeV/c^2 are chosen as extreme values for the merging point because for points below 3.4 GeV/c^2 the fitted curve systematically starts to miss the valley between the J/ψ and ψ', while a fit with $M_{high}^{merge} > 3.5\ GeV/c^2$ is meaningless since above this point the J/ψ is not a dominant signal anymore.

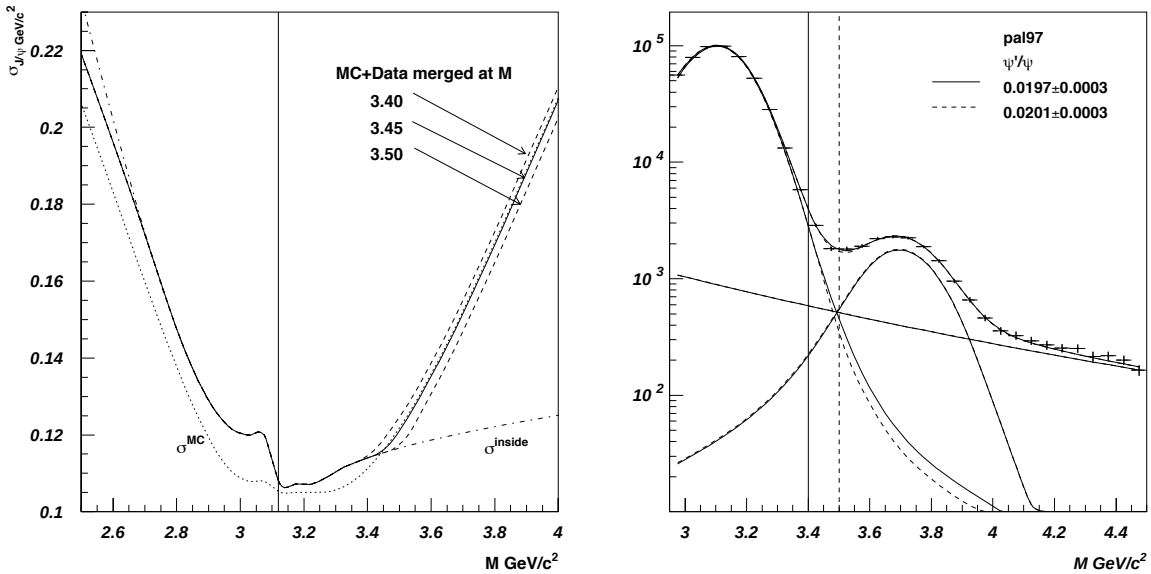

Figure 4.6: (Left) Results of the $\sigma_{J/\psi}(M)$ fit with three different values of the $M_{high}^{merge} = 3.4, 3.45$ and $3.5\ GeV/c^2$: the dotted curve corresponds to the results of the Monte-Carlo fit ($\sigma_{J/\psi}^{MC}(M)$), the dot-dashed is for $\sigma_{J/\psi}^{inside}(M)$ adjusted to data inside the region $2.7 - M_{high}^{merge}$ and the solid and dashed curves are the final $\sigma_{J/\psi}^{data}(M)$; (Right) results of the J/ψ and ψ' fits with the two extreme values of M_{high}^{merge}: solid curves are for 3.4 and dashed ones are for $3.5\ GeV/c^2$.

- Each data set is fitted separately in the whole mass range $1.4 < M < 7.0\ GeV/c^2$, with the following free parameters (individual for each data set):
  the R-factor for the combinatorial background;
  the amplitudes for the J/ψ, ψ' Drell-Yan and $D\overline{D}$ contributions:
  the pole position, left/right dispersions of the J/ψ;
  the mass difference between the J/ψ and ψ' pole positions.

  In order to avoid the bias of the Drell-Yan contribution estimation due to the R-factor being a free parameter, an additional constraint is imposed: the fitted value should not differ from the experimental one by more than one standard deviation in the mass range $4.1 < M < 7.0\ GeV/c^2$ (where Drell-Yan contributes $\sim 95\%$ of events).

  The main aim of this preliminary fit is to find the relatively precise poles positions and widths for the two charmonia states taking into account the underlying continuum contributions.

- Since one cannot expect any strong difference between the scaling of the Drell-Yan and Open Charm contributions with atomic mass number A, in order to decrease the number of degrees of freedom of the fit it is assumed that the $D\overline{D}/Drell-Yan$ ratio is the same for all data sets (of course, letting it to be different in different kinematic domains of the fitted data). To fix this ratio the simultaneous fit of all data sets is done, with free parameters being the amplitudes for the contributions from J/ψ, ψ' and Drell-Yan (individually for each set) and single $D\overline{D}/Drell-Yan$ ratio. The rest of parameters is fixed to values obtained from the previous steop.

- The precise fit of the J/ψ and ψ' shapes in the mass range $2.7 < M < 4.1\ GeV/c^2$ is done, as it is described in Section 4.2.2.

- After fixing in this way all "fine tuning" parameters describing the J/ψ and ψ', the final fit of each data set in the whole mass range $1.4 < M < 7.0\ GeV/c^2$ is done with the free parameters being the amplitudes of J/ψ, ψ' and Drell-Yan contributions (the ratio $D\overline{D}/Drell-Yan$ being kept fixed to value obtained from the simultaneous fit).

The fit of the restricted kinematical regions (e.g. bins in rapidity) proceeds according to the same steps, with only difference that the value of the R-factor is fixed to one obtained from the integrated data fit.

4.4 Acceptances Calculation

For each signal contributing to the $\mu^+\mu^-$ spectrum the acceptances were estimated according to the following procedure:

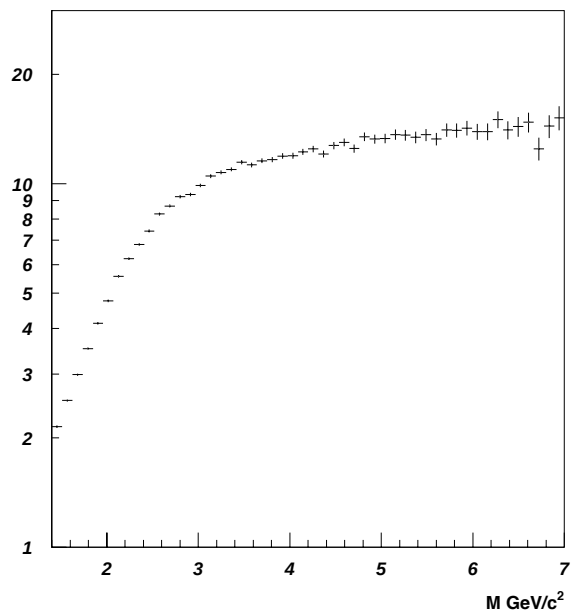

Figure 4.7: Acceptance (in percent) for the Drell-Yan process, as a function of the dimuon mass.

- The Monte-Carlo generated data was treated by the NA50 simulation and reconstruction program (with the same reconstruction options as for the real data).

- After the reconstruction of the Monte-Carlo data, the same cuts were applied as for the real experimental data. The only difference in the cuts is related to the **PDTARG** (Sec. 3.3.2): due to the mentioned drawbacks in the detector response simulation one cannot be sure that the parameters ($\sigma_{PdX}(P)$ and $\sigma_{PdY}(P)$) extracted from the real data will guarantee the flatness of the χ^2-estimated probability distribution for the generated muons. In order to avoid any bias in the acceptance estimation, instead of rejecting all the muons with estimated χ^2 probability below 1% (as it is done with real data), the value of the **PDTARG** probability cut was adjusted in such a way that it rejects exactly 1% of the single muons in the Monte-Carlo sample (as with the real data these constitute the worst, most scattered or wrongly measured muons).

- The acceptance was calculated as the ratio between the number of events that passed all reconstruction/selection cuts and the number of generated events in the same kinematical domain.

Since the differences in the experimental setups is very marginal (only the target material differs, except in the case of the $pW96$, where the BeO preabsorber was used instead of the one made of Al_2O_3), the generation of the Drell-Yan and $D\overline{D}$ contributions was done for a single setup only (since these are very CPU time consuming processes). Fig.4.7 shows the acceptance (in percent) for the Drell-Yan dimuons from pW collisions as a function of their mass. The acceptance for $D\overline{D}$ has a similar shape but lower values, due to its more pronounced tails in the $\cos\theta$ distribution, where the acceptance is virtually zero.

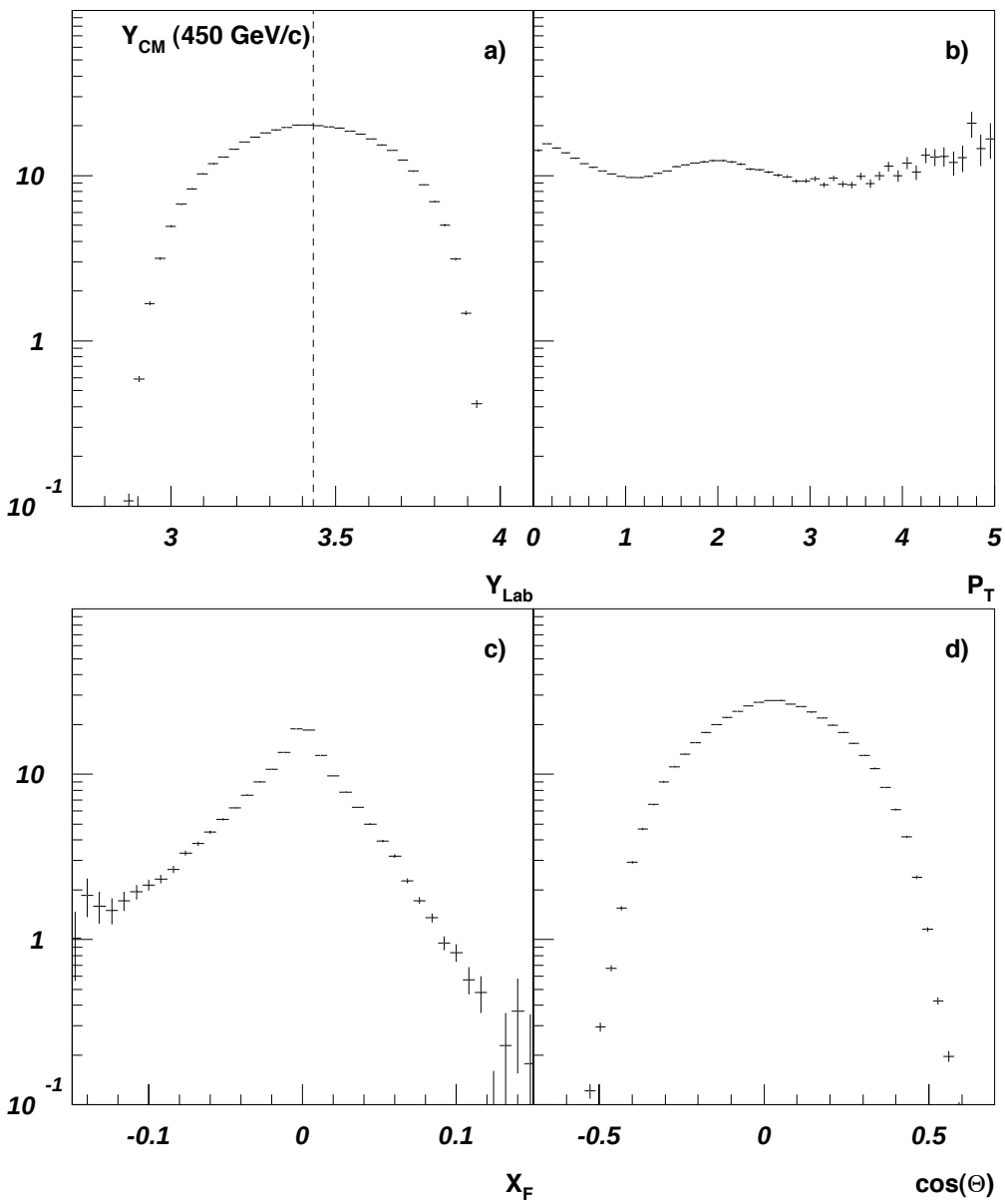

Figure 4.8: Acceptances (in percent) of the J/ψ originated in 450 GeV pA collisions as a function of the dimuon a) rapidity in the laboratory frame, b) transverse momentum, c) Feinman X, d) $\cos\theta$.

Although the generation of J/ψ and ψ', which is quite fast, was done for each setup separately, the acceptances are similar within errors. Fig.4.8 shows the acceptance for the J/ψ in four kinematical variables: Y_{lab}, P_T, X_F and $\cos\theta$.

The summary of the acceptances for the different processes is given in the Tables 7.1 and 7.2 of the Appendix 7.1.

4.5 Absolute Cross Section Calculation

After the extraction from the data of the number of dimuons originated, in any specific process, in collisions with a target of physical length L_{tg} and density ρ_{tg}, one can compute the inclusive cross section σ_x for this process in pA collisions according to

$$\sigma_x = \bar{n_x}\sigma_{pA}^{inel.} \tag{4.12}$$

where $\sigma_{pA}^{inel.}$ is the total inelastic pA cross section

$$\sigma_{pA}^{inel.} = \frac{A}{\lambda_I N_{Avo}} \tag{4.13}$$

with N_{Avo} being the Avogadro number and λ_I the inelastic interaction length (in g/cm^2) and $\bar{n_x}$ is the yield per interaction for the specific process, corrected for the dimuon trigger and reconstruction efficiencies, ε_{trig} and $\varepsilon_{\mu\mu}$ respectively:

$$\bar{n_x} = \frac{N_{\mu\mu}}{N_p\left\{1 - e^{-L_{tg}/(\rho_{tg}\lambda_I)}\right\}\varepsilon_{trig}\varepsilon_{\mu\mu}} \tag{4.14}$$

The total number of incident protons, N_p, is obtained from the integrated value of the Argon counters. Since this factor is one of the main sources of systematic errors, a more detailed description of this procedure follows.

4.5.1 Counting the Number of Incident Protons

All three argon counters (see 2.2.1) have different calibration coefficients, converting the ionization current to number of the incident protons. Fig.4.9 shows the run by run ratios of the different counters for the $pW96$ data set, when their last calibration was done: the left plot shows these ratios as a function of the run number (i.e. time). One can see that the deviations from the average values have a systematic dependence on the beam intensity (right plot), being at the level of $0.4-0.5\%$ for the ratios of Argo1 to Argo2 or Argo3, and practically disappear in the Argo3 to Argo2 ratio ($\sim 0.1\%$). This suggests that Argo1 is closer to saturation, while Argo2 and Argo3 have at least similar deviations from linearity with beam intensity (if any).

Unfortunately, the comparison of the ratios for different data sets shows that the response of the counters changes also with time. Fig.4.10 presents the same ratios for the different data taking periods (in chronological order) averaged over all selected runs for a given data set. From the first to the last data set, Argo1/Argo3, Argo1/Argo2 and Argo3/Argo2 change by 4.6, 2.6 and 1.9%, respectively. This suggests that the most stable counter is Argo3 and its values will be used for computing the integrated number of incident protons in each data set. The coefficients of the 1996 calibration will be used with a 3% systematical error.

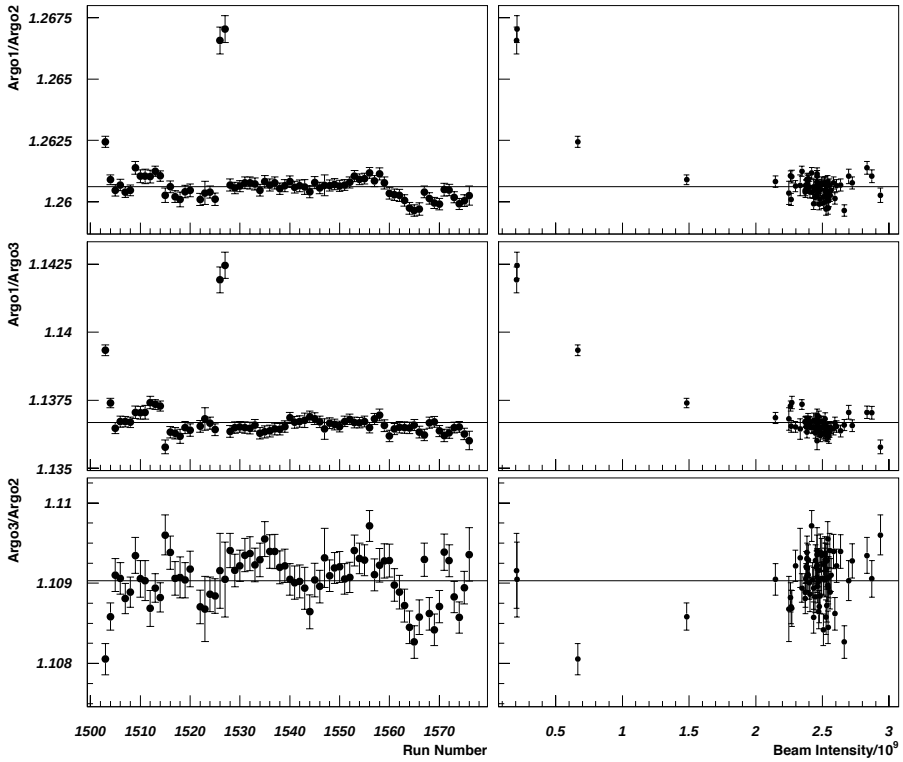

Figure 4.9: Run by run ratios of the three argon counters: from top to bottom : Argo1/Argo2, Argo1/Argo3 and Argo3/Argo2. The left plot shows their dependence on run number (time) while the Right one suggests that the deviations from the average values are caused by their slightly different dependences on the beam intensity.

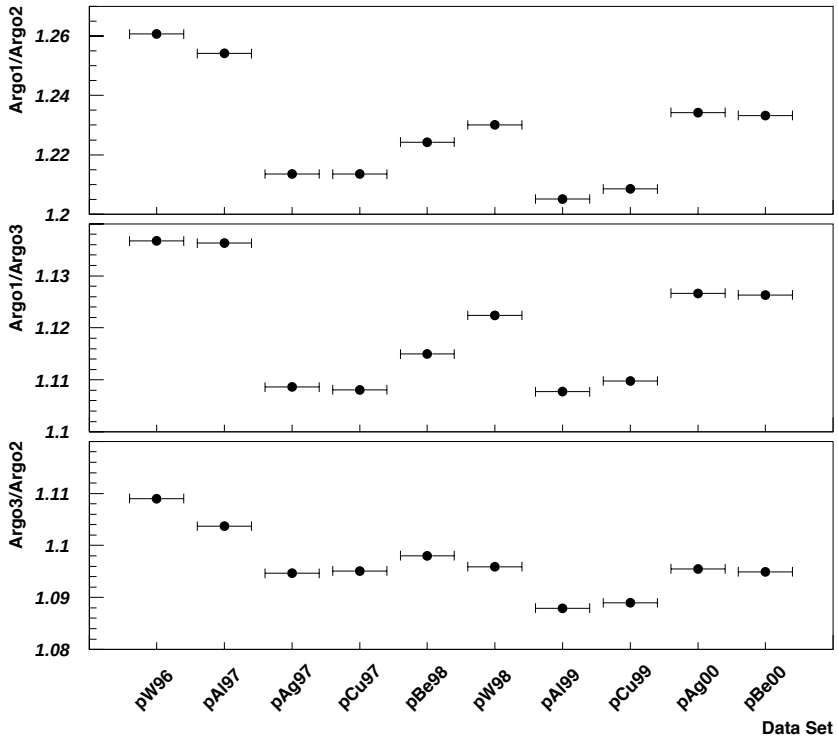

Figure 4.10: Ratios of the three argon counters, averaged over the selected runs of each data set in a chronological order of the data taking period.

4.5.2 Systematic Errors of the Absolute Normalization

Apart from the error of the calibration coefficients of the Argon counters there is an additional systematic error due to the uncertainty in the dimuon reconstruction and trigger efficiency. While the former is estimated on the run by run basis (see Section 3.2.3) the latter is computed only for special (low intensity) runs, normally once or twice per data taking period. Even worse, for some data sets used in the present study the trigger efficiency runs were not taken, in this case the values for the closest data taking period were used.

Figure 4.11 shows for each data set the ratio of the number of reconstructed dimuons with $2.7 < M < 3.5$ to the value of $Argo1$ counter (accounting for the dead time of the detector) corrected for dimuon trigger and reconstruction efficiencies as a function of the run number (Left) and the beam intensity of the run. One can see that this ratio experiences a systematic (time dependent) as well as a random variation far beyond the statistical fluctuations, caused probably by the malfunction of the detectors. In order to account for this variations the RMS divided by the average value of these ratios is taken as a systematic error on the product of the reconstruction and trigger efficiencies.

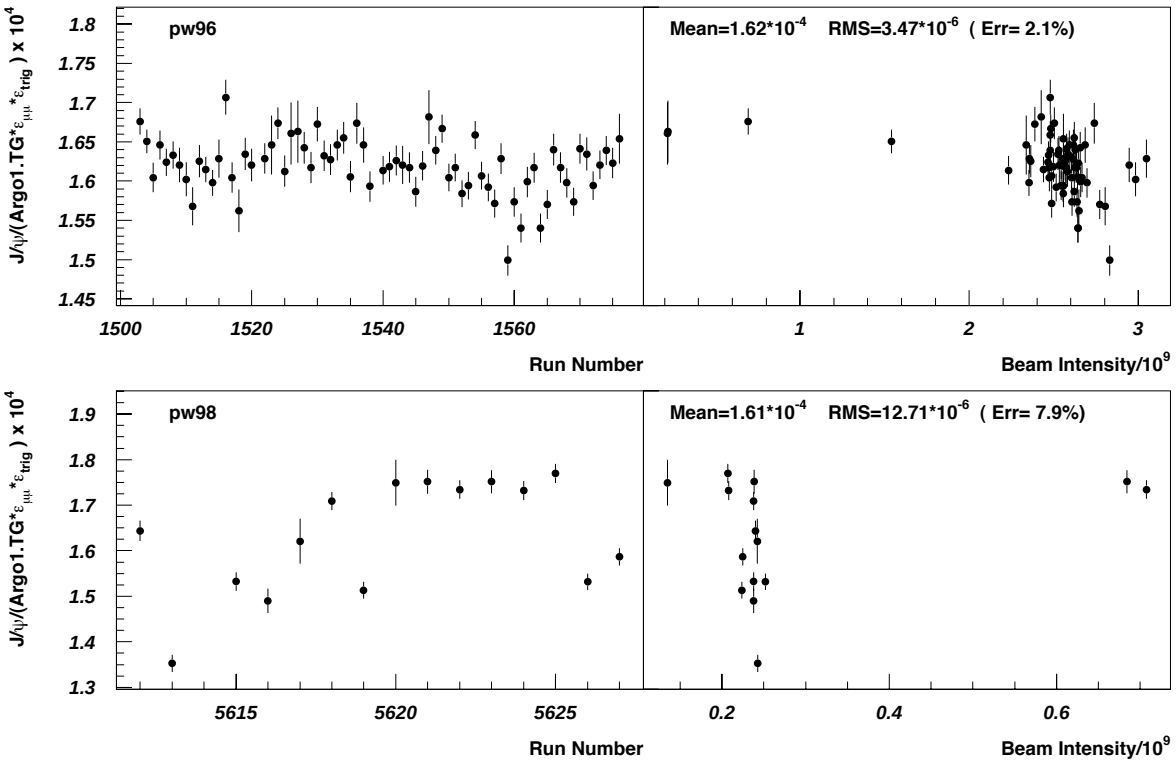

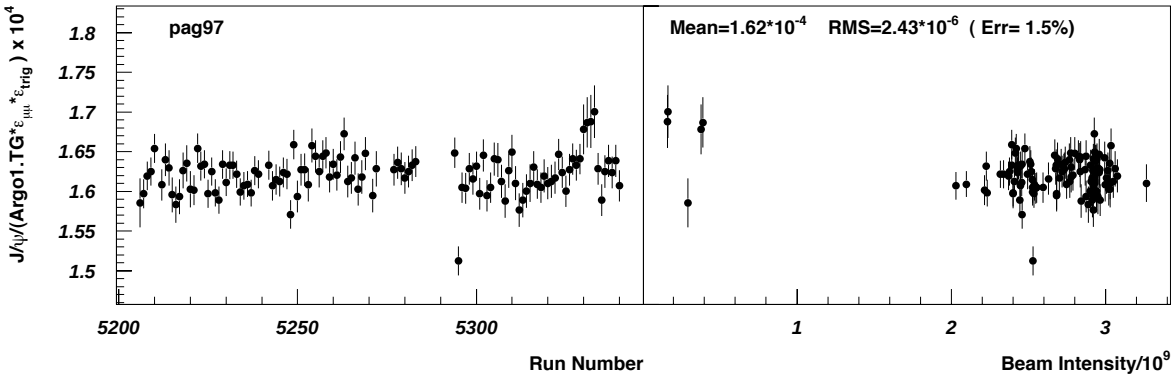
pag97
Mean=1.62*10^-4 RMS=2.43*10^-6 (Err= 1.5%)
J/ψ/(Argo1.TG*ε_μμ*ε_trig) x 10^4
Run Number
Beam Intensity/10^9

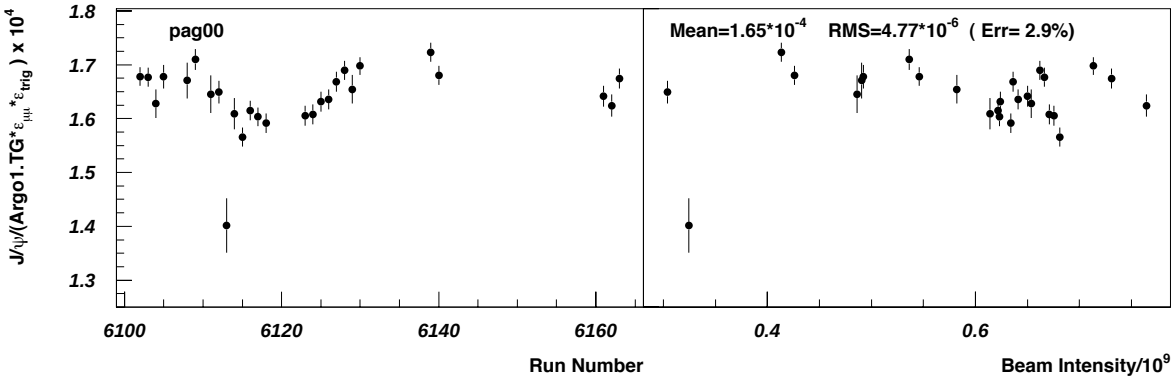
pag00
Mean=1.65*10^-4 RMS=4.77*10^-6 (Err= 2.9%)
J/ψ/(Argo1.TG*ε_μμ*ε_trig) x 10^4
Run Number
Beam Intensity/10^9

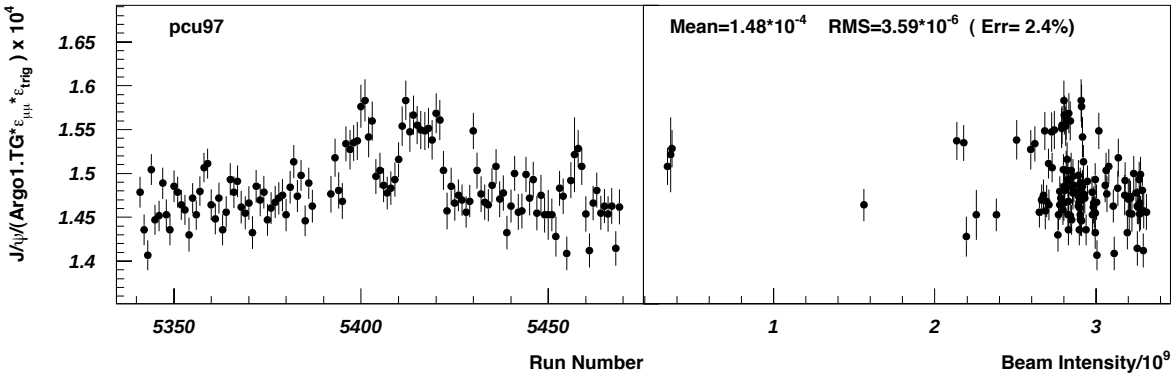
pcu97
Mean=1.48*10^-4 RMS=3.59*10^-6 (Err= 2.4%)
J/ψ/(Argo1.TG*ε_μμ*ε_trig) x 10^4
Run Number
Beam Intensity/10^9

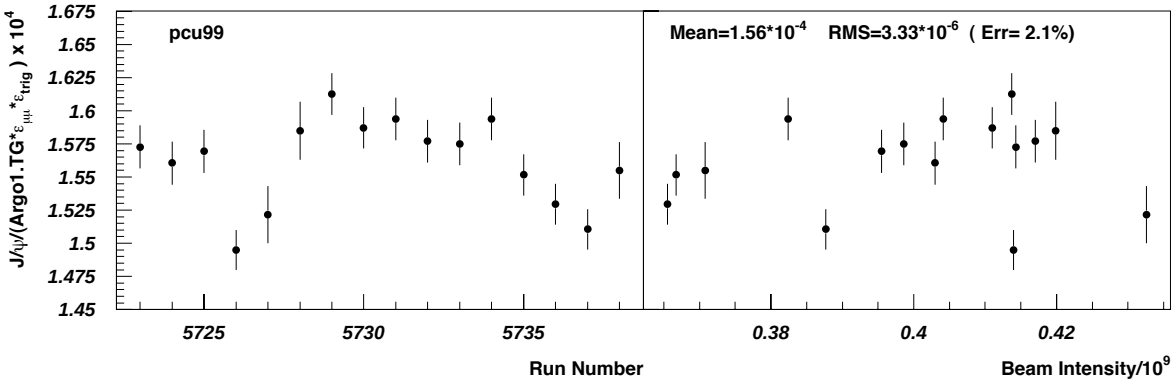
pcu99
Mean=1.56*10^-4 RMS=3.33*10^-6 (Err= 2.1%)
J/ψ/(Argo1.TG*ε_μμ*ε_trig) x 10^4
Run Number
Beam Intensity/10^9

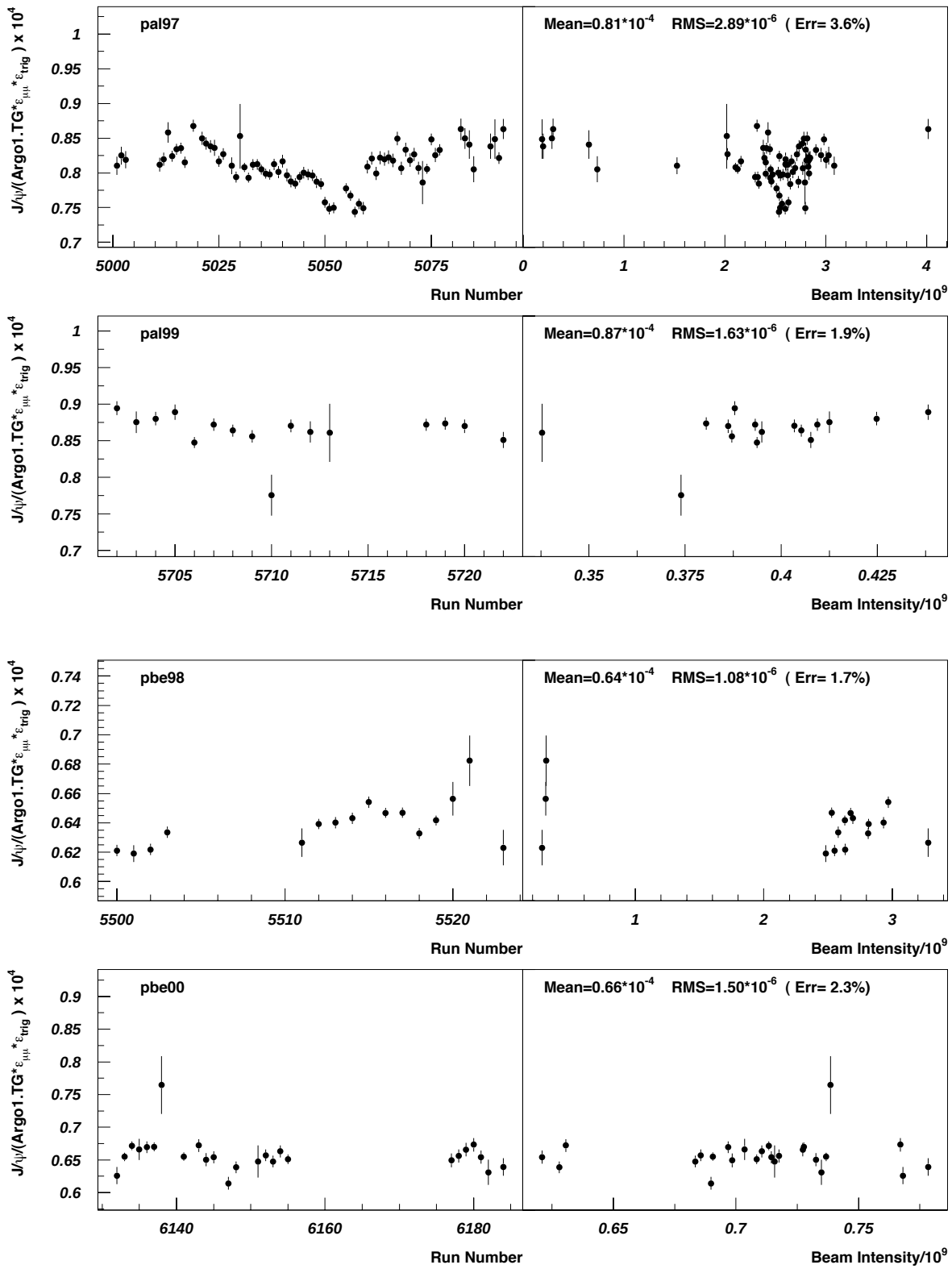

Figure 4.11: Ratio of the number of reconstructed dimuons with $2.7 < M < 3.5$ to the value of *Argo*1 counter (accounting for the dead time of the detector) corrected for dimuon trigger and reconstruction efficiencies as a function of the run number (Left) and the beam intensity of the run. The ratio of the RMS to the average value is taken as a systematic error on the product of the reconstruction and trigger efficiencies

4.5.3 Summary of the Different Data Sets

The Table 4.1 gives a summary of the analyzed data sets: columns 2 to 6 show the integrated number of incident protons (accounting for the dead time of the detector), average intensity per burst, number of opposite sign dimuons with $2.7 < M < 3.5$, measured trigger efficiency, dimuon reconstruction efficiency averaged over all the runs of this set and systematic error on the efficiencies product (see Section 4.5.2).

Data Set	N.prot $\times 10^{-12}$	N.prot $\times 10^{-12}$ **TgtOut**	$< Int >$ $\times 10^{-8}$ (pr/b)	$N_{\mu\mu} \times 10^{-5}$ $2.7-3.5$	ε_{trigg}	$< \varepsilon_{\mu\mu} >$	Error (in%) on $< \varepsilon_{trigg}\varepsilon_{\mu\mu} >$
pW96	28.506	2.43	23.49	5.241	0.870	0.841	2.1
pAg97	43.778	4.72	24.81	8.209	0.888	0.859	1.5
pCu97	45.468	-	26.97	7.618	0.888*	0.844	2.4
pAl97	63.355	3.02	23.03	6.023	0.877	0.872	3.6
pBe98	50.687	4.96	21.66	3.682	0.873	0.857	1.7
pW98	3.694	-	2.73	0.806	0.873*	0.997	7.9
pAl99	10.548	-	3.76	1.239	0.901	0.994	1.9
pCu99	6.920	-	3.80	1.449	0.901*	0.981	2.1
pAg00	8.587	0.23	5.58	1.866	0.857	0.990	2.9
pBe00	14.320	0.29	6.73	1.230	0.857*	0.994	2.3

Table 4.1: Summary of the analyzed data sets. The data sets for which there was no **Trigger Efficiency Run** taken are marked by '*'. The measured value of the closest in time data set is assumed for these cases.

5 Results

5.1 General features of the fitted data

Since the data presented in this work consists of two sets (High and Low intensity) with very different systematics and statistics, the results extracted from these samples should be compared with care. Apart from the general problems of the normalization (calibration coefficients of the argon counters, see Section 4.5.1, the trigger and reconstruction efficiencies, see Section 4.5.2, there are such differences as **a)** the lack of **Target Out** data for the Low intensity sets, where the non-target dimuons contribution was assumed to be the average of the High intensity data rescaled according to the luminosity (see Section 4.1.2); **b)** worse muon momentum resolution (especially at its high values, important for the high mass dimuons) in High intensity data sets due to the higher occupancy in the chambers, which decreases the quality of the **PDTARG** cut (see Section 3.3.2).

These differences should be kept in mind when comparing the results obtained from these two data sets.

The bining used in this study is four equidistant bins in rapidity, covering the $-0.5 < Y_{CM} < 0.5$ region and four in the Feynman X variable (computed here as $2P_z/\sqrt{s}$), covering the $-0.1 < X_F < 0.1$ region. The left plot of Fig. 5.1 shows the correlation between these two binings for the generated and accepted J/ψ dimuons. Since the acceptance of NA50 in X_F has long tails with very low values (below 1%, right plot of Fig. 5.1), in the X_F analysis the tails outside the $-0.1 < X_F < 0.1$ range were cut out, while for the analysis in Y_{CM} bins these events were kept. For this reason the cross sections integrated over all the four X_F bins are somewhat smaller than the ones integrated over the Y_{CM} bins. The right plot of Fig. 5.1) shows the acceptances the for J/ψ in each of the Y_{CM} and X_F bins.

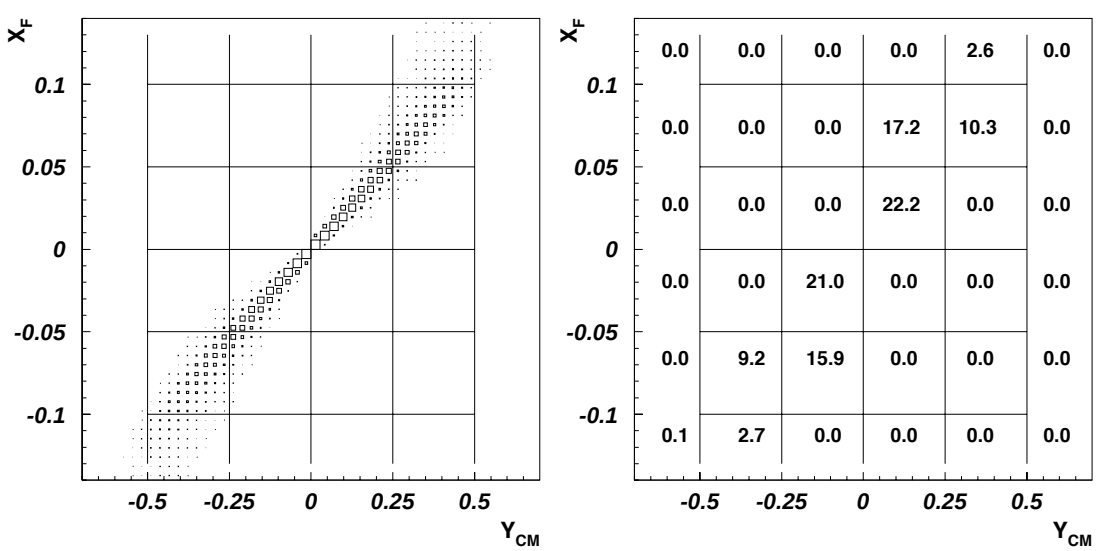

Figure 5.1: (Left) The correlation between the binings in Y_{CM} and X_F used in this analysis for the dimuons with $2.7 < M < 3.5\ GeV/c^2$; (Right) The acceptances (in %) for the J/ψ in the chosen Y_{CM} and X_F bins and outside of them.

The quality of the fits deserves a short comment. For most of the fitted histograms, a good χ^2/NDF is obtained, typically in the range between ~ 0.75 to ~ 1.25. Nevertheless, the fit of some data samples gives rather high values of χ^2/NDF, the worst one being the one of the integrated $pW96$ data, shown on the top plot of Fig. 5.2.

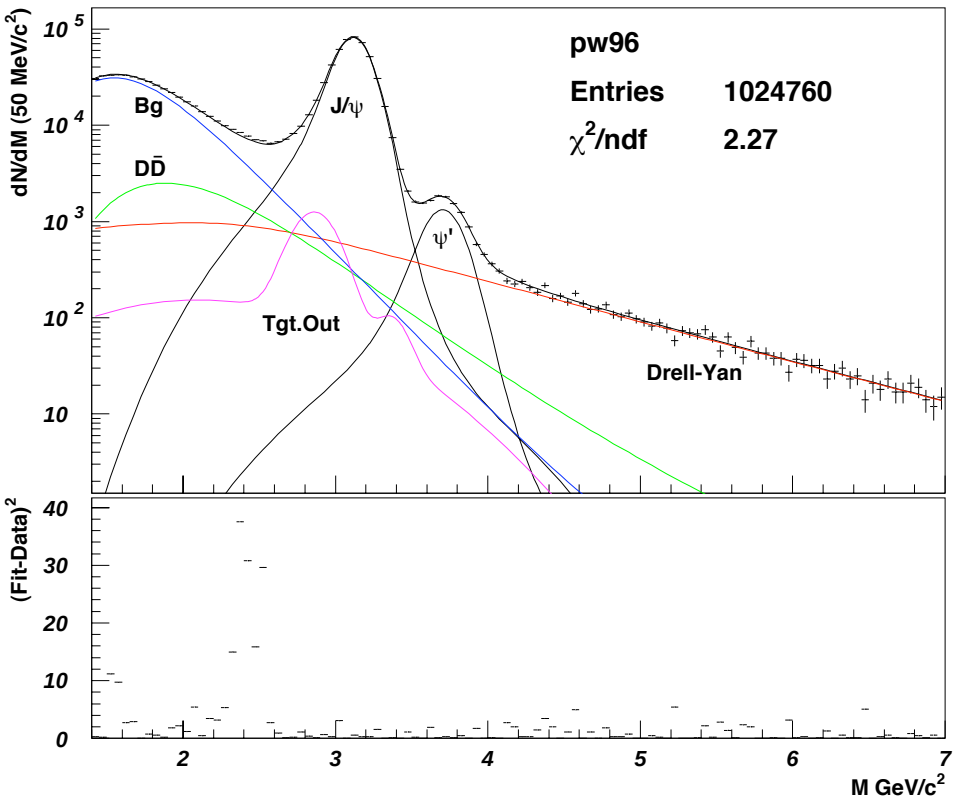

Figure 5.2: Data sample with the "worst" χ/NDF obtained (Top) and bin by bin square of the difference between the measured and the fitted values (Bottom).

A closer look on the bin by bin square of the difference between the measured and the fitted values (bottom plot of Fig. 5.2) shows that the anomalous contribution to the χ^2 comes from the region $2.2 < M < 2.5\ GeV/c^2$. The detailed inspection of the sample of the events cut out but the **PDTARG** cut (where the contribution of the non-target dimuons is very strong) shows that there is a difference between the spectra of dimuons originated outside of the target for the **target out** and the normal runs, which is especially strong in this mass range. The most probable reason for such a difference is an additional contribution of the dimuons originated in the preabsorber from the secondaries produced on the target, which is surely absent in the **target out** runs. Unfortunately, it is impossible to estimate this excess with high enough precision in the data which survived all cuts. Nevertheless, one should note that the discrepancy in this mass range anyway does not inluence by more than a few permille the fitted values for the J/ψ, ψ' and Drell-Yan.

The histograms and the results of the fit for all data samples are presented in the Appendix 7.2.

5.2 Results for the absolute cross sections

This section presents the absolute cross sections (corrected for acceptance) computed separately for the High and Low intensity data sets as it was described in the Section. 4.5. One should keep in mind that apart from the kinematical domains explicitly mentioned in each case, they are all restricted to the $-0.5 < Y_{CM} < 0.5\ GeV/c^2$ and $-0.5 < \cos(\theta) < 0.5$ ranges.

5.2.1 J/ψ cross section

The plots on Fig.5.3 show the calculated J/ψ cross section per nucleon in *nb* (multiplied by the $\mu\mu$ branching ratio) in the four Y_{CM} bins for High (Left) and Low (Right) intensity data sets (the symbols are shifted by hand from the bin center in order to avoid the overlapping). The error bars with the wide ticks are for the statistical errors while the ones with the narrow ticks are the quadratic sums of the statistical and systematic errors. The latter account for the acceptance, reconstruction and trigger efficiency uncertainties and include a uniform 3 % argon counters calibration error.

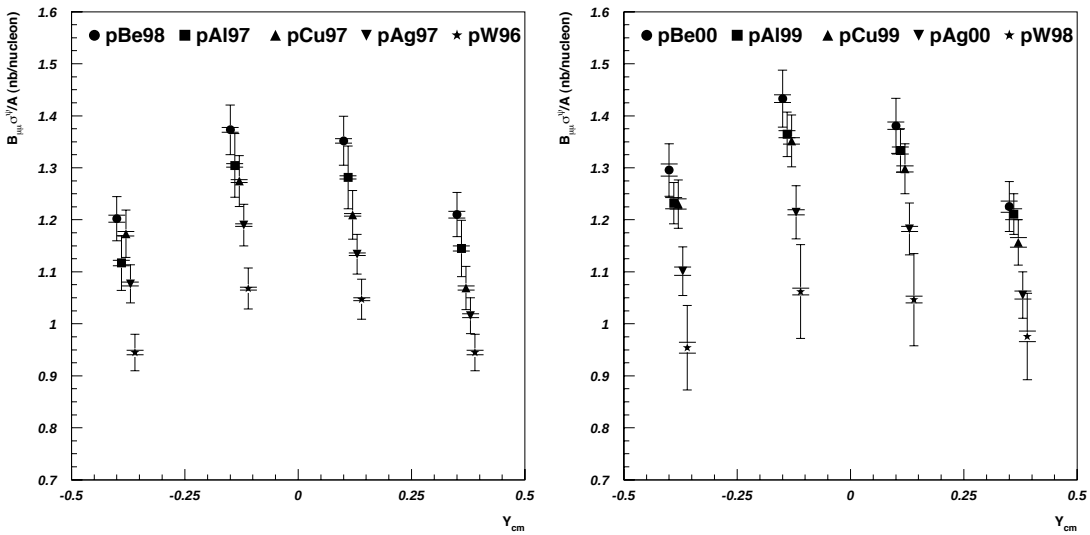

Figure 5.3: J/ψ cross section per nucleon in *nb* (not corrected for the $\mu\mu$ branching ratio) as a function of the rapidity in the center of mass for (Left) High and (Right) Low Intensity data.

	-0.50$< Y <$**0.50**	**-0.50**$< Y <$**-0.25**	**-0.25**$< Y <$ **0.0**	**0.0**$< Y <$ **0.25**	**0.25**$< Y <$ **0.5**
pBe00	5.331±0.017±0.202	1.296±0.012±0.049	1.433±0.007±0.054	1.381±0.007±0.052	1.225±0.011±0.047
pAl99	5.126±0.016±0.158	1.232±0.011±0.038	1.365±0.007±0.042	1.333±0.007±0.041	1.211±0.010±0.038
pCu99	5.025±0.014±0.184	1.230±0.010±0.045	1.352±0.006±0.050	1.298±0.006±0.048	1.157±0.009±0.043
pAg00	4.548±0.011±0.190	1.101±0.008±0.046	1.214±0.005±0.051	1.182±0.005±0.049	1.055±0.007±0.044
pW98	4.022±0.015±0.340	0.954±0.011±0.081	1.062±0.007±0.090	1.047±0.006±0.088	0.976±0.010±0.083
pBe98	5.130±0.010±0.177	1.202±0.007±0.042	1.373±0.004±0.047	1.352±0.004±0.047	1.210±0.007±0.042
pAl97	4.868±0.008±0.228	1.117±0.005±0.053	1.304±0.003±0.061	1.281±0.003±0.060	1.145±0.005±0.054
pCu97	4.712±0.006±0.181	1.173±0.004±0.045	1.275±0.003±0.049	1.209±0.003±0.047	1.069±0.004±0.041
pAg97	4.403±0.005±0.148	1.077±0.004±0.036	1.190±0.002±0.040	1.134±0.002±0.038	1.016±0.004±0.034
pW96	4.005±0.006±0.147	0.945±0.004±0.035	1.068±0.003±0.039	1.047±0.003±0.038	0.945±0.004±0.035

Table 5.1: J/ψ cross section per nucleon in *nb* (not corrected for the $\mu\mu$ branching ratio) for the integrated data and in the four Y_{CM} bins.

The values corresponding to these plots are shown in the Table 5.1 (for each bin the cross section value in *nb* is followed by the statistical and systematic error).

One can notice a small but systematic asymmetry of the distributions for the production in the forward and backward hemispheres. One should note that since the normalization error (except the contribution from the acceptance uncertainy which does depend on the kinematical bin but is negligible) affects in a similar way the computed cross sections for different bins of the same data set, when considering the shape of the distribution one should take into account only statistical errors.

Since the J/ψ production cross section on the partonic level should be symmetric with respect to the rapidity of the center of mass, this asymmetry means weaker suppression for the slower (in the target system) J/ψ's.

The corresponding results for the data in the X_F bins are shown in the Table 5.2 and plotted on Fig.5.4.

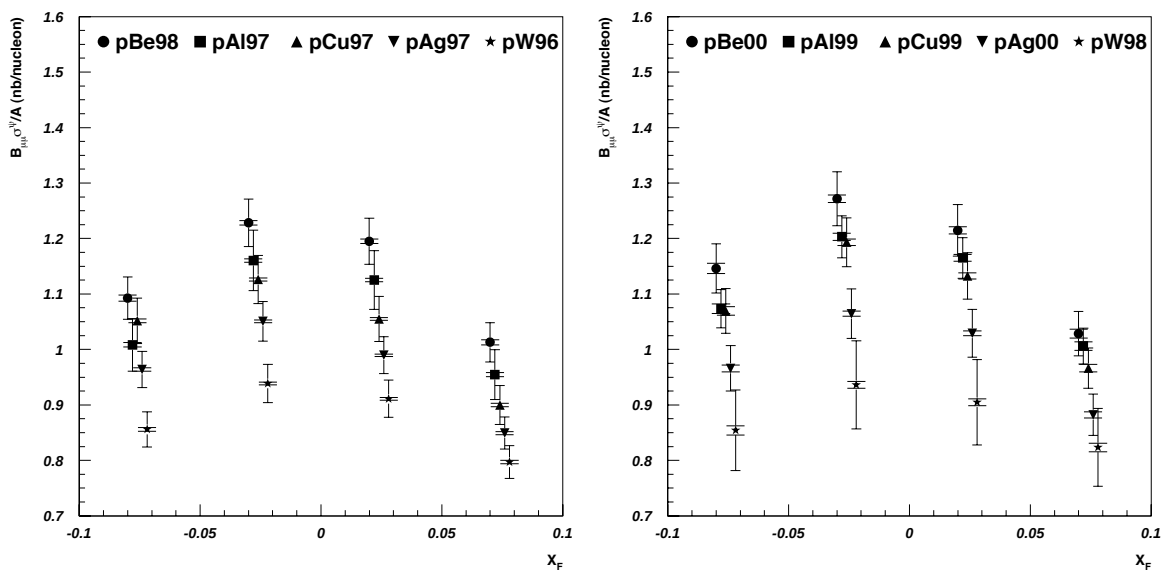

Figure 5.4: J/ψ cross section per nucleon in *nb* (not corrected for the $\mu\mu$ branching ratio) as a function of X_F for (Left) High and (Right) Low Intensity data.

	-0.10< X_F <0.10	**-0.10< X_F <-0.05**	**-0.05< X_F <0.0**	**0.0< X_F <0.05**	**0.05< X_F <0.1**
pBe00	4.677±0.015±0.177	1.146±0.009±0.044	1.272±0.007±0.048	1.215±0.007±0.046	1.029±0.008±0.039
pAl99	4.467±0.014±0.138	1.073±0.009±0.033	1.203±0.007±0.037	1.165±0.006±0.036	1.006±0.008±0.031
pCu99	4.373±0.012±0.160	1.069±0.008±0.039	1.193±0.006±0.044	1.133±0.006±0.042	0.966±0.007±0.036
pAg00	3.953±0.010±0.165	0.966±0.006±0.041	1.064±0.005±0.045	1.029±0.004±0.043	0.882±0.006±0.037
pW98	3.520±0.014±0.297	0.854±0.008±0.072	0.936±0.006±0.079	0.905±0.006±0.076	0.823±0.008±0.070
pBe98	4.536±0.009±0.157	1.093±0.005±0.038	1.228±0.004±0.043	1.195±0.004±0.041	1.013±0.005±0.035
pAl97	4.279±0.007±0.201	1.008±0.004±0.047	1.160±0.003±0.054	1.125±0.003±0.053	0.955±0.004±0.045
pCu97	4.132±0.005±0.159	1.052±0.003±0.041	1.126±0.003±0.043	1.055±0.002±0.041	0.900±0.003±0.035
pAg97	3.855±0.005±0.129	0.964±0.003±0.033	1.051±0.002±0.035	0.990±0.002±0.033	0.849±0.003±0.029
pW96	3.509±0.005±0.129	0.856±0.003±0.032	0.939±0.003±0.034	0.911±0.002±0.033	0.797±0.003±0.029

Table 5.2: J/ψ cross section per nucleon in *nb* (not corrected for the $\mu\mu$ branching ratio) for the integrated data and in the four X_F bins.

One can notice that the values of the cross sections obtained from the High intensity data are systematically lower than the ones from the Low intensity data sets (except the $pW96$ versus $pW98$ points, but the latter has a very large systematic errors). Fig.5.5 shows the ratio of the cross sections from High intensity to the ones of the Low intensity data (for the $-0.5 < Y < 0.5$ range). The fit by a constant line gives the average ratio $R = 0.957 \pm 0.025$. Although, within the systematic errors the ratios of the cross sections for all targets are compatible with this average value, there are no reasons to suspect a systematic error in the reconstruction efficiency estimation depending on the beam intensity (nevertheless, see footnote of the Section 5.2.3, presenting the results for Drell-Yan, where the discrepancies are even larger), the most probable explanation of the differnece in the normalizations could be the difference in the trigger efficiencies (one should remember that they are estimated only from special low intensity runs, normally once per data taking period) or the nonlinear dependence of the argon counters on the beam intensity. Since both reasons deal with the time dependent conditions of the apparatus, the rescaling of all High intensity data, taken at different times by single factor may introduce a bias. For this reason it was decided to not introduce rescaling coefficients but to quote all the values for High and Low intensity data sets separately. Nevertheless, when extracting the parameters describing the charmonia suppression (α, σ_{abs}) from the measured cross sections, apart from the separate results for High and Low intensity data sets I present also the values extracted from the simultaneous fit of both data sets. For this joint fits the values of the Low and High intensity data are multiplied by the factors $2R/(1+R)$ and $2/(1+R)$ respectively (R being the result of the fit of the ratio of High to Low intensity data values by a constant line), so that their ratio after the rescaling is in average equal to unity.

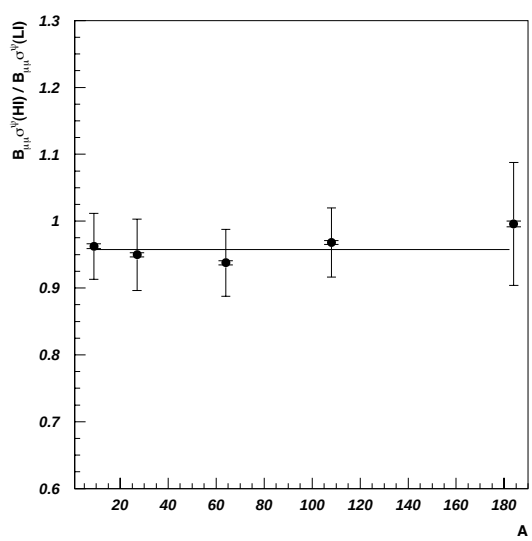

Figure 5.5: Ratio of the J/ψ cross sections (in the $-0.5 < Y < 0.5$ range) from the High and Low intensity data fitted by a constant line ($R = 0.957 \pm 0.025$).

Fig.5.6 shows the quotted J/ψ cross sections per nucleon (the plots on the top are for the cross sections in the $-0.5 < Y_{CM} < 0.5$ range and on the bottom for $-0.1 < X_F < 0.1$) fitted according to the three different suppression parametrizations:
the left plots are for $\sigma_A = \sigma_0 A^{\alpha}$ (the results of the fit are shown on the first line of the legend for each data set) and for the complete Glauber model (second line, the parameters are σ_0 and σ_{abs})
the right pltos show the result for the $\sigma_A = \sigma_0 e^{-<\rho L>\sigma_{abs}}$ parametrization. The values for σ_0

and σ_{abs} are in *nb* and *mb* respectively.

The similar plots for the bin by bin fits are placed in the Appendix 7.2: Fig.7.11 and 7.12 for the Y_{CM} and X_F bins respectively.

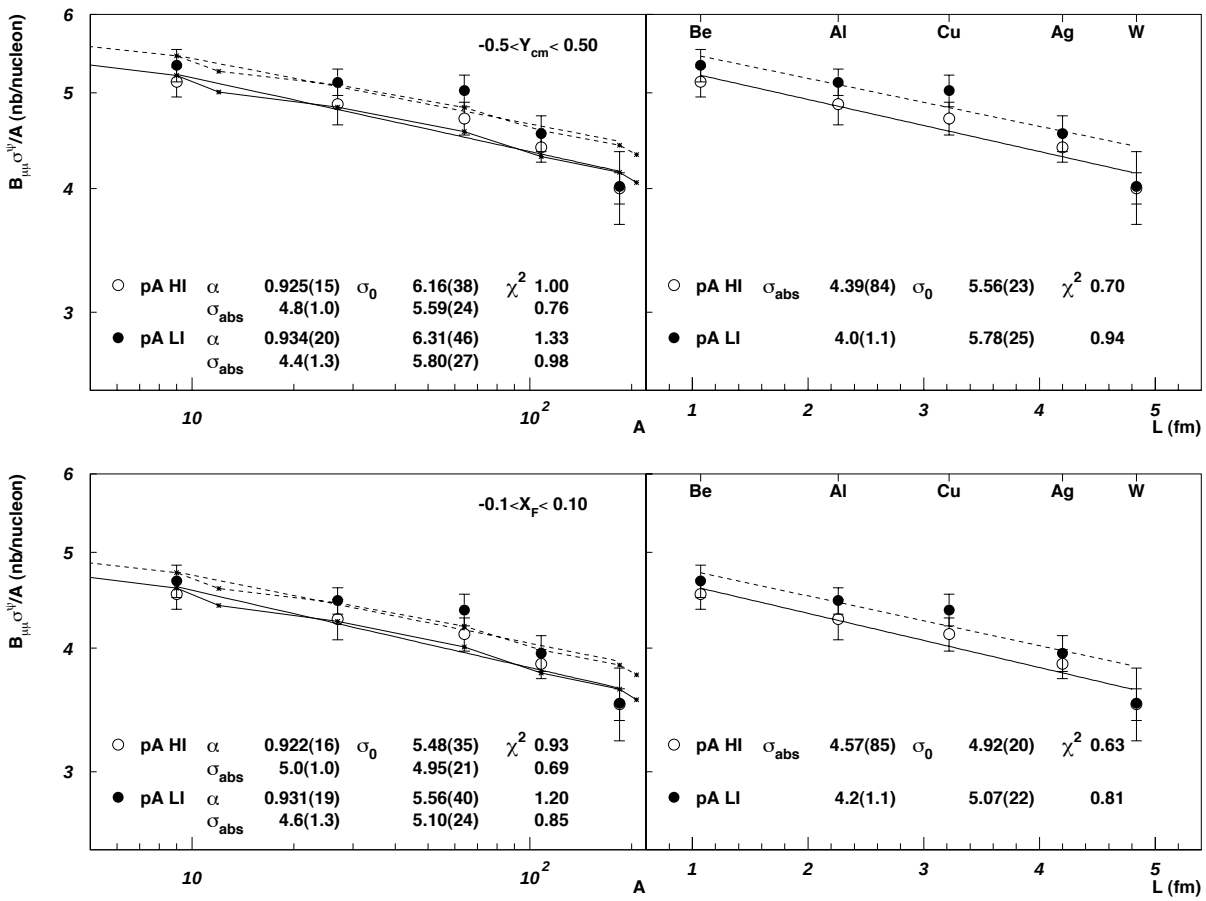

Figure 5.6: J/ψ cross sections per nucleon (for the High (HI) and Low (LI) intensity data sets) in the $-0.5 < Y_{CM} < 0.5$ (Top) and $-0.1 < X_F < 0.1$ (Bottom) ranges fitted by the: (Left) parametrization $\sigma_A = \sigma_0 A^{\alpha}$ (the results are shown on the first line of the legend) and the complete Glauber model (second line); (Right) parametrization $\sigma_A = \sigma_0 e^{-<\rho L>\sigma_{abs}}$. The values for the σ_0 and σ_{abs} are in *nb* and *mb* respectively.

The results of these fits, as well as for the simultaneous fit of the High and Low intensity data (rescaled in the way described above) are plotted on Fig. 5.7 and collected in the Table 5.3. The large symbols in the center of each plot are the suppression parameters for the fit of the cross section in the whole Y_{CM} and X_F ranges.

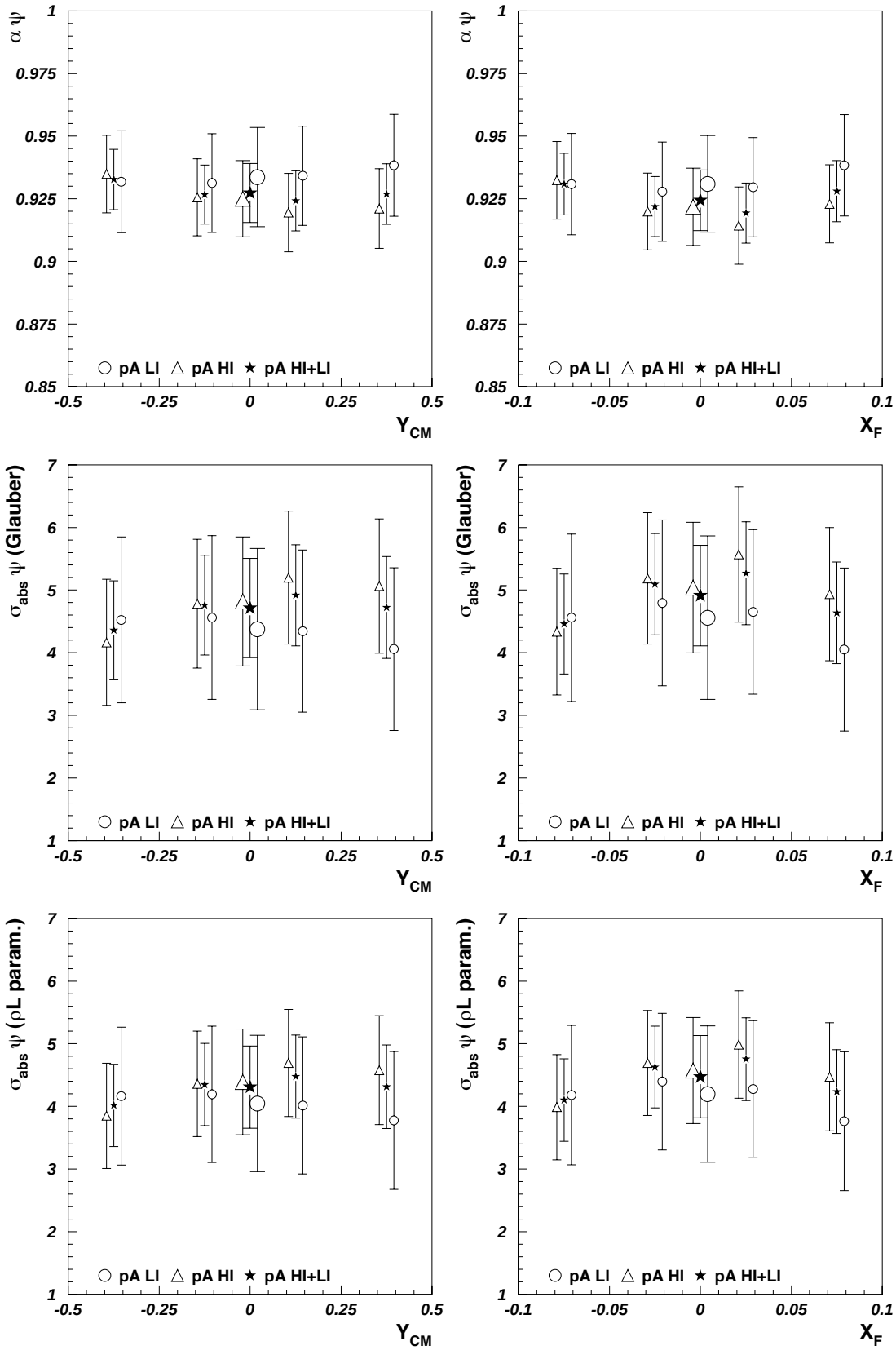

Figure 5.7: J/ψ suppression parameters for various parametrizations fitted in Y_{CM} (Left) and X_F (Right) bins: α parameter (Top); absorption cross section (mb) from the (Middle) complete Glauber model and (Bottom) $\sigma_A = \sigma_0 e^{-<\rho\ L>\sigma_{abs}}$ parametrization.

	-0.50$< Y <$**0.50**	**-0.50**$< Y <$**-0.25**	**-0.25**$< Y <$ **0.0**	**0.0**$< Y <$ **0.25**	**0.25**$< Y <$ **0.5**
High Intensity Data					
α	0.925±0.015	0.935±0.015	0.926±0.015	0.919±0.016	0.921±0.016
σ_{abs} [ρL]	4.4±0.8	3.9±0.8	4.4±0.8	4.7±0.9	4.6±0.9
σ_{abs} [Glb.]	4.8±1.0	4.2±1.0	4.8±1.0	5.2±1.1	5.1±1.1
σ_0 [Glb.]	5.59±0.24	1.30±0.06	1.50±0.06	1.48±0.06	1.31±0.06
Low Intensity Data					
α	0.934±0.020	0.932±0.020	0.931±0.020	0.934±0.020	0.938±0.020
σ_{abs} [ρL]	4.0±1.1	4.2±1.1	4.2±1.1	4.0±1.1	3.8±1.1
σ_{abs} [Glb.]	4.4±1.3	4.5±1.3	4.6±1.3	4.3±1.3	4.1±1.3
σ_0 [Glb.]	5.80±0.27	1.41±0.07	1.56±0.07	1.50±0.07	1.34±0.06
Joint Low+High Intensity Data fit					
α	0.927±0.012	0.933±0.012	0.927±0.012	0.924±0.012	0.927±0.012
σ_{abs} [ρL]	4.3±0.7	4.0±0.7	4.3±0.7	4.5±0.7	4.3±0.7
σ_{abs} [Glb.]	4.7±0.8	4.4±0.8	4.8±0.8	4.9±0.8	4.7±0.8
σ_0 [Glb.]	5.71±0.18	1.35±0.04	1.53±0.05	1.50±0.05	1.33±0.04

	-0.10$< X_F <$**0.10**	**-0.10**$< X_F <$**-0.05**	**-0.05**$< X_F <$**0.0**	**0.0**$< X_F <$**0.05**	**0.05**$< X_F <$**0.1**
High Intensity Data					
α	0.922±0.015	0.932±0.016	0.920±0.015	0.914±0.015	0.923±0.016
σ_{abs} [ρL]	4.6±0.8	4.0±0.8	4.7±0.8	5.0±0.9	4.5±0.9
σ_{abs} [Glb.]	5.0±1.0	4.3±1.0	5.2±1.0	5.6±1.1	4.9±1.1
σ_0 [Glb.]	4.95±0.21	1.18±0.05	1.35±0.06	1.31±0.06	1.10±0.05
Low Intensity Data					
α	0.931±0.019	0.931±0.020	0.928±0.020	0.930±0.020	0.938±0.020
σ_{abs} [ρL]	4.2±1.1	4.2±1.1	4.4±1.1	4.3±1.1	3.8±1.1
σ_{abs} [Glb.]	4.6±1.3	4.6±1.3	4.8±1.3	4.7±1.3	4.0±1.3
σ_0 [Glb.]	5.10±0.24	1.24±0.06	1.39±0.07	1.33±0.06	1.12±0.05
Joint Low+High Intensity Data fit					
α	0.924±0.012	0.931±0.012	0.922±0.012	0.919±0.012	0.928±0.012
σ_{abs} [ρL]	4.5±0.7	4.1±0.7	4.6±0.7	4.8±0.7	4.2±0.7
σ_{abs} [Glb.]	4.9±0.8	4.5±0.8	5.1±0.8	5.3±0.8	4.6±0.8
σ_0 [Glb.]	5.04±0.16	1.21±0.04	1.37±0.04	1.32±0.04	1.11±0.04

Table 5.3: J/ψ suppression parameters fitted in Y_{CM} (top part) and X_F (bottom part) bins. For each data set the values are: α parameter of the $\sigma_A = \sigma_0 A^\alpha$ parametrization, absorption cross section (in *mb*) for the $\sigma_A = \sigma_0 e^{-<\rho\ L>\sigma_{abs}}$ parametrization (marked as "σ_{abs} [ρL]") and the absorption (marked as "σ_{abs} [Glb.]") and the *pN* production (in *nb*) (marked as "σ_0 [Glb.]") cross sections from the complete Glauber model fit.

5.2.2 ψ' cross section

The absolute ψ' cross sections in *nb* (multiplied by the $\mu\mu$ branching ratio) in the four Y_{CM} bins are shown on Fig.5.8 : the left plot is for the High and the right one for the Low intensity data sets. The errors are calculated in a same way as for the J/ψ, with the only difference that the systematic error now has a contribution from the variation of the ψ' value for the fits with different ways of the J/ψ tail continuation (see Section 4.2.2). The Table 5.4 shows the values corresponding to these plots.

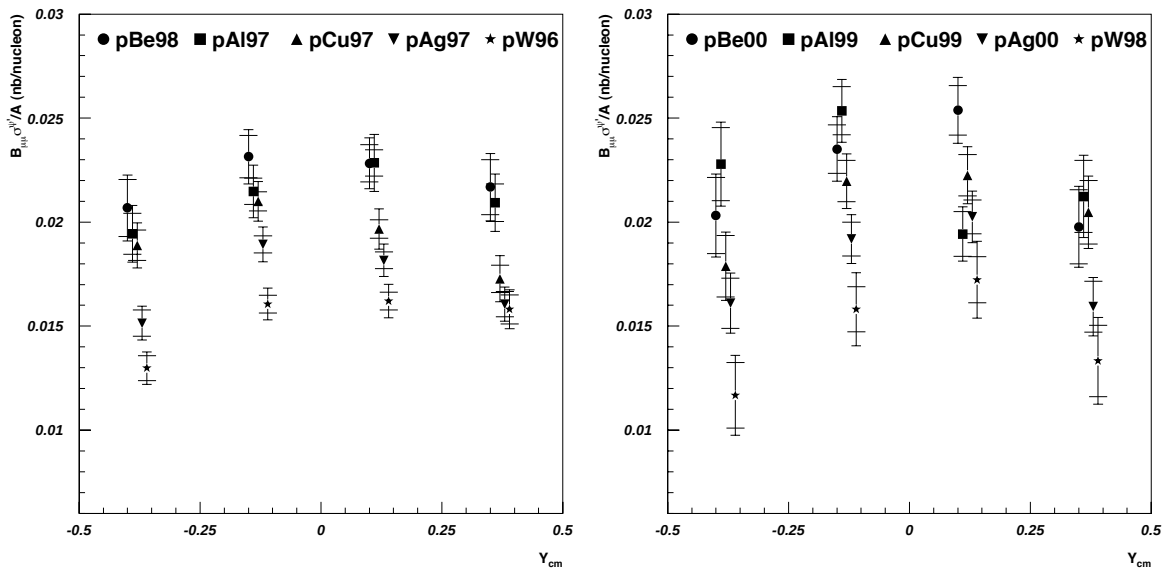

Figure 5.8: ψ' cross section per nucleon in *nb* (not corrected for the $\mu\mu$ branching ratio) as a function of the rapidity in the center of mass for (Left) High and (Right) Low Intensity data.

	-0.50$< Y <$**0.50**	**-0.50**$< Y <$**-0.25**	**-0.25**$< Y <$ **0.0**	**0.0**$< Y <$ **0.25**	**0.25**$< Y <$ **0.5**
pBe00	.0922±.0028±.0038	.0203±.0018±.0008	.0235±.0012±.0010	.0254±.0012±.0010	.0198±.0018±.0008
pAl99	.0878±.0026±.0036	.0228±.0018±.0010	.0254±.0012±.0010	.0194±.0011±.0008	.0212±.0017±.0010
pCu99	.0838±.0023±.0032	.0179±.0015±.0007	.0220±.0010±.0009	.0223±.0010±.0009	.0205±.0015±.0009
pAg00	.0741±.0019±.0032	.0161±.0012±.0008	.0192±.0008±.0008	.0203±.0008±.0009	.0159±.0012±.0007
pW98	.0610±.0026±.0054	.0117±.0016±.0011	.0158±.0011±.0014	.0172±.0011±.0015	.0133±.0017±.0012
pBe98	.0886±.0021±.0032	.0207±.0014±.0008	.0231±.0010±.0008	.0228±.0009±.0008	.0217±.0013±.0009
pAl97	.0841±.0015±.0044	.0194±.0010±.0009	.0215±.0006±.0011	.0228±.0006±.0012	.0209±.0009±.0010
pCu97	.0773±.0011±.0032	.0189±.0007±.0008	.0210±.0005±.0008	.0197±.0004±.0009	.0173±.0007±.0009
pAg97	.0690±.0010±.0025	.0151±.0006±.0005	.0189±.0004±.0007	.0182±.0004±.0007	.0161±.0006±.0005
pW96	.0611±.0010±.0024	.0130±.0006±.0005	.0161±.0004±.0006	.0162±.0004±.0007	.0158±.0007±.0006

Table 5.4: ψ' cross section per nucleon in *nb* (not corrected for the $\mu\mu$ branching ratio) for the integrated data and in the four Y_{CM} bins.

As one can see, in opposite to the J/ψ the distribution of the ψ' is more symmetric with respect to the rapidity of the center of mass, or in other words, the slow (in the target system) ψ''s are more suppressed with respect to the J/ψ's than the fast ones.

The corresponding results for the data in the X_F bins are shown in the Table 5.5 and plotted on Fig. 5.9.

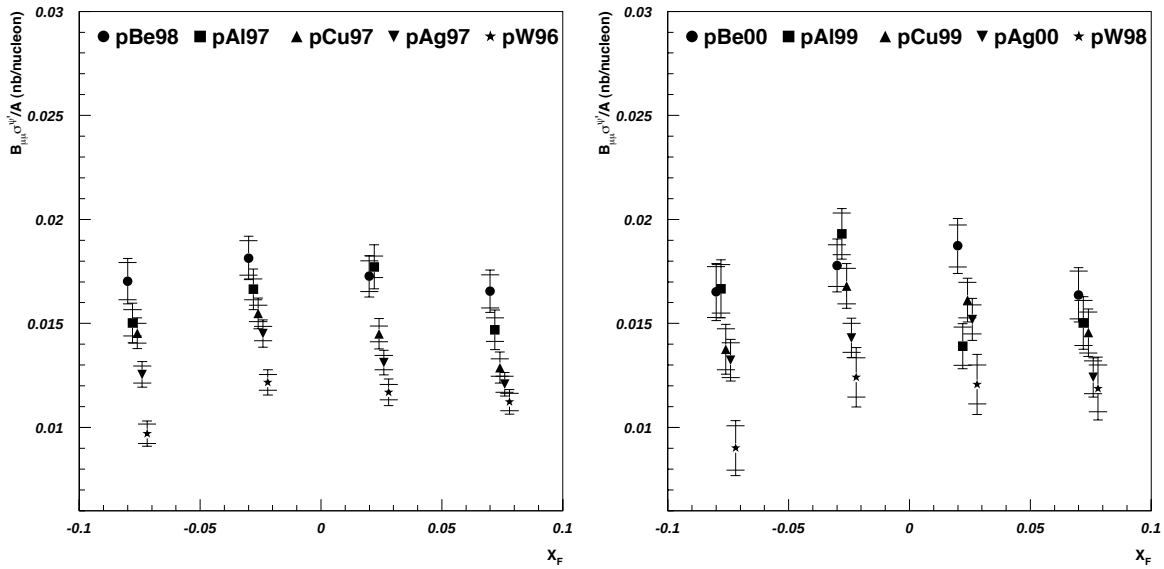

Figure 5.9: ψ' cross section per nucleon in *nb* (not corrected for the $\mu\mu$ branching ratio) as a function of X_F for (Left) High and (Right) Low Intensity data.

	-0.10< X_F <0.10	**-0.10< X_F <-0.05**	**-0.05< X_F <0.0**	**0.0< X_F <0.05**	**0.05< X_F <0.1**
pBe00	.0725±.0022±.0031	.0165±.0012±.0006	.0178±.0010±.0008	.0187±.0010±.0009	.0164±.0011±.0006
pAl99	.0661±.0021±.0025	.0167±.0012±.0008	.0193±.0010±.0007	.0139±.0009±.0006	.0150±.0011±.0006
pCu99	.0640±.0018±.0024	.0138±.0010±.0007	.0168±.0008±.0007	.0161±.0009±.0006	.0146±.0010±.0006
pAg00	.0571±.0015±.0025	.0132±.0008±.0006	.0143±.0007±.0006	.0152±.0007±.0007	.0124±.0008±.0005
pW98	.0477±.0020±.0041	.0090±.0011±.0008	.0124±.0009±.0011	.0121±.0009±.0011	.0119±.0011±.0010
pBe98	.0699±.0016±.0026	.0170±.0009±.0006	.0182±.0008±.0006	.0173±.0007±.0007	.0165±.0008±.0006
pAl97	.0653±.0011±.0033	.0150±.0006±.0007	.0166±.0005±.0008	.0177±.0005±.0009	.0147±.0006±.0008
pCu97	.0583±.0008±.0024	.0145±.0005±.0006	.0155±.0004±.0006	.0145±.0004±.0006	.0129±.0004±.0006
pAg97	.0531±.0007±.0020	.0125±.0004±.0005	.0145±.0004±.0006	.0131±.0003±.0005	.0121±.0004±.0004
pW96	.0474±.0008±.0018	.0097±.0005±.0004	.0122±.0004±.0005	.0117±.0004±.0005	.0112±.0004±.0004

Table 5.5: ψ' cross section per nucleon in *nb* (not corrected for the $\mu\mu$ branching ratio) for the integrated data and in the four X_F bins.

The fit by a constant line of the ratio of the cross sections from the High intensity data to the Low intensity data, shown on Fig.5.10, gives the average factor $R = 0.946 \pm 0.0285$ which is fully compatible with the similar factor obtained for the ratio of the J/ψ cross sections (see Fig.5.5).

As it was done for the J/ψ, Fig.5.11 shows the ψ' cross sections per nucleon fitted according to three different suppression parametrizations:
the left plots are for $\sigma_A = \sigma_0 A^\alpha$ and for the complete Glauber models (second line, the parameters are σ_0 and σ_{abs})
the right plots show the result for the $\sigma_A = \sigma_0 e^{-<\rho L>\sigma_{abs}}$ parametrization (the plots on the top are for the cross sections in the $-0.5 < Y_{CM} < 0.5$ range and on the bottom for $-0.1 < X_F < 0.1$). The values for σ_0 and σ_{abs} are in *nb* and *mb* respectively.

The plots for the bin by bin fits can be found in the Appendix 7.2: Fig.7.13 and 7.14 for the Y_{CM} and X_F bins respectively.

The results of these fits, as well as for the simultaneous fit of the High and Low intensity

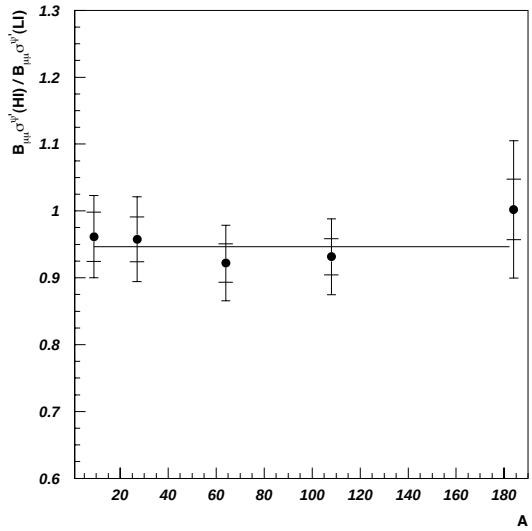

Figure 5.10: Ratio of the ψ' cross sections (in the $-0.5 < Y < 0.5$ range) from the High to the ones of the Low intensity data fitted by a constant line ($R = 0.946 \pm 0.0285$.)

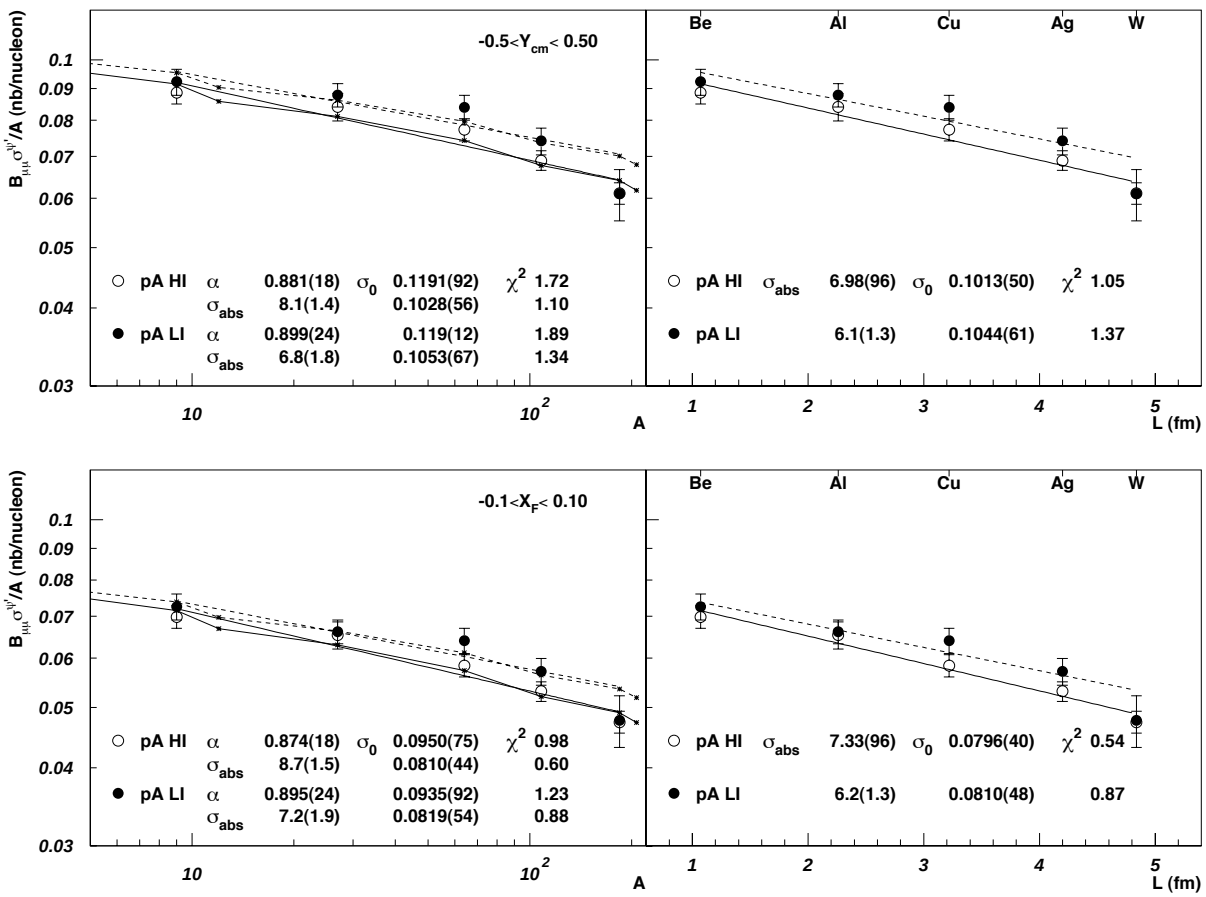

Figure 5.11: ψ' cross sections per nucleon (for the High (HI) and Low (LI) intensity data sets) in the $-0.5 < Y_{CM} < 0.5$ (Top) and $-0.1 < X_F < 0.1$ (Bottom) ranges fitted by the: (Left) parametrization $\sigma_A = \sigma_0 A^{\alpha}$ (the results are shown on the first line of the legend) and complete Glauber model (second line); (Right) parametrization $\sigma_A = \sigma_0 e^{-<\rho L>\sigma_{abs}}$. The values for σ_0 and σ_{abs} are in *nb* and *mb* respectively.

data (rescaled in the same way as it was done for the J/ψ) are plotted on Fig. 5.12 and collected in the Table 5.6. The large symbols in the center of each plot are the suppression parameters for the fit of the cross sections in the whole Y_{CM} and X_F ranges.

	-0.50$< Y <$**0.50**	**-0.50**$< Y <$**-0.25**	**-0.25**$< Y <$ **0.0**	**0.0**$< Y <$ **0.25**	**0.25**$< Y <$ **0.5**
High Intensity Data					
α	0.881±0.018	0.844±0.030	0.887 ±0.022	0.883±0.021	0.878±0.029
σ_{abs} [ρL]	7.0±1.0	9.2±1.5	6.6±1.1	6.8±1.1	6.9±1.5
σ_{abs} [Glb.]	8.1±1.4	11.4±2.5	7.4±1.7	7.7±1.6	8.2±2.2
σ_0 [Glb.]	0.103±0.006	0.026±0.002	0.027±0.002	0.026±0.002	0.025±0.002
Low Intensity Data					
α	0.899±0.024	0.853±0.046	0.893±0.029	0.918±0.034	0.894±0.046
σ_{abs} [ρL]	6.1±1.3	8.9±2.3	6.5±1.5	4.7±1.7	6.6±2.3
σ_{abs} [Glb.]	6.8±1.8	10.3±3.6	7.5±2.2	5.3±2.2	7.3±3.1
σ_0 [Glb.]	0.105±0.007	0.026±0.003	0.028±0.002	0.026±0.002	0.024±0.003
Joint Low+High Intensity Data fit					
α	0.886±0.014	0.847±0.025	0.889±0.017	0.896±0.018	0.885±0.025
σ_{abs} [ρL]	6.7±0.8	9.0±1.2	6.6±0.9	6.0±0.9	6.7±1.2
σ_{abs} [Glb.]	7.7±1.1	11.0±2.0	7.5±1.3	7.0±1.3	7.8±1.8
σ_0 [Glb.]	0.105±0.004	0.026±0.002	0.028±0.001	0.027±0.001	0.025±0.002

	-0.10$< X_F <$**0.10**	**-0.10**$< X_F <$**-0.05**	**-0.05**$< X_F <$**0.0**	**0.0**$< X_F <$**0.05**	**0.05**$< X_F <$**0.1**
High Intensity Data					
α	0.874±0.018	0.835±0.026	0.877±0.023	0.863±0.023	0.870±0.025
σ_{abs} [ρL]	7.3±1.0	9.6±1.3	7.1±1.2	8.0±1.2	7.4±1.4
σ_{abs} [Glb.]	8.7±1.5	12.2±2.3	8.4±1.8	9.5±1.9	8.9±2.1
σ_0 [Glb.]	0.081±0.004	0.021±0.002	0.021±0.001	0.021±0.001	0.019±0.001
Low Intensity Data					
α	0.895±0.024	0.854±0.040	0.894±0.032	0.915±0.037	0.895±0.039
σ_{abs} [ρL]	6.2±1.3	8.6±2.0	6.5±1.7	4.8±1.8	6.2±2.1
σ_{abs} [Glb.]	7.2±1.9	10.4±3.2	7.6±2.4	5.5±2.5	7.2±2.8
σ_0 [Glb.]	0.082±0.005	0.020±0.002	0.022±0.002	0.019±0.002	0.019±0.002
Joint Low+High Intensity Data fit					
α	0.881±0.014	0.841±0.022	0.883±0.018	0.881±0.019	0.878±0.021
σ_{abs} [ρL]	7.0±0.8	9.3±1.1	6.9±1.0	6.9±1.0	7.0±1.1
σ_{abs} [Glb.]	8.3±1.1	11.6±1.9	8.0±1.4	7.9±1.5	8.3±1.6
σ_0 [Glb.]	0.082±0.003	0.021±0.001	0.021±0.001	0.020±0.001	0.019±0.001

Table 5.6: ψ' suppression parameters for various parametrizations fitted in Y_{CM} (top part) and X_F (bottom part) bins. For each data set the values are: α parameter of the $\sigma_A = \sigma_0 A^\alpha$ parametrization, absorption cross section (in *mb*) for the $\sigma_A = \sigma_0 e^{-<\rho\ L>\sigma_{abs}}$ parametrization (marked as "σ_{abs} [ρL]") and the absorption (marked as "σ_{abs} [Glb.]") and the *pN* production (in *nb*) (marked as "σ_0 [Glb.]") cross sections from the complete Glauber model fit.

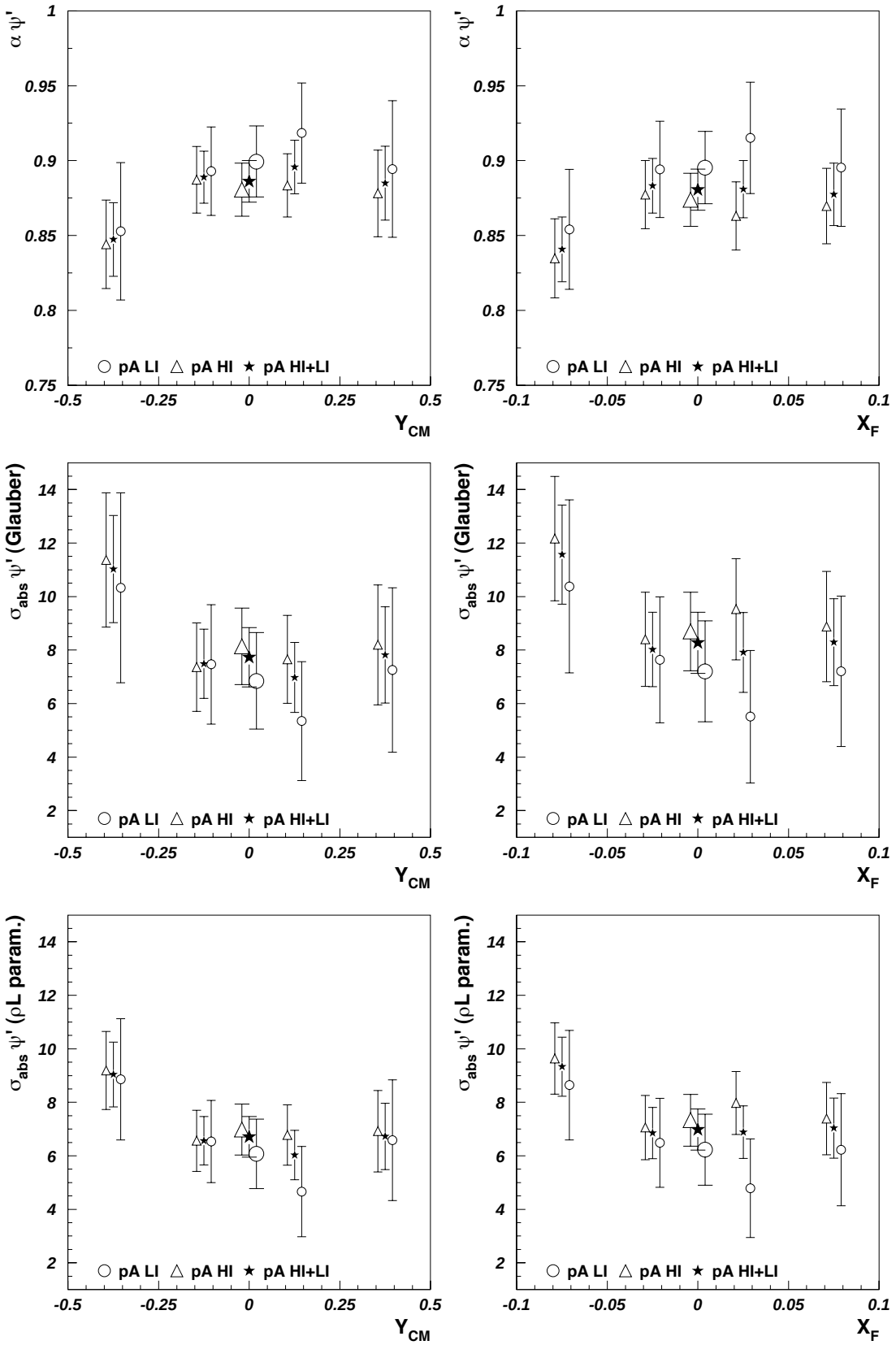

Figure 5.12: ψ' suppression parameters for various parametrizations fitted in Y_{CM} (Left) and X_F (Right) bins: α parameter (Top); absorption cross section (*mb*) from the (Middle) complete Glauber model and (Bottom) $\sigma_A = \sigma_0 e^{-<\rho\ L>\sigma_{abs}}$ parametrization.

5.2.3 Drell-Yan cross section

Although the statistics of both High and Low intensity data sets are too scarce to give any importance to the obtained differential cross sections for the Drell-Yan dimuons, for completeness their cross sections per nucleon are plotted on Fig.5.13 and 5.14 for Y_{MC} and X_F binings respectively and their values are given in the Tables 5.7 and 5.8. The mass range corresponding to these values is $2.9 < M < 4.5\ GeV/c^2$ but it was chosen only because NA38/NA50 traditionally uses the Drell-Yan cross section in this mass range as a reference for the J/ψ. In fact the computed cross section of Drell-Yan and its statistical error is determined by its high mass tail ($M > 4.2\ GeV/c^2$) where it is the only contribution to the mass spectrum. Since the shape of the Drell-Yan mass spectrum, obtained from Monte-Carlo (see Section 4.2.1) is kept constant during the fit and only the normalization is varied, its cross section in any mass range and the corresponding error is obtained by simple rescaling of its high mass value according to the shape predicted by the PYTHIA generator.

Apart from the division by the target atomic mass number all values are corrected for the isospin composition of the target, i.e.

$$\sigma^{DY}/nucleon = \sigma^{DY}(A)\frac{\sigma_{pp}}{\sigma_{pp}\,Z + \sigma_{pn}\,(A-Z)} \tag{5.1}$$

with $\sigma_{pp} = 0.061$ and $\sigma_{pn} = 0.064\ nb$ from the PYTHIA predictions (with *MRSA* parametrization of the parton distribution functions), which gives the isospin correction coefficients 0.973, 0.975, 0.974, 0.973 and 0.971 for Be, Al, Cu, Ag and W targets respectively.

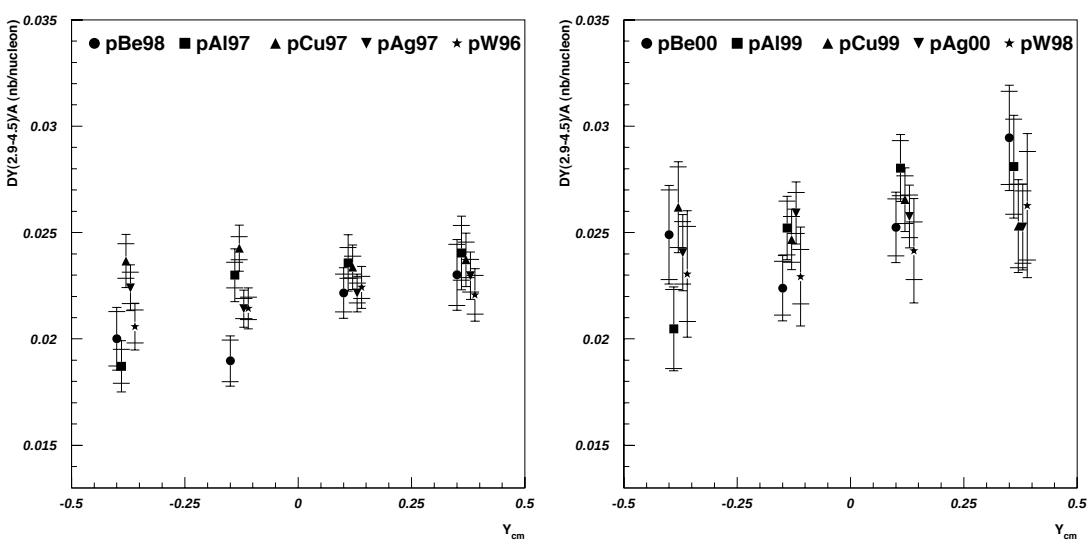

Figure 5.13: Cross sections per nucleon (isospin corrected) for the Drell-Yan in the $2.9 < M < 4.5\ GeV/c^2$ range as a function of the rapidity in the center of mass for High (Left) and Low (Right) intensity data.

One can notice the highly irregular pattern of the obtained distributions, some of the points being a few standard deviations apart from others. What is worse, as one can see on Fig.5.15, even for the integrated data the systematic discrepancy between the High and Low intensity data, which was on the level of 4% for the J/ψ and ψ' cross sections, in case of Drell-Yan is even higher, reaching the factor 0.9 for the fit of the ratio of High to Low intensity data cross

	-0.50$< Y <$**0.50**	**-0.50**$< Y <$**-0.25**	**-0.25**$< Y <$ **0.0**	**0.0**$< Y <$ **0.25**	**0.25**$< Y <$ **0.5**
pBe00	.0977±.0032±.0037	.0249±.0021±.0010	.0224±.0013±.0009	.0252±.0013±.0010	.0295±.0022±.0012
pAl99	.1027±.0031±.0032	.0205±.0019±.0007	.0252±.0013±.0008	.0280±.0013±.0009	.0281±.0022±.0009
pCu99	.1021±.0028±.0038	.0262±.0019±.0010	.0247±.0011±.0009	.0265±.0011±.0010	.0253±.0020±.0010
pAg00	.1012±.0024±.0042	.0241±.0015±.0010	.0259±.0010±.0011	.0258±.0010±.0011	.0253±.0017±.0011
pW98	.945±.0033±.0080	.0231±.0022±.0020	.0229±.0013±.0019	.0241±.0014±.0020	.0263±.0026±.0022
pBe98	.0879±.0020±.0031	.0200±.0013±.0007	.0190±.0010±.0007	.0222±.0009±.0008	.0230±.0014±.0008
pAl97	.0902±.0016±.0042	.0187±.0008±.0009	.0230±.0006±.0011	.0236±.0007±.0011	.0240±.0013±.0012
pCu97	.0951±.0013±.0037	.0237±.0008±.0009	.0243±.0005±.0009	.0234±.0005±.0009	.0237±.0008±.0009
pAg97	.0880±.0011±.0030	.0224±.0007±.0008	.0214±.0005±.0007	.0222±.0005±.0008	.0230±.0008±.0008
pW96	.0867±.0013±.0032	.0206±.0008±.0008	.0214±.0005±.0008	.0224±.0005±.0008	.0221±.0009±.0008

Table 5.7: Cross sections per nucleon (isospin corrected) for Drell-Yan in the $2.9 < M < 4.5\ GeV/c^2$ range as a function of the rapidity in the center of mass.

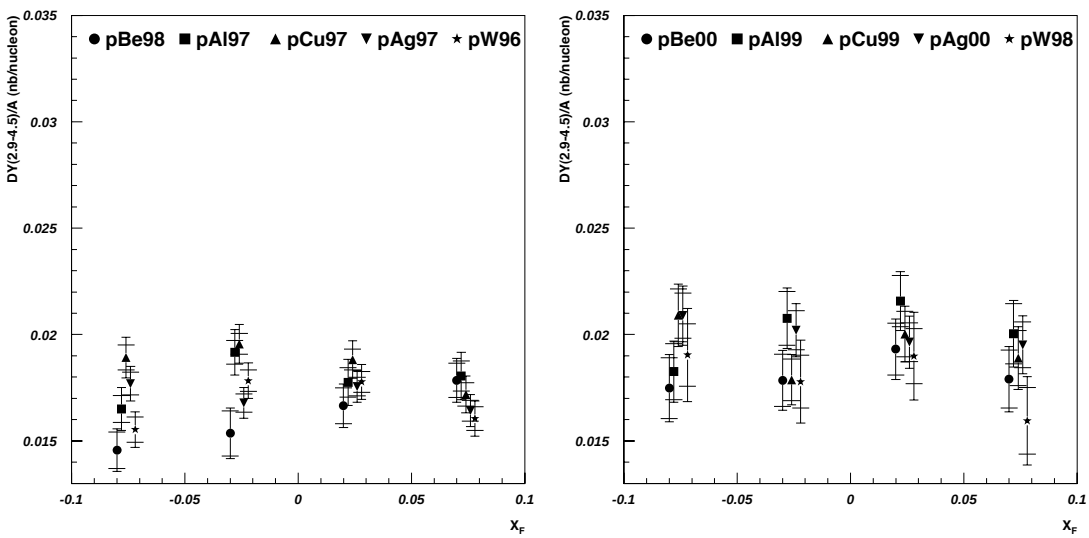

Figure 5.14: Cross sections per nucleon (isospin corrected) for Drell-Yan in the $2.9 < M < 4.5\ GeV/c^2$ range as a function of the X_F for High (Left) and Low (Right) intensity data.

	-0.10$< X_F <$**0.10**	**-0.10**$< X_F <$**-0.05**	**-0.05**$< X_F <$**0.0**	**0.0**$< X_F <$**0.05**	**0.05**$< X_F <$**0.1**
pBe00	.0726±.0026±.0028	.0175±.0014±.0007	.0178±.0012±.0007	.0193±.0012±.0007	.0179±.0014±.0007
pAl99	.0819±.0027±.0025	.0183±.0013±.0006	.0208±.0013±.0007	.0216±.0012±.0007	.0200±.0014±.0006
pCu99	.0775±.0023±.0029	.0209±.0012±.0008	.0179±.0010±.0007	.0200±.0011±.0007	.0189±.0013±.0007
pAg00	.0802±.0020±.0034	.0209±.0011±.0009	.0202±.0009±.0009	.0196±.0009±.0008	.0195±.0011±.0008
pW98	.0703±.0028±.0059	.0190±.0015±.0016	.0178±.0012±.0015	.0190±.0013±.0016	.0159±.0016±.0014
pBe98	.0679±.0017±.0024	.0146±.0009±.0005	.0154±.0011±.0005	.0166±.0008±.0006	.0178±.0008±.0006
pAl97	.0719±.0014±.0034	.0165±.0006±.0008	.0192±.0006±.0009	.0177±.0007±.0008	.0181±.0007±.0009
pCu97	.0752±.0011±.0029	.0189±.0006±.0007	.0196±.0005±.0008	.0188±.0005±.0007	.0172±.0005±.0007
pAg97	.0687±.0010±.0023	.0177±.0005±.0006	.0168±.0004±.0006	.0176±.0004±.0006	.0164±.0005±.0006
pW96	.0659±.0011±.0024	.0155±.0006±.0006	.0178±.0005±.0007	.0178±.0005±.0007	.0161±.0006±.0006

Table 5.8: Cross sections per nucleon (isospin corrected) for Drell-Yan in the $2.9 < M < 4.5\ GeV/c^2$ range as a function of the X_F.

sections by a constant line[1]. Nevertheless, the fact that for each intensity set the integrated cross sections stay constant (within the errors) for different targets justifies the usage of the Drell-Yan cross section as a reference for the J/ψ.

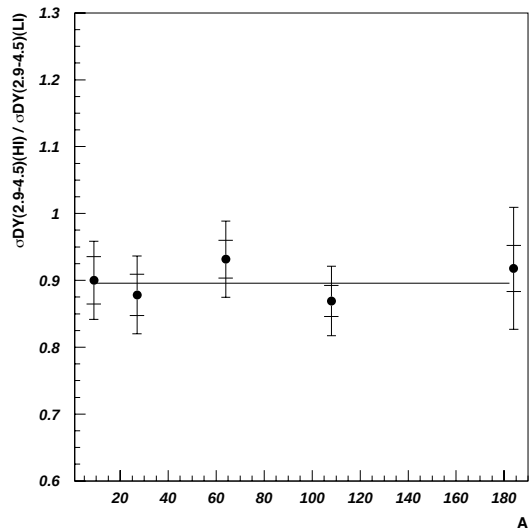

Figure 5.15: Ratio of the Drell-Yan cross sections (in the $-0.5 < Y < 0.5$ range) from the High and Low intensity data fitted by a constant line.

[1]This raises the question whether the efficiency of the dimuon reconstruction is indeed independent on the kinematics as it was shown on the mixed sample of Monte-Carlo and experimental data in the Section 3.2.3. If this is the case then one can imagine an additional source of high mass dimuon loss, which is not accounted in the reconstruction efficiency estimation procedure: even if the pieces of the muon track in the Forward and Backward NA50 telescopes were reconstructed, the muon could be rejected on the level of the association of these pieces in the center of the toroidal magnet. Since for a very high momentum muons the bending angle in the magnet is small (i.e. the tracks in the Forward and Backward telescopes are almost parallel), the spread of the estimated point of their maximum approach along the beam axis is larger than the one for the low momentum muons (originated, in average, in the decays of the dimuons with lower masses). Allowing larger deviations of the maximum approach point from the magnet center is not a good solution since this would lead to a sharp increase of the spurious track contamination which can spoil the reconstruction for all masses. Unfortunately, the usage of the more sophisticated algorithms for the association of the tracks in the Forward and Backward telescopes (like global fit of the track passing all chambers) is very problematic within the framework of the existing reconstruction software. Nevertheless, it should be implemented in the NA50 successor, NA60 experiment.

5.3 Results for the cross sections ratios

Due to the uncertainty in the parameters entering in the absolute cross section calculation (the luminosity, trigger and reconstruction efficiencies, etc.) the final (systematic) error on the computed values appears to be much larger that the pure statistical error (factor ~ 30 for the J/ψ cross section from the High Intensity data). This situation is avoided if one uses ratios of cross sections, in which case the errors from the normalization uncertainties are absent and the only systematic errors left are the ones coming from the acceptances correction and the fitting procedure (particularly, the adequacy of the Monte-Carlo based fitting functions to the real experimental spectra). This section studies the ratios of the cross sections of the ψ' to the J/ψ and of the J/ψ to the Drell-Yan (the ratio ψ' to DY is not informative due to the large statistical errors of both signals even in the total data samples).

5.3.1 ψ' to J/ψ ratio

Fig.5.16 shows the ratio of the cross sections for the ψ' and J/ψ (not corrected for the difference in the $\mu\mu$ branching ratios) in the four Y_{CM} bins: the left plot is for the High and the right one for the Low intensity data sets. The values are presented in the Table 5.9. The systematic errors are determined by the variation of the results of the ψ' fit for different J/ψ tail shapes (see Section 4.2.2) and to some extent by the uncertainties of the acceptances (which are very small and anyway, affect all data samples in the same way). At the same time a glance on the values corresponding to the Low intensity data in the restricted kinematical bins shows that the errors are seriously underestimated. The reason is that the low statistics of these samples affects the systematics of the fit - it is not enough to fix neither the positions of the ψ''s pole nor the J/ψ tail continuation under it. An additional source of error is the lack of **target out** data. In this situation the suppression parameters extracted from the Low intensity data in the restricted kinematical domains have no importance by themselves but are useful only to show the compatibility with the results from the High intensity data.

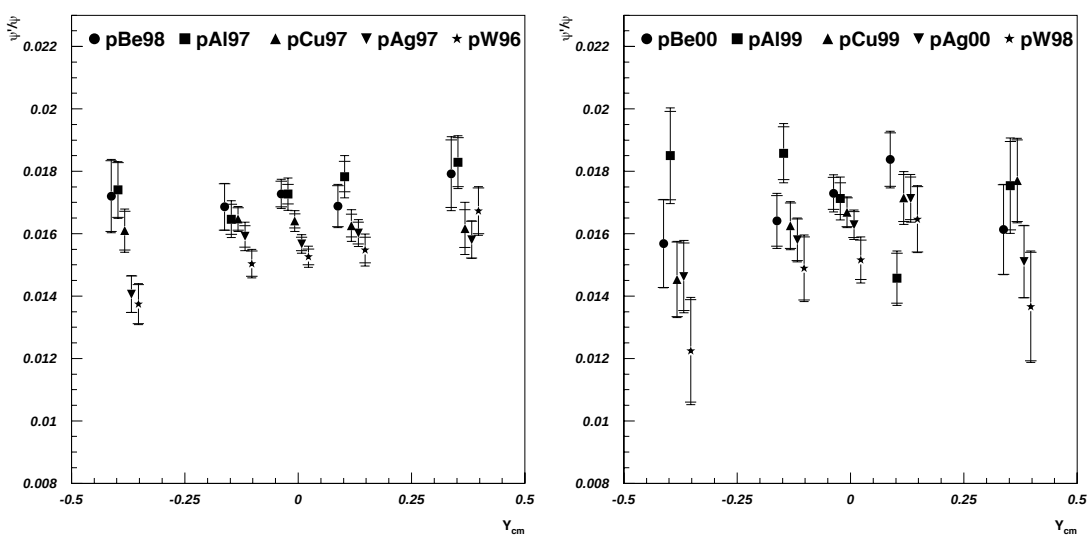

Figure 5.16: Ratios of the ψ' and J/ψ cross sections (not corrected for the $\mu\mu$ branching ratios) as a function of the rapidity in the center of mass for (Left) High and (Right) Low Intensity data.

	-0.50< Y <0.50	**-0.50< Y <-0.25**	**-0.25< Y < 0.0**	**0.0< Y < 0.25**	**0.25< Y < 0.5**
Be00	.0173±.0005±.0003	.0157±.0014±.0002	.0164±.0008±.0004	.0184±.0009±.0003	.0161±.0014±.0002
Al99	.0171±.0005±.0005	.0185±.0014±.0006	.0186±.0008±.0004	.0146±.0008±.0004	.0175±.0014±.0006
Cu99	.0167±.0005±.0002	.0145±.0012±.0002	.0163±.0007±.0002	.0171±.0008±.0004	.0177±.0013±.0004
Ag00	.0163±.0004±.0002	.0146±.0011±.0004	.0158±.0007±.0002	.0171±.0007±.0003	.0151±.0012±.0001
W98	.0152±.0006±.0004	.0122±.0016±.0005	.0149±.0010±.0003	.0165±.0010±.0002	.0137±.0017±.0004
Be98	.0173±.0004±.0002	.0172±.0011±.0003	.0169±.0007±.0001	.0169±.0007±.0002	.0179±.0011±.0005
Al97	.0173±.0003±.0004	.0174±.0009±.0002	.0165±.0005±.0003	.0178±.0005±.0005	.0183±.0008±.0003
Cu97	.0164±.0002±.0002	.0161±.0006±.0003	.0165±.0004±.0002	.0163±.0004±.0004	.0162±.0006±.0006
Ag97	.0157±.0002±.0002	.0141±.0006±.0001	.0159±.0003±.0003	.0160±.0003±.0002	.0158±.0006±.0001
W96	.0153±.0003±.0002	.0137±.0006±.0002	.0150±.0004±.0002	.0155±.0004±.0003	.0167±.0007±.0003

Table 5.9: Ratios of the ψ' and J/ψ cross sections (not corrected for the $\mu\mu$ branching ratios) for the integrated data and in the four Y_{CM} bins.

The corresponding results for the data in the X_F bins are shown in the Table 5.10 and plotted on Fig.5.17.

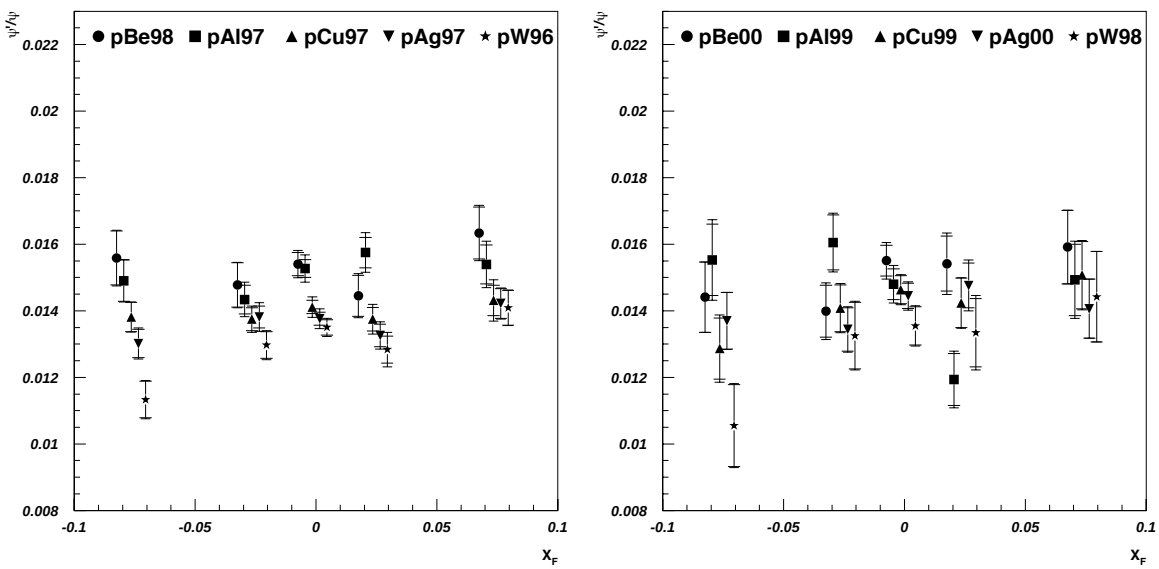

Figure 5.17: Ratios of the ψ' and J/ψ cross sections (not corrected for the $\mu\mu$ branching ratios) as a function of the X_F bin for (Left) High and (Right) Low Intensity data.

As one can see from Fig.5.18, showing the ratios of the ψ' / J/ψ from High and Low intensity data (integrated over the whole kinematical domain) fitted by a constant line, the two sets are compatible within the errors ($R = 0.987 \pm 0.015$). Therefore, when extracting the parameters of the suppression of the ψ' with respect to the J/ψ, in opposite to what was done in the case of the absolute cross sections, no rescaling parameter will be introduced during the simultaneous fit of the High an Low intensity data sets.

Concerning the parametrizations used to compare the suppression of the ψ' and J/ψ, one should note that the precision of even High Intensity data is by far not enough to perform the fit according to the complete Glauber model. Thus one is limited to the usage of the $\sigma_A = \sigma_0 A^\alpha$

	-0.10$< X_F <$**0.10**	**-0.10**$< X_F <$**-0.05**	**-0.05**$< X_F <$**0.0**	**0.0**$< X_F <$**0.05**	**0.05**$< X_F <$**0.1**
pBe00	.0155±.0005±.0003	.0144±.0011±.0001	.0140±.0008±.0003	.0154±.0008±.0004	.0159±.0011±.0001
pAl99	.0148±.0005±.0003	.0155±.0011±.0006	.0161±.0008±.0003	.0119±.0008±.0004	.0149±.0011±.0004
pCu99	.0146±.0004±.0002	.0129±.0009±.0004	.0141±.0007±.0002	.0142±.0007±.0001	.0151±.0010±.0003
pAg00	.0144±.0004±.0002	.0137±.0009±.0001	.0134±.0007±.0002	.0148±.0007±.0004	.0141±.0009±.0001
pW98	.0135±.0006±.0002	.0105±.0012±.0003	.0133±.0010±.0002	.0133±.0010±.0004	.0144±.0014±.0001
pBe98	.0154±.0003±.0002	.0156±.0008±.0002	.0148±.0007±.0001	.0145±.0006±.0002	.0163±.0008±.0003
pAl97	.0153±.0003±.0003	.0149±.0006±.0001	.0143±.0004±.0003	.0158±.0005±.0004	.0154±.0006±.0004
pCu97	.0141±.0002±.0002	.0138±.0004±.0001	.0137±.0003±.0002	.0137±.0004±.0003	.0143±.0005±.0004
pAg97	.0138±.0002±.0002	.0130±.0004±.0002	.0138±.0003±.0003	.0133±.0003±.0002	.0142±.0004±.0001
pW96	.0135±.0002±.0002	.0113±.0005±.0002	.0130±.0004±.0002	.0128±.0004±.0003	.0141±.0005±.0001

Table 5.10: Ratio of the ψ' and J/ψ cross sections (not corrected for the $\mu\mu$ branching ratio) for the integrated data and in the four X_F bins.

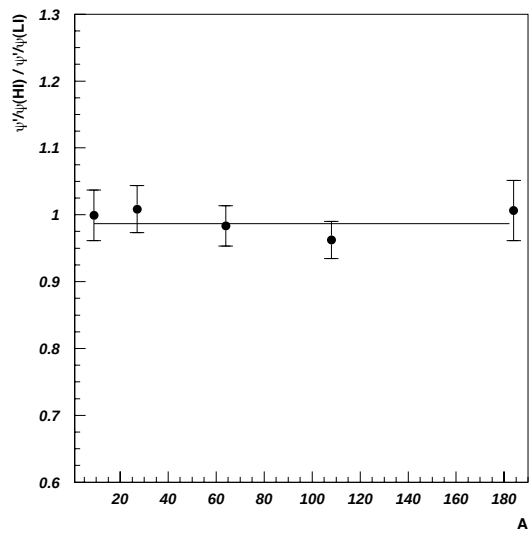

Figure 5.18: Ratios of the values of ψ' / J/ψ cross sections (in the $-0.5 < Y < 0.5$ range) from the High and Low intensity data fitted by a constant line ($R = 0.987 \pm 0.015$).

and $\sigma_A = \sigma_0 e^{-<\rho L>\sigma_{abs}}$ parametrizations, and in this case we will be able to extract only the relative suppression of the ψ' with respect to the J/ψ (i.e. the fitting functions are $\sigma_{\psi'}/\sigma_{J/\psi} = R_0 A^{\alpha_{\psi'}-\alpha_{J/\psi}}$ and $\sigma_{\psi'}/\sigma_{J/\psi} = R_0 e^{-<\rho L>(\sigma_{abs}^{\psi'}-\sigma_{abs}^{J/\psi})}$).

Fig.5.19 shows the ratios of the cross sections integrated over the $-0.5 < Y_{CM} < 0.5$ (top plot) and $-0.1 < X_F < 0.1$ (bottom) ranges fitted according to these two different suppression parametrizations: the left column is for $R_0 A^{\Delta\alpha}$ parametrization while the right one is for the $R_0 e^{-<\rho L>\Delta\sigma_{abs}}$; the plots on the top are for the cross sections in the $-0.5 < Y_{CM} < 0.5$ range and on the bottom for $-0.1 < X_F < 0.1$). The values for $\Delta\sigma_{abs} = \sigma_{abs}^{\psi'} - \sigma_{abs}^{J/\psi}$ are in mb.

The plots for the bin by bin fits can be found in the Appendix 7.2: Fig.7.15 and 7.16 for the Y_{CM} and X_F bins respectively.

The results of these fits, as well as for the simultaneous fit of the High and Low intensity data, are collected in the Table 5.11 and are plotted on the Fig. 5.20.

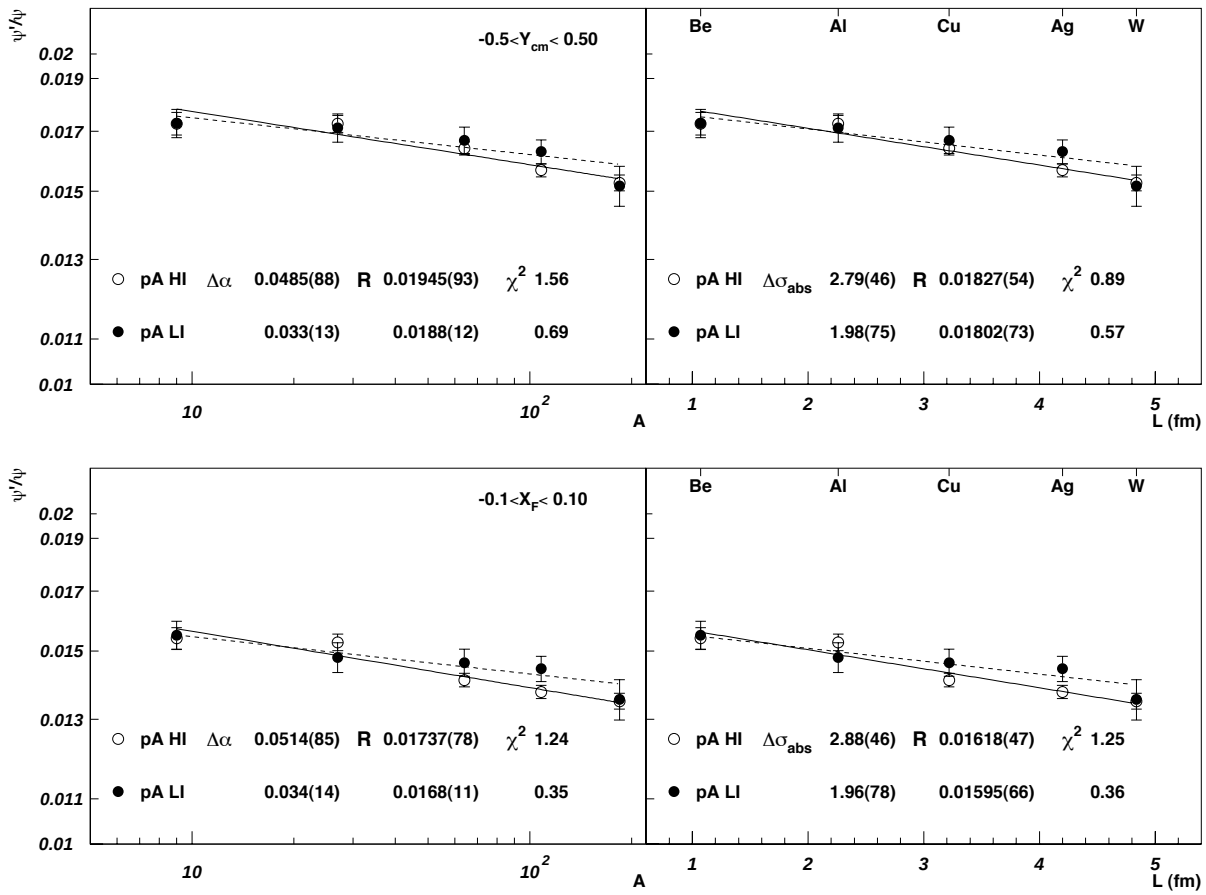

Figure 5.19: Ratio of the ψ' and J/ψ cross sections (for the High (HI) and Low (LI) intensity data sets) in the $-0.5 < Y_{CM} < 0.5$ (Top) and $-0.1 < X_F < 0.1$ (Bottom) ranges fitted by the: (Left) parametrization $R_0 A^{\Delta\alpha}$; (Right) parametrization $R_0 e^{-<\rho L>\Delta\sigma_{abs}}$. The values for the $\Delta\sigma_{abs}$ are in *mb*.

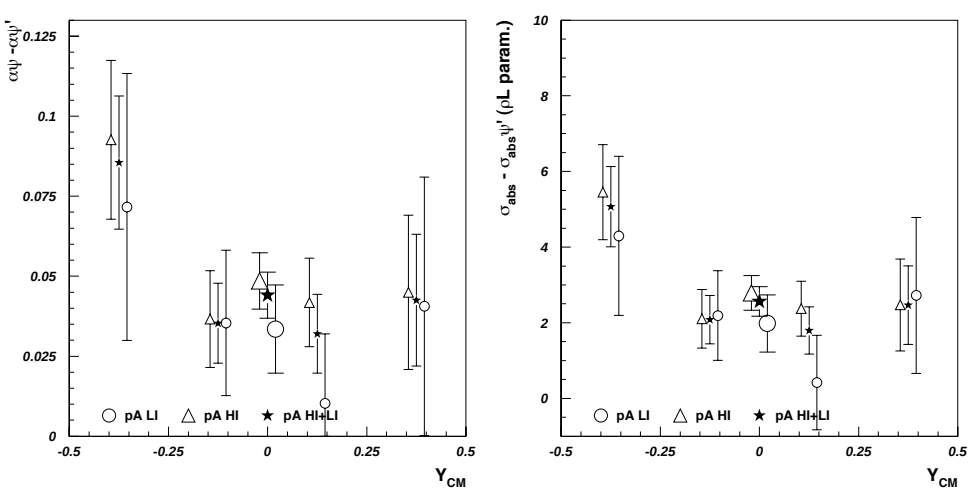

Figure 5.20: Parameters of the suppression of the ψ' with respect to the J/ψ for various parametrizations fitted in Y_{CM} bins: (Left) $R_0 A^{\Delta\alpha}$ parametrization , (Right) $R_0 e^{-<\rho L>\Delta\sigma_{abs}}$ parametrization.

	-0.50$< Y <$**0.50**	**-0.50**$< Y <$**-0.25**	**-0.25**$< Y <$ **0.0**	**0.0**$< Y <$ **0.25**	**0.25**$< Y <$ **0.5**
High Intensity Data					
$\Delta\alpha$	0.048±0.009	0.093±0.025	0.037±0.015	0.042±0.014	0.045±0.024
R_0 $[A^\alpha]$	0.0233±0.0009	0.0297±0.0031	0.0222±0.0015	0.0221±0.0012	0.0230±0.0020
$\Delta\sigma_{abs}$ $[\rho L]$	2.8±0.5	5.5±1.3	2.1±0.8	2.4±0.7	2.5±1.2
R_0 $[\rho L]$	0.0218±0.0004	0.0261±0.0016	0.0211±0.0008	0.0208±0.0008	0.0215±0.0013
Low Intensity Data					
$\Delta\alpha$	0.034±0.014	0.072±0.042	0.035±0.023	0.010±0.022	0.041±0.040
R_0 $[A^\alpha]$	0.0222±0.0012	0.0264±0.0043	0.0223±0.0020	0.0198±0.0020	0.0216±0.0035
$\Delta\sigma_{abs}$ $[\rho L]$	2.0±0.8	4.3±2.1	2.2±1.2	0.4±1.2	2.7±2.1
R_0 $[\rho L]$	0.0212±0.0006	0.0240±0.0023	0.0214±0.0012	0.0194±0.0011	0.0208±0.0019
Joint Low+High Intensity Data fit					
$\Delta\alpha$	0.045±0.007	0.084±0.021	0.037±0.012	0.035±0.012	0.041±0.021
$\Delta\sigma_{abs}$ $[\rho L]$	2.6±0.4	5.0±1.1	2.2±0.6	1.9±0.6	2.4±1.0
R_0 $[\rho L]$	0.0216±0.0004	0.0253±0.0017	0.0212±0.0007	0.0204±0.0007	0.0212±0.0011

	-0.10$< X_F <$**0.10**	**-0.10**$< X_F <$**-0.05**	**-0.05**$< X_F <$**0.0**	**0.0**$< X_F <$**0.05**	**0.05**$< X_F <$**0.1**
High Intensity Data					
$\Delta\alpha$	0.051±0.009	0.098±0.021	0.039±0.016	0.061±0.016	0.052±0.019
R_0 $[A^\alpha]$	0.0225±0.0008	0.0314±0.0027	0.0198±0.0013	0.0207±0.0014	0.0257±0.0021
$\Delta\sigma_{abs}$ $[\rho L]$	2.9±0.5	5.6±1.1	2.2±0.8	3.5±0.8	2.8±1.0
R_0 $[\rho L]$	0.0208±0.0005	0.0272±0.0014	0.0186±0.0008	0.0190±0.0008	0.0237±0.0012
Low Intensity Data					
$\Delta\alpha$	0.034±0.014	0.070±0.035	0.030±0.025	0.008±0.029	0.038±0.034
R_0 $[A^\alpha]$	0.0213±0.0009	0.0276±0.0038	0.0193±0.0020	0.0168±0.0020	0.0244±0.0032
$\Delta\sigma_{abs}$ $[\rho L]$	2.0±0.8	4.0±1.8	1.9±1.3	0.2±1.5	2.2±1.8
R_0 $[\rho L]$	0.0203±0.0007	0.0250±0.0020	0.0186±0.0011	0.0165±0.0010	0.0232±0.0020
Joint Low+High Intensity Data fit					
$\Delta\alpha$	0.048±0.007	0.089±0.018	0.037±0.013	0.048±0.014	0.048±0.017
R_0 $[A^\alpha]$	0.0222±0.0007	0.0301±0.0022	0.0197±0.0011	0.0196±0.0011	0.0254±0.0016
$\Delta\sigma_{abs}$ $[\rho L]$	2.7±0.4	5.1±0.9	2.1±0.7	2.7±0.7	2.7±0.9
R_0 $[\rho L]$	0.0207±0.0004	0.0265±0.0012	0.0186±0.0006	0.0183±0.0007	0.0235±0.0010

Table 5.11: Parameters of the suppression of ψ' with respect to the J/ψ fitted in Y_{CM} (Top) and X_F (Bottom) bins: For each data set the values are: $\Delta\alpha$ and R_0 (marked as "R_0 $[A^\alpha]$") of the $R_0 A^{\Delta\alpha}$ parametrization; absorption cross section (in *mb*) and R_0 (marked as "R_0 $[\rho L]$") for the $R_0 e^{-<\rho L>\Delta\sigma_{abs}}$ parametrization.

5.3.2 J/ψ to Drell-Yan ratio

As it was mentioned in Section 5.2.3, the strong fluctuations of the measured Drell-Yan cross sections make it impossible to extract any useful information from its bin by bin values. For this reason Fig.5.21 shows the ratios of the J/ψ and Drell-Yan cross sections in the whole Y_{MC} (top plot) and X_F ranges, fitted according to the follwing parametrzations:
the left column is for $\sigma^{J/\psi}/\sigma^{DY} = RA^{\alpha}$ (the results of the fit are shown on the first line of the legend for each data set) and for the complete Glauber model (second line, the parameters are R and σ_{abs});
the right column is for the $\sigma^{J/\psi}/\sigma^{DY} = Re^{-<\rho L>\sigma_{abs}}$ parametrization.

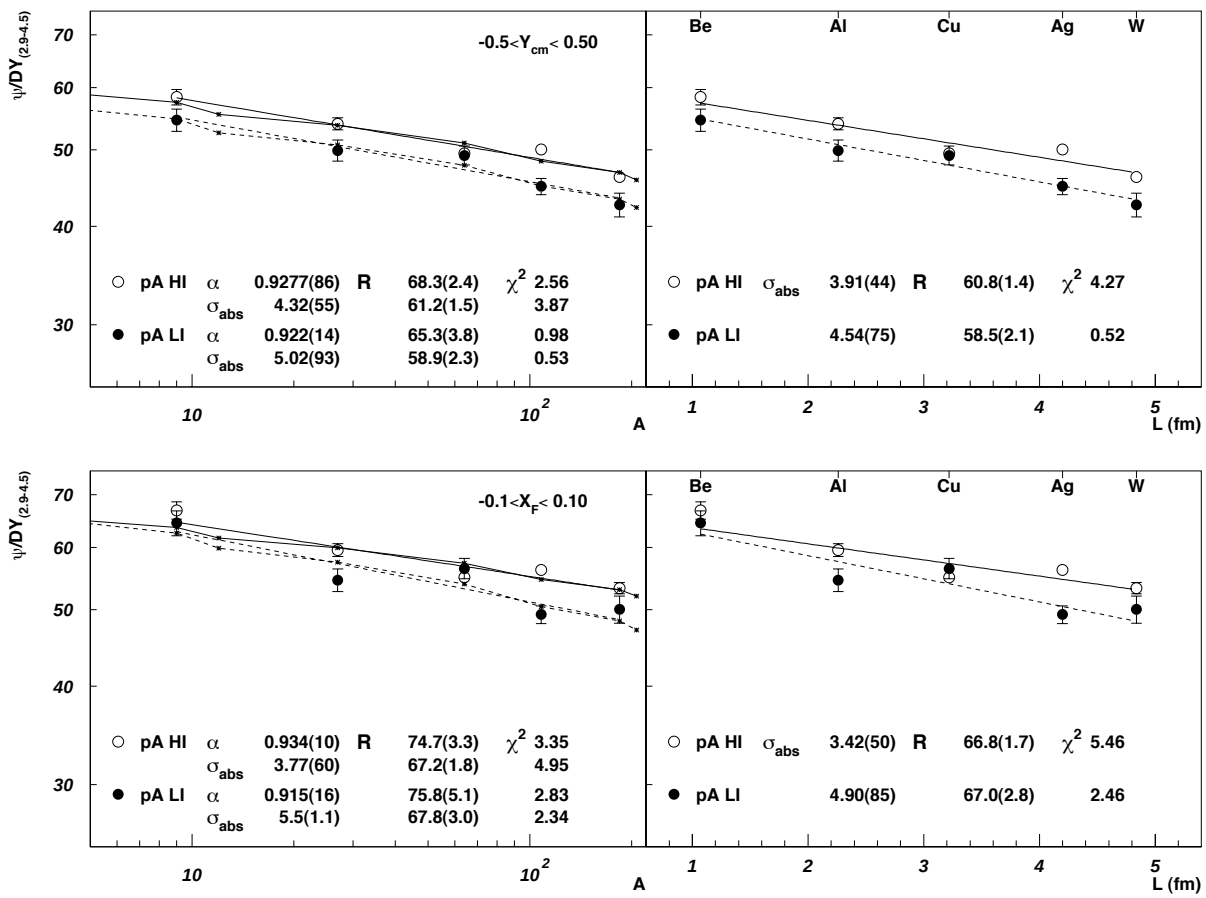

Figure 5.21: Ratios of J/ψ cross sections to the isospin corrected cross sections of Drell-Yan in the $2.9 < M < 4.5\ GeV/c^2$ range (for the High (HI) and Low (LI) intensity data sets) in the $-0.5 < Y_{CM} < 0.5$ (Top) and $-0.1 < X_F < 0.1$ (Bottom) ranges fitted by the: (Left) parametrization RA^{α}(the results are shown on the first line of the legend) and the complete Glauber model (second line); (Right) parametrization $Re^{-<\rho L>\sigma_{abs}}$. The values for the σ_{abs} are in mb.

One can see that despite the systematic difference between the High and Low intensity data in what concerns the absolute cross sections, the J/ψ suppression parameters (α and σ_{abs}) extracted from the ratios of the J/ψ over Drell-Yan are in good agreement for both data sets. Besides, these parameters are also compatible with the values extracted from the fits to the J/ψ absolute cross sections.

5.4 Comparison with Previous Results

In this section the cross sections obtained are compared with previous NA38 and NA51 450 *GeV* *pA* results. These data were collected with slightly different setups, with the magnet placed 90 *cm* downstream from its NA50 position, thus shifting the rapidity acceptance towards higher values. For this reason the reconstruction was done in the $-0.4 < Y_{CM} < 0.6$ range, so the comparison requires a small rescaling of these data. The inspection of the J/ψ rapidity distribution shows that in order to rescale the cross sections in the NA38/NA51 range to the interval $-0.5 < Y_{CM} < 0.5$ one has to multiply them by the factor 1.016. Apart from this factor one has to account for the higher (by the factor 1.0534) calibration coefficients for argon counters used for these data anlysis. Thus, an overall correction factor 1.07 was applied to these cross sections (first column of the Table5.12, while the rescaled values are shown in the second one).

pp	5.50 ± 0.36	5.88 ± 0.38
pD	5.66 ± 0.38	6.06 ± 0.41
pC	4.65 ± 0.33	4.97 ± 0.35
pAl	4.15 ± 0.29	4.44 ± 0.31
pCu	4.19 ± 0.29	4.48 ± 0.31
pW	3.71 ± 0.26	3.97 ± 0.28

Table 5.12: J/ψ cross section per nucleon in *nb* (not corrected for the $\mu\mu$ branching ratio) measured by NA38 (*pC*, *Al*, *Cu* and *W* targets) [83] and NA51 (*pp* and *pD*) [82] experiments at 450 *GeV*. The first column shows the original values from the references, while the second one shows the rescaled cross sections.

Fig. 5.22 shows the dependence of the J/ψ cross section per nucleon on the target mass number fitted with (Left) A^{α} parametrization; (Center) complete Glauber model calculation; (Right) $e^{-<\rho L>\sigma_{abs}}$ parametrization. On each plot the NA51 *pp* and *pD* points are fitted together with the ones of NA38 data (solid lines), High (dashed) and Low (dotted) intensity data analyzed in this work. One can see, that, although within the errors the results of the fits are compatible,

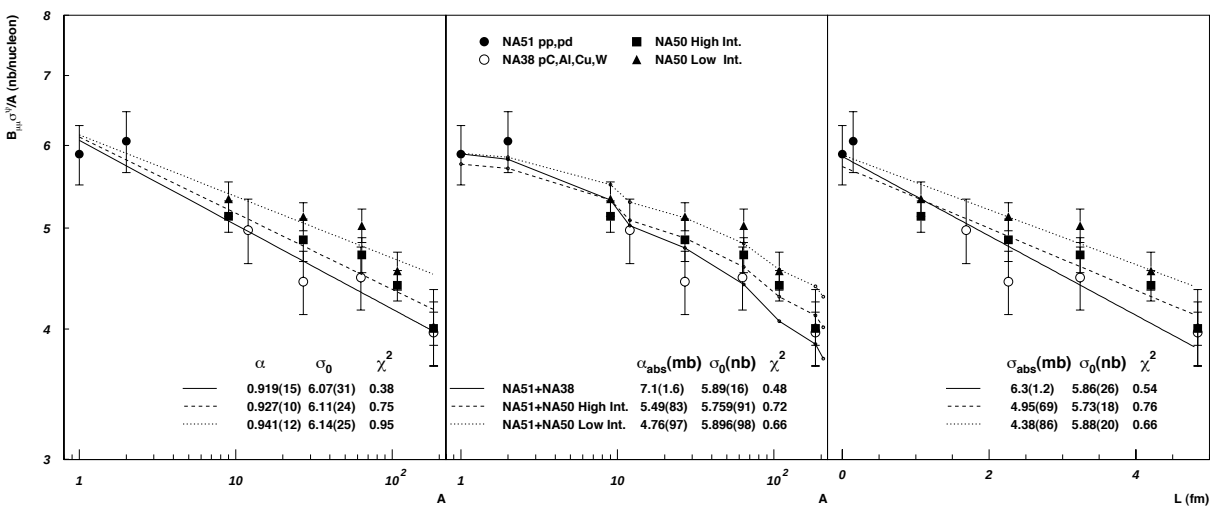

Figure 5.22: Fit of the dependence of the J/ψ cross section per nucleon on the target mass number with (Left) A^{α} parametrization; (Center) complete Glauber model calculation; (Right) $e^{-<\rho L>\sigma_{abs}}$ parametrization. Each plot compares three different combinations of data sets: NA51 measurements of *pp* and *pd* cross sections with NA38 results for *pC*, *pAl* and *pW* (solid line), NA51 with High (dashed) and Low (dotted) intensity data.

the combination of NA51 and NA38 data shows much stronger suppression parameters than the two others.

As for the Drell-Yan, the cross sections per nucleon measured by NA51 for pp and pD interactions (0.1005 ± 0.0032 and 0.0994 ± 0.0032 nb respectively, rescaled to $2.9 < M < 4.5$ GeV/c^2 range) should be multiplied by the factor 1.043 in order to account for the different rapidity domains and argon counter calibration coefficients, which gives 0.1049 ± 0.0033 and 0.1036 ± 0.0033 nb. As one can see on Fig.5.23 where they are plotted together with the cross sections calculated in this study, the values obtained from the Low intensity data set are fully compatible with the Drell-Yan cross section and independent (within the accuracy of the NA50 values) on the target mass number, while the mentioned systematic difference in the normalizaton factors of the High and Low intensity data sets makes the direct comparison of the former one with NA51 data meaningless.

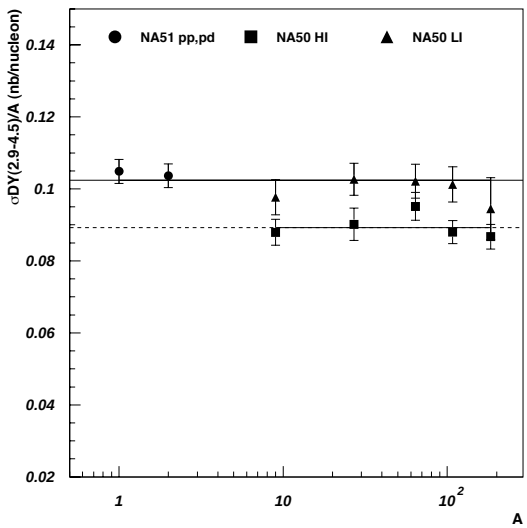

Figure 5.23: Drell-Yan cross sections per nucleon (in nb) obtained by the NA51 experiment compared with the results of the present study.

6 Conclusions and Outlook

6.1 Summary of the results

The main purpose of this work was to measure the difference in the suppression magnitude of the J/ψ and ψ' cross sections in pA collisions and to check if it depends on such longitudinal kinematic variables of the meson as the rapidity or X_F. To obtain these results the computed absolute cross sections and their ratios were fitted by the three generally accepted parametrizations:

1) $\sigma_A = \sigma_0 A^{\alpha}$

2) $\sigma_A = \sigma_0 e^{-<\rho L>\sigma_{abs}}$

3) the complete Glauber model

First of all, one should note that the two analyzed (High and Low intensity) data sets with very different statistics and systematics, despite of the giving slightly different absolute cross sections for the J/ψ and ψ' (which points to an overall normalization problem) are fully compatible in what concerns their suppression. This allows to perform a simultaneous fit of both sets, thus decreasing the final error on the obtained suppression parameters.

The essential results in Y_{CM} bins are presented in Fig.6.1 for the parametrization **(1)** and Fig.6.2 for the **(2)**. The plots on the left show the suppression parameters obtained from the fits of the absolute cross section while those on the right are from the cross sections ratios (thus having smaller errors). The large symbol in the center of each plot shows the value of the parameter obtained from the data integrated over the whole rapidity range. The values correspond to the simultaneous fit of the High and Low intensity data sets. The results for the X_F bins are very similar so they are not shown here.

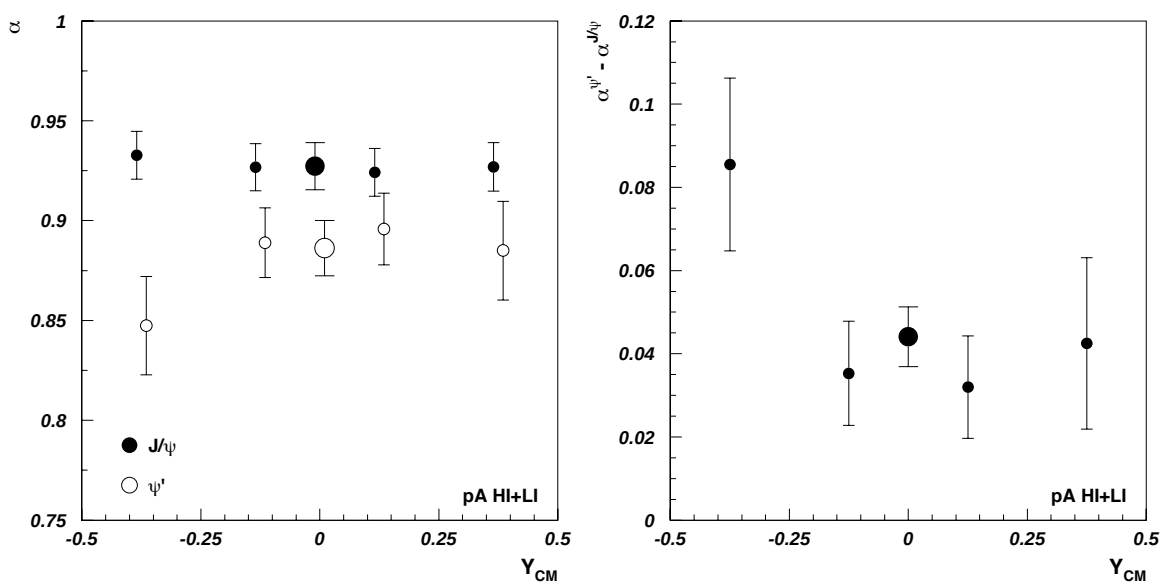

Figure 6.1: (Left) α parameters for the J/ψ and ψ' as a function of the Y_{CM} obtained from the absolute cross sections fit; (Right) Their difference obtained from the fit of the ψ' to J/ψ cross sections ratios.

The data confirms the recent finding by the E866/NuSea collaboration that in *pA* interactions the ψ' is more suppressed than the J/ψ: the averaged value of the α from the parametrization **(1)** is 0.927 ± 0.012 for the J/ψ while for the ψ' it is equal to 0.886 ± 0.014 (using the absolute cross sections) and the $\alpha^{\psi'} - \alpha^{J/\psi}$ is 0.045 ± 0.007 from the cross sections ratio fits. Similarly, the parametrization **(2)** gives for the J/ψ the absorption cross section 4.3 ± 0.7 *nb* versus 6.7 ± 0.8 *nb* for the ψ' and the fit of the cross sections ratios yields $\sigma_{abs}^{\psi'} - \sigma_{abs}^{J/\psi} = 2.6 \pm 0.4$ *nb*.

Within the errors the J/ψ suppression magnitude stays constant over the rapidity and X_F ranges accessible to the NA50 spectrometer. Concerning the ψ', although the errors on the obtained suppression parameters are too large to allow definite claims, both High and Low intensity data sets show a stronger suppression in the lowest $-0.5 < Y_{CM} < 0.5$ bin (a similar behaviour is observed for the X_F bining). The visual inspection of the J/ψ (Fig.5.3) and ψ' (Fig.5.8) distributions in rapidity or X_F supports this conclusion.

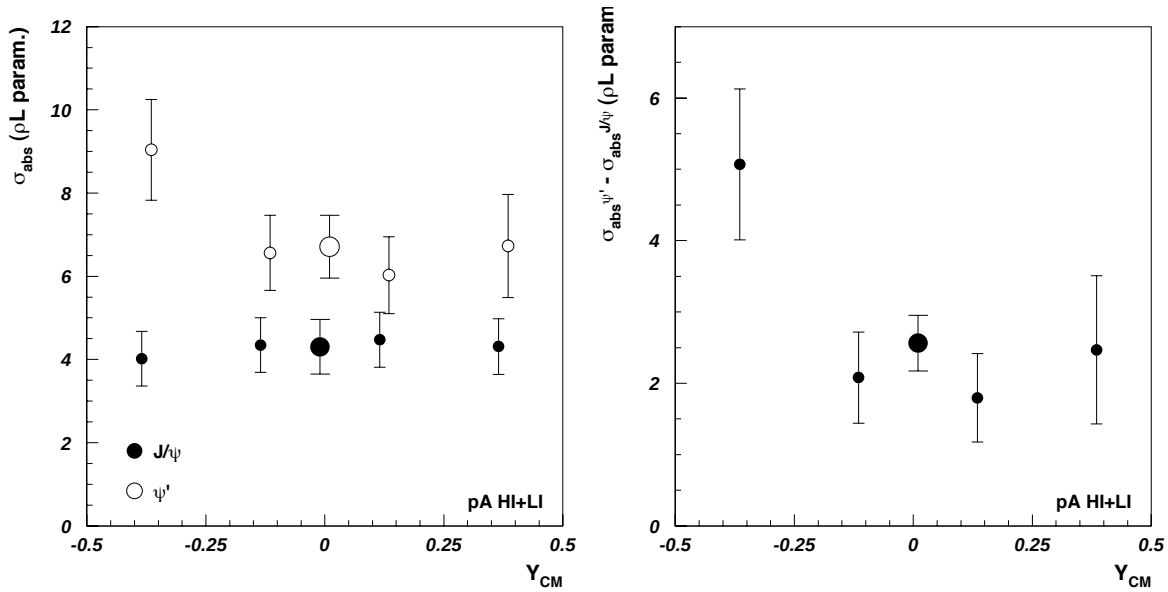

Figure 6.2: (Left) Absorption cross sections (*mb*) from $\sigma_A = \sigma_0 e^{-<\rho L>\sigma_{abs}}$ parametrization for the J/ψ and ψ' as a function of the Y_{CM} obtained from the absolute cross sections fit; (Right) Their difference obtained from the fit of the ψ' to J/ψ cross sections ratios.

In what concerns the results on the Drell-Yan cross sections, they are less conclusive. The difference in the absolute cross sections extracted from High and Low intensity data is larger for the Drell-Yan than for the J/ψ and ψ', which suggests that despite the applied efforts to adapt the NA50 reconstruction software to the High intensity data, there are still problems with the efficiency of its reconstruction. While the Low intensity data is compatible with the previous measurements by the NA51 experiment of the Drell-Yan cross section in *pp* and *pD* interactions, the values obtained from the High intensity data are $\sim 10\%$ lower. Still, the suppression parameters extracted from the ratios of the J/ψ to Drell-Yan cross sections are in agreement with the ones obtained from the absolute J/ψ cross sections from both data sets.

6.2 Future: NA60 Experiment

As it was explained in the preceding chapters, the main difficulties for the comparative study of the J/ψ and ψ' in *pA* and moreover in nucleus-nucleus collisions are

- Insufficient mass resolution of NA50. The ψ' should be separated from the tail of the J/ψ, which is not an easy task to do especially in the absence of a 100% reliable Monte-Carlo prediction.

- The strong contribution from dimuons originated outside of the target. It can be fought in two ways: **(1)** by taking special runs without the target to obtain its mass spectrum and account for it during the normal data fit; **(2)** by applying cuts like the **PDTARG** which tries to eliminate the muons not converging to the target. NA50 uses both of these methods, but unfortunately, none of them ensures complete solution of the problem. The **target out** runs require considerable amount of time to collect enough statistics, still the mass spectrum obtained from them is not fully adequate to the spectrum of the non-target dimuons of the normal runs. The difference comes from the interactions of the secondaries produced on the target with the hadron absorber (a contribution which is absent in the **target out** runs). The **PDTARG** cut strongly reduces the contamination of the mass spectrum by the non-target dimuons, but they are not eliminated entirely and the price to pay for this cut is a loss of statistics and a possible bias of the signal spectrum due to its dependence on the muons kinematics.

These problems will be solved to large extent in the recently approved NA60 experiment [84] - successor of NA50. Without trying to cover all the topics to be investigated by this new experiment, a short presentation will be given, with emphasis on its advantages in the study of the J/ψ and ψ' compared to NA50.

The layout of the proposed experiment is presented on the Fig.6.3. Its main difference with respect to NA50 consists of the compact vertex spectrometer placed between the target and the hadron absorber. It consists of 10 planes of silicon pixel detectors placed inside a dipole magnet. Its purpose is the measurement of the trajectories and momenta of the charged particles before they enter the hadron absorber. The vertical field has an average intensity of 2.5 T over 30 cm along the beam axis (in contrary to 1.6T mentioned in the proposal, another magnet will be used). The pixel detectors are based on the Alice1 pixel readout chip, developed in the framework of the ALICE and LHC-B experiments. Each chip is a matrix of 256×32 pixels with binary readout. The cell size is $50 \times 425\ \mu m^2$ [85]. The total number of chips is 88, corresponding to 721 000 channels. The pixel chips are glued on 300 micron thick ceramic supports, which also provide the readout and control bus lines to which the chips are connected by ultrasonic wire-bonding. The multi-layer ceramic bus is mounted on a common support together with a flexible kapton cable, which ends in a standard connector. The electrical connection between the ceramic and the kapton is also achieved by wire-bonding. Since the measurements are very demanding, a specially designed system will ensure correct installation, calibration and monitoring of the positions of the pixels.

The measurement of the muon trajectories before they enter in the absorber, almost completely eliminates the contribution from the multiple scattering in the reconstructed dimuon mass, improving its resolution to $\sim 70\ MeV/c^2$ at the mass of J/ψ (to be compared with $\sim 120 Mev/c^2$ of the present setup).

The setup will also be equipped by the Beamscope detector, two stations of silicon microstrip detectors placed upstream of the target, each composed of an X and a Y plane. The detectors are centered on the beam axis and are operated at $130K$ to take advantage of the Lazarus effect [86]. The microstrip detectors measure the transverse coordinates of each incoming particle, providing a strict constraint in the determination of the interaction point, relative to which the offset of the muon tracks will be determined.

The Beamscope, together with the new target system, consisting of 5-7 sub-targets, each 1.5 mm thick and with 0.5 mm radius, will be placed into a vacuum vessel, which eliminates the triggers from interactions with air nearby of the target (especially important for the heavy ion runs). The precise measurement of the interaction vertex position together with the excellent angular and coordinate resolution of the vertex spectrometer (the muon trajectories are extrapolated to the target with precision of $\sim 40\mu m$) is expected to solve definitively the problem of the dimuons originated outside of the target.

These features of NA60 should allow to perform a very clean measurement of the J/ψ and ψ' production both with proton and ion beams.

One should note that in the case of the pA runs it will be possible to measure the ψ' not only by its direct dimuon channel, but also via the $\psi' \to J/\psi + \pi^+\pi^-$ decay, triggering the J/ψ in the dimuon spectrometer and detecting the $\pi^+\pi^-$ pair in the vertex spectrometer. This should provide additional independent check for the systematics of the ψ' measurement.

Additionally, for the pA runs, a 1 mm Pb plate will be inserted between the target system and the vertex spectrometer. Its aim is to convert the photons from $\chi_c \to J/\psi + \gamma$ decays. Together with the measurement of the ψ' this will provide information about the contribution of the heavier charmonia states to the measured J/ψ cross section.

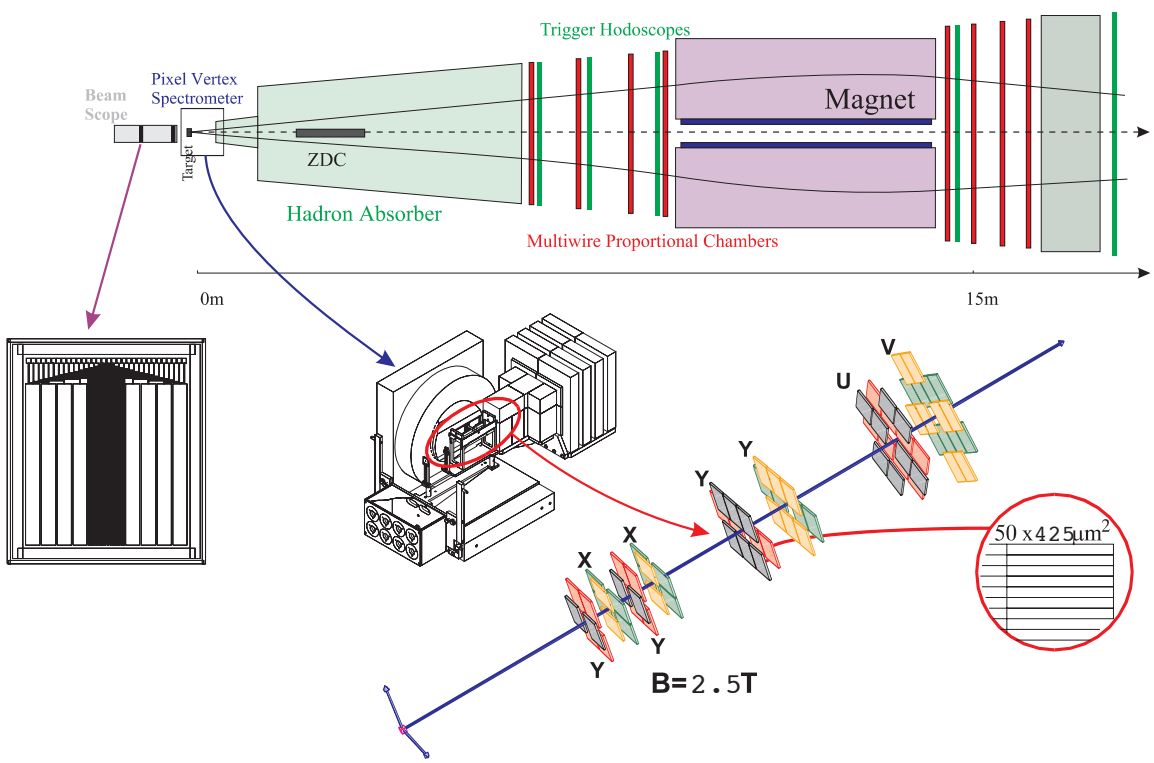

Figure 6.3: Layout of the NA60 experiment.

References

Chapter 1

[1] J. Cleymans et al. Phys.Rep. **130** (1986) 217.
[2] S. Gotllieb et al. Phys.Rev. **D35** (1987) 3972.
[3] R. Hagedorn, Suppl.Nuovo Cimento **3** (1965) 147.
[4] R. Hagedorn, proceedings of Quark Matter 84, Helsinki 1984, Springer-Verlag.
[5] Phys.Rev.Lett. **67** (1991) 302. K. Born et al.
[6] http://www.cern.ch/CERN/Announcements/2000/NewStateMatter/science.html
[7] L.van Hove, Phys.Lett. **B118** (1982) 138.
[8] L.van Hove, Z.Phys. **C21** (1983) 93.
[9] J.D. Bjorken, Phys.Rev. **D27** (1983) 140.
[10] J. Rafelski, B. Müller, Phys.Rev.Lett. **48** (1982) 1066; Erratum: *ibid*. **56** (1986) 2334.
[11] G.E. Brown and M. Rho, Phys.Rev.Lett. **6**6 (1991) 2720.
[12] F. Karsch, K. Redlich and L. Turko, Z. Phys. **C60** (1995) 519.
[13] G. Agakichev *et al*. (NA45/Ceres Collaboration), Phys.Rev.Lett. **75** (1995) 1272.; Phys.Lett. **B422** (1998) 405.
[14] G.Q. Li, C.M. Ko and G.E. Brown, Nucl.Phys. **A606** (1996) 568.
[15] G.Q. Li, C.M. Ko, G.E. Brown and H. Sorge, Nucl.Phys. **A611** (1996) 539.
[16] E.L. Bratkovskaya and W. Cassing, Nucl.Phys. **A619** (1997) 413.
[17] R.Rapp and J.Wambach, Eur.Phys.J. **A6** (1999) 415.
[18] J.D. Bjorken, Acta Phys.Polon. **B23** (1992) 637.
[19] J. Kapusta, P. Lichard , D. Seibert, Phys. Rev. **D44** (1991) 2774; Erratum: *ibid*. **D47** (1993) 4171.
[20] R. Rapp and E. Shuryak, Phys.Lett. **B473** (2000) 13.
[21] M.C. Abreu *et al*. (NA38/50 Collaboration), Euro.Phys.J **C13** (2000) 69.
[22] T.Matsui and H.Satz, Phys. Lett. **B178** (1986) 416.
[23] A.D.Martin et *et al*. Phys.Lett.**B306** (1993) 145.
[24] H.Plothow-Besch, Comp. Phys. Comm. **75** (1993) 396.
[25] S. Gavin *et al*., Int. J. Mod. Phys. **A10** (1995) 2961.
[26] R.Vogt, Phys.Rev. **C61** (2000) 035203.
[27] D.M. Alde *et al*. (E772 Collaboration), Phys. Rev. Lett. **64** (1990) 2479.
[28] K.J. Eskola, V.J. Kolhinen and P.V. Ruuskanen, Nucl.Phys. **B535** (1998) 351; K.J. Eskola, V.J. Kolhinen and C.A. Salgado, hep-ph/9807297.
[29] A.D. Martin *et al*., Eur. Phys. J. **C4** (1998) 463.
[30] J.W. Cronin *et al*, Phys.Rev. **D11** (1975) 3105.
[31] D. Antreasyan, *et al*, Phys. Rev. **D 19** (1979) 764. P.B. Straub, *et al*, Phys. Rev. Lett. **68** (1992) 452.
[32] P. Bordalo, *et al*, (NA10 Collaboration), Phys. Lett. **B193** (1987) 373.
[33] M.A. Vasiliev *et al*, (E866 Collaboration), Phys. Rev. Lett. **83** (1999) 2304.
[34] J.C. Collins, D.E. Soper and G. Sterman, in *Perturbative Quantum Chromodynamics*, ed. A.H. Mueller (World Scientific, Singapore, 1989), 1.

[35] V. Barger, W.Y. Keung, and R.N. Philips, Z. Phys. **C6** (1980) 169; Phys. Lett. **91B** (1980) 253.
[36] P.Braun-Munzinger, D.Miśkowiec, A.Drees and C. Lourenço, Eur. Phys. J., **C1** (1998) 123
[37] G.A. Schuler and R. Vogt, Phys.Lett. **B387** (1996) 181.
[38] S. Frixione *et al.*, CERN-TH/97-16 (hep-ph/9702287), (Heavy Flavours II, ed. by A.J. Buras and M. Lindner, World Sci., Singapore, (1998) 609).
[39] M. Aguilar-Benitez *et al.* (NA16 Collaboration), Phys. Lett. **B135** (1984) 237.
[40] M. Aguilar-Benitez *et al.* (NA27 Collaboration), Z. Phys. **C31** (1986) 491; Z. Phys. **C40** (1988) 321.
[41] R. Ammar *et al.* (E743 Collaboration), Phys. Rev. Lett. **61** (1988) 2185.
[42] K. Kodama *et al.* (E653 Collaboration), Phys. Lett. **B263** (1991) 573; Phys. Lett. **B284** (1992) 461.
[43] M.J. Leitch *et al.* (E789 Collaboration), Phys. Rev. Lett. **72** (1994) 2542.
[44] G.A. Alves *et al.* (E769 Collaboration), Phys. Rev. Lett. **77** (1996) 2388.
[45] S. Barlag *et al.* (NA32 Collaboration), Z. Phys. **C39** (1988) 451; Z. Phys. **C49** (1991) 555.
[46] M. Adamovich *et al.* (WA92 Collaboration), CERN-PPE/96-180.
[47] L. Apanasevich *et al.* (E706 Collaboration), Fermilab-Pub-97/030-E.
[48] Z. Lin and X.N. Wang, Phys. Lett. **B444** (1998) 245.
[49] L. Capelli *et al.* (NA50 Collaboration), Workshop on Charm Production in Nucleus-Nucleus Collisions, CERN, Dec. 1999; http://www.cern.ch/HIPS/charm/dec99/na50/
[50] L. Capelli, proceedings of Quark Matter 2001, to be published.
[51] E.L. Berger and D. Jones, Phys.Rev. **D23** (1981) 1521.
[52] R. Baier and R. Rückl, Z. Phys. **C19** (1983) 251.
[53] G.A.Schuler, hep-ph/9403387, 1994.
[54] F. Abe *et al.* (CDF Collaboration), Phys. Rev. Lett. **71** (1993) 3421.
[55] G.T. Bodwin, E. Braaten and G.P. Lepage, Phys. Rev. **D51** (1995) 1125.
[56] R.D.Pisarski and O.Alvarez, Phys.Rev. **D26** (1982) 3735.
[57] F.Takagi, Phys.Rev. **D34** (1986) 1646.
[58] D.Gross, R.D.Pisraski and L.G.Yaffe, Rev.Mod.Phys **53** (1981) 43.
[59] A.Yukawa, Nucl.Phys. **A498** (1989) 227c.
[60] F.Karsch and H.Satz, Z.Phys. **C51** (1991) 209.
[61] A.Bussière *et al.* (NA38 Collaboration), Proc. of QM'87, Nordkirchen, Germany, 1987; Z.Phys. **C38** (1988) 117.
[62] C. Baglin *et al.* (NA38 Collaboration), Phys. Lett. **B220** (1989) 471.
[63] C. Lourenço, Proceedings of Quark Matter 96, Nucl.Phys. **A610** (1996) 552.
[64] D.Kharzeev, C.Lourenço, M.Nardi and H.Satz, Z.Phys. **C74** (1997) 307.
[65] L. Ramello for the NA50 Collaboration, Proceedings of Qurk Matter 97, Nucl.Phis. **A638** (1998) 261.
[66] M.C.Abreu *et al.* (NA50 Collaboration), Phys.Lett **B466** (1999) 408.
[67] C.Gerschel and J.Hüfner, Phys.Lett. **B207** (1988) 253.
[68] C.Gerschel and J.Hüfner, Z.Phys. **C56** (1992) 171.
[69] J.-P.Blaisot and J.-Y.Ollitraut, Phys.Rev.Lett. **77** (1996) 1703.
[70] M.C.Abreu *et al.* (NA50 Collaboration), Phys.Lett **B410** (1997) 37.
[71] M.C.Abreu *et al.* (NA50 Collaboration), Phys.Lett **B477** (2000) 28.
[72] M.J.Leitch *et al.* (E866/NuSea Collaboration), Phys.Rev.Lett. **84** (2000) 3256.

[73] L. Gerland *et al.*, Nucl.Phys. **A663-664** (2000) 1019.
[74] Y.B. He, J. Hüfner and B.Z. Kopeliovich, Phys.Lett. **B477** (2000) 93.
[75] F. Arleo *et al.*, Phys. Rev. **C61** (2000) 054906
[76] R.J.Glauber, in Lectures in Theoretical Physisc, edited by W.E.Brittin and L.G.Dunham (Interscience, NY, 1959), **Vol.1**, p.315.
[77] H.De Vries, C.W.De Jager and C.De Vries, Atomic Data and Nuclear Data Tables **36** (1987) 495.
[78] B. Andersson, G. Gustafson and B. Nielsson-Almquist, Nucl.Phys. **B281** (1987) 289; B. Nielsson-Almquist and E. Stenlund, Comp.Phys.Comm., **43** (1987) 387.

Chapter 2

[79] L. Anderson *et al.* (NA10 Collaboration), Nucl.Inst.Meth. **223** (1984) 26.

Chapter 4

[80] L.Fredj, Thése de l'université Blaise Pascal, Clermont-Ferrand, 1991.
[81] T. Sjöstrand, Comp. Phys. Comm. **82** (1994) 74.

Chapter 5

[82] M.C.Abreu *et al.* (NA51 Collaboration), Phys.Lett **B438** (1998) 35.
[83] M.C.Abreu *et al.* (NA38 Collaboration), Phys.Lett **B444** (1998) 516.

Chapter 6

[84] NA60 proposal, SPSC/P 316, http://na6i.web.cern.ch/NA6i/proposal/index.html.
[85] ALICE Collaboration, CERN/LHCC 99-12, ALICE TDR 4, 18 June 1999.
[86] V.G.Palmieri et al., Nucl.Instrum.Meth. **A413** (1998) 475.

7 Appendix

7.1 Acceptance values for different processes

The Tables 7.1 and 7.2 give the acceptances in % for the J/ψ, ψ' and Drell-Yan dimuons in the $2.9 < M < 4.5\ GeV/c^2$ range in the different rapidity and X_F bins. The acceptances are calculated in the kinematical domain $-0.50 < Y_{CM} < 0.50$ and $|\cos(\theta)| < 0.5$. The numbers are given only for the *pAg* setup, the differences between the various setups are smaller than the quoted errors.

	-0.50< Y <0.50	-0.50< Y <-0.25	-0.25< Y < 0.0	0.0< Y < 0.25	0.25< Y < 0.5
J/ψ	14.69±0.02	7.41±0.03	20.36±0.06	21.54±0.06	8.01±0.04
ψ'	17.29±0.03	9.75±0.04	24.16±0.07	24.45±0.07	9.17±0.04
Drell-Yan	14.87±0.06	8.28±0.09	21.19±0.14	21.63±0.14	7.71±0.08

Table 7.1: The acceptances (in %) for the J/ψ, ψ' and Drell-Yan dimuons in the $2.9 < M < 4.5\ GeV/c^2$ range in different rapidity bins.

	-0.10< X_F <0.10	-0.10< Y <-0.05	-0.05< Y <0.0	0.0< Y <0.05	0.05< Y <0.1
J/ψ	16.73±0.03	10.60±0.05	21.10±0.06	22.28±0.06	11.64±0.05
ψ'	21.36±0.04	16.46±0.07	25.65±0.08	25.96±0.08	16.52±0.07
Drell-Yan	17.86±0.07	13.24±0.13	21.91±0.16	22.62±0.16	13.05±0.12

Table 7.2: The acceptances (in %) for the J/ψ, ψ' and Drell-Yan dimuons in $2.9 < M < 4.5\ GeV/c^2$ range in different X_F bins.

7.2 The Fitted Data Samples

In this section the plots with various fits are presented.

Fits of the mass spectra:

For each histogram the total numbers of the fitted opposite sign events, obtained χ^2/NDF of the fit, number of the J/ψ dimuons, ratio of the ψ' to the J/ψ and of the J/ψ to the Drell-Yan events is printed (not corrected for the acceptances). The errors shown in the parenthesis are for the corresponding last digits.

The data samples are:

- Fig.7.1: all sets of the High and Low intensity data fitted in the whole $-0.5 < Y_{CM} < 0.5$ range.
- Fig.7.2: all sets fitted in the $-0.5 < Y_{CM} < -0.25$ range.

- Fig.7.3: all sets fitted in the $-0.25 < Y_{CM} < 0.0$ range.
- Fig.7.4: all sets fitted in the $0.0 < Y_{CM} < 0.25$ range.
- Fig.7.5: all sets fitted in the $0.25 < Y_{CM} < 0.5$ range.
- Fig.7.6: all sets of the High and Low intensity data fitted in the whole $-0.1 < X_F < 0.1$ range.
- Fig.7.7: all sets fitted in the $-0.1 < X_F < -0.05$ range.
- Fig.7.8: all sets fitted in the $-0.05 < X_F < 0.0$ range.
- Fig.7.9: all sets fitted in the $0.0 < X_F < 0.05$ range.
- Fig.7.10: all sets fitted in the $0.05 < X_F < 0.1$ range.

Plots of the J/ψ cross sections fitted by three different suppression parametrizations: $\sigma_A = \sigma_0 A^{\alpha}$, Glauber model and $\sigma_A = \sigma_0 e^{-<\rho L>\sigma_{abs}}$

- Fig.7.11: in four Y_{CM} bins.
- Fig.7.12: in four X_F bins.

Plots of the ψ' cross sections fitted by three different suppression parametrizations:

- Fig.7.13: in four Y_{CM} bins.
- Fig.7.14: in four X_F bins.

Plots of the ratio of the ψ' cross section to the one of the J/ψ fitted by the two different suppression parametrizations:
$\sigma_{\psi'}/\sigma_{J/\psi} = R_0 A^{\alpha_{\psi'} - \alpha_{J/\psi}}$ and $\sigma_{\psi'}/\sigma_{J/\psi} = R_0 e^{-<\rho L>(\sigma_{abs}^{\psi'} - \sigma_{abs}^{J/\psi})}$

- Fig.7.15: in four Y_{CM} bins.
- Fig.7.16: in four X_F bins.

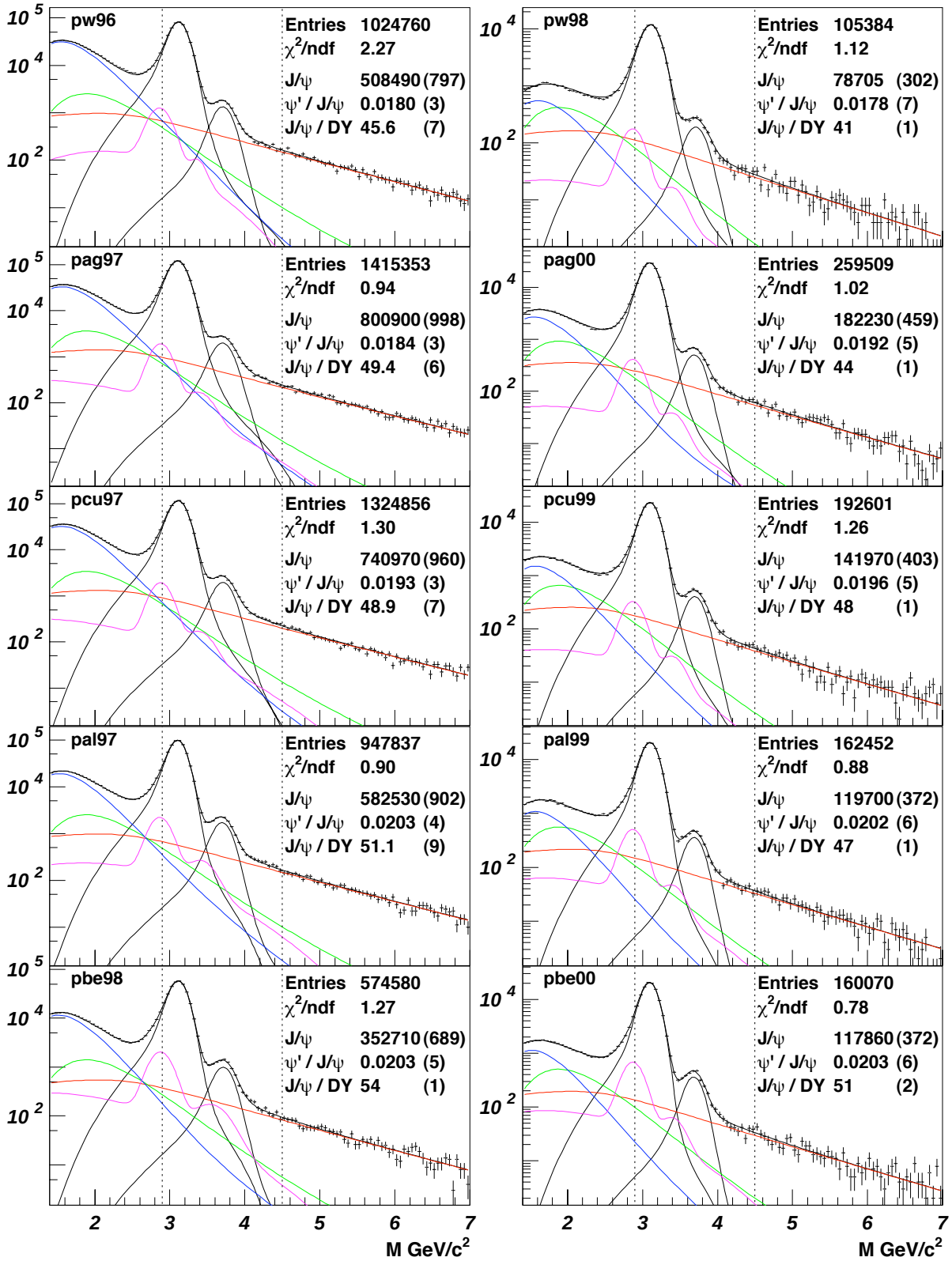

Figure 7.1: Fit for all data sets in the $-0.5 < Y_{CM} < 0.5$ range. For each histogram the total numbers of the fitted opposite sign events, obtained χ^2/NDF of the fit, number of the J/ψ dimuons, ratio of the ψ' to the J/ψ and of the J/ψ to the Drell-Yan events in the $2.9 < M < 4.5\ GeV/c^2$ range (shown by the dotted lines) is printed (not corrected for the acceptance). The errors shown in the parenthesis are for the corresponding last digits.

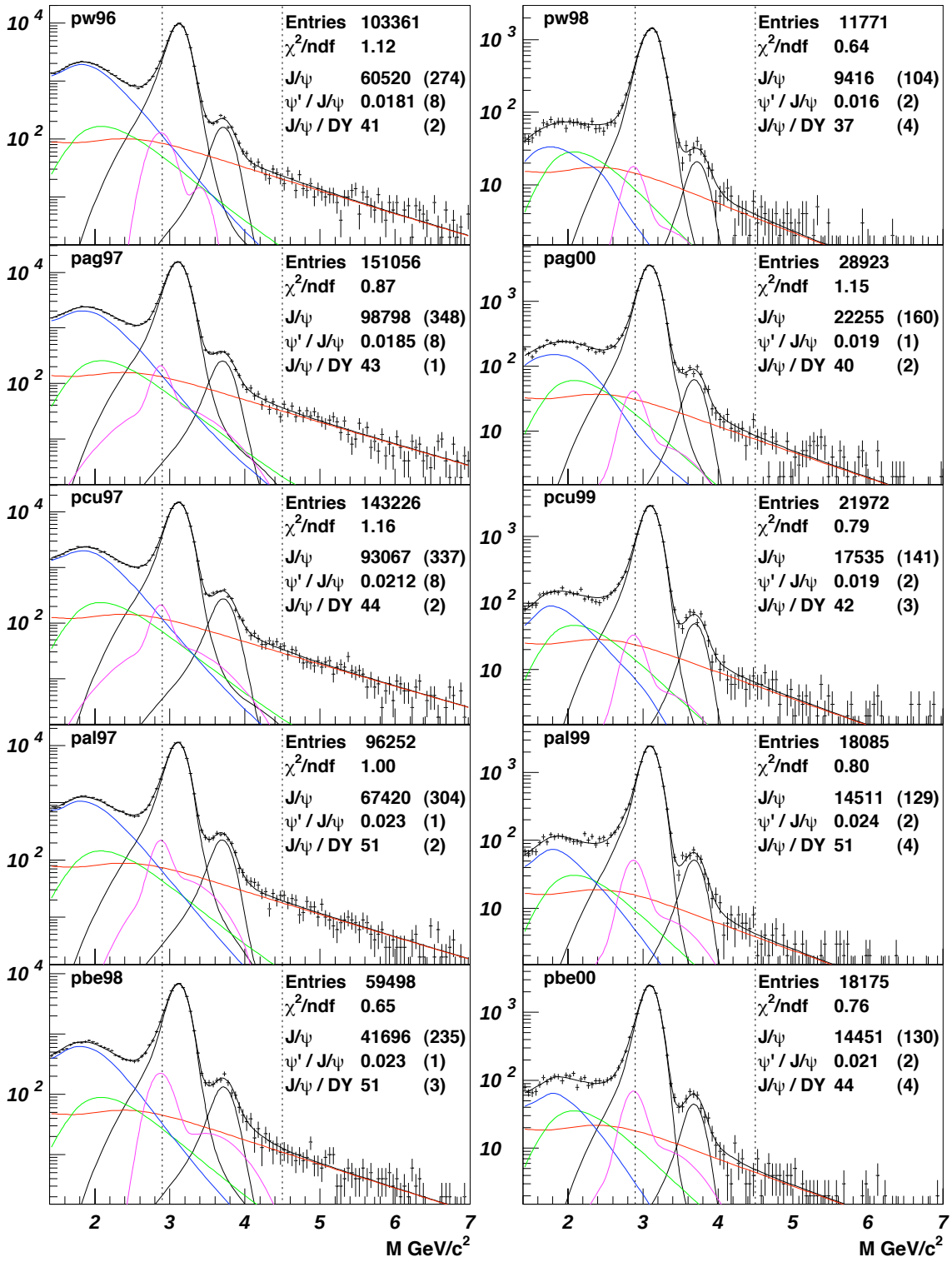

Figure 7.2: Fit for all data sets in the $-0.5 < Y_{CM} < -0.25$ range.

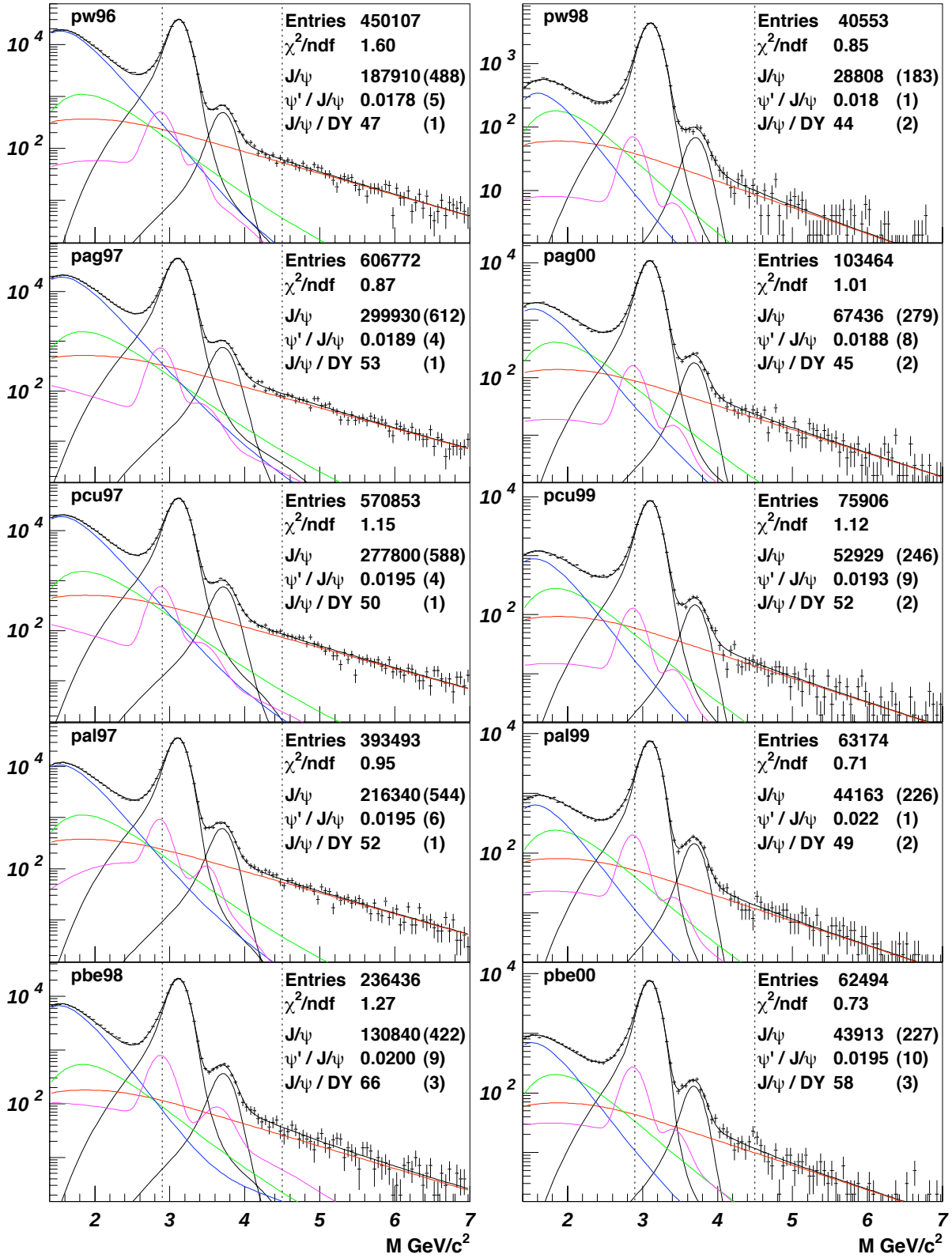

Figure 7.3: Fits for all data sets in the $-0.25 < Y_{CM} < 0.0$ range.

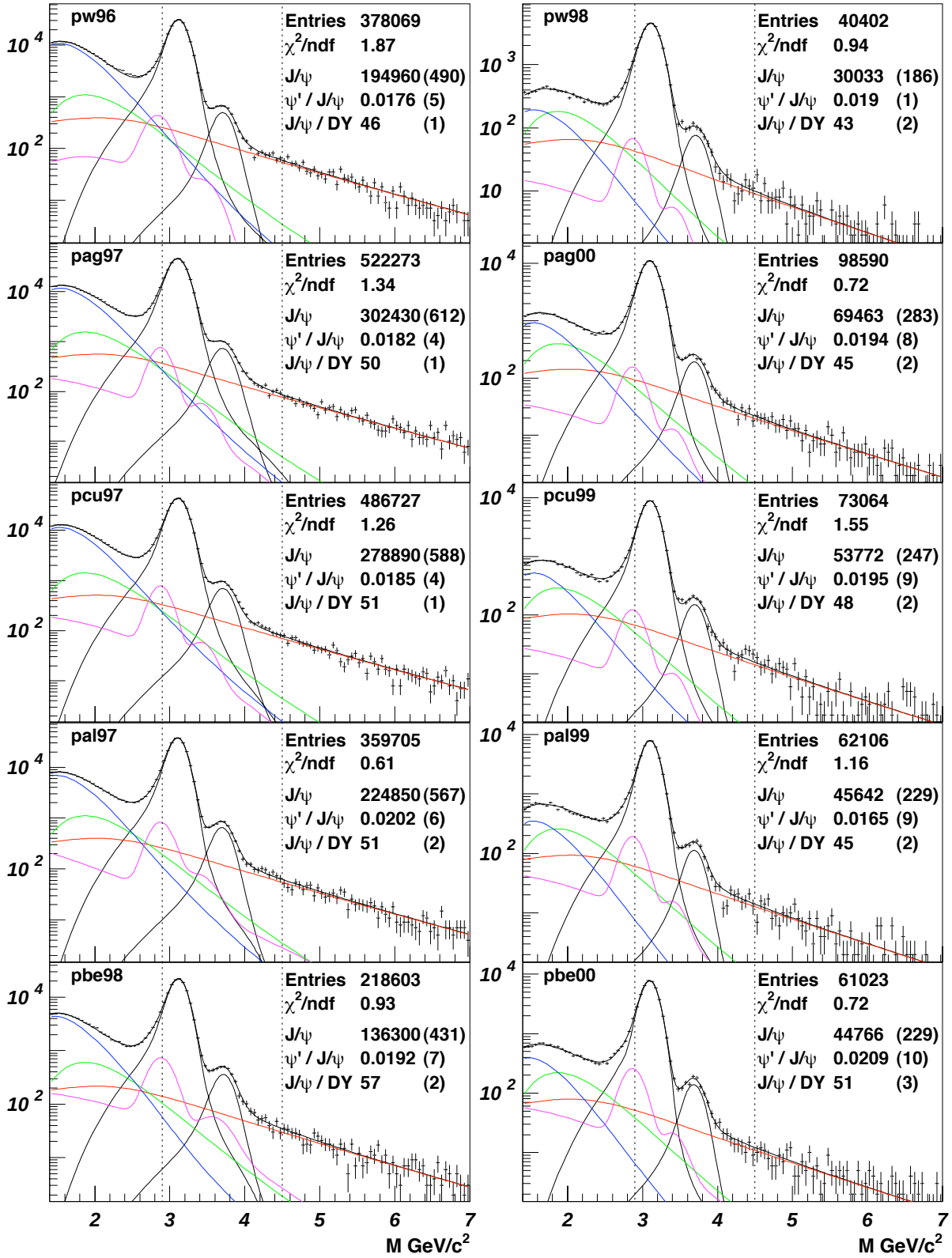

Figure 7.4: Fits for all data sets in the $0.0 < Y_{CM} < 0.25$ range.

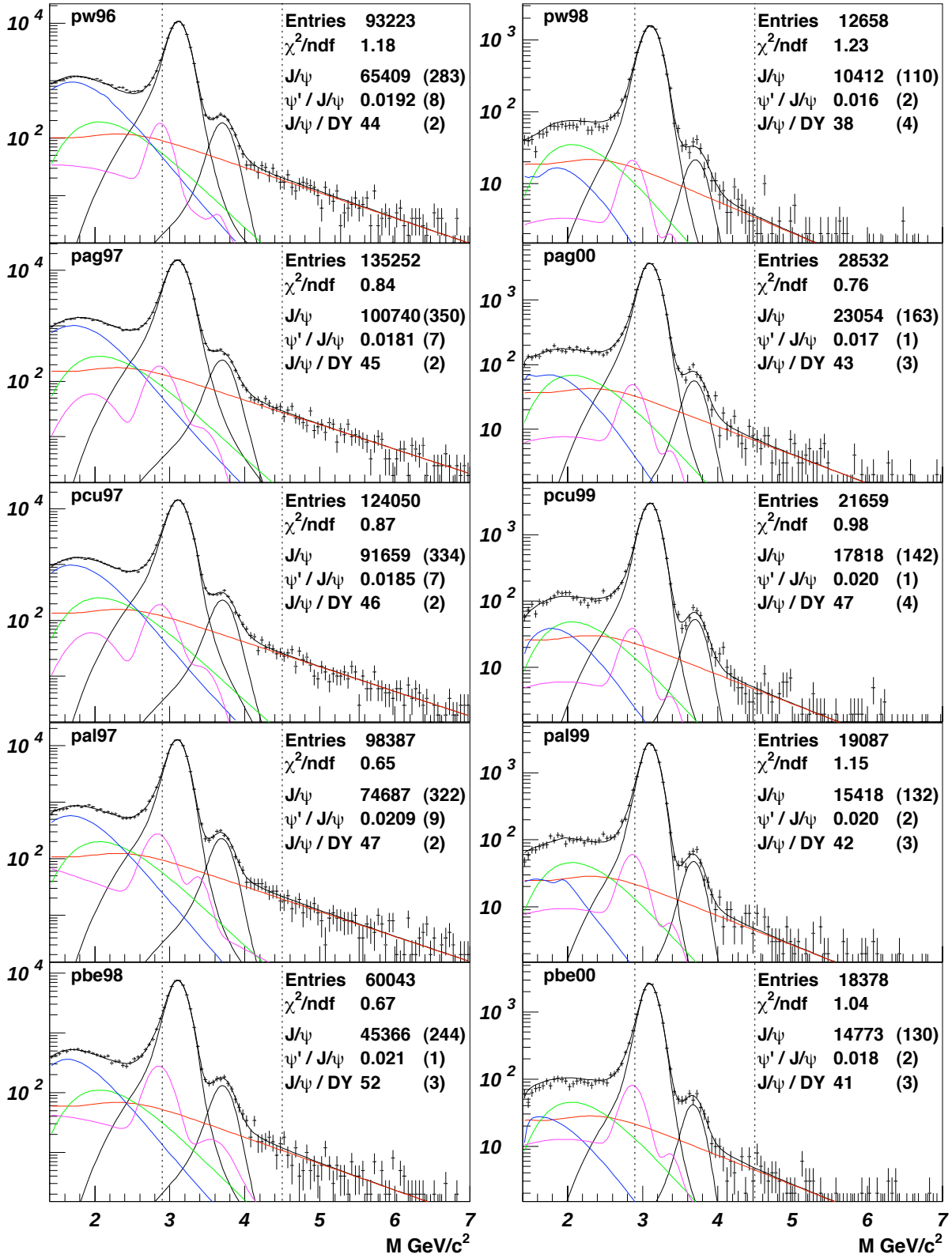

Figure 7.5: Fits for all data sets in the $0.0 < Y_{CM} < 0.5$ range.

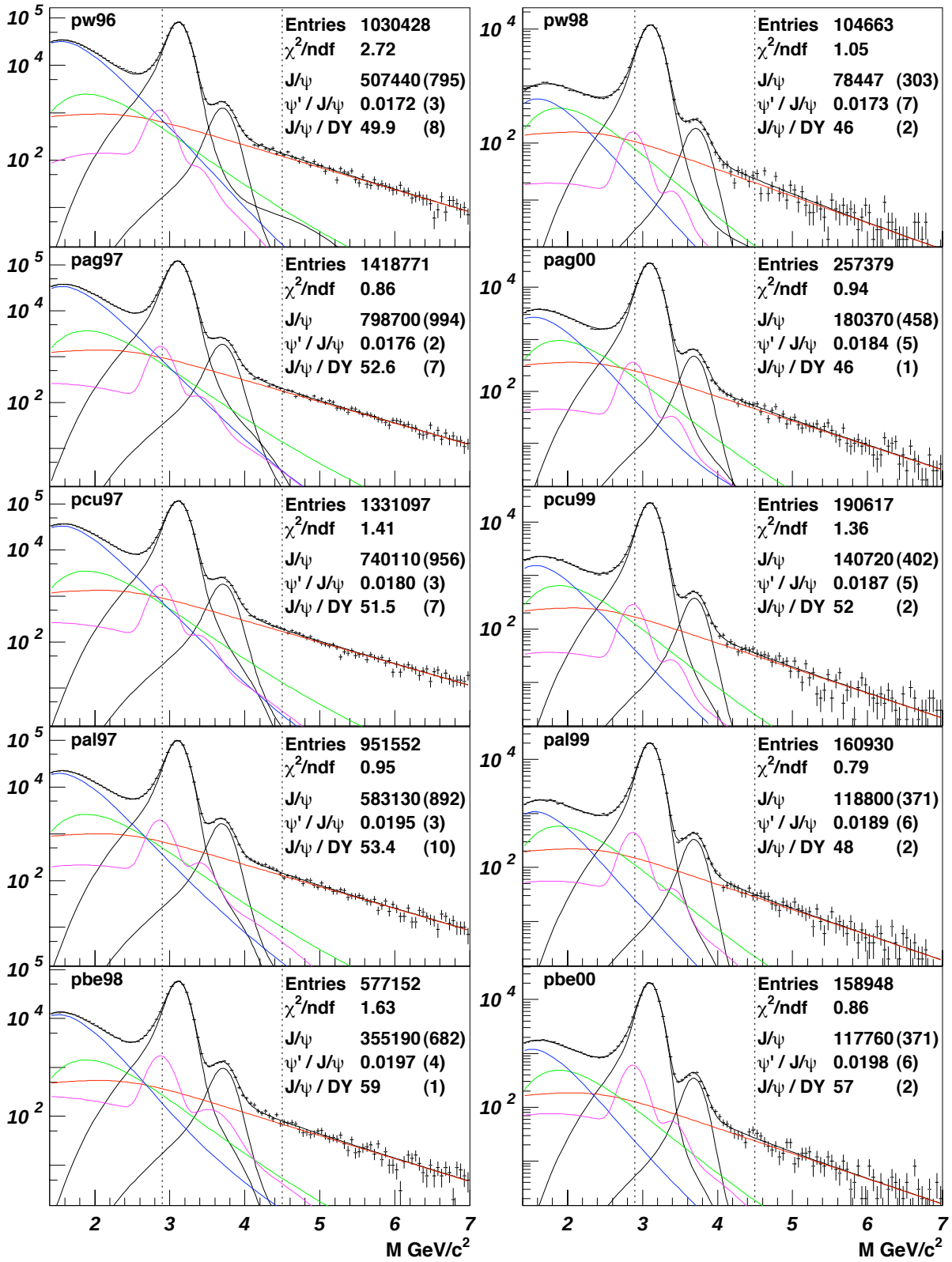

Figure 7.6: Fits for all data sets in the $-0.1 < X_F < 0.1$ range.

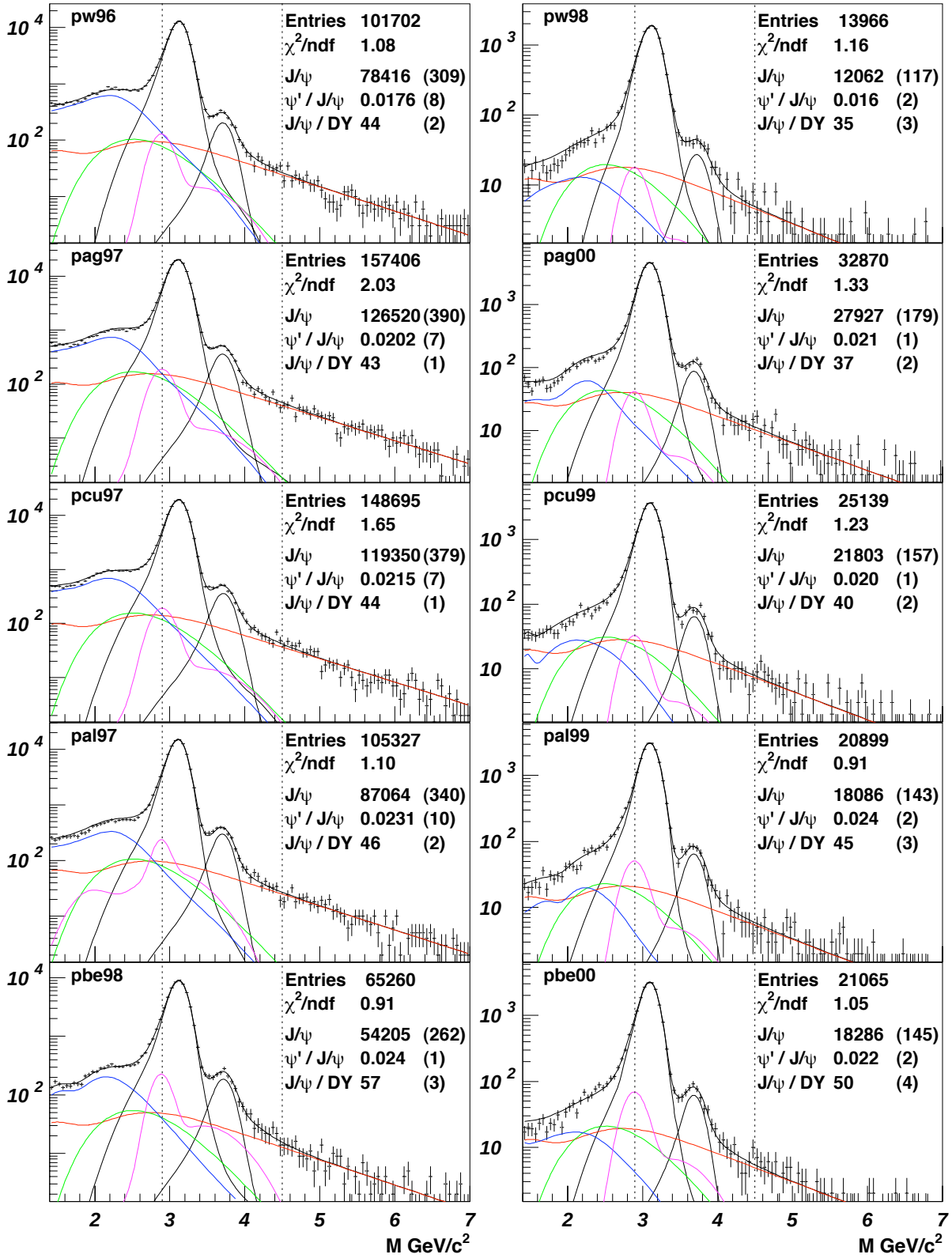

Figure 7.7: Fits for all data sets in the $-0.1 < X_F < -0.05$ range.

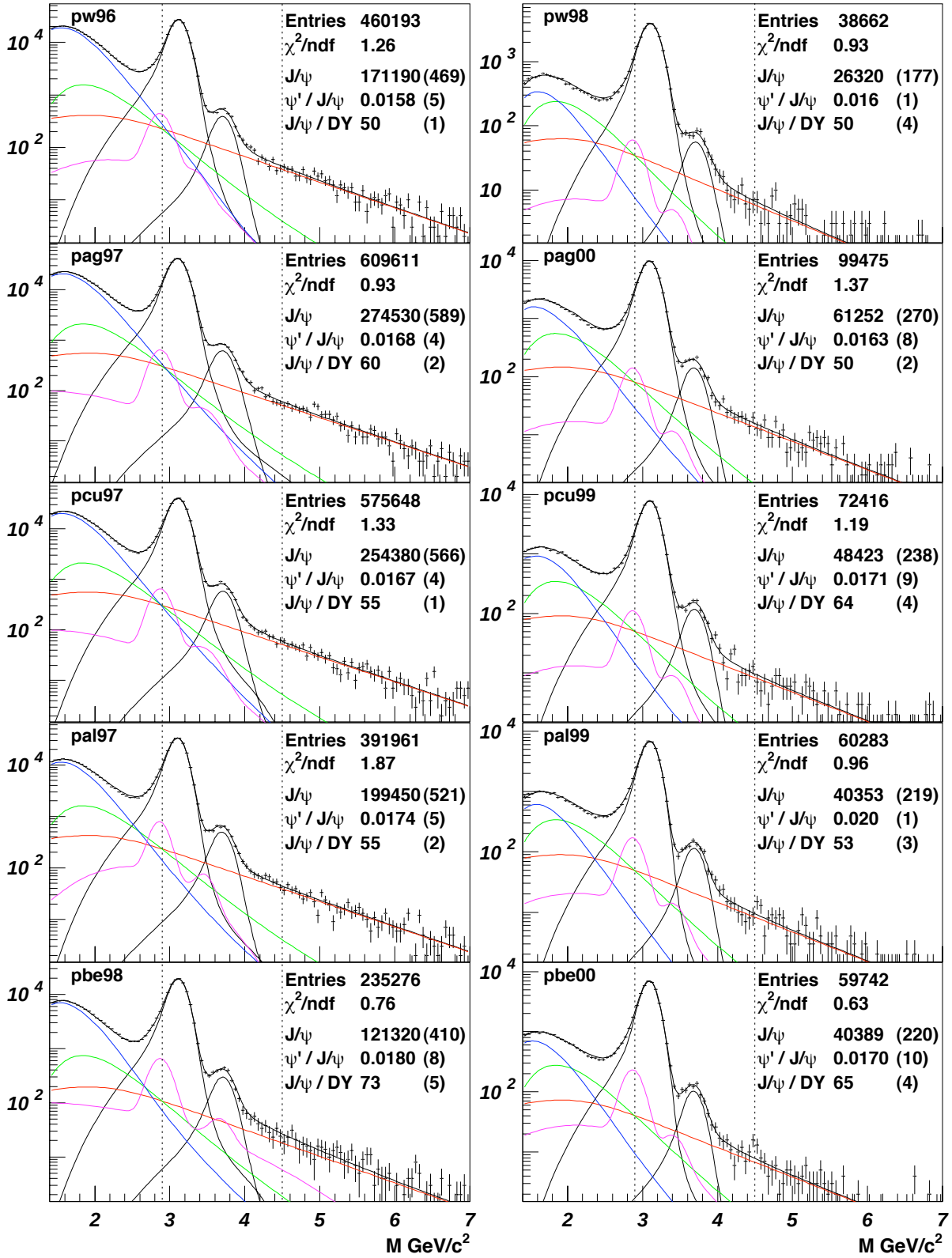

Figure 7.8: Fits for all data sets in the $-0.05 < X_F < 0.0$ range.

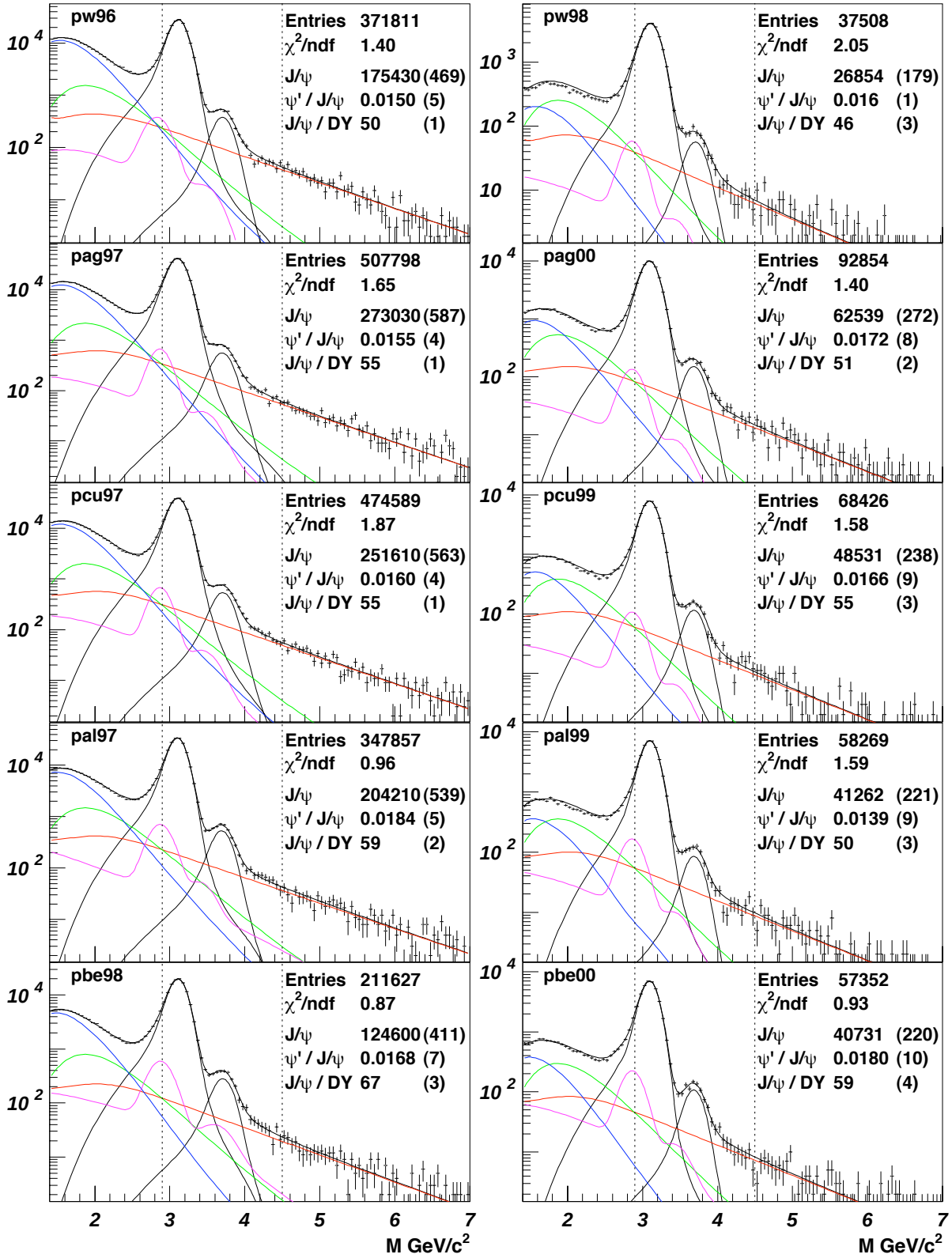

Figure 7.9: Fits for all data sets in the $0.0 < X_F < 0.05$ range.

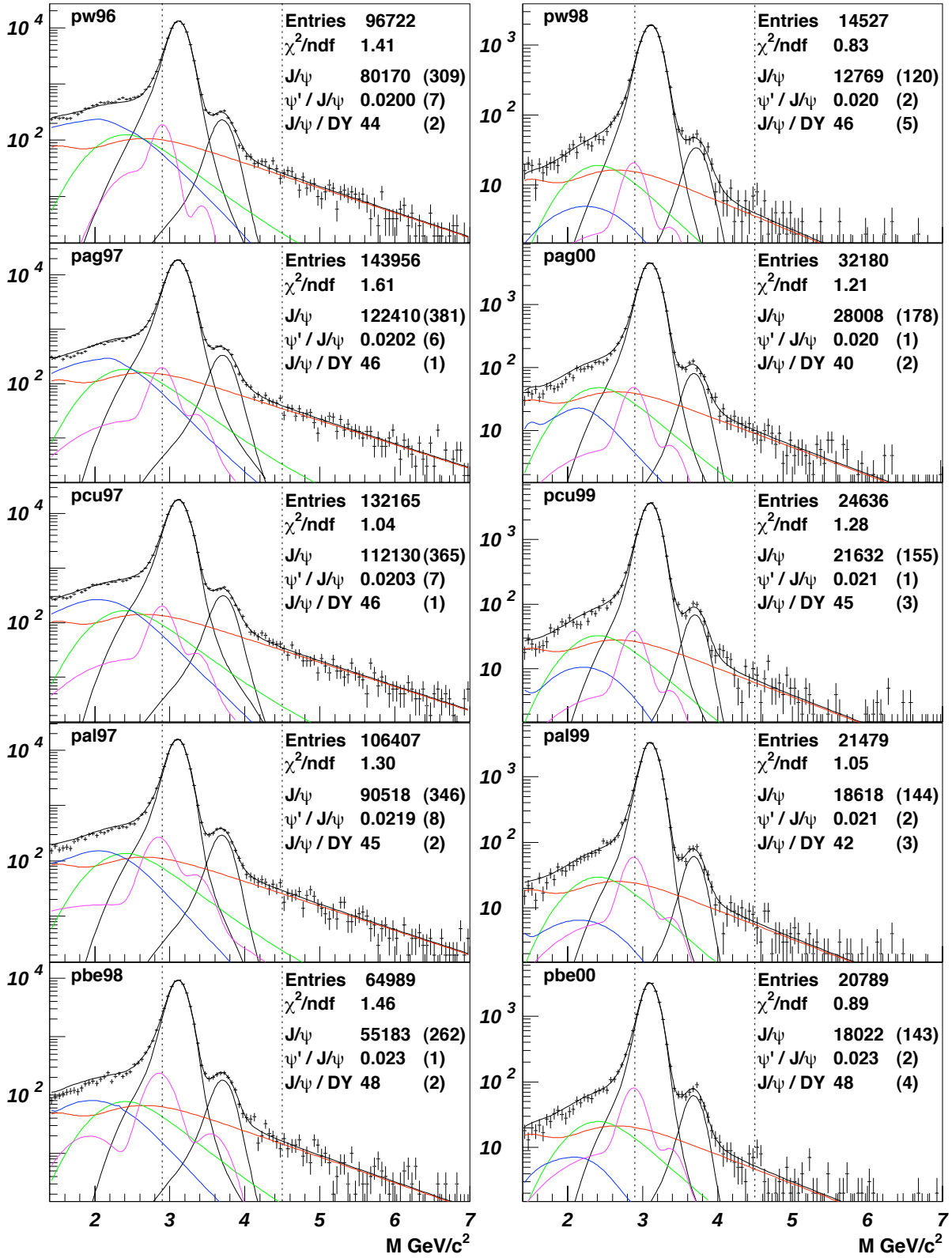

Figure 7.10: Fits for all data sets in the $0.05 < X_F < 0.1$ range.

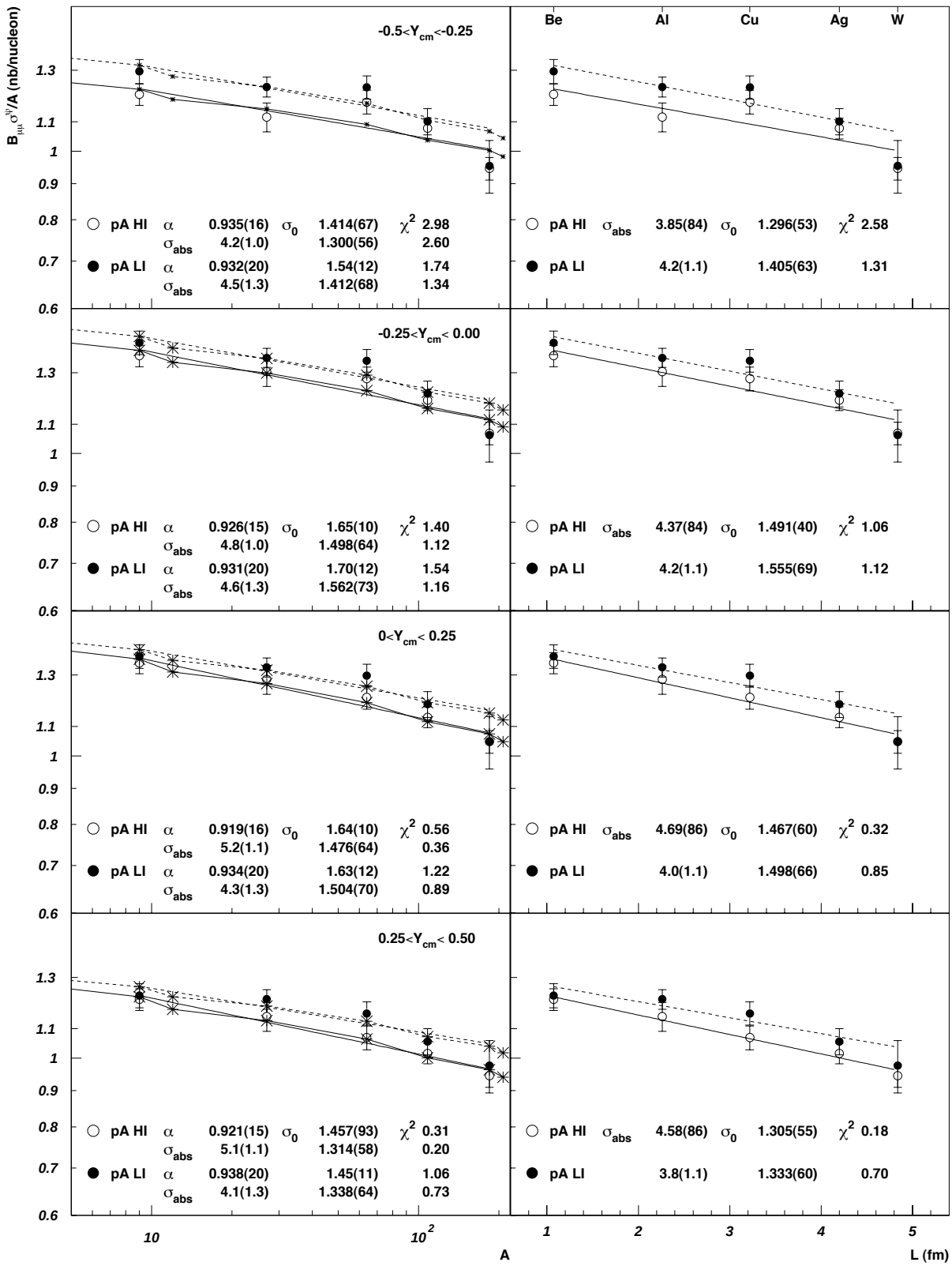

Figure 7.11: The J/ψ cross sections per nucleon (for the High (HI) and Low (LI) intensity data sets) in four Y_{CM} bins fitted by the: (Left) parametrization $\sigma_A = \sigma_0 A^{\alpha}$ (the results are shown on the first line of the legend) and the complete Glauber model (second line); (Right) parametrization $\sigma_A = \sigma_0 e^{-<\rho L>\sigma_{abs}}$. The values for the σ_0 and σ_{abs} are in *nb* and *mb* respectively.

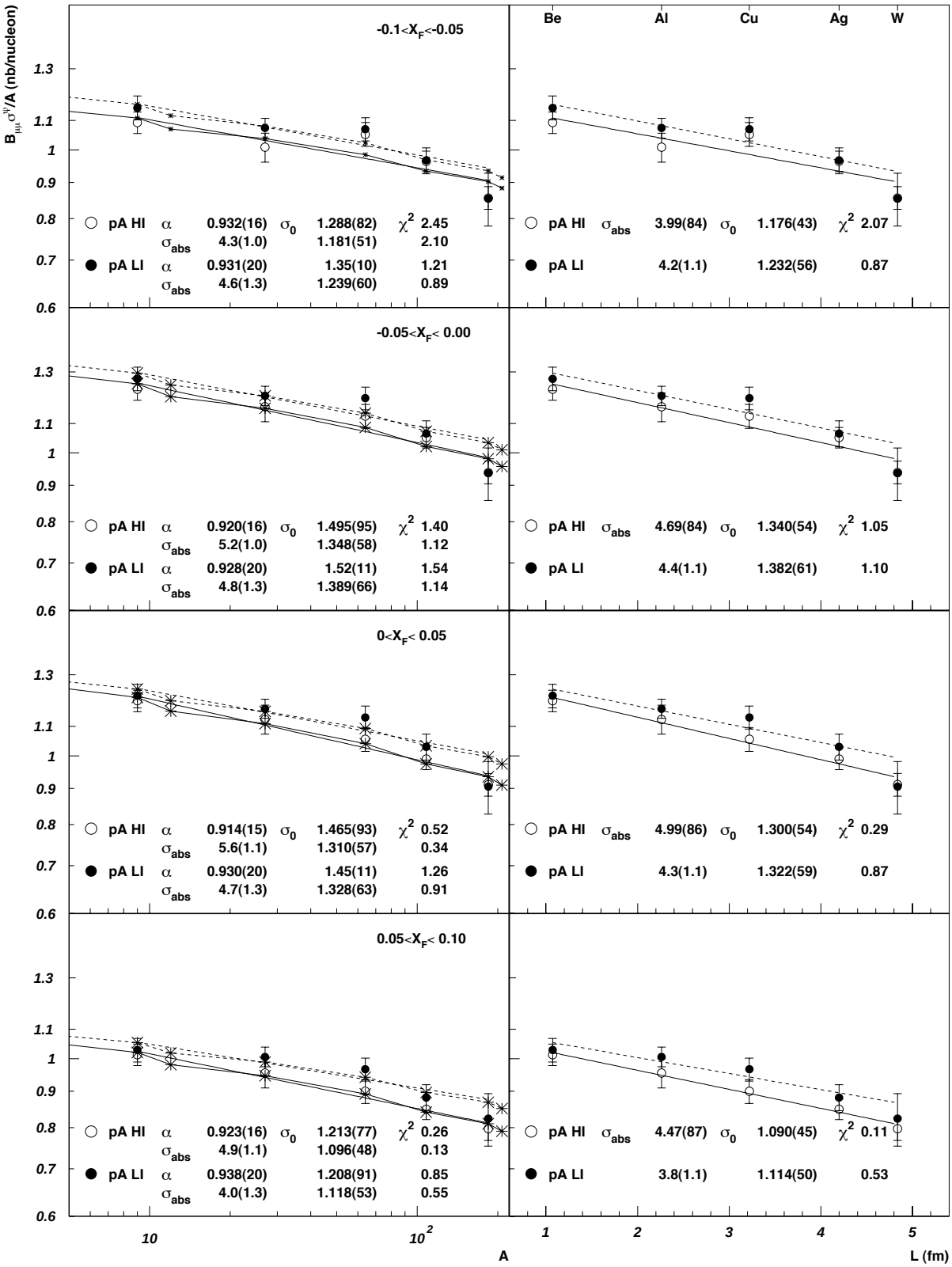

Figure 7.12: The J/ψ cross sections per nucleon (for the High (HI) and Low (LI) intensity data sets) in four X_F bins fitted by the: (Left) parametrization $\sigma_A = \sigma_0 A^{\alpha}$ (the results are shown on the first line of the legend) and the complete Glauber model (second line); (Right) parametrization $\sigma_A = \sigma_0 e^{-<\rho L>\sigma_{abs}}$. The values for the σ_0 and σ_{abs} are in *nb* and *mb* respectively.

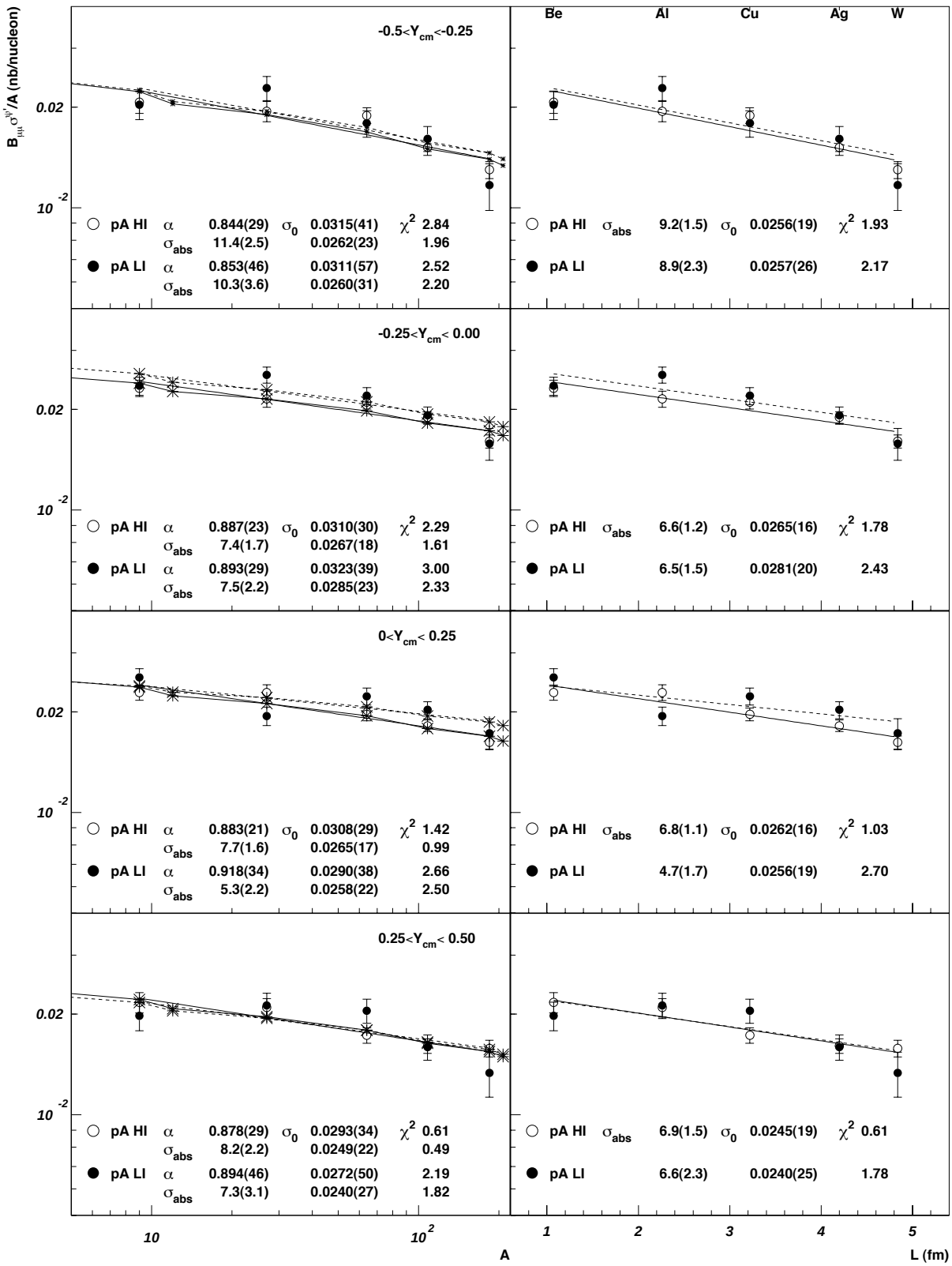

Figure 7.13: The ψ' cross sections per nucleon (for the High (HI) and Low (LI) intensity data sets) in four Y_{CM} bins fitted by the: (Left) parametrization $\sigma_A = \sigma_0 A^{\alpha}$ (the results are shown on the first line of the legend) and complete Glauber model (second line); (Right) parametrization $\sigma_A = \sigma_0 e^{-<\rho L>\sigma_{abs}}$. The values for the σ_0 and σ_{abs} are in *nb* and *mb* respectively.

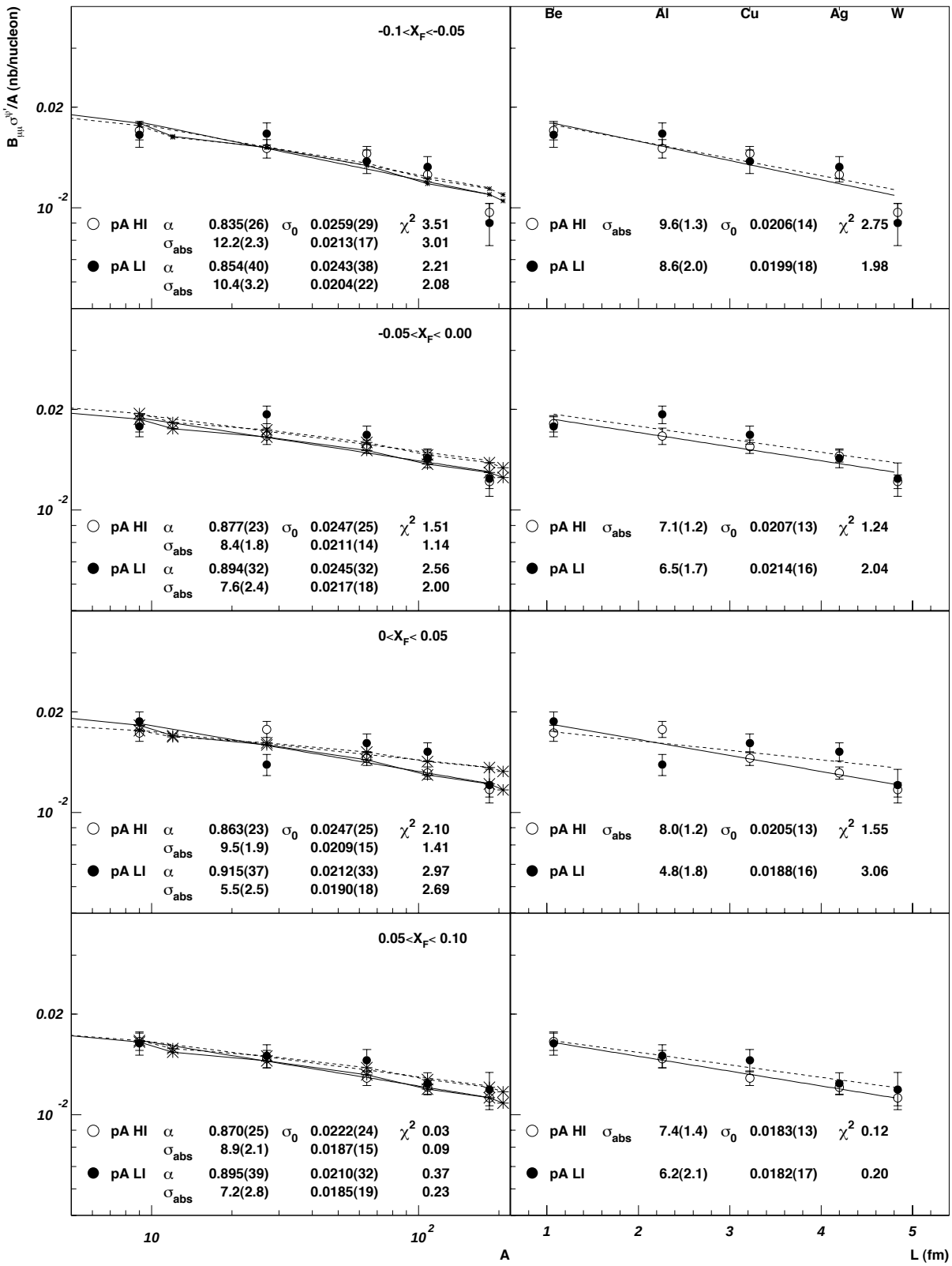

Figure 7.14: The ψ' cross sections per nucleon (for the High (HI) and Low (LI) intensity data sets) in four X_F bins fitted by the: (Left) parametrization $\sigma_A = \sigma_0 A^{\alpha}$ (the results are shown on the first line of the legend) and complete Glauber model (second line); (Right) parametrization $\sigma_A = \sigma_0 e^{-<\rho L>\sigma_{abs}}$. The values for the σ_0 and σ_{abs} are in *nb* and *mb* respectively.

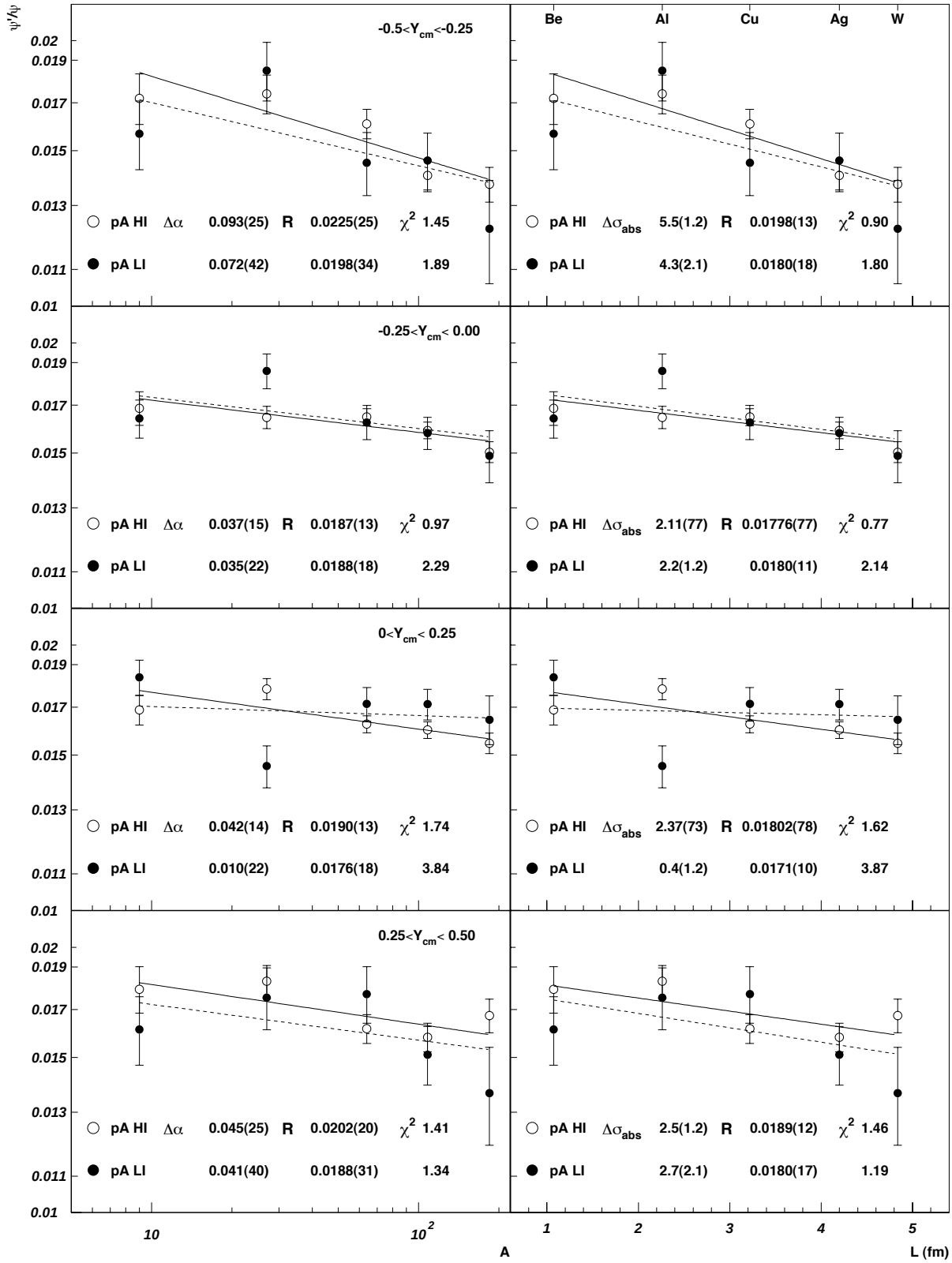

Figure 7.15: The ratio of the ψ' to J/ψ cross sections per nucleon (for the High (HI) and Low (LI) intensity data sets) in four Y_{CM} bins fitted by the: (Left) parametrization $R_0 A^{\Delta\alpha}$; (Right) parametrization $R_0 e^{-<\rho L>\Delta\sigma_{abs}}$. The values for the $\Delta\sigma_{abs}$ are in *mb*.

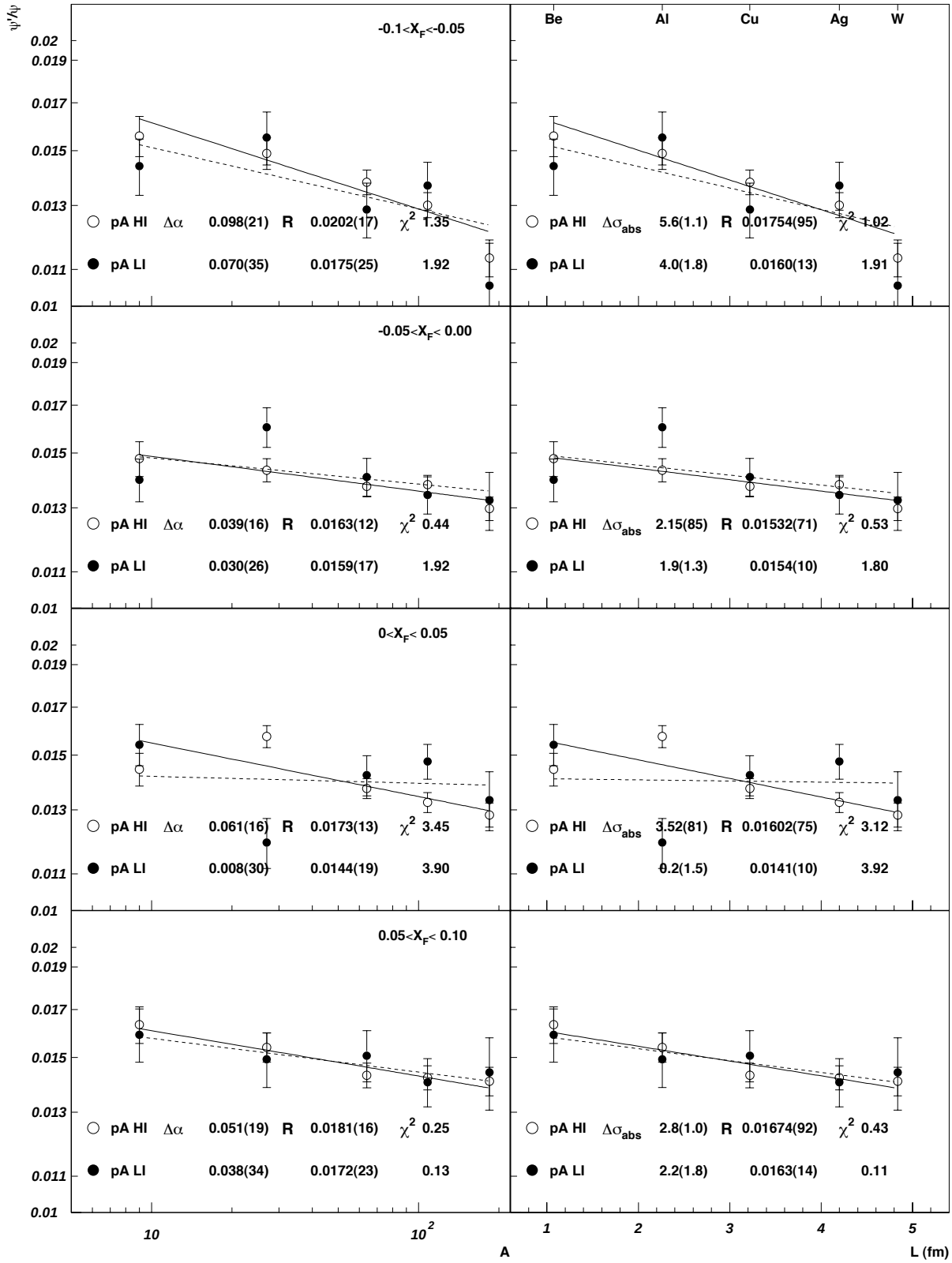

Figure 7.16: The ratio of the ψ' to J/ψ cross sections per nucleon (for the High (HI) and Low (LI) intensity data sets) in four X_F bins fitted by the: (Left) parametrization $R_0 A^{\Delta\alpha}$; (Right) parametrization $R_0 e^{-<\rho L>\Delta\sigma_{abs}}$. The values for the $\Delta\sigma_{abs}$ are in *mb*.